



HAL
open science

Modélisation de l'écoulement du jeu radial en compresseurs axiaux

Christophe Montsarrat

► **To cite this version:**

Christophe Montsarrat. Modélisation de l'écoulement du jeu radial en compresseurs axiaux. Other. Université de Lyon, 2021. English. NNT : 2021LYSEC014 . tel-03544200

HAL Id: tel-03544200

<https://theses.hal.science/tel-03544200>

Submitted on 26 Jan 2022

HAL is a multi-disciplinary open access archive for the deposit and dissemination of scientific research documents, whether they are published or not. The documents may come from teaching and research institutions in France or abroad, or from public or private research centers.

L'archive ouverte pluridisciplinaire **HAL**, est destinée au dépôt et à la diffusion de documents scientifiques de niveau recherche, publiés ou non, émanant des établissements d'enseignement et de recherche français ou étrangers, des laboratoires publics ou privés.



Numéro d'ordre : 2021LYSEC14

THÈSE DE DOCTORAT DE L'UNIVERSITE DE LYON
opérée au sein de l'Ecole Centrale de Lyon

Ecole doctorale N° 162
Mécanique, énergétique, génie civil et acoustique (MEGA)
Spécialité : Mécanique des fluides

Soutenue publiquement le 09/04/2021 par :
Christophe Montsarrat

**Tip-leakage flow modelling
in axial compressors**

Devant le jury composé de :

Marcello MANNA	Professeur, Université de Naples Federico II	Rapporteur
Nicolas BINDER	Professeur, ISAE-SUPAERO	Rapporteur
Vincent BRION	Docteur, Ingénieur de recherche ONERA	Examinateur
Isabelle TRÉBINJAC	Professeure émérite, Ecole Centrale de Lyon	Examinatrice
Jérôme BOUDET	Maître de conférences HDR, Ecole Centrale de Lyon	Directeur de thèse
Julien MARTY	Docteur, Ingénieur de recherche ONERA	Co-directeur de thèse
Eric LIPPINOIS	Ingénieur, Safran Aircraft Engines	Invité

"En effet, la sérénité - et non la vérité - est le but qu'il faut poursuivre : ce qui nous perd et nous tourmente, c'est notre volonté de tout savoir, de croire qu'un problème possède toujours une solution."
— tiré des *Essais* de Michel de Montaigne.

ACKNOWLEDGEMENTS/REMERCIEMENTS

S'il y a bien une phrase qui résume mon évolution tout au long de ma thèse, c'est celle-ci. Et je m'y suis toujours raccroché, dans ma thèse comme dans ma vie, depuis que j'ai redécouvert Montaigne et sa magnifique philosophie de vie ¹, au milieu de ma thèse. Les moments de tensions, d'incertitude, sont nombreux et normaux dans un travail de recherche mais j'ai appris avec le temps que le plus important était de les prendre avec du recul, avec sérénité et dans un état d'esprit apaisé. C'est à chaque fois comme cela que j'ai réussi à avancer dans mes travaux, et surtout à maintenir un équilibre du point de vue personnel. Il y a des jours, des semaines où rien ne marche, eh bien soit ! La situation s'est maintes fois débloquée quand j'ai laissé les choses reposer et quand je suis revenu vers elles l'esprit calme et serein. Parfois ce n'est pas que le problème ne possède pas de solution mais simplement qu'il est mal posé. J'ai évidemment beaucoup appris en aérodynamique pendant ces trois années de thèse mais j'ai surtout appris sur moi-même, ma gestion des émotions et ma capacité à mener au bout un long projet comme la thèse. Je n'aurais jamais pu mener ces travaux à bien tout seul et je veux commencer ce manuscrit en remerciant toutes celles et tous ceux qui m'ont permis de rendre tout cela possible.

Je remercie le jury pour avoir accepté d'évaluer mes travaux et particulièrement Nicolas Binder pour avoir rapporté mon manuscrit puis présidé le jury. Vos remarques et suggestions ont contribué à améliorer le manuscrit dans la compréhension de sa structure et permettent, j'espère, de mieux en apprécier le contenu.

Je veux remercier mes trois encadrants Julien, Eric et Jérôme pour m'avoir accompagné et suivi tout au long de ses travaux, pour leur lucidité et leurs conseils, qui m'ont bien souvent permis de sortir des mauvais chemins et me remettre sur les rails. Julien, merci pour ton aide au début de ma thèse, pour m'avoir introduit aux simulations CFD et à toute la boîte à outils (une boîte bien remplie...!) qui les accompagnent. Eric, je veux te remercier particulièrement pour ton soutien toujours sans faille, ta bienveillance, ton aide aussi bien technique que morale, et ta passion pour les turbomachines et l'aérodynamique de manière plus générale, qui m'auront inspiré, même à distance la plupart du temps. Et aussi pour tous tes conseils montagnards ! Jérôme, je tiens aussi à te remercier particulièrement pour ton accompagnement toujours riche de précieux conseils. Tu as toujours su trouver les mots justes, me remettre dans la bonne direction quand je faisais fausse route, m'interpeller et me redonner envie lorsque la motivation manquait mais aussi me tempérer lorsque je débordais un peu trop d'idées.

Côté Safran, je veux remercier Simon M., William R., Alexandre M. et Grégory D. pour nos

¹Merci à François Busnel et ses petites chroniques littéraires pour m'avoir fait replonger dans ce livre d'ailleurs !

discussions, aux JDD ou ailleurs. Merci aussi à toute l'équipe YHMA pour votre accueil pour les quelques semaines passées avec vous au tout début de ma thèse.

Je veux remercier toutes les personnes de l'ONERA avec qui j'ai travaillé, et particulièrement mes collègues d'H2T, pour tous les bons moments passés là-bas pendant ma première année de thèse, toutes les discussions dans la salle café mais aussi pour toutes les bonnes soirées que j'ai passées avec vous. Merci aux turbomachinistes pour m'avoir initié au domaine. Raphaël, Lionel, Benjamin F., merci pour votre aide et pour toutes les discussions que j'ai pu avoir avec vous. Merci particulier à toi Benjamin F., c'était un plaisir de partager mes galères de néophyte à la ZDES avec toi. J'en profite pour remercier Fabien G., Sébastien D. et Nicolas R. pour leur aide sur la ZDES. Merci aussi à Alain Refloch pour sa grande réactivité et pour m'avoir permis de bénéficier des heures de calculs sur Cobalt. Merci à Maxime puis Camille avec qui j'ai eu le plaisir de partager mon bureau pendant cette année-là. Merci à Luis, Miguel, Michel, Benjamin G., Amaury, Rami, Cédric pour leur bonne humeur, nos discussions riches et variées, pour tous les afterworks H2T. Un merci particulier à Luis, ta passion pour l'aérodynamique est contagieuse et les discussions avec toi ont toujours été inspirantes. Merci aussi à Simon B. et Benjamin D. pour nos discussions du coin café. Un merci particulier pour ce dernier : nos thèses se sont chevauchées pendant un bon moment et tes travaux expérimentaux et numériques sur les écoulements de jeu ont largement été mis à contribution pour mes travaux. Merci encore au reste de l'équipe pour votre accueil !

Bien évidemment, je veux aussi remercier tout le LMFA, avec qui j'ai passé mes deux dernières années de thèse. Merci à tous les doctorants, Gabriel, Aurélien, Nicolas P., Martin R., Ivo, Anne-Lise, Valdo, Thomas, Florent, Alexandra pour nos toutes nos discussions turbomachines mais aussi pour tous les bons moments passés avec vous, pour tous les litres de bières aux 3B, pour les soirées au petit salon (à l'époque...), les pique-niques à la tête d'or ou à Miribel, le tennis ou même la montagne. On s'est malheureusement tous moins vus pendant cette longue période Covid mais je garderai forcément un bon souvenir de ces moments avec vous. Un merci tout particulier à Gabriel avec qui j'ai eu le grand plaisir de partager mon bureau pendant ces deux années passées au LMFA. On a pu partager nos joies, nos déceptions, nos baisses de motivation, nos doutes, râler sur elsA ou réécrire le monde sur notre (très !) précieux tableau blanc. Merci aussi à toute l'équipe pédagogique avec qui j'ai pu avoir de nombreuses discussions, toujours intéressantes. Et merci à toute l'équipe en général aussi, à tous ceux que j'ai pu croiser aux afterworks aux 3B ou ailleurs.

Les conditions sanitaires pour la soutenance étaient spéciales et elle n'a malheureusement pu se tenir qu'à travers un écran. J'en garde un souvenir impérissable et mémorable, grâce à tout votre soutien à tous, malgré la distance. Je remercie mes amis Marc, Charles, Elsa, Corentin, Joris, Paul, Quentin, Pierre qui m'ont suivi à travers ces trois ans jusqu'à la soutenance et jusqu'à la dépendaison de crémaillère à Lyon qu'on a pu fêter ensemble après le déconfinement, en guise de rattrapage de fin de thèse. Merci aussi à Grégoire, Léopold et Sébastien, un plaisir d'avoir fêté ça avec vous aussi. Merci également à Rémi, Amélie, Marc D., Romain, Sacha, Felix, Tess, Valentin, Arthur, Théo, Harold, Salambô, Cécile, Morgane et Elodie.

Enfin, je veux remercier toute ma famille qui a assisté à la soutenance. Cela m'a fait très chaud au cœur de vous voir tous connectés pour me soutenir. Un vrai soutien qui m'a donné de

la force et de l'envie pour défendre mes travaux. Je remercie tout particulièrement ma maman qui était à Lyon malgré les conditions sanitaires. Je te remercie plus généralement pour ton soutien de toujours, pour ta bienveillance, ton dynamisme, ta joie de vivre et simplement pour tout l'amour que tu m'as toujours porté.

ABSTRACT

Tip-leakage flow (TLF) represents a major limitation in compressor performance, complexifying the blade designs at the tips. Affecting both the losses and the performance, the tip-leakage vortex (TLV) forming at the tip of rotor blades is a dominant vortical structure that all designers aim to reduce. The TLV is mostly influenced by three parameters whose increase is detrimental to the performance of the compressor: the blade loading, the boundary layer at casing, and the tip gap size τ . The present thesis investigates the influence of the tip gap size on TLF. More specifically, the present work focuses on the evolution of three mean characteristics of the TLV with τ , whose variations can be directly related to the performance of the compressor rotor: the position where the TLV detaches from the blade, its trajectory, and its circulation Γ .

In order to investigate the influence of the tip gap size, two different methods are used in the present work. The first method relies on a Zonal Detached Eddy Simulation (ZDES), a hybrid RANS/LES approach, enabling to resolve the largest turbulent eddies where it is required. Such a method, generally more costly, is also generally more appropriate for secondary flows such as TLF than simulations based on RANS turbulence models. In particular, this enables a refined analysis on the turbulent fluctuations within the TLV. The second method is a low-order method, whose development is here carried out on tip-leakage flow configurations, gauging its capabilities when accounting for the tip gap size. The Vortex Lattice Method (VLM) relies on the use of vortex singularities to replicate the presence of an aerodynamic body, which induces a perturbation on the velocity field. This approach is computationally cheap and is dedicated to preliminary design, when a large quantity of geometries have to be evaluated.

A sensitivity study on the tip gap size is conducted on the third rotor of an experimental high-speed compressor with the use of ZDES. Three tip gap sizes are tested. The time-averaged analysis confirms results from the literature on the position of the detachment point. It also indicates that the mean trajectory of the TLV could be predicted by a model, based on the knowledge of the midspan loading. Finally, it puts forward the increase of circulation with the tip gap size, with a larger TLV core and higher levels of axial vorticity. The unsteady analysis focuses on the interaction between the neighbouring TLV and the TLF developing within the gap: the intensity of the double leakage phenomenon is largely affected by the tip gap size. The vortex fragmentation only observed with the largest gap could be related to the more intense double leakage and a possible vortex wandering, with low-frequency oscillations.

The use of the VLM on a simplified experimental TLF configuration, consisting of a single blade interacting with a casing endwall, shows that it is accurate for predicting the TLV circulation for

large tip gaps but it requires improvements to account for the viscous effects on the diffusion of the TLV detaching from the blade and its interaction with the casing endwall. A diffusion model is developed as a correction to the original VLM in order to account for these effects. By considering the turbulent mixing of pairs of contra-rotating analytical vortices, the experimental increase of the circulation is well captured by the corrected VLM over a large range of tip gaps. Further developments are needed regarding the prediction of the blade loading, in order to predict the position of the detachment point. Also, in the continuity of this work, further developments are needed to use the VLM module on compressor rotors, in the long-term objective of building a fast and accurate predesign tool.

Keywords: Axial compressor, Tip-leakage flow (TLF), Tip-leakage vortex (TLV), Vorticity, Circulation, Zonal-Detached Eddy Simulation (ZDES), Vortex Lattice Method (VLM), Modelling

RÉSUMÉ

Les écoulements de jeu en tête d'aubes de rotors représentent une limitation majeure sur les performances d'un compresseur et complexifient le dessin des aubes en tête. La formation du tourbillon de jeu en tête de pale de rotor induit d'importantes pertes dans la zone de tête, réduisant de fait les performances du compresseur. Le tourbillon de jeu est une structure tourbillonnaire dominante dans la zone de tête, particulièrement influencée par trois paramètres : la charge en tête d'aube, l'épaisseur de la couche limite au carter et la taille du jeu τ . La présente étude vise à caractériser l'influence de la taille de jeu sur l'écoulement de jeu. Plus précisément, elle s'intéresse à trois caractéristiques du tourbillon de jeu, dont les variations peuvent être associées à la baisse des performances du rotor : la position du détachement du tourbillon sur l'extrados de la pale, sa trajectoire dans le canal inter-aubes et sa circulation Γ .

Dans le but d'étudier l'influence de la taille de jeu, deux méthodes sont utilisées dans la présente étude. La première méthode est une approche haute-fidélité. La ZDES (Zonal Detached Eddy Simulation) est une approche hybride RANS/LES qui permet de résoudre les grandes échelles de la turbulence, dans les zones d'intérêt. Ce type de méthodes représente un bon compromis entre coût et précision de calcul. Le fait de résoudre les fluctuations des plus grandes échelles turbulentes dans le tourbillon de jeu est particulièrement intéressant en comparaison de simulations basées sur un modèle de turbulence RANS, dans l'optique d'une analyse instationnaire de l'écoulement en tête de pale de rotor. La seconde approche s'intéresse aux capacités d'une méthode potentielle, méthode basse-fidélité, appliquée aux écoulements de jeu. La méthode des panneaux tourbillonnaires (VLM) utilise une distribution de singularités tourbillonnaires pour reproduire l'objet aérodynamique, dont la présence induit une perturbation du champ de vitesses. Cette approche, peu coûteuse en calcul, est destinée aux étapes de pré-dimensionnement quand une grande variété de géométries doit être évaluée.

Une étude paramétrique sur la taille de jeu est réalisée sur le troisième rotor d'un compresseur haute-vitesse expérimental en utilisant la ZDES. Trois tailles de jeu sont testées. L'analyse moyennée en temps confirme les résultats de la littérature sur la position de détachement du tourbillon de jeu. Elle montre aussi que la trajectoire du tourbillon peut être prédite à l'aide d'un modèle analytique basé sur la connaissance de la charge à mi-envergure. Enfin, l'augmentation de la circulation avec la taille de jeu est observée, avec un tourbillon dont le cœur est plus large et des niveaux de vorticit  axiale plus importants. L'analyse instationnaire se concentre sur l'interaction entre le tourbillon voisin et l'écoulement de jeu : l'intensit  du double  coulement de jeu est affect e de mani re importante par la taille du jeu. La d composition

du tourbillon de jeu, observée uniquement dans le cas du plus grand jeu, pourrait être due à l'amplification du double écoulement de jeu, responsable d'oscillations basses fréquences du tourbillon. L'amplitude de ces oscillations, plus importante dans le cas du plus grand jeu, pourrait expliquer la déstructuration du tourbillon observée uniquement dans le cas du plus grand jeu.

L'utilisation de la VLM sur une configuration expérimentale d'un aubage en porte-à-faux avec une paroi fixe, dont la distance entre les deux (le jeu) peut être modifiée, montre que la méthode est suffisamment précise pour la prédiction de la circulation du tourbillon pour les plus grands jeux. Pour les petits jeux, une correction visqueuse a été développée et ajoutée au module VLM afin de capturer l'augmentation de la circulation avec la taille de jeu. Cette correction se base sur un nouveau modèle de diffusion considérant le mélange turbulent de deux tourbillons analytiques contra-rotatifs. La correction visqueuse permet une excellente prédiction de la circulation sur une large gamme de jeux. Toutefois, des améliorations supplémentaires sont à étudier afin de mieux prédire la charge en tête de pale avec la VLM et ainsi la position de détachement du tourbillon de jeu. Aussi, des développements restent à apporter afin de pouvoir appliquer la méthode potentielle et le modèle de diffusion à un rotor de compresseur.

Mots-clés : Compresseur axial, Écoulements de jeu, Tourbillon de jeu, Vorticité, Circulation, Zonal-Detached Eddy Simulation (ZDES), Méthode des panneaux, Vortex Lattice Method (VLM), Modélisation

INTRODUCTION	1
I WHAT IS TIP-LEAKAGE FLOW?	5
1 LITERATURE REVIEW ON TIP-LEAKAGE FLOW	7
1.1 Aerodynamics of compressors in turbomachines	9
1.1.1 Generalities on turbomachinery	9
1.1.2 Compressor performance	11
1.1.3 Compressor loss sources	13
1.1.4 Instabilities in compressors	17
1.2 Three-dimensional flows in turbomachines	22
1.2.1 Corner separations	22
1.2.2 Tip-leakage flow	24
1.3 Influent parameters on tip-leakage flow	29
1.3.1 Tip gap size	29
1.3.2 Casing boundary layer	32
1.3.3 Loading	32
1.3.4 Relative motion	35
1.3.5 Rotor-stator interactions	36
1.3.6 The double leakage phenomenon	38
1.3.7 Technological effects	39
1.4 Modelling tip-leakage flow	40
1.4.1 From the single blade towards high-speed compressors	41
1.4.2 Jet based models	42
1.4.3 Blockage models	43
1.4.4 Vorticity based models	44

1.5	Synthesis on the literature	51
II	METHODS FOR ANALYZING TIP-LEAKAGE FLOW	55
2	STRATEGIES FOR TIP-LEAKAGE FLOW SIMULATIONS	57
2.1	Introduction on simulating turbulence	58
2.1.1	The Navier-Stokes equations	58
2.1.2	Strategies for fluid dynamics simulations	59
2.2	Reynolds Averaged Navier-Stokes Equations (RANS)	61
2.2.1	Principle	61
2.2.2	Turbulence modelling	62
2.2.3	Compressible case	63
2.2.4	The Spalart-Allmaras model	63
2.3	Large Eddy Simulation (LES)	63
2.3.1	Strategy and use	63
2.3.2	Subgrid scale models	64
2.3.3	Estimation of the CPU cost	66
2.4	Zonal Detached Eddy Simulation (ZDES)	67
2.4.1	Introduction to hybrid simulations	67
2.4.2	Presentation of the ZDES	69
3	VALIDATION OF THE VORTEX LATTICE METHOD AND APPLICATION TO TIP-LEAKAGE FLOW	73
3.1	Introduction	74
3.2	Singularity methods	75
3.2.1	Potential flow theory	75
3.2.2	The problem of the wing	77
3.2.3	Application to three-dimensional bodies	81
3.2.4	Development of the module <i>PyLiSuite</i>	88
3.3	Validation of <i>PyLiSuite</i>	88
3.3.1	Two-dimensional validation	88
3.3.2	Three-dimensional validation	90
3.3.3	Influence of the HSV angle	92
3.4	Application to tip-leakage flow	96
3.4.1	Influence of the endwalls	97
3.4.2	Grid criterion on the tip gap size	100
3.4.3	Implementation of the symmetry condition	101
3.4.4	Generation of casing	102
3.4.5	Periodicity	105
3.4.6	Compressibility correction	108
3.5	Summary on the method	109

III	INFLUENCE OF THE TIP GAP SIZE ON TIP-LEAKAGE FLOW	111
4	ZDES INVESTIGATION OF TIP-LEAKAGE FLOW ON A HIGH-PRESSURE COMPRES-	
	SOR	113
4.1	Definition of the configuration	114
4.1.1	Experimental setup	114
4.1.2	Computational domain	116
4.1.3	Numerical setup	118
4.1.4	Boundary conditions	119
4.2	Parametric study on the tip clearance size	120
4.2.1	Presentation of the study	120
4.2.2	Performance	121
4.2.3	Radial profiles	122
4.2.4	Tip flow analysis	124
4.2.5	Mean tip-leakage vortex analysis	128
4.2.6	Unsteady analysis	135
4.2.7	The vortex wandering	144
4.3	Conclusions	147
5	EVALUATION OF THE VORTEX LATTICE METHOD ON A TLF CONFIGURATION AND	
	MODELLING OF THE TIP-LEAKAGE VORTEX	149
5.1	Presentation of the experiment	151
5.1.1	The experimental rig <i>S2l</i>	151
5.1.2	Experimental measurements	151
5.1.3	Numerical results	153
5.2	Evaluation of VLM on <i>S2l</i>	154
5.2.1	Conditions of application	154
5.2.2	Distribution of bound circulation	155
5.2.3	Shed circulation	156
5.2.4	Detachment point	161
5.2.5	Trajectory of the TLV	163
5.3	Construction of a viscous model	165
5.3.1	Viscous diffusion of a vortex dipole	165
5.3.2	Estimation of the eddy viscosity	168
5.3.3	Principle of the new model	169
5.3.4	Application to <i>S2l</i>	171
5.3.5	Axial evolution of Γ_{TLV}	174
5.3.6	Prediction of the circulation on <i>S2l</i>	174
5.4	Viscous model applied to VLM	176
5.4.1	Description of the new model	176
5.4.2	Results on the circulation	178
5.5	Discussions	181

5.5.1	Endwall/TIV interaction	181
5.5.2	Estimation of the eddy viscosity	181
5.5.3	Application to CREATE?	182
5.6	Conclusions	183
CONCLUSIONS		185
APPENDICES		191
A	DETAILS ON THE MODELS	191
A.1	Storer and Cumpsty's model	192
A.1.1	Derivation of the equations	192
A.1.2	Application to a simple case	194
B	COMPLEMENTS ON POTENTIAL FLOW METHODS	197
B.1	Prandtl's lifting line theory	198
B.1.1	The lifting line equation	198
B.1.2	Glauert's method	199
B.2	Three types of singularities	200
B.2.1	The source	200
B.2.2	The doublet	200
B.2.3	The vortex	201
B.3	Analytical vortices	202
C	PRELIMINARY STUDY TO THE ZDES APPROACH	205
C.1	Calibration of the boundary conditions	206
C.1.1	Three-stage simulation	206
C.1.2	Calibration of the ZDES simulation	208
C.2	Comparisons of RANS/ZDES results	213
C.2.1	Performance	214
C.2.2	Radial profiles	214
C.2.3	Tip flow analysis	217
D	COMPLEMENTS ON CHAPTER 4	227
D.1	Derivation of the circulation around a rotor blade	228
BIBLIOGRAPHY		231

List of Figures

1	Effect of the intensity and the position of the TLV in a rotor passage on the compressor performance.	2
1.1	Illustrations of turbofans.	10
1.2	Compression ratio as a function of the mass flow rate, normalized with respect to the design point, for an axial-flow and a centrifugal compressor [5].	11
1.3	Velocity triangles in the $(x, r\theta)$ plane for a constant radius, assuming the hub and casing radii are constant.	12
1.4	Characteristic map of a compressor.	13
1.5	Velocity profiles on blade walls, adapted from Bullock based on the cascade experiment of Lieblein [15].	15
1.6	Illustration of secondary flows within a compressor blade passage, from Moyle (1991) [98].	16
1.7	Sketch explaining the rotating stall process, from Emmons et al. [49].	18
1.8	Contours of $V_x > 0$ at midspan on the third stage of the research compressor CREATE [25]. The blue pockets indicate the position of the stall cells.	18
1.9	Representation of part-span cells propagating on rotor blades [49].	19
1.10	Two types of inceptions for rotating stall, from Camp and Day [17].	20
1.11	Time evolution of wall static pressure with modal and spike inceptions giving rise to rotating stall [17].	20
1.12	Sketch of the two different types of surge that can develop in a compressor, here on the design characteristic curve of the compressor.	21
1.13	Illustration of a corner separation between the endwall and the blade suction side [51].	23
1.14	Corner separation topology as proposed by Schulz <i>et al.</i> [121].	24
1.15	Lei's criterion for corner separation [83].	25
1.16	Sketch illustrating the formation of the tip-leakage vortex (TLV).	26

1.17 Streamlines of the mean flow in the blade tip region, from the LES simulation from Boudet <i>et al.</i> [11].	27
1.18 Axial development of the TLF loss coefficient $\bar{\zeta}_x$, from You <i>et al.</i> [153].	28
1.19 Schematic of a Rankine vortex on the evolution of v_θ with r , from Brookfield [14].	29
1.20 Effect of tip clearance size on the performance of a 6-stage compressor, adapted from Cumpsty (1989) [31].	30
1.21 Illustration of the mechanisms leading to high incidence and stall, where the stall flow coefficient is plotted as a function of the tip gap size, from [62].	31
1.22 Influence of the momentum thickness on the TLV trajectory, from Deveaux's RANS simulations [42].	33
1.23 Illustration of the spike-type scenario proposed by Vo <i>et al.</i> , from Tan <i>et al.</i> [136].	34
1.24 Topology of the flow in the clearance region with spike type inception. Presence of a tornado-like vortex identified by Yamada <i>et al.</i> [148].	35
1.25 Summary of the two types of stall inception related to the flow topology in the clearance region, from Tan <i>et al.</i> [136].	35
1.26 Effect of relative motion on the tip clearance velocity profiles and the position of the tip-leakage vortex relative to the suction side, adapted from Deveaux [42]. . .	36
1.27 Comparison of cases without (upper blade) and with (lower blade) incoming wake interaction with TLV.	37
1.28 Influence of a passing wake on the TLV near the tip, from Mailach <i>et al.</i> [87]. . .	38
1.29 Illustration of the double leakage occurring in steady and unsteady conditions, from [124].	39
1.30 Losses variations with a squealer, from Wlassow [147].	40
1.31 List of the main effects encountered by the tip-leakage flow from the single blade configuration to a high-speed compressor.	41
1.32 Schematic of Storer and Cumpsty's model of leakage jet mixing with mainstream flow, adapted from [134].	43
1.33 Velocity profile in a crossflow plane downstream of the clearance exit, from Khalid [73].	45
1.34 Schematic of Khalid's wake TLF model, based on the two-dimensional modelling of Hill.	45
1.35 Schematic of the lifting line model used by Lakshminarayana and Horlock, the shadowed blade corresponds to the fictive mirror line used in this model.	46
1.36 Illustration of the vortex characteristics used in Lakshminarayana's model [79]. .	48
1.37 Illustration of the evolution of the TLV in the successive crossflow planes, from an unsteady two-dimensional model flow, from Chen's thesis [20].	50
2.1 Classification of the most common methods used when simulating turbulent flows, adapted from [118].	60
2.2 Evolution of the normalized mean axial velocity with y^+ for a canonical boundary layer, adapted from [105].	66
2.3 Summary on the three modes of the zonal approach ZDES.	70

2.4	Example of use of the zonal strategy on a three-element aerofoil [36].	71
3.1	Discretization of an aircraft into source panels, from Katz and Plotkin [72].	75
3.2	Illustration of the potential flow problem, where the velocity components are to be calculated at point P	77
3.3	Basic definitions and notations for the wing airfoil, adapted from Katz and Plotkin [72].	78
3.4	Decomposition of the thin airfoil problem into a thickness and a lifting problem.	79
3.5	The horseshoe vortex (in red) modelling a wing of span b . Points A and B are at each tip of the wing.	82
3.6	Illustration of the lifting line approach as developed by Prandtl, from [72].	83
3.7	Decomposition of the angle of attack α as a function of the effective angle α_e and the induced angle α_i	83
3.8	Illustration of the Vortex Lattice Method (VLM) for a flat plate. The flat plate is discretized by horseshoe vortices in red. The collocation points are indicated by the blue squares.	85
3.9	Illustration of the Vortex Lattice Method (VLM) for a flat plate. The flat plate is discretized by horseshoe vortices in red.	86
3.10	Illustration of the Vortex Lattice Method (VLM) for a flat plate. Trailing vortices are shed to infinity with an angle θ_{HSV} with the x -axis.	87
3.11	Flat plate configuration in two dimensions.	89
3.12	Validation of the <i>PyLiSuite</i> VLM on the lift and pressure difference coefficients c_l and Δc_p , for a flat plate. Aspect ratio $AR = b/c = 1000$	90
3.13	Validation of the <i>PyLiSuite</i> VLM on the NACA0012 airfoil with $AR = 1000$	91
3.14	Validation of the VLM module <i>PyLiSuite</i> on the spanwise normalized circulation distribution.	91
3.15	Grid of the elliptical wing used for VLM, and comparison with the lifting line theory results. The blue line corresponds to the results from the lifting line theory coded numerically in <i>PyLiSuite</i> , the black dashed line is the analytical result from lifting line theory.	93
3.16	Evolution of C_{l_α} with the aspect ratio AR for the elliptical wing, from the analytical expression, numerical lifting line theory (<i>PyLiLi</i>) and VLM (<i>PyLiSu</i>).	93
3.17	Wake thickness in the airfoil plane due to the HSV angle.	94
3.18	Impacts of the trailing vortices in the plane $x = 1.05c$, right downstream the trailing edge of the flat plate. Comparison between two HSV angles for $\alpha = 5^\circ$ and $AR = 1$. The contour colours correspond to the positions from which the legs of the HSV are shed (0: leading edge to 1: trailing edge) and the size of the disks relates to the intensity of the vortices.	95
3.19	Evolution of the relative error on the lift coefficient on the flat plate with $\alpha = 5^\circ$, with the reference case at $\theta_{HSV} = 0^\circ$, as a function of the wake width-to-span ratio w_{wake}	96
3.20	Wake thickness in the airfoil plane generated by a surface distribution of vortices.	96

3.21	Sketches of the four cases of reference regarding the two conditions of symmetry. The dashed lines indicate that the surface is a mirror blade. The TLF configuration corresponds to case 11.	98
3.22	Grid convergence on the lift coefficient. N_{pts} represents the number of points chordwise and spanwise, with a constant growth ratio $g = 1.05$	99
3.23	Evolution of the ratio $c/\Delta_{0,c}$ with the number of points used on a bigeometric distribution, with a constant growth ratio $g = 1.05$	99
3.24	Spanwise circulation distribution for the four cases, with the 37×37 converged grid.	100
3.25	Evolution of the lift coefficient obtained with <i>PyLiSuite</i> , with the camber formulation, on the NACA0012 and NACA4412 airfoils, with an aspect ratio $AR = 1$ and $\alpha = 5^\circ$. Five different tip gap sizes are tested for configuration 11.	101
3.26	Evolution of the normalized bound circulation with the span comparing the reduced system to the complete linear system in case 11. The convergence to the theoretical symmetry condition is obtained in the second figure with 5 blades on each side of the central blade (total: 10 blades).	102
3.27	Views of the configuration with a plate generated for modelling the presence of a casing.	103
3.28	Grid convergence on the lift coefficient with a plate generated for casing, in the case of a flat plate blade. Comparison with the case of reference 11 with a symmetry condition.	103
3.29	(a) Comparison of the circulations from the symmetry condition and the application of a casing plate, with $L_{casing} = 12c$. (b) CPU time indicated as a function of the extension of the casing.	104
3.30	Total number of points for $L_{casing}/c = 12$ with the grid criteria applied on the blade ($AR = 1$) and the casing plate, as a function of the tip gap size.	105
3.31	Sketch of a 11-blade linear cascade generated with <i>PyLiSuite</i>	106
3.32	Test of the periodicity and the periodicity condition with <i>PyLiSuite</i> on case 00.	107
3.33	Test of the periodicity and the periodicity condition with <i>PyLiSuite</i> on case 11.	107
3.34	Lift coefficient C_L with the Prandtl-Glauert correction, for the two VLM formulations.	109
4.1	Picture of the compressor CREATE.	115
4.2	Meridian view of CREATE.	115
4.3	Screenshot of the computational domain used for the study. The inlet plane and two planes of reference (280 and 28A) from the experiment are indicated.	117
4.4	Explanation of the use of the second mode of ZDES applied on a compressor rotor.	118
4.5	Boundary layer profile at casing in plane 280, upstream the rotor.	121
4.6	Compression and temperature ratio distributions between planes 28A and 280.	123
4.7	Radial distributions of normalized axial velocity and relative fluid angle β in plane 280.	124

4.8	Radial distributions of normalized axial velocity and relative fluid angle β in plane 28A.	125
4.9	Eddy-to-molecular viscosity ratio contours for the three tip gap sizes. Isolines represent the two values of the sensor f_d indicated in the legend. A LES resolution corresponds to $f_d = 1$ and a RANS resolution to $f_d = 0$. The locations of the cutting planes are the same as in Figure C.19.	126
4.10	Isosurfaces of Q-criterion colored by normalized helicity from -1 (blue) to 1 (red).	126
4.11	Entropy contours at 94% height for the three different gaps.	127
4.12	Entropy contours at 97% height for the three different gaps.	127
4.13	Pressure difference coefficient at midspan and at the tip (99% blade span).	128
4.14	(a) Screenshot of the blade and clearance for CREATE A (clearance in red). (b) Zoom in the clearance near the leading edge on the suction side of the blade.	129
4.15	Normalized leakage velocity profiles in the clearance of each case, in the prolongation of the suction side of the blade. The red squares indicate the respective position of the maximal magnitude of leakage velocity. The green dots indicate the positions of the slope breaks for CREATE A and B.	130
4.16	View on the suction side and tip of the blade. Time averaged streamlines at the tip of the blade and contours of the normalized static pressure on the blade skin.	131
4.17	Contours of the density at 94% height for the three cases. The mean trajectory of the TLV, determined graphically, is indicated by the black line if possible to be identified clearly. The red dashed line shows the mean trajectory from Chen's correlation.	132
4.18	Contours of the density at 97% height for the three cases. The mean trajectory of the TLV, determined graphically, is indicated by the black line if possible to be identified clearly. The red dashed line shows the mean trajectory from Chen's correlation.	133
4.19	Evolution of the mean vorticity magnitude through cutting planes perpendicular to the suction side of the blade (at 10, 21, 40, 61, 95 % c_a), for the three gap sizes. The same scale is used for the vorticity magnitude in the three figures.	133
4.20	Radial distribution of the normalized circulation $\Gamma(r) = -s(r) \frac{\Delta V_\theta}{U_\infty c_a}$ for the three gap values, compared with the LDA measurements on CREATE A.	135
4.21	Power spectral density of the axial velocity expressed in dB as a function of the frequency. The reference velocity for the gain calculation is set to $U_{ref} = 1$ m/s.	136
4.22	Power spectral density for the static pressure expressed in dB as a function of the frequency and the dimensionless Strouhal number, based on the respective tip gap size of each case. The reference pressure is set to $p_{ref} = 2 \times 10^{-5}$ Pa.	137
4.23	Streamwise evolution of the resolved turbulence level contours (in %) in planes perpendicular to the suction side of the blade (10, 21, 40, 61 and 95% axial chord.) The green squares indicate the position of the slope change in the leakage velocity plot.	138

4.24	Location of the probes where the spectra are extracted in red, following the trajectory of the TLV. The black grid shows the grid of probes where the spectra can be extracted at this height.	140
4.25	Power spectral density of the axial velocity at probes 1, 2 and 3. The reference velocity is $U_{ref} = 1 \text{ m/s}$	141
4.26	(a) Location of the three probes for case C. (b) Power spectral density of the axial velocity at probes 1, 2 and 3. The reference velocity is $U_{ref} = 1 \text{ m/s}$	143
4.27	(a) Illustration of the wandering motion of the TLV core (in blue) in a rotor passage around mean position over time (in red dashed). In these conditions, the amplitude of the oscillations is such that a spillage occurs in front of the leading edge of the neighbouring blade, likely to trigger a rotating stall due to a spike inception. (b) Illustration of the excitation of the TLV oscillations from one passage to another. D indicates the detachment point of the TLV in both figures.	146
5.1	Sketch of the tip-leakage flow configuration $S2l$ on a single blade.	152
5.2	Description of the TLV from the 5-hole probe measurements with $\tau/c = 3.5\%$. Dotted lines represent the positive vorticity, solid lines the negative vorticity, adapted from [42].	153
5.3	Discretization used on the flat plate between the hub ($y = b$) and the tip ($y = 0$). 37 points chordwise and 92 points spanwise. The red lines represent the legs of the shed horseshoe vortices along the span.	155
5.4	(a) Evolution of the lift coefficient C_L with respect to the tip gap size τ obtained with VLM. (b) Spanwise distribution of lift with VLM and from the RSM simulation with a no-slip condition at casing and $\theta/c = 0.6\%$	156
5.5	Normalized circulation of the TLV at position $x/c = 1.05$, as a function of the tip gap size, from the experiment, from the RSM based on a non-penetration condition at casing, and from the integration of the shed vorticity with VLM. The circulation is normalized by $U_\infty c$	158
5.6	(a) Sketch of two infinite vortices of opposite circulation $\Gamma = 0.5 U_\infty c$ (about the value predicted by VLM for the larger gaps, see Figure 5.5) at 2τ from each other. (b) Induced angle at point $P(x, r = c)$ as a function of the normalized tip gap size τ/c	159
5.7	(a) Sketch of two semi-infinite vortices of opposite circulation $\Gamma = 0.5 U_\infty c$ at 2τ from each other. (b) Induced angle at point $P(x = 0.5c, r = c)$ as a function of the normalized tip gap size τ/c	160
5.8	Axial evolution of Γ_{TLV} predicted with VLM and RSM with a non-penetration condition at casing.	162
5.9	Axial evolution of the pressure difference coefficient Δc_p for three tip gap sizes, (a) at midspan, and (b) at the tip ($y = 2\% b$, the tip being at $y = 0$).	163

5.10 Lateral trajectory of the TLV, comparing VLM with Chen’s correlation to numerical and experimental results (a) VLM, LDA measurements and RSM with a no-slip condition at casing. (b) VLM and RSM with non-penetration and no-slip conditions. The black crosses indicate the approximate position of the detachment point of the TLV (DP). 164

5.11 Contours of vorticity of the evolved Lamb dipole, from [140]. Solid lines represent the positive vorticity, dashed lines the negative one. 167

5.12 Evolution with time of the Lamb dipole, from [39]. Solid lines represent the positive vorticity contours, dashed lines the negative one. 167

5.13 Turbulent analytical line-vortex model from Owen [102], represented by the evolution of the circumferential velocity V_θ , denoted U in the figure, with the radius r 169

5.14 Sketch of the modelled interaction of two contra-rotating Lamb-Oseen vortices diffusing with time. 171

5.15 TLV core radius growth predicted by the model from the leading edge. The axial vorticity resulting from the mixing of the two vortices is integrated at the four different stations in the figure. Station 1 in particular corresponds to the plane of the experimental measurements. 172

5.16 Normalized axial vorticity against the radius in the tip region. The distributions of ω_x are plotted independently for the two vortices. The solid lines represent the evolution of $\omega_x^+(r, t)$, the dashed lines that of $\omega_x^-(r, t)$ 173

5.17 Normalized axial vorticity resulting from the sum of the two vorticities, against the radius in the tip region. 173

5.18 (a) Normalized circulation of the TLV as a function of the dimensionless time $\tilde{t} = t/T_0$ introduced by Delbende and Rossi [39] with $T_0 = \frac{\Gamma}{4r^2}$. (b) Evolution of $\Delta t_{phys}/T_{adv}$ with respect to the tip gap size, duration time over which the circulation decrease fits well with the DNS, for $\Lambda = 0.32$ 175

5.19 Normalized circulation of the TLV as a function of the tip gap size at four different axial stations from the model (triangles), compared with Γ_{TLV} obtained with the experiment (round), the RANS RSM with a no-slip condition at casing (crosses) and the RANS RSM with a symmetry condition at casing (squares). Two values of Λ are tested. (a) The equivalent of Λ is $\nu_t/\nu = 46$. (b) The equivalent of Λ is $\nu_t/\nu = 150$ 176

5.20 Normalized circulation shed at the blade tip as a function of x/c , as predicted by the VLM. 177

5.21 Illustration of the viscous correction integrated to the chordwise distribution of shed circulation predicted by VLM. (a) Chordwise distribution of mirror shed circulations. (b) Application of the viscous model to the i^{th} vortex pair. 179

5.22 Normalized circulation of the TLV with respect to the normalized tip gap size, predicted by the two-vortex model and the model based on VLM, compared to the experiment and the RANS. 179

5.23	Axial evolution of the normalized circulation Γ_{TLV} for three tip gap sizes, captured by the model and compared to the RANS. (a) RSM with a non-penetration condition at casing, $\Lambda = 0.58$ for the VLM model. (b) RSM with a no-slip condition at casing, $\Lambda = 1.5$ for the VLM model.	180
5.24	Sketch of a cambered blade from which the TLV detaches at DP . The camber line over which the HSV are distributed is indicated by the dashed red line.	183
A.1	Loss in efficiency due to tip clearance flow for a repeating stage of compressor for 50% degree of reaction, from model's application.	195
B.1	Decomposition of the angle of attack α as a function of the effective angle α_e and the induced angle α_i from equation (B.4).	199
B.2	Streamlines due to the doublet vector μ oriented in the axis direction x	201
B.3	(a) Normalized tangential velocity as a function of the distance to the core for three analytical vortices. (b) Resulting axial velocity $\omega_x(r)$	203
C.1	Illustration of the computational domain used for the 3-stage RANS simulation of the preliminary study. The blades shown are deformed on purpose in the picture.	208
C.2	Characteristic compressor map and isentropic efficiency of CREATE from the experimental measurements and obtained with the 3-stage RANS-SA approach. The operating point picked for the simulation is indicated with the blue square. The quantities are normalized by the experimental values obtained at the experimental nominal point.	209
C.3	Comparison between the target profiles from the 3-stage simulation and the resulting profiles in plane 280 with the isolated row.	210
C.4	Illustration of the calibration process after the first iteration.	211
C.5	Calibrated inlet profiles after thirteen iterations. The red profiles are those kept for the simulations.	212
C.6	Comparison of the static pressure profiles from the 3-stage RANS simulation and for the isolated rotor (RANS-SA and ZDES) in plane 28A.	213
C.7	Compression and temperature ratio distributions between planes 28A and 280.	215
C.8	Radial distributions of normalized axial velocity and relative fluid angle β in plane 280.	216
C.9	Radial distributions of normalized axial velocity and relative fluid angle (or deviation angle) β in plane 28A downstream rotor 3.	217
C.10	Contours of μ_t/μ in plane 280 with RANS and ZDES. The isolines of the protection function f_d are also shown for the ZDES. The dashed lines indicate $f_d = 0.99$ (LES zones), the solid lines $f_d = 0$ (RANS zones).	218
C.11	Contours of total pressure in plane 280 with RANS and ZDES. The isolines of the protection function f_d are also shown for the ZDES. The dashed lines indicate $f_d = 0.99$ (LES zones), the solid lines $f_d = 0$ (RANS zones).	219

C.12 Contours of μ_t/μ in plane 28A with RANS and ZDES. The isolines of the protection function f_d are also shown for the ZDES. The dashed lines indicate $f_d = 0.99$ (LES zones), the solid lines $f_d = 0$ (RANS zones). 220

C.13 Contours of total pressure in plane 28A with RANS and ZDES. The isolines of the protection function f_d are also shown for the ZDES. The dashed lines indicate $f_d = 0.99$ (LES zones), the solid lines $f_d = 0$ (RANS zones). 220

C.14 Eddy-to-molecular viscosity ratio contours for RANS and ZDES cases. In the right-hand figure, isolines represent the two values of the sensor f_d indicated in the legend. A LES resolution corresponds to $f_d = 1$ and a RANS resolution to $f_d = 0$. Planes perpendicular to the suction side of the blade at 0, 10, 21, 40, 61, 95% c_a 221

C.15 Q-criterion colored by normalized helicity from -1 (blue) to $+1$ (red). The value for the Q-criterion is the same in both figures. This Q-criterion is computed on the time-averaged flow conditions. 222

C.16 Map of the opposite of the relative tangential velocity in the tip region, time-averaged in the rotor frame of reference, at 75% axial chord, between 73.5 and 98% height over one passage. The shadow zone approximates the position of the blade. 223

C.17 Entropy contours at 94% height for RANS and ZDES approaches, with the same scale. 224

C.18 Entropy contours at 97% height for RANS and ZDES approaches, with the same scale. 224

C.19 Vorticity contours on planes perpendicular to the suction side at 10%, 21%, 40%, 61% and 95% c_a , for the steady RANS approach and the ZDES approach. 225

D.1 Velocity triangles illustrating the modification of the deviation $\beta_{2,2d}$, here an underturn, due to the presence of the TLV, inducing the angle β_{2i} 228

List of Tables

2.1	Criteria on the wall grid size expressed in wall units for three resolutions [118].	67
3.1	Main developments (left-hand column) and possible future improvements (right-hand column) of the VLM developed in the present thesis regarding TLF.	110
4.1	Number of blades per each row of CREATE.	115
4.2	Summary on the different types of measurements carried out on CREATE, used in the present thesis.	116
4.3	Summary of the main numerical parameters for the ZDES simulations on the third rotor of CREATE.	119
4.4	Tip gap values normalized by the largest gap value, for the parametric study.	121
4.5	Performance recap for the three different gaps of the study, normalized by the values of the nominal operating point from the experiment on CREATE A.	122
4.6	Estimation of the TLV angle based on the density contours and Chen's correlation.	132
4.7	Summary on the sensitivity analysis to the tip gap size on the third rotor of CREATE.	145
5.1	Main parameters of the experiment.	151
5.2	Tip gap sizes tested with VLM on <i>S2L</i>	154
5.3	Position of the local maximum of Δc_p at the tip, for the different tip gap sizes plotted in Figure 5.9, predicted by RSM.	163
C.1	Recap of the main numerical parameters of the 3-stage simulation.	207
C.2	Performance of the third rotor. Quantities normalized so as to be equal to 1 for the experimental design point.	214

Abbreviations

AR Aspect ratio $AR = \frac{b^2}{S}$, where S is the surface area.

DDES Delayed Detached Eddy Simulation

DES Detached Eddy Simulation

DNS Direct Numerical Simulation

DP Detachment point

HSV Horseshoe Vortex

IGV Inlet Guide Vane

LDA Laser Doppler Anemometry

LES Large Eddy Simulation

PSD Power Spectral Density

RANS Reynolds-Averaged Navier-Stokes Simulation

rpm Revolutions per minute

RSM Reynolds Stress Model

SA Spalart-Allmaras

SEM Synthetic-Eddy Method

SGS Subgrid Scale

t.e. Trailing edge

TLF Tip-leakage flow
TLV Tip-leakage vortex
URANS Unsteady RANS
VLM Vortex Lattice Method
WMLES Wall-modelled Large Eddy Simulation
WRLES Wall-resolved Large Eddy Simulation
ZDES Zonal Detached Eddy Simulation

Greek letters

α Absolute pitchwise fluid angle
 α Angle of attack
 α_i Induced angle, responsible for the generation of the induced drag
 β Relative pitchwise fluid angle. Also referred to as incidence in the inlet rotor plane as β_1 - β'_1 defines the incidence angle on the rotor
 β'_1 Metal angle, between the mean camber slope of the rotor blade at the leading edge and the axial direction
 ω Vorticity $\omega = \nabla \times \mathbf{u}$
 τ Viscous stress tensor
 δ Boundary layer thickness
 δ_{ij} Kronecker symbol
 η Kolmogorov length scale
 η_c Camber of the airfoil
 η_l Lower side of the airfoil
 η_t Thickness of the airfoil
 η_u Upper side of the airfoil
 γ Heat capacity ratio
 γ Stagger angle, angle between the horizontal axis and the chord line
 Γ_b Bound circulation

Γ_{TLV}	Circulation of the tip-leakage vortex
Λ	Coefficient in Owen's correlation [102]
$\mu_t = \rho\nu_t$	Dynamic eddy viscosity
μ_t/μ	Eddy-to-molecular viscosity ratio
ν	Molecular viscosity
ν_t	Kinematic eddy viscosity
ω_x	Axial vorticity
$\bar{\Delta}$	Subgrid length scale
Φ	Velocity potential
Π	Compression ratio
ρ	Density
τ	Tip gap size
τ_{exp}	Experimental temperature ratio
τ_{RANS}	Temperature ratio from RANS
τ_{ZDES}	Temperature ratio from ZDES
θ	Boundary layer momentum thickness
θ_{HSV}	Trailing vortex angle, defined between the legs of the HSV and the axial direction
$\tilde{\nu}$	Pseudo-viscosity in Spalart-Allmaras RANS model
$\tilde{\nu}$	Turbulent value of the SA model
ε_{TLV}	TLV angle relative to the blade, estimation of its mean trajectory in the passage
φ	Absolute pitchwise fluid angle

Indices and exponents

$(.)^+$	Length scale in wall units
$(.)_1$	Inlet rotor plane
$(.)_2$	Inter rotor-stator plane
$(.)_3$	Outlet rotor plane

- $(\cdot)_s$ Static value
 $(\cdot)_t$ Total value
 $(\cdot)_w$ Wall value
 $(\cdot)_\infty$ Freestream conditions
 $(\cdot)_{sgs}$ In the subgrid scale

Miscellaneous

- 280 Inlet plane of the third rotor of CREATE
28A Outlet plane of the third rotor of CREATE
S2l Tip-leakage flow experimental configuration at ONERA: parametric study on the tip gap size on a single blade interacting with the endwall.
elsA CFD software developed by ONERA and co-owned by Safran and Airbus
PyLiSuite Code developed on VLM in the present thesis
CREATE A Corresponding to the experimental configuration CREATE2bis
CREATE B Corresponding to the experimental configuration CREATE2
CREATE C Numerical case with the smallest tip gap on the third rotor

Operators

- ∇ Nabla
 $\frac{D}{Dt}$ Material derivative

Latin letters

- f Body force vector
 I Identity matrix
 q Heat flux vector
 R Reynolds stress tensor R_{ij}
 S Strain-rate tensor S_{ij}
 Δc_p Pressure coefficient difference, blade loading
 $\Delta h(r)$ Blade loading at radius r
 \dot{m} Mass flow rate

LIST OF SYMBOLS

γ	Circulation per unit span
ω	CREATE speed revolution $\omega = 11543 \text{ rpm}$
$\rho \mathbf{u}$	Momentum vector
b	Span
c	Chord length
c_a	Axial chord
C_L	3D lift coefficient
c_l	2D lift coefficient
f_d	Protection function used in the DDES and the ZDES for the RANS treatment of the boundary layer
K	Retained vorticity coefficient K , introduced by Lakshminarayana and Horlock [81]
k	Turbulent kinetic energy (TKE)
K_{Chen}	Constant from Chen's correlation on the TLV trajectory [20]
L	Lift
l	Lift per unit span
l_0	Characteristic length scale of the large turbulent structures
M	Mach number
p	Pressure
q^2	Double of the resolved total turbulent energy (mean and fluctuations)
r	Radius
R_c	Core radius of Lamb's analytical vortex
R_{gas}	Specific gas constant for air
Re	Reynolds number $Re = \frac{VL}{\nu}$
$s(r)$	Blade spacing or blade pitch of the row at radius r
t_w	Width of the wake generated by the legs of the HSV of VLM
T_{adv}	Advective time
T_{bp}	Blade passing period $\frac{2\pi}{\omega}$

Tu	Turbulence level
U_∞	Freestream velocity
U_{tip}	Velocity of the rotor at the tip
V_x	Axial velocity
V_θ	Absolute tangential velocity
W_θ	Relative tangential velocity
w_{wake}	Wake width-to-span ratio $w_{wake} = t_w/b$
St	Strouhal number $St_l = \frac{fl}{r_{tip}\omega}$, based on the length scale l

INTRODUCTION

With the aim of achieving a zero-carbon emission airplane, engine manufacturers have been investigating on new engine designs that could help go towards that long-term objective. On the occasion of the ASME TurboExpo conference 2020, Airbus announced they would invest massively on the research and development of hydrogen engines. Such engines are still far from being developed securely for an aircraft but the use of hydrogen could completely change the emission rates due to aircraft transportations.

Meanwhile, turbojet engines remain the most common and efficient engines on the market of airplanes in the middle term. Reducing the fuel consumption on such turbomachines remains a very challenging international issue that could not only impact the carbon emissions on current engines but also represent beneficial solutions for the next generation of engines to come.

Generally, an important breakthrough is sought to significantly improve the performance of aircraft engines. In the frame of new engine design developments, engine designers need better low-order tools, that are predictive, robust and fast. Massive optimization strategies rely on the use of such rapid methods to find the best possible design, responding to objectives fixed by the designer in terms of engine performance, towards less aerodynamic losses. Such optimizations cannot be associated to other computational fluid dynamics (CFD) simulations since the cost of a massive number of simulations testing different designs is still out of reach nowadays with a reasonable computational time. Even the poorest RANS simulations need at least half an hour to run.

The principle of a jet engine is to generate thrust by accelerating the flow. To achieve that, the primary circuit of heat engines mainly consists of compressors, a combustion chamber, turbines and a nozzle. The air is first compressed before being heated in the combustion chamber where the fuel is burned, releasing energy that is given to the exhaust gas. This gas is then expanded through the turbines and accelerated through the nozzle, to give rise to the thrust. Over its path, the flow undergoes losses that importantly reduce the efficiency of the engine and consequently increase the fuel consumption, and hence the carbon emissions on every flight. Designing optimal blades is hampered by the complexity of turbomachinery flows, highly tridimensional, in a confined space with very thick boundary layers and high compressibility effects,

whose accurate prediction is very difficult. These losses have been reduced a lot over the past few years but further progress is still sought today.

This thesis particularly explores the compressor rotor performance. The flow in a rotor passage is very complex and perturbed by several vortical structures, responsible for large losses within the passage. These three-dimensional flows affect the performance of the compressor and rotor designs must account for that. The present thesis focuses on *tip-leakage flow* (TLF), a phenomenon encountered at the tip of rotor blades. Because of the existing gap between the casing wall and the blade tip, ensuring that there is no friction, the pressure difference across the blade induces a flow in the pitch direction that rolls up into a vortex, the tip-leakage vortex (TLV). This vortex disturbs the flow in the tip region and can be responsible for up to 30% total losses for the machine [41].

The presence of the TLV directly affects the mass flow rate and the compression ratio that are importantly reduced. Besides, the TLV can be involved in the onset of aerodynamic instabilities, which then imposes a reduced operating range for the compressor design. Throughout the thesis, the analysis of the TLV will be done through three of its characteristics: where it detaches from the blade, its trajectory after the detachment, and its intensity. Figure 1 shows the effect of the position of the TLV in the rotor passage on its performance. It can be seen that the performance is drastically lowered when the TLV gets closer to the leading edge of the neighbouring blade ($\varepsilon_2 > \varepsilon_1$) along with a larger intensity, quantified by its circulation Γ .

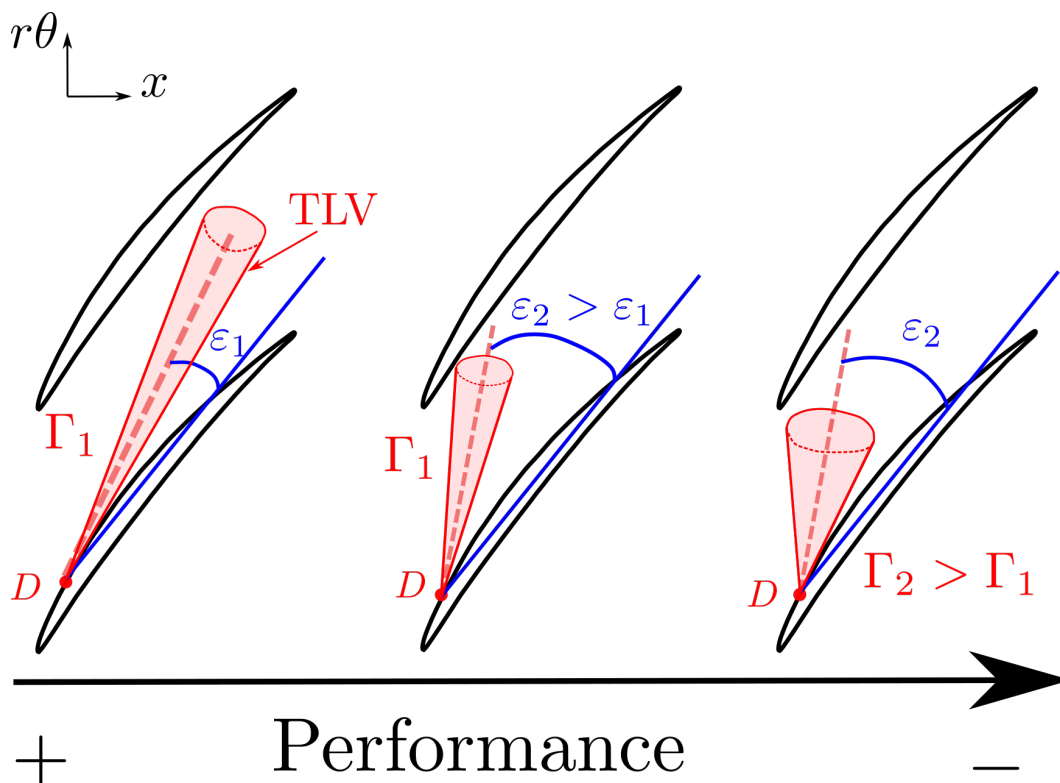


Figure 1: Effect of the intensity and the position of the TLV in a rotor passage on the compressor performance.

Different parameters have direct influence on the TLV characteristics. Amongst them, the

loading of the blade, the thickness of the casing boundary layer, and the tip gap size. The latter constitutes the one investigated in the present work. How does the tip gap size affect the performance of the compressor? How to model the influence of the tip gap size on the three TLV characteristics?

The present work aims at analyzing and modelling the influence of the tip gap size on the flow, with different levels of fidelity. First, the complex turbulent dynamics of the tip-leakage vortex is investigated with a high-resolution method. Second, a simplified modelling is sought for the purpose of compressor predesign.

The thesis is organized following three main parts. The first part reviews the existing work on compressor performance and specifically on TLF. This gives an in-depth description of the flow topology in the tip region of rotors as well as different types of TLF modelling that have been used in the past. Some of the models presented will also be used in the present work regarding the prediction of the TLV characteristics.

The second part describes the methods used for the prediction of the flow characteristics as a function of the tip gap size τ . Chapter 2 introduces the CFD strategies used for TLF simulations and particularly focuses on a hybrid RANS/LES method that will be used for our simulations. Chapter 3 presents the Vortex Lattice Method (VLM), a potential method that has been particularly used for external aerodynamics and that is here applied to wall-bounded flows.

Finally, the third part exhibits how these two methods are applied. Both have their interest to respond to the main objective of the present work:

- Chapter 4 investigates the use of ZDES on a compressor configuration to understand the influence of the tip gap size on the flow. Such a method allows a detailed view of the flow for such complex phenomena occurring at the blade tip. Three tip gap sizes are tested in the present work with that flow resolution on a high-speed compressor rotor. The three TLV characteristics are specifically studied in a mean-flow analysis. An unsteady flow analysis completes the investigation in terms of tip gap size influence.
- Chapter 5 uses the VLM constructed in Chapter 3 in order to gauge its possibilities for preliminary design. The results of the VLM, completed with a viscous correction, are evaluated on a simplified tip-leakage configuration (single blade, static), in comparison to experimental data. A particular attention is paid to the evolution of the TLV characteristics with the tip gap size.

Part I

WHAT IS TIP-LEAKAGE FLOW?

LITERATURE REVIEW ON TIP-LEAKAGE FLOW

Contents

1.1	Aerodynamics of compressors in turbomachines	9
1.1.1	Generalities on turbomachinery	9
1.1.2	Compressor performance	11
1.1.3	Compressor loss sources	13
1.1.4	Instabilities in compressors	17
1.2	Three-dimensional flows in turbomachines	22
1.2.1	Corner separations	22
1.2.2	Tip-leakage flow	24
1.3	Influent parameters on tip-leakage flow	29
1.3.1	Tip gap size	29
1.3.2	Casing boundary layer	32
1.3.3	Loading	32
1.3.4	Relative motion	35
1.3.5	Rotor-stator interactions	36
1.3.6	The double leakage phenomenon	38
1.3.7	Technological effects	39
1.4	Modelling tip-leakage flow	40
1.4.1	From the single blade towards high-speed compressors	41
1.4.2	Jet based models	42
1.4.3	Blockage models	43

1.4.4 Vorticity based models	44
1.5 Synthesis on the literature	51

1.1 Aerodynamics of compressors in turbomachines

1.1.1 Generalities on turbomachinery

1.1.1.1 Principle of turbomachinery

Turbomachinery is used in a wide variety of fields: wind turbines converting the energy from the wind into electricity, gas or steam turbines used in power plants, rocket and aircraft engines constitute good examples. All these turbomachines work thanks to the energy exchange between the fluid (e.g. water, air) and the rotating blades involved in the process. These rotating blades, also called rotors, can either give power to the fluid, subsequently increasing its pressure, or produce power by expanding the fluid to a lower pressure. Compressors and pumps constitute the former. Turbines are defined by the latter. In this thesis, compressors of aircraft engines are investigated.

Aircraft engines use the combination of both compressors and turbines to generate the thrust powering the airplane. The air entering the engine is first sucked up through the fan and compressed down to the combustion chamber by several compressor stages. The idea is to optimize the conditions in which the combustion will occur in the combustion chamber to maximize the enthalpy given to the fluid (total pressure and temperature). Downstream the combustion chamber, the turbines expand the exhaust gas and convert the potential energy of the fluid into kinetic energy. One part of this energy drives the rotation of the compressors attached to the same shaft as the turbines. Finally, the exhaust gas continues its expansion through the nozzle where it is accelerated and eventually generates the thrust ¹:

$$T = \dot{m}_1 \Delta V \quad (1.1)$$

where \dot{m}_1 is the mass flow rate and ΔV the velocity difference between the exit and the inlet planes of the engine. In order to generate more thrust, one can therefore play on the mass flow rate or increase the acceleration of the flow between the inlet and the outlet. It can be shown that playing on the former is more efficient, on the propulsive efficiency which is largely reduced for large values of exit velocities.

Most designs of civilian aircraft engines are double-flux turbofans for that reason. Their design is large to allow large values of mass flow rates. Figure 1.1 shows a sketch of such an engine and the example of the LEAP engine designed by Safran Aircraft Engines and General Electric. The air entering the engine through the fan is splitted into two fluxes: the primary flux which powers the engine as described in the previous paragraph, and the secondary flux which generates most of the thrust, about 80%. Designs of aircraft engines currently tend to increase the ratio between the secondary and primary mass flows, making engines bigger and bigger.

Compressors (resp. turbines) can further be classified into two categories depending on the direction of the flow relative to the axis of rotation of the rotor. The flow can indeed follow a path parallel to the axis of rotation of the rotor, falling into the *axial-flow compressors* category. The flow can also follow a path mainly perpendicular to the axis of rotation. These

¹For an adapted nozzle

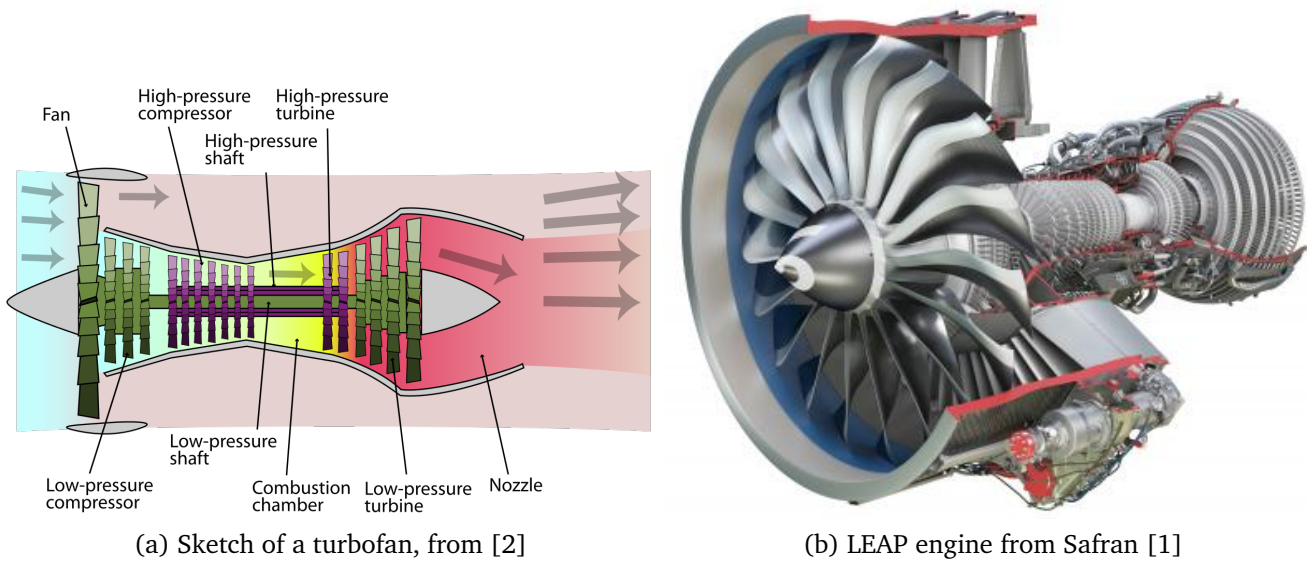


Figure 1.1: Illustrations of turbofans.

machines are called *radial or centrifugal flow compressors*. Due to the change in radius occurring in centrifugal compressors, one stage generally achieves higher pressure ratios than one axial-flow compressor stage. Their main drawback concerns the mass flow rate per unit surface area which is generally reduced a lot for higher pressure ratios. In comparison, axial-flow compressors require several stages for the same pressure ratio but the mass flow rate is greater. Figure 1.2 shows an illustration comparing the characteristic map of a centrifugal compressor compared to a 5-stage axial compressor. The selection depends on the application and the performance aimed for. For example, helicopter engines largely rely on centrifugal compressors for their lower volume. Currently, the most common designs of turbofans use several stages of axial-flow compressors, for their better efficiency associated to the higher mass flow rate offered. However, big progress has been made on centrifugal compressors and new types of architectures mixing both axial and centrifugal compressors have been in development lately.

1.1.1.2 Principle of a compressor stage

Let us now go into more details on how a compressor stage works. It consists of a rotating part, the *rotor*, and a static part, the *stator*. The role of the rotor is to give energy to the fluid by deviating the flow in the direction of rotation of the rotor. The energy transferred - hence the pressure rise - depends on two main parameters, summarized by Euler's equation [44]:

$$\Delta h_0 = c_p \Delta T_0 = \Delta(UV_\theta) = \underbrace{U(V_{\theta_2} - V_{\theta_1})}_{\text{axial-flow compressor}} \quad (1.2)$$

The variation of stagnation enthalpy $\Delta h_0 > 0$ therefore depends on the rotation speed $U = r\omega$ of the rotor and the tangential velocity variation $\Delta V_\theta > 0$, *i.e.* how much the flow is deviated by the rotor. The role of the stator for a compressor is to convert the kinetic energy increase

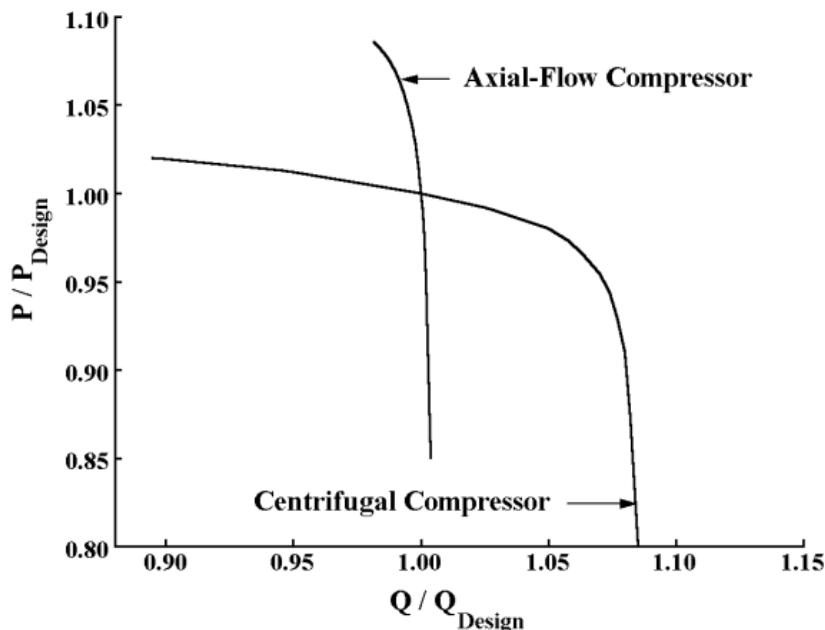


Figure 1.2: Compression ratio as a function of the mass flow rate, normalized with respect to the design point, for an axial-flow and a centrifugal compressor [5].

into static pressure. The stator also deviates the flow but no work is exchanged since the stator is not moving. The flow is redirected by the stator towards the axial direction before being energized by another stage of compressor. Figure 1.3 shows a velocity diagram summarizing the working of one compressor stage, represented by a blade-to-blade cut in the $(x, r\theta)$ plane. The figure introduces general notations characterizing the flow through a compressor. \mathbf{V} and \mathbf{W} respectively denote the velocity in the absolute frame of reference and relative frame of reference (attached to the rotation of the rotor). The angles introduced α and β are respectively associated to these velocities, resp. in the absolute and the relative frame of reference. The indices 1 and 2 here indicate the inlet and the outlet of the rotor. As can be seen in the figure, the tangential component of the absolute velocity increases through passage of the rotor, illustrating equation (1.2).

1.1.2 Compressor performance

The overall performance of a compressor can be described by a characteristic map as shown in Figure 1.4. This compressor map gives an overview of the possible ranges of mass flow and pressure ratios the compressor can work on for different rotational speeds of the shaft. In other words, the compressor can operate at any point of the area between the surge and choke lines. The surge line corresponds to an *instability line* where the compressor can no longer withstand the adverse pressure gradient imposed. These instabilities are discussed in section 1.1.4. The *surge margin line* corresponds to the safety line imposed by designers above which the compressor must not operate. This represents a major source of possible improvement since being able to operate at lower mass flow rates can yield significant amounts of fuel saved by

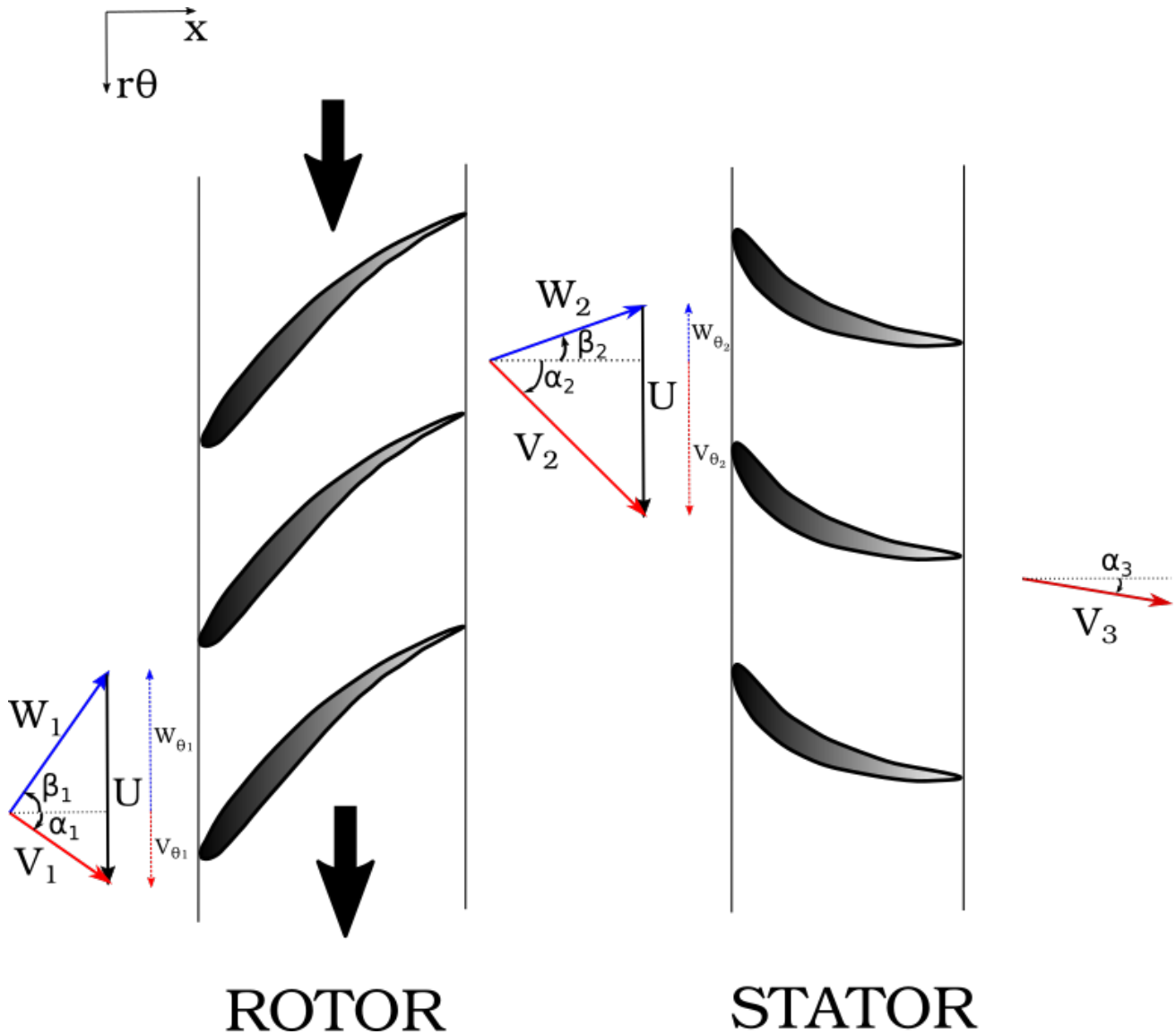


Figure 1.3: Velocity triangles in the $(x, r\theta)$ plane for a constant radius, assuming the hub and casing radii are constant.

increasing further the pressure rise. The design point chosen by the designer fixes the nominal speed represented by the $100\%N_n$ curve in the figure. This point serves as a reference and generally corresponds to the highest efficiency of the compressor. The compressor can operate for different speed regimes: depending on the flight phase, the engine must be able to operate at different rotational speeds. In the compressor map, one can see how the range of mass flow rate, over which the compressor can operate, decreases with greater rotational speeds. This can be explained with Euler's equation (1.2): the compressor cannot undergo a loading greater than $\Delta h_{0,max}$, corresponding to a maximum pressure rise Π_{max} and the greater the rotational speed, the less the flow can be deviated. The *operating line* is the line on which the efficiency of the compressor is theoretically close to optimal for a fixed ω . The choice for the operating line depends on the designer but the compressor is operated as much as possible on this line.

Finally, the *choke line* is characterized by a choked flow, *i.e.* the Mach number has reached unity in a constriction. The mass flow rate cannot be increased from here. For high rotational speeds, this is clearly visible through the vertical lines on the curves leaving from the choke line. For a certain range of pressure ratios, the mass flow rate remains nearly constant.

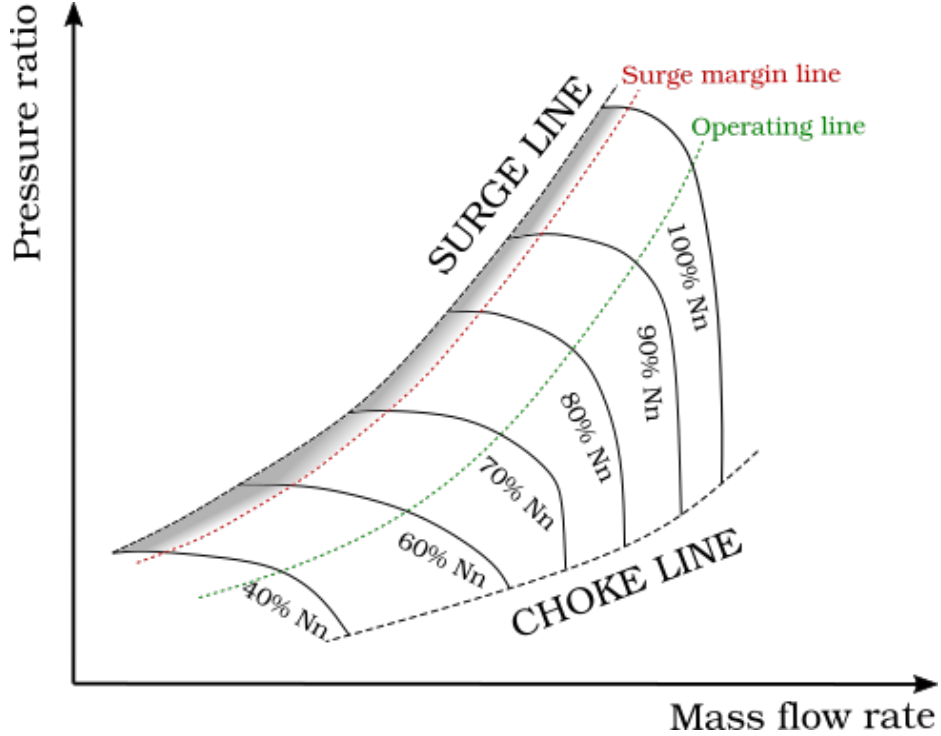


Figure 1.4: Characteristic map of a compressor.

The efficiency is an indicator of the compressor performance. Different definitions exist for the efficiency depending on the assumptions made on the flow. The simplest definition compares the flow to an isentropic flow in adiabatic and subsonic conditions. The isentropic efficiency is defined as the ratio between the stagnation enthalpy necessary to reach the pressure rise in ideal conditions $\Delta h_{0,is}$, without any entropy increase, and the actual stagnation enthalpy Δh_0 :

$$\eta_{is} = \Delta h_{0,is} / \Delta h_0 \quad (1.3)$$

which can be rewritten

$$\eta_{is} = \frac{1 - (p_{02}/p_{01})^{\frac{\gamma-1}{\gamma}}}{1 - T_{02}/T_{01}} \quad (1.4)$$

This definition can be extended to a polytropic efficiency by introducing infinitesimal transformations occurring between states 1 and 2. For sufficiently high pressure ratios, this definition is more suitable for comparing the efficiency of different machines [44].

1.1.3 Compressor loss sources

The flow in a compressor is probably one of the most complex. In a confined space with very large speeds, the flow undergoes strong viscous and compressible effects, such as boundary layer

separations, mixing processes or shocks, all sources of losses, representing a strong limitation to turbomachinery performance that every designer wishes to understand and overcome. It is possible to classify loss sources into two main categories [40] [44] [77]:

1. Two-dimensional losses: arising from the blade boundary layers far from the casing (*profile losses*), the hub boundary layer, and the shock waves
2. Three-dimensional losses including tip-leakage losses and endwall losses. The former will largely be dealt with through the thesis but the latter as well since they interact with each other.

1.1.3.1 Two-dimensional losses

Profile losses

As described in section 1.1.1, the more the fluid can be deviated, the more energy is brought to the flow with the rotation of the rotor. However, deviating more the fluid means an increase of the incidence. With this increase, viscous effects become significant and the boundary layer attached to the blade eventually separates. An important drag increase can be observed due to the thickening of the wake from the blades. Lieblein [84] developed a criterion to estimate when the flow conditions may lead to separation. He observed that the boundary layer thickens more on the suction side of the blade and is therefore the major contributor to the wake formed downstream. Velocity profiles on pressure and suction sides obtained in Lieblein's cascade experiments are shown in Figure 1.5. Lieblein noticed that the boundary layer is thicker when the velocity difference between the maximum and the minimum velocity is high, characterizing high levels of diffusion. A significant flow deceleration indeed often leads to a separation due to the massive adverse pressure gradient. His criterion based on his experiments is the following:

$$DF = \frac{V_{max} - V_2}{V_{max}} \quad (1.5)$$

Nevertheless, the maximum velocity is hardly obtained without measurements. Based on correlations between the maximum velocity and the momentum thickness θ , a more suitable criterion for designers is derived for incompressible flows [85] [15]. It is based on the inlet velocity V_1 , the outlet velocity V_2 and the deflection ΔV_θ :

$$DF = 1 - \frac{V_2}{V_1} + \frac{1}{2\sigma} \frac{\Delta V_\theta}{V_1} \quad (1.6)$$

where $\sigma = c/s$ is the solidity of the blade row, indicating the ratio between the chord and the pitch. One term corresponds to the deceleration of the flow and the second to the deviation of the flow. Increasing too much one of these may give a diffusion factor greater than the limit fixed to about $DF = 0.6$, for which the flow separates and the total pressure losses surge. A more general criterion, also derived by Lieblein, can be found for compressible flows [84].

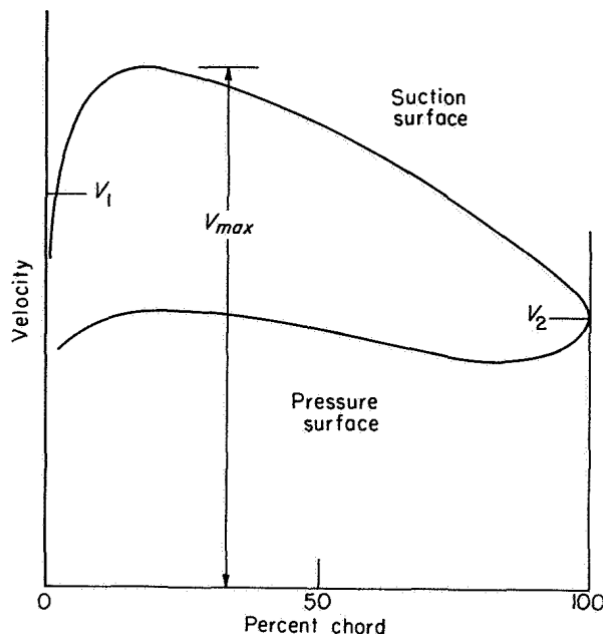


Figure 1.5: Velocity profiles on blade walls, adapted from Bullock based on the cascade experiment of Lieblein [15].

Shock losses

Shock losses stem from the shock structures found at the leading edge of transonic compressors, *i.e.* for Mach numbers greater than 0.7. For this range of Mach numbers, shock waves and thicker boundary layers are responsible for extra losses. Transonic compressors present however advantages for their higher mass flow rates and the lower deviation required to achieve high compression ratios, due to the large speed of the rotor blades U . Usually, this type of compressors is made of thin rotor blades with a very sharp leading edge in order to reduce the losses. Koch and Smith [77] present a model yielding shock losses depending on the bluntness of the leading edge, inspired from existing models in the literature [112] [152].

1.1.3.2 Three-dimensional losses

Greitzer introduces *secondary flows* as flows associated to the generation of a streamwise component of vorticity [59]. The name derives from the fact that a *primary flow* can usually be identified along a passage following a primary flow direction. The secondary motion comes and disturbs this primary direction due to the presence of vortical structures. Figure 1.6 shows an illustration of the different secondary flows encountered in a compressor blade passage.

In turbomachines, boundary layers at the endwalls sheared by the relative motion of the rotor blades and large viscous effects are submitted to secondary flows playing a major role in their development. They rapidly thicken as the flow moves through the stages of the compressor, interacting with the mainstream flow, modifying significantly the axial velocity distribution, and increasing the *blockage effect*. This not only decreases the efficiency of the compressor since less

work is given to the fluid, but also reduces the mass flow capacity of the machine and hence its operating range.

Crocco's equation [27] relates the entropy and enthalpy gradients to the vorticity ω for steady potential flows:

$$\mathbf{u} \times \boldsymbol{\omega} = \nabla h_t - T \nabla s \quad (1.7)$$

For incompressible flows, it can be simplified, showing directly how vorticity affects the total pressure gradients:

$$\mathbf{u} \times \boldsymbol{\omega} = \nabla P_t / \rho \quad (1.8)$$

In turbomachinery, secondary flows are of major importance when it comes to designing rotor or stator blades since they have a big impact on losses. Several processes are at stake in the generation of streamwise vorticity. The strong interaction between the different types of secondary flows makes it difficult to clearly distinguish them but three-dimensional losses are usually responsible for 50% of the total losses, the other 50% coming from the two-dimensional losses described previously. Denton [40] further divides the losses in turbomachinery into three categories, the last two falling into the three-dimensional losses:

1. The profile losses
2. The secondary losses due to the endwall boundary layers
3. The tip leakage losses due to tip-leakage flows

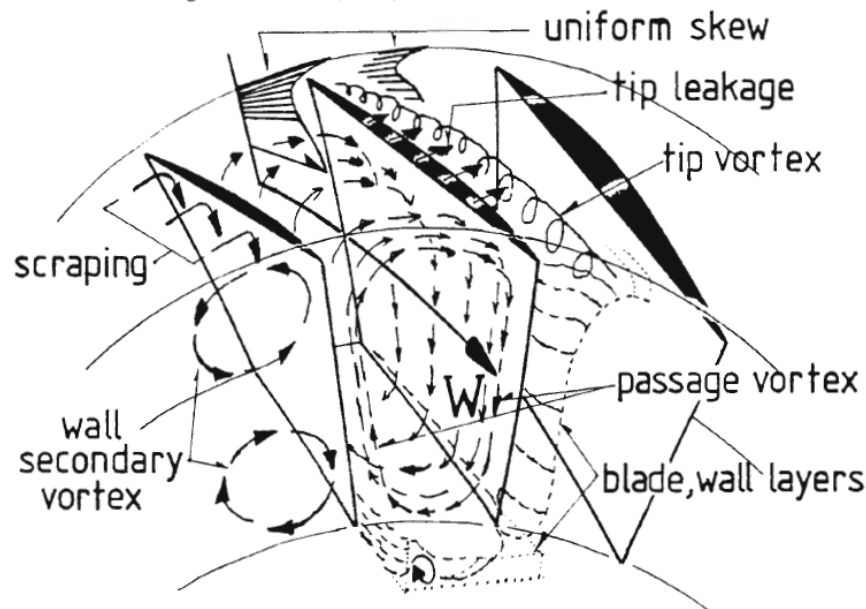


Figure 1.6: Illustration of secondary flows within a compressor blade passage, from Moyle (1991) [98].

Figure 1.6 shows the complexity of the flow within a blade passage and the different interactions between the vortices and the boundary layers. Nonetheless, two major types of three-

dimensional flows in turbomachinery can be presented as they represent the largest sources of 3D losses:

1. *Corner separations* resulting from the interaction of the blade and endwall boundary layers, causing separation, which for certain configurations may induce massive losses and even stall.
2. *Tip leakage flows* (TLF), driven by pressure difference through the clearances at the tip of the blades or vanes. On rotors, a gap can be found between the casing and the tip of the blades to ensure the rotation without rubbing against casing. This gap undergoes a pressure difference across rotor blades from which originates the *tip-leakage flow*. These flows quickly roll up into vortex structures, causing major losses in the compressor. Their interaction with the casing and blade boundary layers generates even further losses. As described by Denton [40], they contribute to about 30% of the total losses of many machines.

Their impact on the performance of turbomachinery is discussed in section 1.2.

1.1.4 Instabilities in compressors

As described in section 1.1.3, blades are designed to operate so that the flow does not separate. However, depending on the flight regime, accelerations or decelerations require the engine to operate off-design. These off-design conditions can induce a local increase of the incidence on certain blades due to the reduction of mass flow. If the incidence is increased too much, the flow can separate on the blade and even lead to a massive separation where *stall* occurs. Well-known phenomenon for aircrafts and characterized by a brutal lift decrease and drag increase, any pilot wants to avoid getting too close to stall. When compressor rows stall, the blade loading also undergoes an abrupt lift decrease and drag increase, which can also be seen as a massive loading deficit for a rotor. On a rotor, this massive separation can move with the rotation of the blades and progress from one blade to another. These rotating cells characterize the phenomenon called *rotating stall*, precursor of surge, as shown by Day [33]. This section is dedicated to the description of these two phenomena, whose better comprehension still represents a big challenge for compressor designers after more than 75 years of research [34].

1.1.4.1 Rotating stall

Rotating stall can be explained by Figure 1.7, a sketch used by Emmons *et al.* [49] to explain the process of rotating stall they observed on their experiments back at the time. For low mass flow rates, close to the surge line showed in the previous section, the flow is very sensitive to small disturbances which can locally increase the incidence on one blade of the row. This increased incidence suddenly yields a massive separation on one or several blades. In Figure 1.7, the massive separation induces a large deviation at the inlet of the next blade which then leads to its stall. The stall of the next blade subsequently reduces the incidence on the blade

before, provoking the reattachment of the boundary layer. The stall cell propagates against the direction of the rotor in the relative frame of reference. Generally, these cells propagate between 30% and 80 % of the rotation speed in the absolute frame of reference. The trigger leading to rotating stall can come from several causes; this is further discussed in section 1.2.

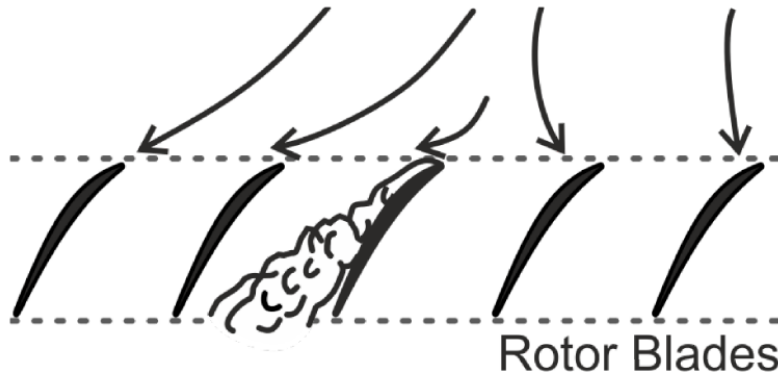


Figure 1.7: Sketch explaining the rotating stall process, from Emmons et al. [49].

An illustration of stall cells observed in an axial compressor, from Crevel's numerical simulations [25], is shown in Figure 1.8. Twenty four blue pockets, the stall cells, can be seen, corresponding to important axial velocity deficits.

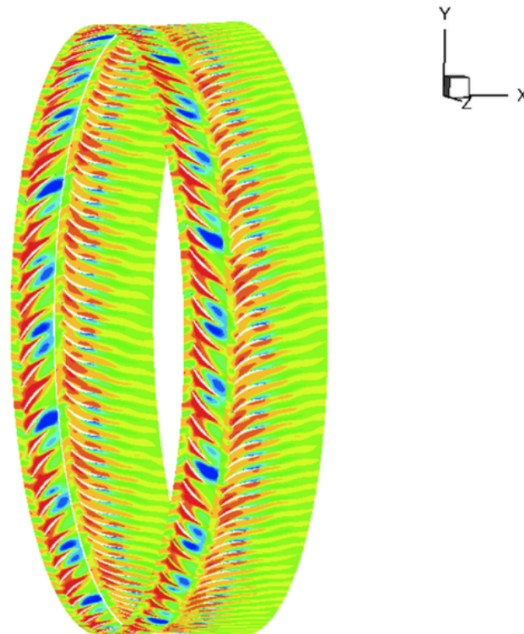


Figure 1.8: Contours of $V_x > 0$ at midspan on the third stage of the research compressor CREATE [25]. The blue pockets indicate the position of the stall cells.

These cells can be of different types as they can populate part of the span or the full span. Generally, part-span rotating cells characterize a progressive stall, with a hysteresis of lower

intensity, and rotate with a higher speed than full-span cells. Full-span cells can develop from part-span cells, intensifying the hysteresis. The rotating stall can also be abrupt with a sudden drop of pressure ratio. This brutal phenomenon can lead to surge. This latter abrupt stall is usually found in the rear stages of high pressure compressors with a high hub-to-casing radius ratio. Figure 1.9 illustrates the formation of part-span cells, here formed between about 30 % height and the casing.

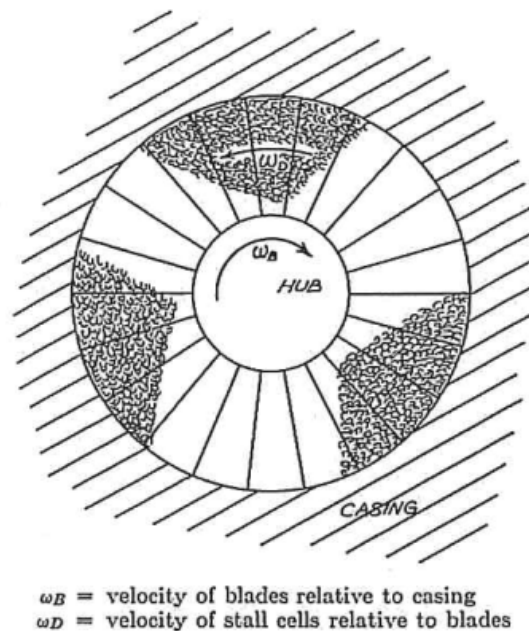


Figure 1.9: Representation of part-span cells propagating on rotor blades [49].

Another interesting point concerns the inception of rotating stall. It always occurs close to the zero slope of the characteristic curve on which the compressor operates, but it does not always occur on the positive slope of the characteristic curve. This defines Camp and Day's criterion on the inception of rotating stall, which can be of two types: *modal* or *spike* inception. The inception is of particular importance since the prestall warnings are not the same depending on the type of inception. In particular, warnings associated to spike inception only occur a few revolutions before rotation stall is set off. Countering this type of stall can therefore be more complicated. These inceptions are characterized by the length-scale of the disturbance associated with them. A modal inception is linked to a long length-scale disturbance whereas a spike disturbance can be measured in terms of blade pitches. Figure 1.10 summarizes Camp and Day's criterion: if the rotor critical incidence is to the right of the peak of the characteristic curve, a spike inception will occur. Otherwise, the disturbance will be of modal type.

A spike type inception is indicated in Figure 1.11 as measured at casing on a low-speed compressor by Camp and Day [17]. Four pairs of pressure transducers at the same radial and azimuthal positions are placed upstream and downstream of the rotor concerned. The spike emerges at position 2 and rapidly turns into rotating stall after only two revolutions. Modal inception compares differently: a low intensity oscillation appears breaking the flow axisymmetry,

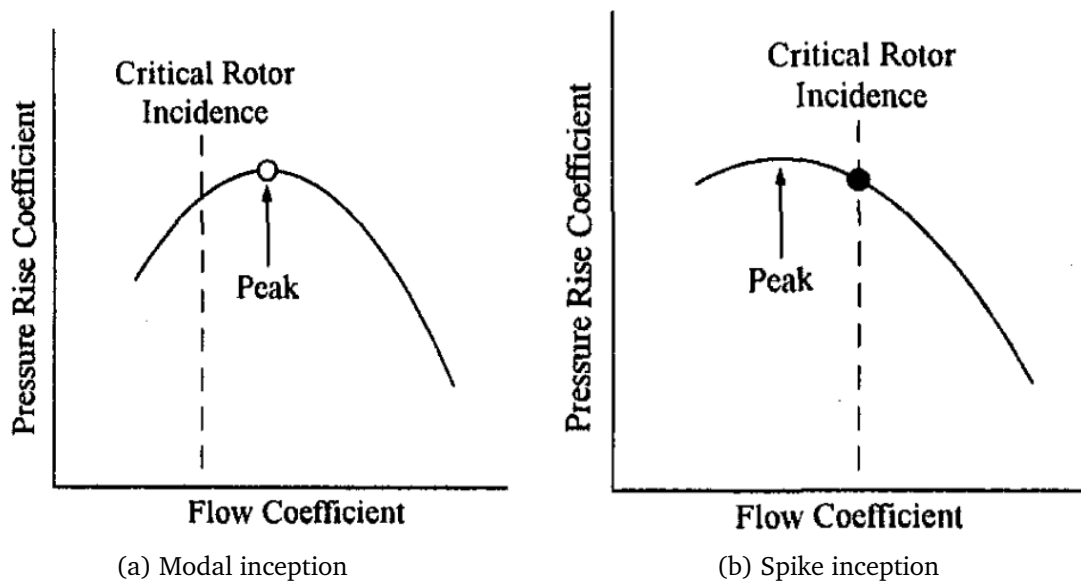


Figure 1.10: Two types of inceptions for rotating stall, from Camp and Day [17].

and smoothly develops into rotating stall. For Camp and Day’s compressor, the rotating stall appears 6 or 7 revolutions after the modal oscillation has started developing.

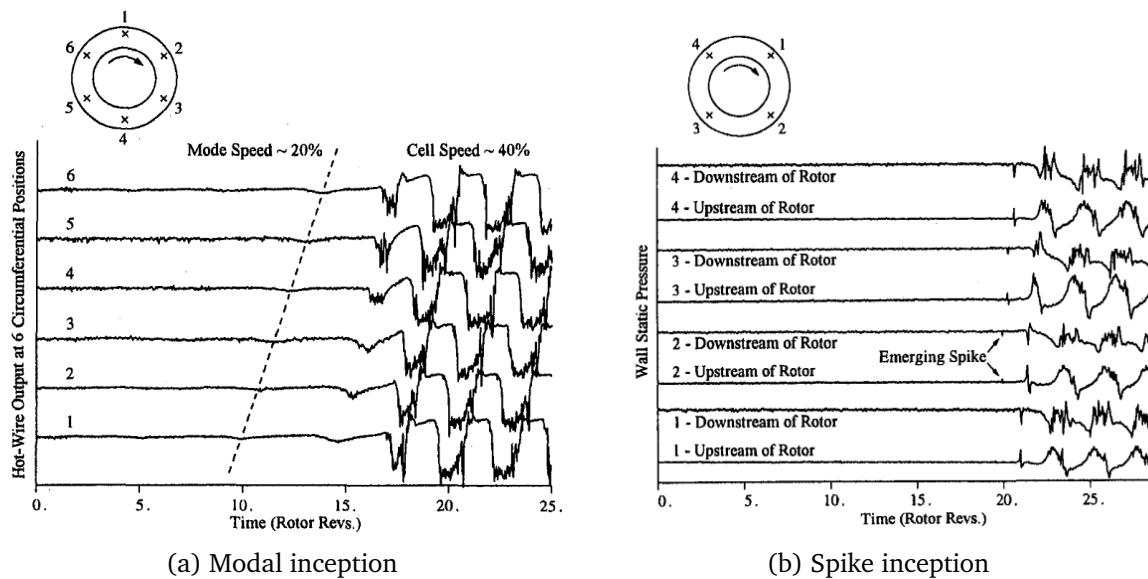


Figure 1.11: Time evolution of wall static pressure with modal and spike inceptions giving rise to rotating stall [17].

As shown by Day [33], rotating stall is a precursor of surge. He even states in [34] that rotating stall causes surge. This has also been shown by experiments and numerical simulations on the high-pressure axial compressor CREATE [24] [26]. Experimentally, they observe that rotating disturbances already appear at stable points and grow in intensity when the compressor

is throttled. These disturbances give rise to full span stall cells which eventually lead to surge.

As explained by Moore [96], this phenomenon triggers an important hysteresis which can only be broken by significantly unthrottling the machine, reincreasing the mass flow rate and hence reenergizing the flow. This discharge, as recalled by Day, is always greater than that at which the compressor first stalled. This hysteresis can be responsible for premature fatigue on the blades and must be exited quickly.

1.1.4.2 Surge

While rotating stall is an azimuthal disturbance of the flow, generally localized on one row, highly unsteady and breaking the axisymmetry of the flow, surge can rather be described as a one-dimensional axial perturbation, affecting the whole compressor. During surge, the mass flow rate is submitted to oscillations which, for stronger surges, can lead to flow reversal with negative mass flow rates. In other words, the inertia of the fluid is no longer sufficient to balance the strong adverse pressure gradients and the flow naturally tends to return to lower pressure regions. Contrary to rotating stall, the mass flow rate is not constant during surge.

Let us return to the characteristic map described in the previous section. Figure 1.12 shows the two existing types of surge:

1. The mild surge, inducing oscillations of the mass flow rate, but with a mass flow always positive.
2. The deep surge, with more intense oscillations of the mass flow leading to flow reversal.

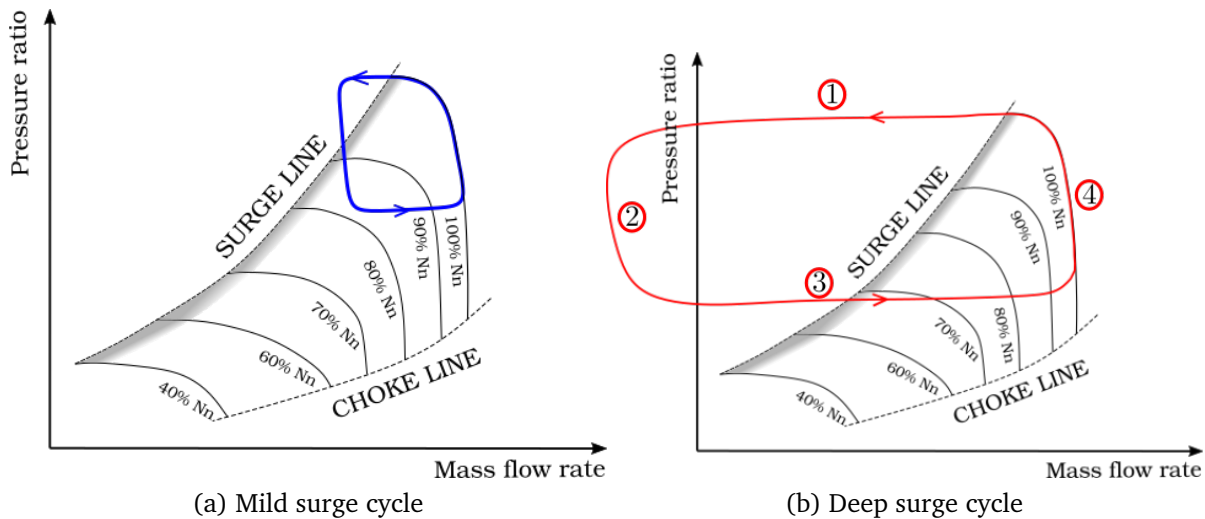


Figure 1.12: Sketch of the two different types of surge that can develop in a compressor, here on the design characteristic curve of the compressor.

Crevel *et al.* [26] distinguish four phases during deep surge, describing the general working of the phenomenon, observed in Figure 1.12:

1. **Surge inception:** The incidence increase leads to a global stall on all the blades of the row, which therefore blocks all the passages and explains the diminution of the mass flow rate.
2. **Reversed-flow phase:** The mass flow rate is now negative and the downstream volume is emptying, yielding a drop in the pressure ratio of the compressor.
3. **Recovery:** The adverse pressure gradient has decreased towards a reasonable value that the compressor can deal with, which leads the mass flow to increase again.
4. **Repressurization:** Now that the mass flow has recovered up to the characteristic curve on which the compressor operates at this speed U , the compression ratio increases again until a new surge cycle begins if the machine is not unthrottled, *i.e.* if the downstream volume is refilled to the same level which led to the first surge cycle.

Greitzer's [58] works on surge led to the development of a model representing the global behaviour of the system during surge. In particular, a parameter B is introduced that groups all the variables to be considered in the onset of the instability. This parameter enables to indicate whether the compressor will stall or surge. A low value of B indicates a stable behaviour of the system. Increasing it further, a critical value is reached where rotating stall appears. Even further, a higher value of B suggests the occurrence of surge. The parameter can be described by the ratio between the pressure forces and the inertial forces. The critical values can vary from one compressor design to another.

The mechanical consequences of such an instability are described by Mazzawy [90] and Schönborn *et al.* [120]. The former proposes different surge load models resulting from the propagation of very energetic pressure waves caused by surge. The latter shows that the surge load may consist of two consecutive phenomena: the pressure shock already observed by Mazzawy followed by possible aeroelastic excitations.

As discussed in the next section, the disturbances responsible for the occurrence of these phenomena generally find their origins at the tip of rotor blades. Tip leakage flows are particularly concerned.

1.2 Three-dimensional flows in turbomachines

Briefly introduced with three-dimensional losses, corner separations and tip-leakage flows are described more in details in this section in order to answer the following questions. What is their topology? How do they impact the performance of the compressor?

1.2.1 Corner separations

In addition to the adverse pressure gradient and the secondary flows in the blade passage, the mixing between the boundary layers at the endwalls and on the suction side of the blade may, in some conditions, lead to a three-dimensional separation called corner separation. Figure

1.13 shows an illustration of a corner separation occurring at the hub on the suction side of a stator or rotor blade. Streamlines bounding the region where the flow is separated are clearly visible and a separation vortex is formed. Generally, the phenomenon is more likely to occur when the root of the blade is more loaded, corresponding to a higher incidence. Dring *et al.* [48] experimented on a highly loaded rotor and observed a strong corner separation on the suction side, which rapidly turned into full-span stall cells characteristic of rotating stall. On a multistage low-speed compressor, Wisler [146] found a large region of separated flow on the suction surface of the first rotor hub at peak efficiency, with large total pressure losses.

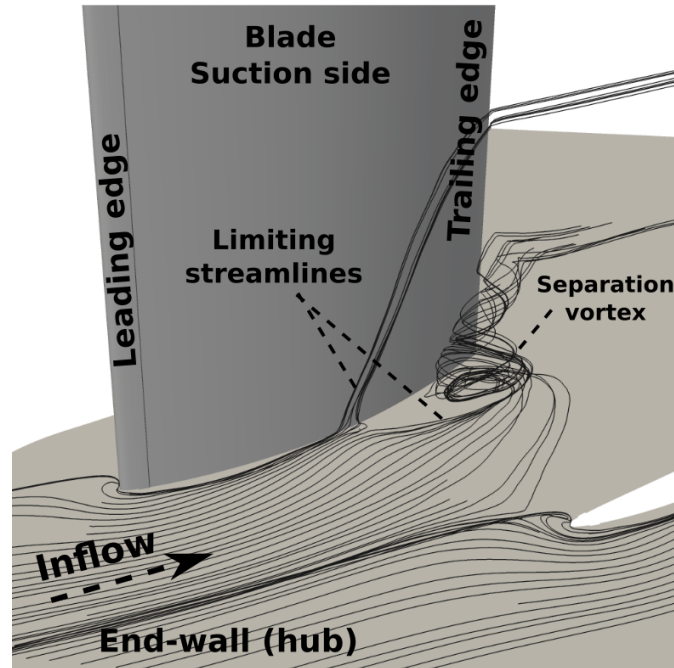


Figure 1.13: Illustration of a corner separation between the endwall and the blade suction side [51].

On stators, corner separation can occur all the same at casing and hub as shown by Schulz *et al.* [121] for five different incidences on an experimental compressor rig. They proposed a corner separation topology, as shown in Figure 1.14, from their visualizations. Two vortices, one on the hub, another on the blade, are identified indicating two regions of backflow, also called *foci* in the classification of critical points in separations [32]. The topology proposed assumes the presence of a ring vortex extending from the blade and from the endwall away from the corner, bounded by the streamlines called *limiting streamlines* in the sketch. Generally, this topology can be observed in massive corner separations, when the corner separation is *open*. Other topologies for less intense corner separations only present one focus on the suction side of the blade, as for example observed by Marty and Aupoix on the first stator of a 3-stage compressor [88], therefore indicating no flow reversal on the endwall.

Based on a large set of about one hundred numerical simulations on different geometries, Lei *et al.* established a criterion for corner separation, summarized in Figure 1.15. The stall indicator S is plotted as a function of a diffusion parameter D , a modified Lieblein's diffusion coefficient to

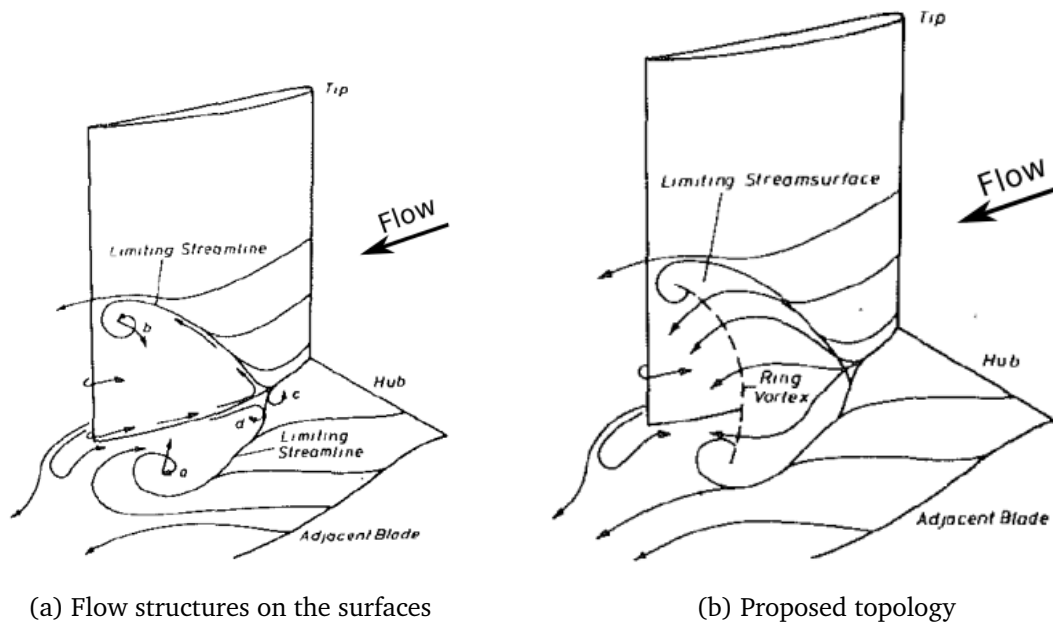


Figure 1.14: Corner separation topology as proposed by Schulz *et al.* [121].

account for the effect of incoming boundary layer skew. The stall indicator S can be described as a difference of blade loading coefficients between two spanwise positions, at midspan and close to the endwall, here the hub. The idea is that when corner separation becomes massive, the loading decreases near the hub and S increases. In the figure, two branches are clearly visible, corresponding to the two topologies of corner separation described above:

- A one-focus topology limited to the suction side of the blade for $D < 0.4$.
- An open corner separation with two foci and a reversed flow on the hub for $D > 0.4$, where the stall indicator S is increased abruptly.

1.2.2 Tip-leakage flow

Tip-leakage flow is found at the tip of rotors of compressors and turbines. Due to the pressure difference across the blade, a leakage flow forms in the gap from the pressure side (PS) to the suction side (SS) of the blade, as illustrated by Figure 1.16. The strong acceleration near the pressure side leads to a separation of the flow and the formation of a *vena contracta* that may or may not reattach, depending on the thickness of the blade [40]. Moving towards the suction side and downstream in the passage, the leakage flow rolls up when mixing the mainstream flow, thus forming the tip-leakage vortex (TLV) shown in Figure 1.16. Rains [111] was one of the first to model tip-leakage flow. He divided the flow into these two main regions:

1. The first region where the fluid is accelerated and the *vena contracta* forms.
2. The second where mixing takes places with the mainstream flow and generates losses.

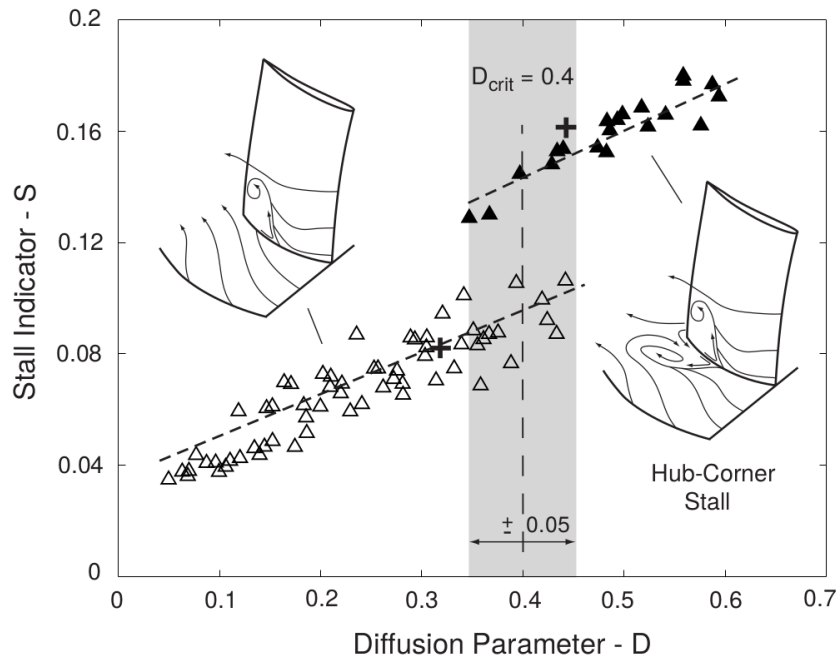


Figure 1.15: Lei's criterion for corner separation [83].

His model is based on the assumption that the pressure gradients across the blade are much greater than along the blade. It is thus possible to decompose the flow into a throughflow component and a crossflow component, considered as a jet, normal to the throughflow. The mass flow rate within the clearance can simply be estimated for incompressible inviscid flows from the velocity component normal to the blade V_{tlf} :

$$V_{tlf} = \sqrt{2 \frac{P_{ps} - P_{ss}}{\rho}} \quad (1.9)$$

Equation (1.9) may simply be rewritten as a function of the pressure coefficients and the undisturbed velocity V_∞ :

$$V_{tlf}/V_\infty = C_d \sqrt{\Delta c_p} \quad (1.10)$$

A discharge coefficient C_d , quantifying the effective cross section (vena contracta), is applied to calculate the resulting leakage mass flow rate. To account for the losses, Rains considers that the kinetic energy associated to the crossflow normal to the blade is never recovered and dissipated. The loss in efficiency from this assumption can be calculated. Vavra [141] and Yaras and Sjolander [150] used the same idea with a non uniform chordwise loading, *i.e.* with the pressure difference ΔP being a function of the axial component x . They noticed that the region near the leading edge is more affected by the presence of the TLV and so is the pressure gradient across the blade in that region. The first thirty percent chord of the blade are modified accordingly. More interestingly, Chen's works [20] showed that the clearance flow was driven by the blade loading away from the clearance region, which pushes into considering midspan blade loadings in TLF models, as done for example by Storer and Cumpsty [134].

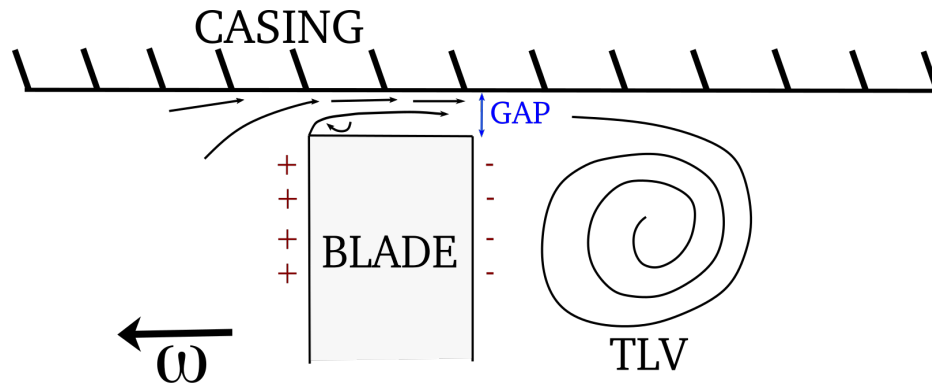


Figure 1.16: Sketch illustrating the formation of the tip-leakage vortex (TLV).

Depending on the size of the gap, the topology of the flow can change. Two extreme cases can be conjured up:

1. A case with no clearance at all, with no space between the casing and the blade.
2. A case with an infinite clearance, equivalent to considering that there is no endwall.

The flow in the first case corresponds to what can be found on a compressor stator at casing, with a frequent corner separation, described in the previous section. The second case is similar to the flow around an airplane wing, with a tip vortex shed at the trailing edge of the wing. This last phenomenon is essentially inviscid and losses can be estimated through the calculation of the induced drag, generated by the presence of this vortex.

The size of tip gaps on rotors of axial-flow compressors generally varies between 1 and 3 % chord and a TLV is formed and detaches between about 20 % and 30 % chord, depending on the blade loading. As observed by Grilliat [60], the detachment occurs close to the point where the adverse pressure gradient is maximal, also corresponding to the point where the transversal component of the velocity is maximal. More details on the influence of tip gap size are given in section 1.3.

The classical topology of the vortex structures found in the rotor passages is shown in Figure 1.17, from a LES simulation [11] performed on a fan test rig in the tip-flow region. The TLV is clearly identified as the major source of vorticity in the passage, fed by the little tip separation vortices (TSV). The induced vortex (IV) results from the interaction between the TLV and the casing boundary layer, and rotates in the opposite sense of rotation compared to the TLV. This phenomenon has been clearly identified by Brion [13]. The vortex pair (TLV and IV) mutual interaction moves the system away from the endwall, where the IV formed. This phenomenon, identified by Barker and Crow [7], is called the *rebounding* effect of the vortices. If Rains and Chen consider the mechanism behind the formation of the TLV as inviscid, it is clear that viscosity has an influence on its development in the blade passage after its detachment. The presence of the secondary vortex proves it.

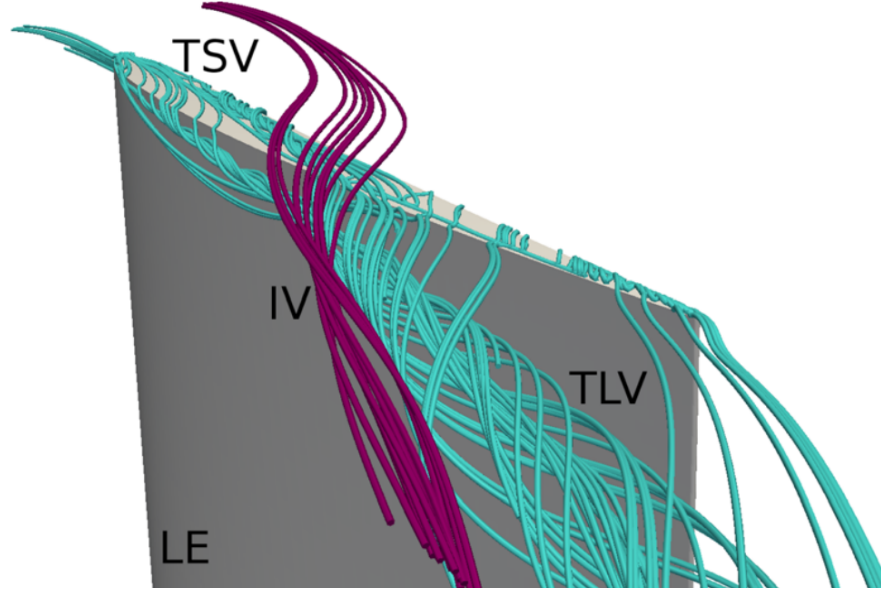


Figure 1.17: Streamlines of the mean flow in the blade tip region, from the LES simulation from Boudet *et al.* [11].

This topology was also observed by You *et al.* [153] in the tip clearance region of a linear cascade with a moving endwall, where the TLV is observed as the predominant vortical structure in the clearance region together with multiple induced vortices. The structural vortices present a reduced streamwise velocity and a sign change in the crossflow velocity components, especially in the core region. The TLV can be identified by high streamwise and pitchwise vorticity magnitudes. The presence of the TLV is also characterized by large Reynolds stresses and turbulent kinetic energy (TKE) in the clearance region. They estimate the losses due to TLF by calculating the TKE caused by TLF. Figure 1.18 shows the evolution of their tip-leakage loss coefficient derived from TKE, normalized by the inlet kinetic energy upstream the blade. As it can be seen, the loss coefficient $\bar{\zeta}_x$ reaches its maximum a little downstream of the trailing edge and slowly decays, still generating important losses 1.5 chords downstream the trailing edge.

Following its detachment, the vortex core diffuses and its radius increases. Also, the maximum vorticity is reduced downstream with the diffusion of the vortex. Yaras *et al.* [149] used Lamb's formulation of a line vortex diffusion [82] to model the development of a TLV downstream of a linear cascade of turbine blades. The vortex model accounts for the evolutions over time of the core radius R and the axial vorticity ω_x :

$$\omega_x(r, t) = \frac{\Gamma}{\pi R^2} e^{-\frac{r^2}{R^2}} \quad (1.11)$$

Here the circulation Γ designates the circulation of the TLV at its maximum, before its diffusion, right at the moment where it detaches from the blade. The core radius diffusion is calculated with a turbulent viscosity ν_t , following Owen's correlation [102]. More details on analytical models of line vortices are given in Appendix B. This analytical vortex model will be used similarly in Chapter 5.

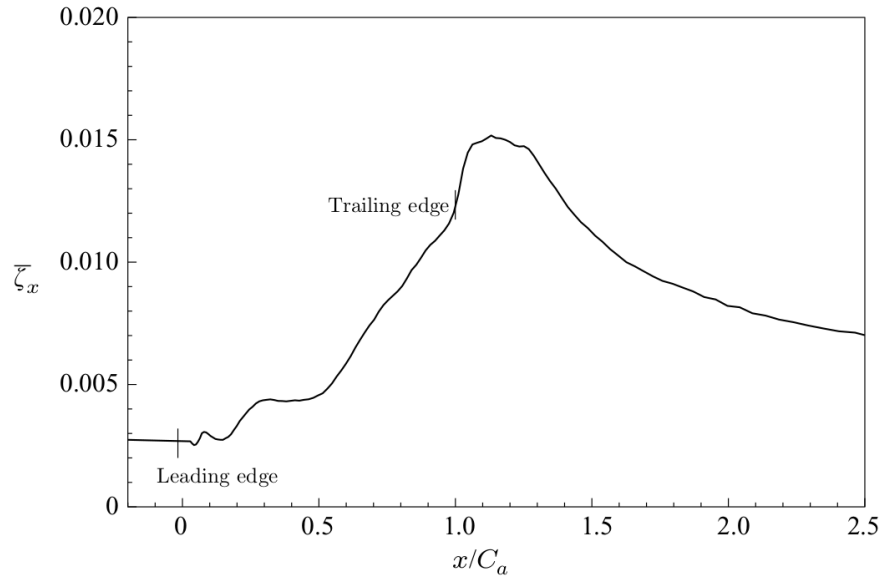


Figure 1.18: Axial development of the TLF loss coefficient $\bar{\zeta}_x$, from You *et al.* [153].

Brookfield [14] chose to model the vortex with a similar approach by distinguishing two regions of the vortex, following a Rankine distribution on the tangential velocity V_θ :

1. The vortex core flow containing all the axial vorticity.
2. The outer flow, irrotational.

Figure 1.19 shows the distribution of velocity from the center of the core to the edge of the vortex. The approach he used is interesting to analyze the sensitivity of the vortex core flow to adverse pressure gradients in a confined duct. His study put forward the existence of a critical swirl ratio, calculated as the ratio of the tangential velocity and the axial velocity at the vortex core edge $V_\theta/V_x = \sqrt{2}$, where a large core expansion abruptly occurs. The author associates that to the occurrence of a *vortex breakdown*. His results showed that the adverse static pressure gradient accelerates the swirl ratio growth and would promote such a phenomenon. However, this critical ratio is rarely reached in compressors and generally remains lower than 1. The impact of the turbulent viscosity on the swirl ratio is the same and tends to increase it.

The topology of TLF can be described by a blockage approach. According to Khalid *et al.* [75], blockage can be defined as a reduction in effective flow area due to velocity defect. In his thesis, he shows how the blockage area in the clearance region increases due to TLF and that this increase can directly be related to the onset of instabilities. According to Brookfield, the blockage due to TLF grows linearly with the suction side pressure side in the rotor passage, making TLF very sensitive to the adverse pressure gradient in the passage. The important thickening of the casing boundary layer across rotors of compressors had also been shown by Koch and Smith [77] and Mellor and Wood [91].

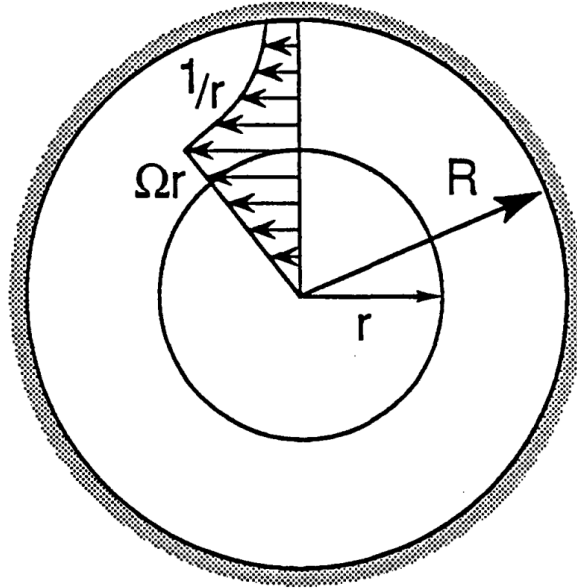


Figure 1.19: Schematic of a Rankine vortex on the evolution of v_θ with r , from Brookfield [14].

1.3 Influent parameters on tip-leakage flow

In order to optimize designs regarding tip-leakage flow, it is necessary to understand what parameters affect it and how much. The list of criteria in this section is probably not exhaustive but aim to be as large as possible.

1.3.1 Tip gap size

The clearance size of rotors has a big effect on both performance and off-design conditions as shown in Figure 1.20, from Cumpsty [31]. With $\tau/c = 3.4\%$, the isentropic efficiency and the operating range are significantly reduced, losing about 0.03 of efficiency and nearly 10% of surge margin. The tendency would therefore suggest that the smaller the gap the better, but it has been observed in other experiments and simulations that the aerodynamic optimal size is not necessarily the smallest gap, as it is discussed in this section.

From an industrial point of view, the size also depends on mechanical constraints such as vibrations or deformations of the blade, due to high thermal constraints for example (more serious phenomenon for turbine blades). Dong *et al.* [45] investigated the tip clearance changes due to thermal effects and centrifugal variations. With their model, validated on a 11-stage axial compressor, they showed that the tip clearance size could vary between 0.1 and 0.4 % span from near choke to near stall conditions on the rear stages. Moreover, this has not only an impact on pressure rise and efficiency but also on stage matching. The experiment of Berdanier and Key (2015) [8] confirmed the fact that tip clearance size is sensitive to loading conditions, with similar orders of magnitude.

Doukelis *et al.* [46] carried out experiments on an annular compressor cascade for four dif-

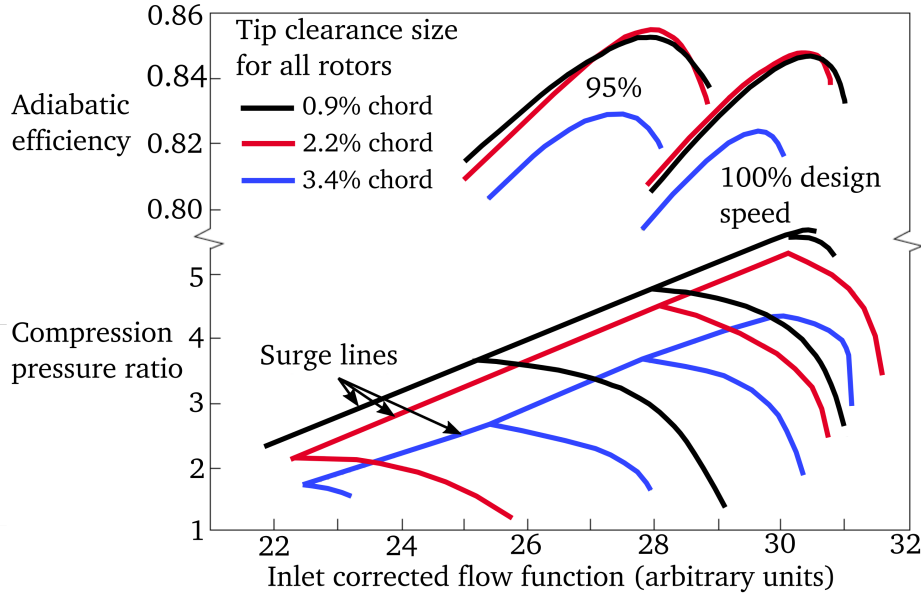


Figure 1.20: Effect of tip clearance size on the performance of a 6-stage compressor, adapted from Cumpsty (1989) [31].

ferent gap sizes. They observed an increase of the losses in the clearance region with increasing gaps, due to the increase of the TLV size. Their study also showed that the point of detachment of the TLV gets closer to the trailing edge for increased gaps. Kang and Hirsch [70] did the same observation in their experiment on NACA65 airfoils, with a shift more apparent for higher incidences at off-design conditions. Inoue *et al.* [66] noted the same behaviour with variations of the intensity slighter for large gaps, in their case with τ/c of more than 4 %.

Regarding the formation of the TLV, criteria exist to state whether it is inviscid or not. Following the criterion given by Rains [111], Chen proposed a very similar criterion considering the thickening of the boundary layer in the clearance with a laminar law. He derived a criterion based on the chord length c , the blade thickness t , the Reynolds number Re , the pressure difference coefficient, across the blade, and the tip gap size τ :

$$\delta^*/\tau = \frac{2}{\sqrt{Re}} \sqrt{\frac{2}{\Delta c_p} \frac{c}{\tau}} \sqrt{\frac{t}{c}} \quad (1.12)$$

where δ^* is the displacement thickness. Based on this correlation, Chen [20] estimates that the viscous effects are not significant if $\delta^*/\tau < 10\%$. Given classical values for compressors², the ratio δ^*/τ stays below 10% and the flow within the clearance can be considered as an inviscid process. As other studies also showed it [98], Chen observed that the decrease in efficiency and loading varies almost linearly with the clearance size τ , for gap sizes between 1% and 4% chord length.

This is however qualified by the process described by Hewkin-Smith *et al.* [62] in which two competing phenomena act in the clearance region, depending on the gap size. In their study, the

² $\Delta c_p \approx 0.5$, $Re = 500000$, $t/c = 5\%$, $\tau/c \approx 2\%$

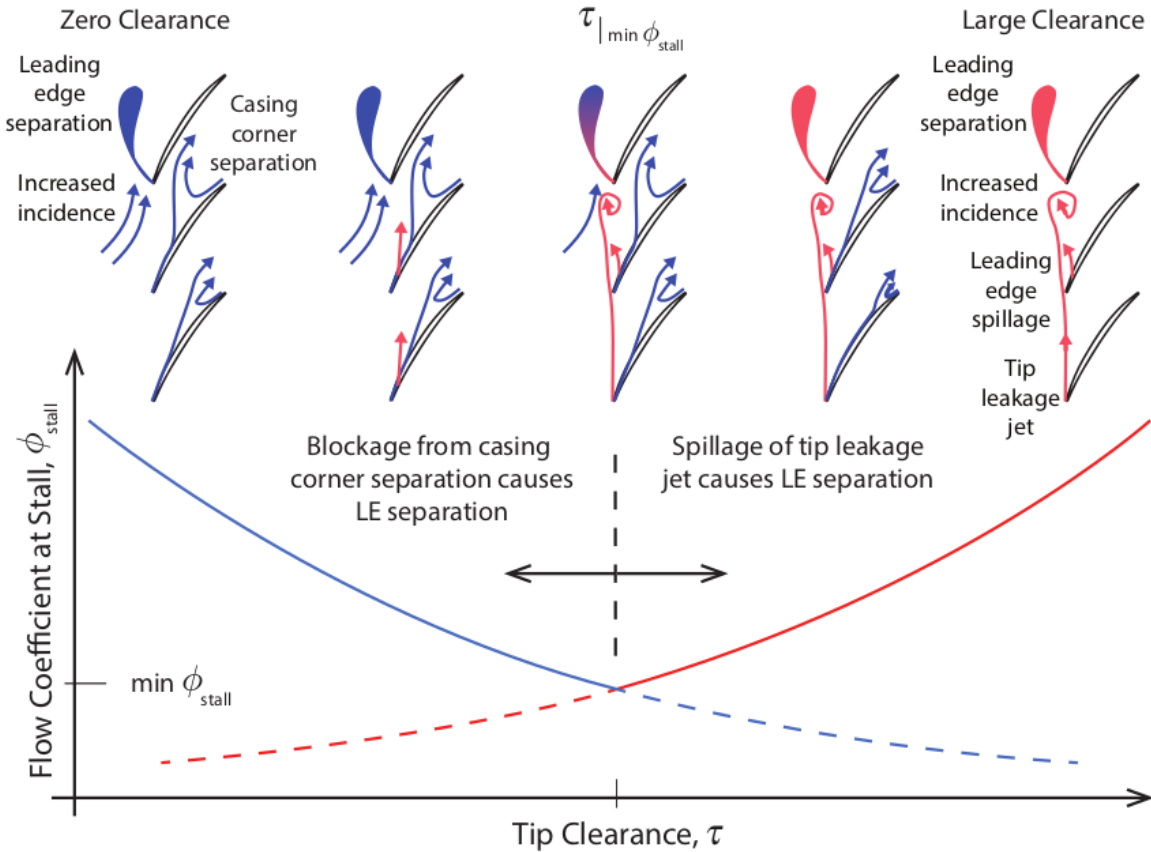


Figure 1.21: Illustration of the mechanisms leading to high incidence and stall, where the stall flow coefficient is plotted as a function of the tip gap size, from [62].

optimal point where the surge margin is maximal is obtained for a small clearance τ_{opti} different from zero. Their explanation puts forward the existence of a casing corner separation for smaller gaps than τ_{opti} that is responsible for the decreasing losses observed from zero clearance to τ_{opti} . In this range, the TLV, they explained, reenergizes the flow and reduces the casing corner separation, improving the incidence conditions. For gaps larger than the optimum, the vortex becomes much more intense and the topology described in the previous section is observed in their RANS simulations. This is summarized in Figure 1.21. This is consistent with what Storer and Cumpsty [134] observed in their experiment, in which they calculated losses due to TLF for two boundary layer thicknesses. For the thin boundary layer, the existence of an optimum for a non-zero clearance was also observed but for the thicker boundary layer, the evolution was linear as obtained by Chen. Besides, the losses calculated with the thicker boundary layer were twice as large for almost all the tip clearance sizes tested. It thus seems that the inlet casing boundary layer has a strong impact on TLF.

1.3.2 Casing boundary layer

In 1970, Smith [127] was one of the first to assess the growth of the boundary layer through the different stages of the compressor. Different from a classical two-dimensional boundary layer, as the one described by Schlichting [119] for example, it is subject to important shear stresses due to the motion of the rotors and contains varieties of vortex structures, which make it three-dimensional. Smith introduces new integral parameters to characterize the boundary layer developing on the endwalls of compressors. In particular, the tangential force thickness ν quantifies the loss of tangential blade force in the endwall boundary layer, *i.e.* the reduction of work done by the blade, from equation (1.2). The growth of the endwall boundary layers - at hub and casing - is particularly interesting since it can directly be linked to the onset of stall: as pressure rise increases, the boundary layers get thicker and thicker up to the maximum pressure rise for which instabilities start appearing. This is further discussed in section 1.4 with Khalid's model [73] who clarified the relation between the blockage area and the onset of instabilities.

The point here is to discuss the influence of the incoming casing boundary layer on tip-leakage flow. In the rear stages of compressors, as the flow is throttled, the boundary layer can be very thick: how does it impact tip-leakage flow? Brandt *et al.* [12] carried out a numerical study on varying the inflow conditions upstream of a single-stage compressor and analyzed the impact of the boundary layer thickness on TLF. One of their conclusions is that a thicker boundary layer moves the point of rolling-up of the TLV closer to the leading edge, which then induces more total pressure losses. They indeed observed that the vortex propagated farther downstream through the passage with a larger radial displacement of the vortex center. Their main result concerns a qualitative criterion on the amount of losses and the reduction of the surge margin due to TLF: for an increased δ/τ ratio, the detachment point moves towards the leading edge and the performance is degraded. Deveaux [42] confirmed the influence of the casing boundary layer thickness and showed that it has a strong influence on the lateral position of the TLV while virtually none on its vertical position, on a single blade configuration. Figure 1.22 shows the influence of the momentum thickness on the trajectory of the TLV for a tip clearance $\tau = 1\% c$ and for a fixed incidence.

Inoue *et al.* [66], in their experiment on an axial compressor, investigated the variations of the different integral quantities of the boundary layer (displacement, momentum and tangential force thicknesses), which rapidly increase with tip gap sizes for small values but vary less for larger gaps. The thickness of the inlet boundary layer has an impact on these variations. It seems that for a sufficiently thick boundary layer, increasing further the tip clearance has no more effect on these integral quantities.

1.3.3 Loading

The effects of blade loading are of particular importance when studying tip leakage flow. As mentioned in section 1.1, there is a maximum pressure rise at which the compressor can operate before the instabilities arise. The corresponding loading is influenced a lot by TLF, that has been identified as a major initiator of rotating stall and surge. This subsection deals with the influence

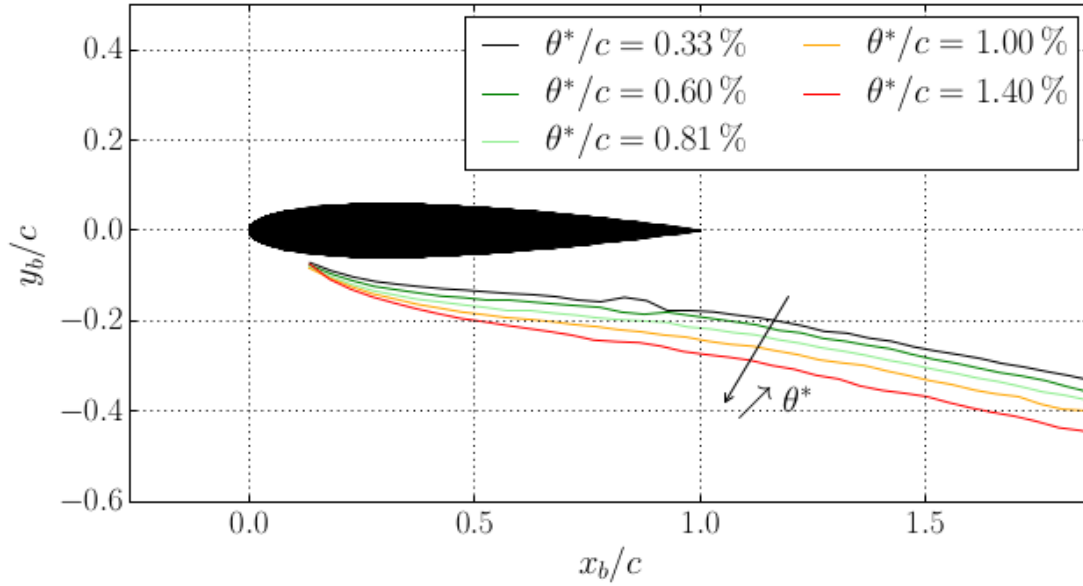


Figure 1.22: Influence of the momentum thickness on the TLV trajectory, from Deveaux’s RANS simulations [42].

of the incidence on the TLV and the subsequent effects on the rotor, both in terms of loss and stability.

Courtiade [23] investigated the unsteady flow and instabilities in the high-speed 3.5 stage compressor CREATE, further described in section 4.1. Numerous unsteady measurements were made with this experimental setup; on total pressure and temperature, and velocity. They were performed on four different operating points from the peak efficiency point to the last stable point before surge. Following the isospeed curve, the mass flow is progressively decreased towards the onset of surge. When throttling, and thus increasing the overall loading by lowering the mass flow rate, the trajectory of the tip-leakage vortex is shifted upstream, its circulation increases and the axial velocity decreases. Towards the trailing edge, the tip clearance flow and the casing boundary layer keep extending spanwise, increasing blockage. This was observed on first and third rotors where laser measurements were carried out.

Riéra [114] performed zonal detached eddy simulations (ZDES), a hybrid RANS/LES approach, on the first rotor of CREATE and investigated the effects of loading. Two simulations were validated on the experiments and compared: one at peak efficiency, and the other near surge. Riéra observed that the tip-leakage vortex extends azimuthally and is shifted upstream, closer to the leading edge, near surge. He also noted that near surge, the separation of the boundary layer on the casing is more intense as well as the intensity of the induced vortex. Also, the shock on the suction side is stronger and a local inversion of the flow arises.

Bettner and Elrod [9] carried out an experiment on a single stage compressor to study the effect of loading on the endwall boundary layers, which thickened significantly with loading. A link is made between the blockage area in the clearance region and the pressure rise by Khalid *et al.* [75]. In particular, a limiting value of the blockage area can be used as a criterion for

compressor stability. The principal mechanism behind the growth of blockage area is the low total pressure regions, especially the TLV core, which become larger for an increased loading or tip clearance.

This establishes a link between TLF and the onset of instabilities. More research has been done to have a more detailed view on one of the precursors of rotating stall. Vo *et al.* [142] determined two conditions on the spike type inception of rotating stall, related to TLF:

1. The interface between TLF and the incoming flow must be parallel to the plane of leading edges, *i.e.* TLF is aligned with the leading edge plane, resulting in spillage into the adjacent passage.
2. A tip clearance backflow is initiated in the aft part of the passage, from the spillage of the other adjacent passage, leading to the impingement of the flow on the pressure side of the blade in the current passage, yielding a local reversed flow and blockage.

The criterion established by Vo in his thesis followed the numerical study of Hoying *et al.* [64], who first noted the line-up of the TLV with the leading-edge plane. It is summarized by Figure 1.23.

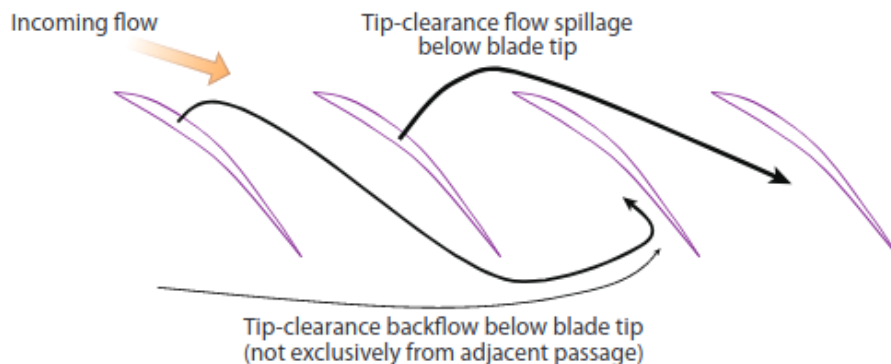


Figure 1.23: Illustration of the spike-type scenario proposed by Vo *et al.*, from Tan *et al.* [136].

Another study of Yamada *et al.* [148] concluded on the same two phenomena occurring when spike arises. Their DES simulation on an axial compressor indicated the presence of a tornado-like vortex, illustrated in Figure 1.24, connecting the casing endwall to the suction side of the blade and generating massive blockage. This massive blockage would be the cause of the leading edge separation and then spike observed.

Figure 1.25 from Tan *et al.* summarizes well the link between the topology of the flow in the clearance region and the type of stall inception.

As mentioned before, this massive blockage in the passage is not necessarily caused by a typical tip-leakage flow topology. For example, the study of Choi *et al.* already mentioned [21] showed that a massive hub corner separation was responsible for mass flow and incidence redistribution, the rotating stall therefore originating at the root. Pullan *et al.* [110] also noted the formation of leading edge separation vortices for shrouded blades, hence with no tip clearance,

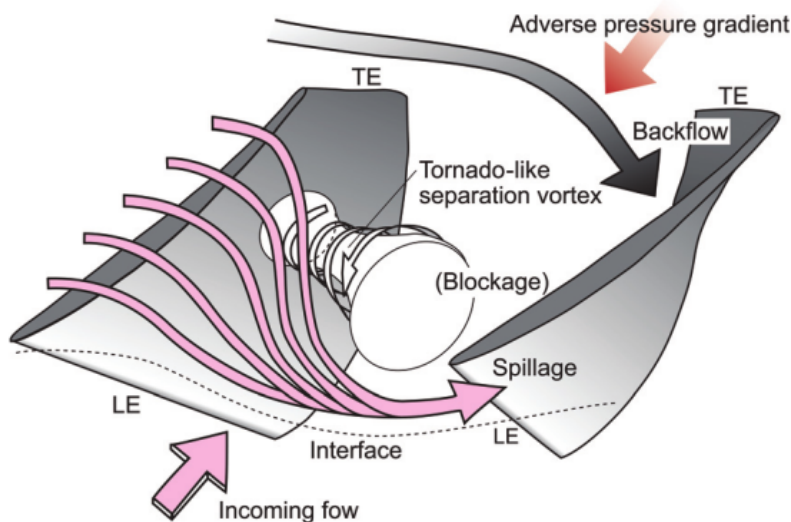


Figure 1.24: Topology of the flow in the clearance region with spike type inception. Presence of a tornado-like vortex identified by Yamada *et al.* [148].

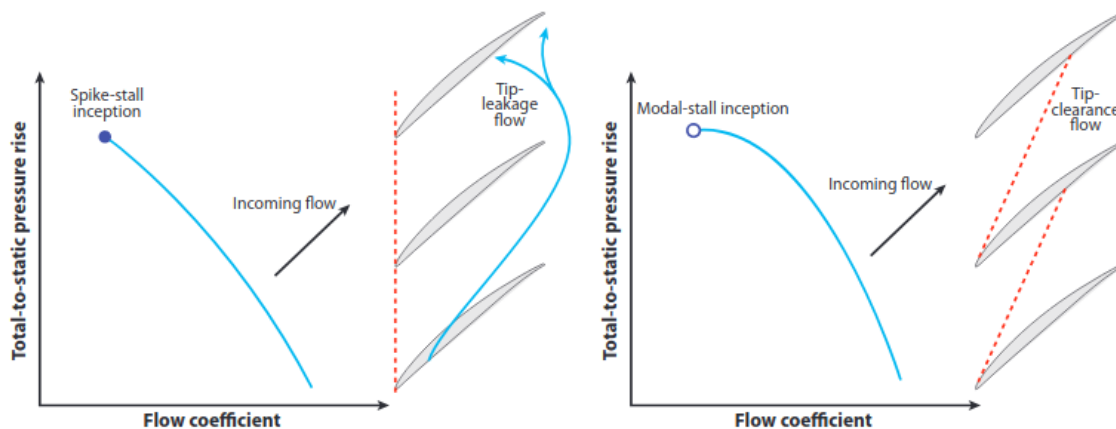


Figure 1.25: Summary of the two types of stall inception related to the flow topology in the clearance region, from Tan *et al.* [136].

due to a corner separation. Finally, the work of Hewkin-Smith *et al.* [62] showed that for small values of tip clearances, a casing corner separation is more likely to develop and could therefore be seen as another cause of leading edge separation in that case.

1.3.4 Relative motion

The relative motion between the casing and the blades is an important influence that must be considered on the evolution of TLF. The effect of the rotation induces the presence of a *scraping vortex* that adds up to the tip-leakage vortex, as observed by Allen and Kofskey [3]. This vortex has a negative effect on the flow in the clearance region since it rotates in the same direction

as the TLV, which increases further the vorticity [143]. The mechanisms driving the TLF are the same as with a motionless endwall, but the vortex core is displaced due to the motion, and the vortex is flattened and sheared due to the rotation. Despite the effects on the position of the vortex, the rotation does virtually not change the streamwise velocity deficit at the vortex center. Doukelis *et al.* [46] obtained the same detrimental effect on their annular compressor cascade and noticed that the losses were more sensitive to the clearance size when relative motion was added. For turbines, Yaras and Sjolander [151] observed on their cascade that the wall motion reduced considerably the strength of the TLV. The scraping vortex in that case presents a vorticity opposed to that of the TLV.

Another way to see this effect is summarized by Figure 1.26. For compressors, the relative motion of the casing increases the mass flow rate in the clearance because of the friction. The leakage flow is assumed to be entirely converted into vorticity when mixing with the mainstream flow. The TLV is enhanced by the relative motion and gains in intensity. On the contrary, for turbines, the mass flow rate in the clearance is reduced and subsequently the TLV intensity is lowered.

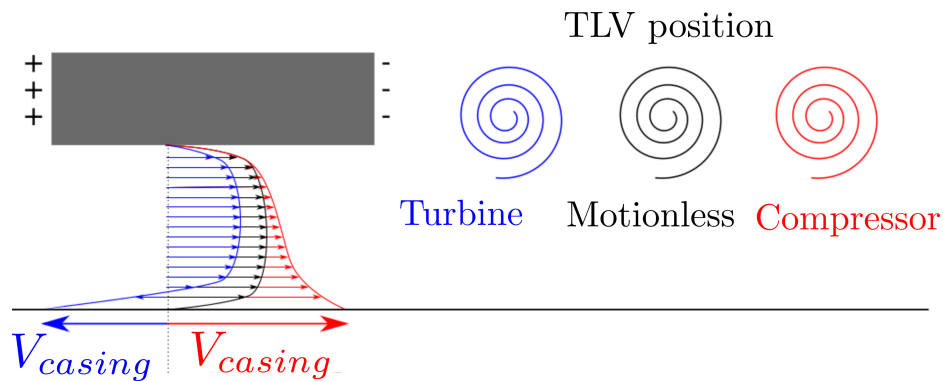


Figure 1.26: Effect of relative motion on the tip clearance velocity profiles and the position of the tip-leakage vortex relative to the suction side, adapted from Deveaux [42].

Lakshminarayana [79] infers the existence of the scraping vortex analytically by calculating an optimum size of tip clearance based on the sum of the secondary flow and leakage circulations, defining the optimal case as the one for which the flow is completely irrotational. This definition yields optimal tip clearances between 3 to 5% chord applied to compressor blades, whereas the classical values are rather between 1 and 1.5% chord. He then explains the large difference by the existence of a scraping vortex adding another circulation not taken into account in his model, induced by the relative endwall motion for actual compressors.

1.3.5 Rotor-stator interactions

Rotor-stator interactions are defined by the interaction of all the different flow structures generated due to the presence of the rows. This concerns wakes, potential effects, the corner separation vortices and more interestingly here, the tip-leakage vortex and the other structures in the clearance region. Courtiade [23] investigated these effects on the performance of the

research compressor CREATE and divided them into three categories of pressure interactions. Here, the review deals with the interactions between the TLF and the other structures found in the literature.

Gourdain *et al.* [56] studied the effects of tip clearance dimensions and casing treatment on the main structures in the tip region with different configurations of CREATE with URANS simulations. The most interesting observations concern the wakes and their role in destabilizing the flow. Their interaction with the tip-leakage flow in the tip region is more and more important when the mass flow is reduced or the tip clearance is increased. The trajectory of the TLV is then shifted upstream closer to the leading edge of the neighbour blade, which consequently makes it more intense. They put in evidence the role of the wake in destabilizing the trajectory of the TLV. Figure 1.27 shows how the trajectory of the vortex impacted by the wake gets closer to the leading edge plane, augmenting the risk of triggering rotating stall by a spike inception.

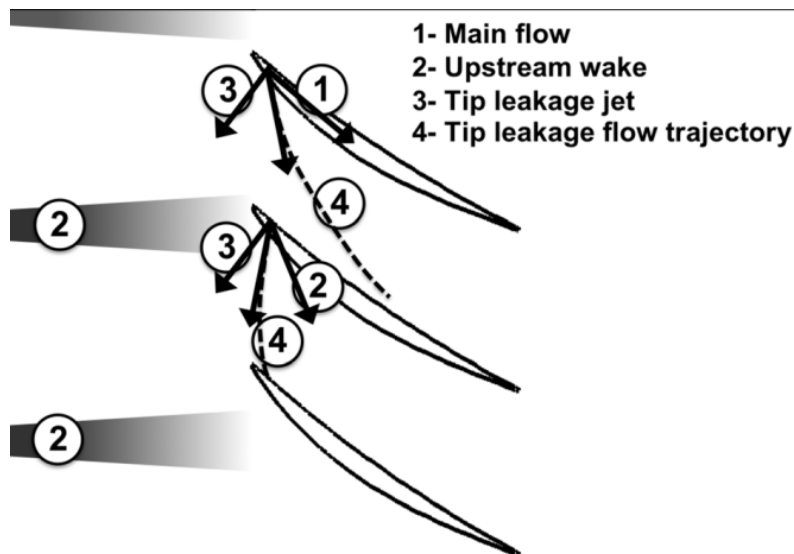


Figure 1.27: Comparison of cases without (upper blade) and with (lower blade) incoming wake interaction with TLV.

Mailach *et al.* [87] studied the interaction between the wakes from stator blades and the third rotor of a 4-stage low-speed axial compressor. Their Laser Doppler Anemometry (LDA) measurements showed that the TLV was much impacted by the passing wakes. The wake impact affects the vortex orientation, the maximum clearance mass flow rate and periodically changes the blade loading. This induces pulsations on the TLV and hence on the blockage generated. The interaction is illustrated by Figure 1.28. Pairs of counter-rotating vortices from the wake interact with the TLV and subsequently give birth to counter-rotating vortices in the TLV as well. These vortices then interact with the next passing wakes, which explains the periodical pulsation of the TLV. The authors therefore hypothesized that near stall, the interaction of the passing wakes could be involved in the rotating stall inception as the blockage area periodically pulsates. Too close to the critical value, from a slight excess in the blockage area due to the oscillations could originate a spike and the development of a rotating stall.

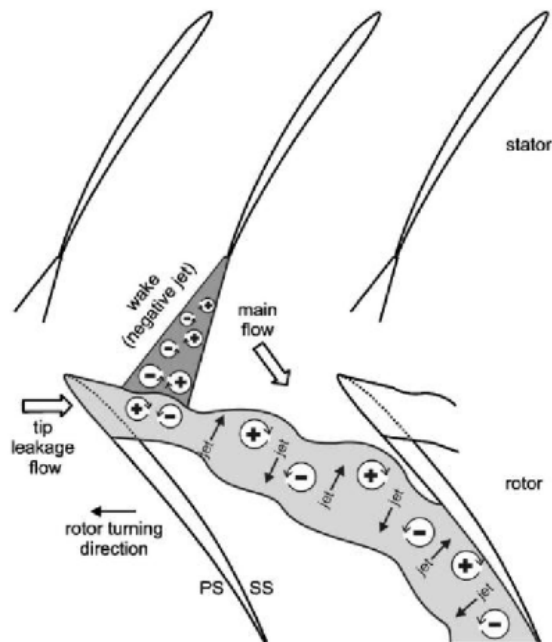


Figure 1.28: Influence of a passing wake on the TLV near the tip, from Mailach *et al.* [87].

1.3.6 The double leakage phenomenon

For highly loaded conditions and even for design conditions for some modern compressor designs [124], the trajectory of the tip-leakage vortex detaching from the blade suction side may be such that the TLV impinges the pressure side of the neighbouring blade. This creates an interaction between the TLV and the tip-leakage flow developing within the gap of the neighbouring blade. The phenomenon was first referred to as double-leakage by Khalsa *et al.* [76] [74]. Different effects are induced by this phenomenon, generally detrimental for the compressor performance, in terms of blockage and passage losses. The simulations of Sirakov and Tan [124] confirmed the impact of the double leakage on rotor performance but also showed how the rotor-stator interaction, especially the passing wake interacting with the TLV, could temporarily deflect the trajectory of the TLV and prevent double leakage, in unsteady conditions. Related to what was explained in the previous section about rotor-stator interaction, Sirakov and Tan showed that the effect of the passing wake is to induce pulsations of the TLV and temporarily suppress the occurrence of double leakage. Figure 1.29 illustrates the steady and unsteady behaviours of the double-leakage phenomenon. In the middle of the bottom row, the effect of the wake can be noticed on the suppression of the double leakage at that instant.

This phenomenon will be of particular interest in Chapter 4.

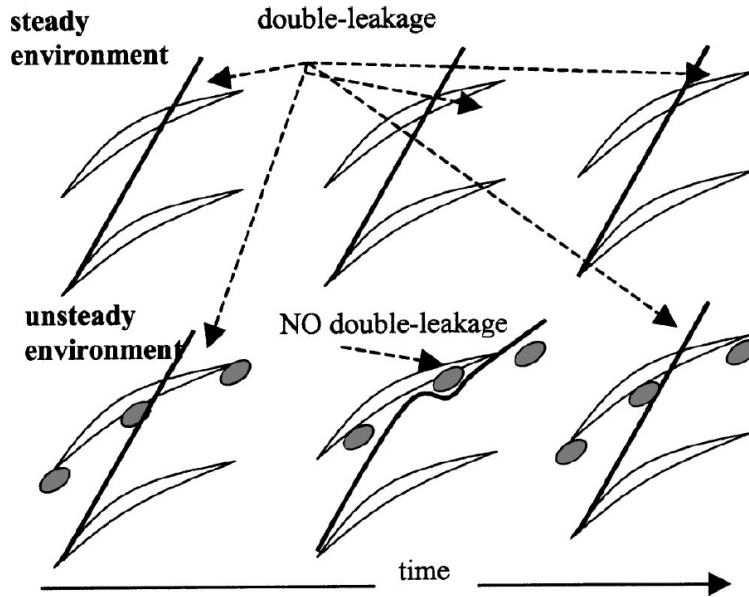


Figure 1.29: Illustration of the double leakage occurring in steady and unsteady conditions, from [124].

1.3.7 Technological effects

Technological effects can be used to control and reduce the impact of TLF on compressor performance. This subsection deals with the most common passive ways of controlling TLF.

Casing treatment Crook, in his thesis [28], mentions the earliest studies on casing treatment, that were first applied to fans. The goal was to improve stall margin by reenergizing the flow in the clearance region, which is known as a critical region regarding compressor performance. Usually, the casing treatment consists of circumferential or axial grooves, or a combination of both directions. Crook's work is interesting since the objective was mainly to understand the mechanisms at stake with casing treatment and explain improvements in the compressor performance, by analyzing the flow features in the endwall region, especially near stall. In their numerical investigations, Crook *et al.* [29] showed that the two main effects of casing treatment are:

1. The low total-pressure fluid at the rear of the passage is sucked up with the casing treatment.
2. The TLV core is reenergized by the recirculations.

This, in turn, reduces the blockage area and increases the pressure rise capabilities. Works of Schönweitz *et al.* [122] and Perrot *et al.* [104] support this view. Generally, the disturbances imposed by the grooved casing on the vortex tend to limit its spreading, which is beneficial for the operating range. Gourdain *et al.* [56] applied a honeycomb-like casing treatment to the third

rotor of the research compressor CREATE with grooves inclined axially and circumferentially. For the same tip gap size, the casing treated proves to be better in terms of compressor stability:

1. The operating range was expanded with the casing treatment.
2. Coherently, the blockage area is largely reduced in the third rotor.
3. The casing treatment impacts the incidence by reducing the axial velocity deficit in the casing region, which is critical on the third rotor of this compressor.
4. The pressure difference across the rotor near leading edge, where the vortex gains most of its intensity, is well reduced.

All these results showed a real beneficial impact on the control of TLF and improvements on the operating range of the compressor. Nonetheless, it must be brought up that the casing treatment may reduce the maximum isentropic efficiency.

Squealers Another way of reducing TLF losses is to modify the geometry of the blade at the tip by using squealers as shown in Figure 1.30. This is particularly used on turbine blades because it has an impact on the thermal loading of the blades, but the effect is interesting to mention regarding the effects on TLF. The metal removed near the tip modifies the TLF by sucking part of it near the leading edge and reinjecting it near the trailing edge. In turn, the mass flow is reduced in the clearance and hence the losses in the clearance region.

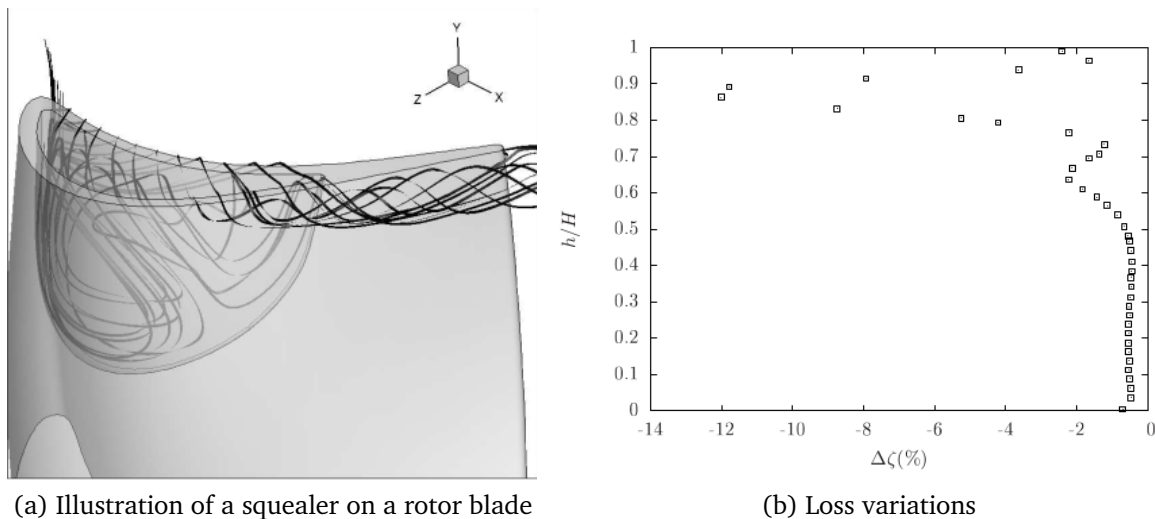


Figure 1.30: Losses variations with a squealer, from Wlassow [147].

1.4 Modelling tip-leakage flow

1.4.1 From the single blade towards high-speed compressors

Understanding the tip-leakage flow passes through different levels of representation towards a high-speed compressor such as those encountered in a real turbomachine. Figure 1.31 indicates the main effects driving the tip-leakage flow for different types of TLF configurations, from the single blade to the high-speed compressor. The list is certainly not exhaustive but reports the most common effects found in the literature. Being able to correctly model all these effects altogether would probably yield a good TLF model.

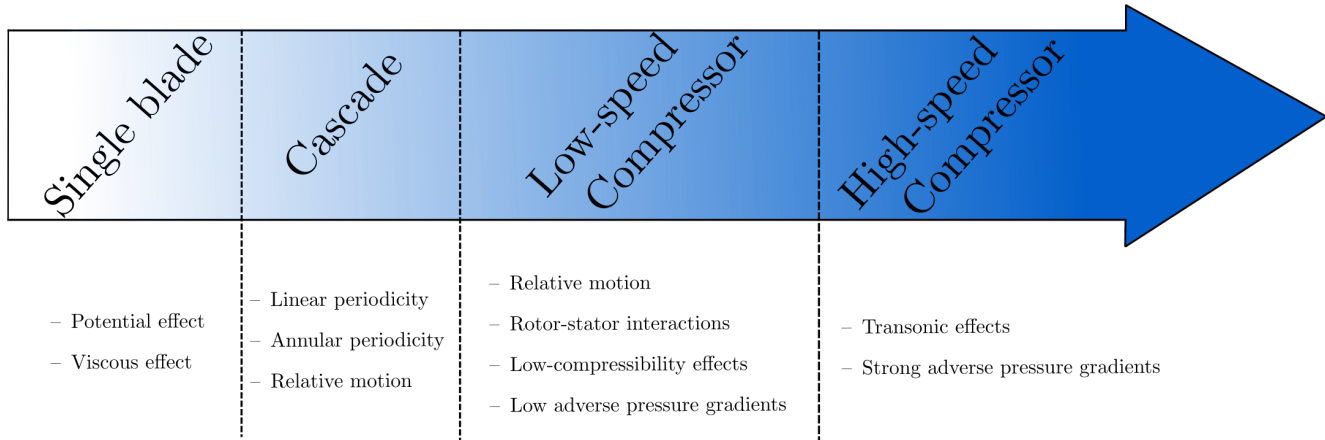


Figure 1.31: List of the main effects encountered by the tip-leakage flow from the single blade configuration to a high-speed compressor.

The simplest case is the single blade TLF configuration. Classically, experiments consist in investigating the flow between two blade tips spaced of 2τ , or the flow in a wind tunnel on a blade whose tip is at the distance τ from the endwall. In these configurations, τ can be chosen sufficiently large to neglect viscous effects [81]. The order of magnitude of representative tip gap sizes for compressors is about 1% chord length and viscous effects cannot be neglected. The proximity of the blade tip to the endwall typically induces a strong interaction between the boundary layer and the TLV.

The periodicity can be investigated on TLF cascades, in which the blades are repeated periodically. The pitchwise proximity of the blades with one another influences their loading and, subsequently, the TLF. The cascade geometries can be linear or annular. The former is more widespread for cascade experiments but the latter is closer to a real compressor rotor.

The next level of representation is the low-speed compressor. The relative motion between the casing and the rotor impacts the trajectory and the circulation of the TLV. The rotor-stator interactions represent the influence of the other blade rows through the passing wakes or the unsteady potential effects. The low compressibility effects are found in the spatial density variations due to higher Mach numbers (> 0.3) in the flow field. This impacts the lift of the rotor blades, hence their loading, decreased by the flow compressibility.

The rotation of the rotor combined to the flow deflection achieves a compression all along the blade chord, which means that the flow undergoes an adverse total pressure gradient. If the revolution speed of the rotor (or the deflection imposed by the rotor design) is high, the adverse

pressure gradient in the blade passage along the chord may be strong. Its impact on the TLV development in the passage cannot be neglected. Finally, the speed of some rotors at the tip can be so high that the local Mach number can exceed 0.7: the presence of shocks or supersonic regions may cause important perturbations on the TLV behaviour.

Different approaches have been used to model TLF. We have seen that the tip-leakage flow was driven by the pressure difference between pressure and suction sides of rotors. Some authors therefore focus on the clearance region where a jet forms to finally mix out with the mainstream flow in the passage, according to Rains' theory. Another approach, already brought up through Khalid's works, is to consider the growth of the casing boundary layer and the increased blockage area, directly related to the higher losses and stall inception. Finally, others focus on the vortex itself, which by its intensity and the significant levels of vorticity is the source of the losses.

1.4.2 Jet based models

1.4.2.1 A mixing loss model

Storer and Cumpsty [134] developed a model regarding losses due to TLF. It follows on from the topology described by Rains where the encounter of the leakage jet and the mainstream flow generates the losses due to their mixing. This model gives a good estimate of tip clearance losses for incompressible flows. Two equations are necessary to get a first estimate of the losses based on dimensionless variables characterizing the axial compressors row (aspect ratio, clearance-to-span ratio, blade loading, flow coefficient). Through the losses in stagnation pressure, these two equations enable to quickly assess the loss in efficiency depending on the compressor design. It therefore gives an interesting first estimate of the best design fitted for minimum losses in efficiency. This orientates the more expensive simulations to be performed, focusing on designs whose losses are minimum with the model.

The model can be simply explained by figure 1.32. The loss is generated by the mixing of the leakage jet with the mainstream flow. The flow is assumed incompressible and each stream enters in the control volume with a uniform and equal speed V . The loss is therefore due to the difference in direction of the two streams and the loss generation can then be calculated along the chord, just knowing the angle ζ .

The knowledge of two parameters is necessary to use the model: the section ratio $\chi = a/A$ and the mean jet angle ζ . The losses are calculated in terms of total pressure loss using these two parameters in the following equation:

$$\frac{\Delta P_0}{\frac{1}{2}\rho V_{exit}^2} = \chi \sin \zeta \left(\frac{2 + \chi \sin \zeta - 2 \cos \zeta}{(1 + \chi \sin \zeta)^2} \right), \quad (1.13)$$

The derivation of this equation and the assumption made are detailed in Appendix A.

A very similar model has also been developed by Denton [40], with less restrictive assumptions. Denton's model can indeed be applied to compressible flows and does not consider the

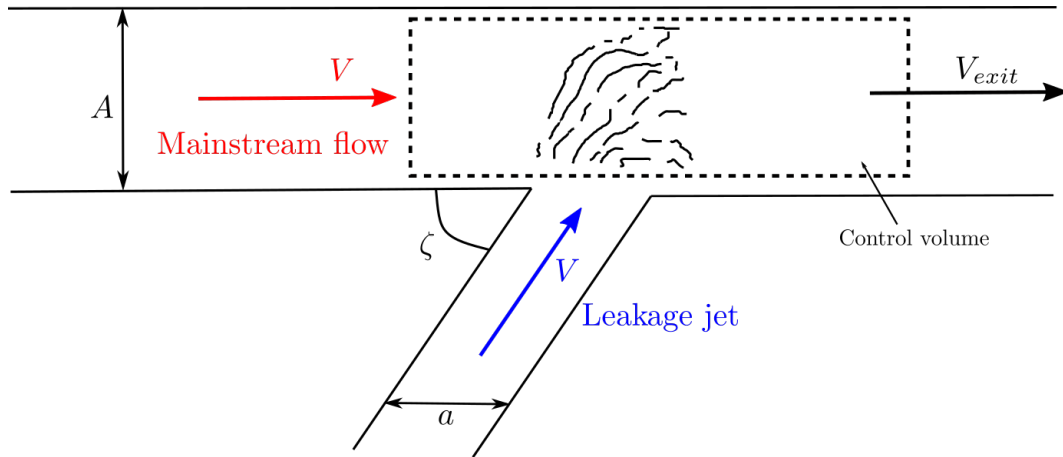


Figure 1.32: Schematic of Storer and Cumpsty’s model of leakage jet mixing with mainstream flow, adapted from [134].

jet and mainstream velocities to be equal. The idea is to calculate the rise in entropy due to the mixing of the jet with the main flow due to the difference in direction and magnitude of the two velocities. The model however needs the velocity distributions as inputs.

1.4.2.2 Kinetic energy of the jet

Instead of considering the mixing process itself to estimate the losses, another idea is to calculate the kinetic energy associated to the leakage flow passing in the clearance. As done by Rains or Vavra [111] [141], this energy is considered as never recovered and hence lost. It therefore suffices to estimate leakage flow to get the tip-leakage losses.

1.4.3 Blockage models

1.4.3.1 Endwall boundary layer growth modelling

As described by Smith [127], tip-leakage flow has a direct impact on the growth of the boundary layer at casing. The growth of the cumulated hub and casing endwall boundary layers is well described in Aungier’s model [5]. The three-dimensional aspects are considered and the integral quantities defining the boundary layer are calculated through each stage of the compressor. The estimate of the displacement and tangential force thicknesses δ^* and v , introduced by Koch and Smith [77], is done iteratively from the characteristics of the boundary layer at the compressor inlet.

1.4.3.2 Khalid’s model

This subsection describes the main features of Khalid’s model regarding the blockage area defined in his thesis whose variations with tip clearance are modelled.

The essential features addressed in Khalid’s model are the following:

1. The total pressure deficit due to TLF.
2. The pressure rise in the passage.
3. The mixing of the low total pressure regions.

Khalid builds the blockage model from a two-dimensional turbulent wake model, from Hill *et al.* [63], in an adverse pressure gradient. The characteristics of the wake (width and depth) are related to the initial integral quantities of the wake (displacement and momentum thicknesses) and their development with the streamwise position is given by the model, considering turbulent mixing acting on the wake. Figure 1.33 shows the leakage velocity profiles in a crossflow plane right after the clearance exit, near the suction side of the blade, and farther downstream where the velocity profile can be seen as a wake, v_m being the component in the mainstream direction. It can be seen that the leakage component is quickly dissipated downstream of the clearance, the mainstream component only remaining.

Following this observation, Khalid develops a wake model on the development of v_m to account for the blockage growth along the passage. The blade suction side is discretized into n elementary wakes of length Δl_n , that are independent with one another, *i.e.* assuming in the model that they do not interact with one another. The lengths Δl_n are assumed constant in the wake development throughout the passage. The lengths Δl_n can be expressed as functions of the local tip-leakage angle α and the chord length Δc_n of the wake concerned. The growth of the wake is modelled with Hill's two-dimensional model, which relates the width b and depth β of the wake to the integral quantities δ^* and θ . The model is illustrated in Figure 1.34. Storer and Cumpsty's model gives the mainstream component of the flow at the clearance exit for every position and the initial integral quantities of the wake are then obtained. The final values at the trailing edge are yielded with Hill's model. Each of them contributes to the overall blockage area calculated at this position as the sum of the blockage areas from every elementary wake.

Physically, this does not correspond to what occurs in the passage, since the TLV is actually mixing the flow. The independence of the wakes from one another in their development then seems unphysical, but the main point of Khalid's predictions is not to model these interactions but only the blockage due to TLF. The influence of mixing on the wake paths is well captured by Khalid's model and his results agree well with different three-dimensional computations. Khalid's model demonstrated a main aspect in the mechanism of blockage: the response of low total pressure regions to the passage pressure rise, the detailed chordwise distribution being unimportant. Another aspect is the main contribution to the blockage area of the wakes originating near the leading edge, showing TLF most energetic structures and losses are formed near the leading edge.

1.4.4 Vorticity based models

Another way of estimating the losses is to consider the TLV generated itself. The idea is to calculate the losses from the vortex characteristics, by looking at the induced drag or the total pressure loss. The goal of this type of models is to estimate two main parameters describing the characteristics of the TLV:

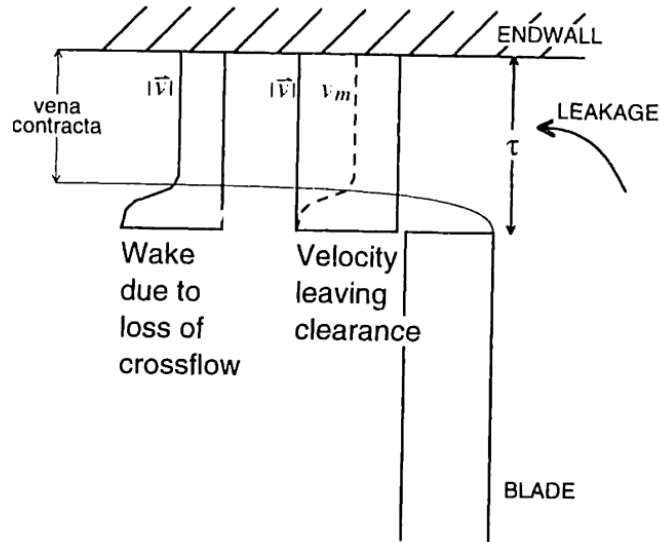


Figure 1.33: Velocity profile in a crossflow plane downstream of the clearance exit, from Khalid [73].

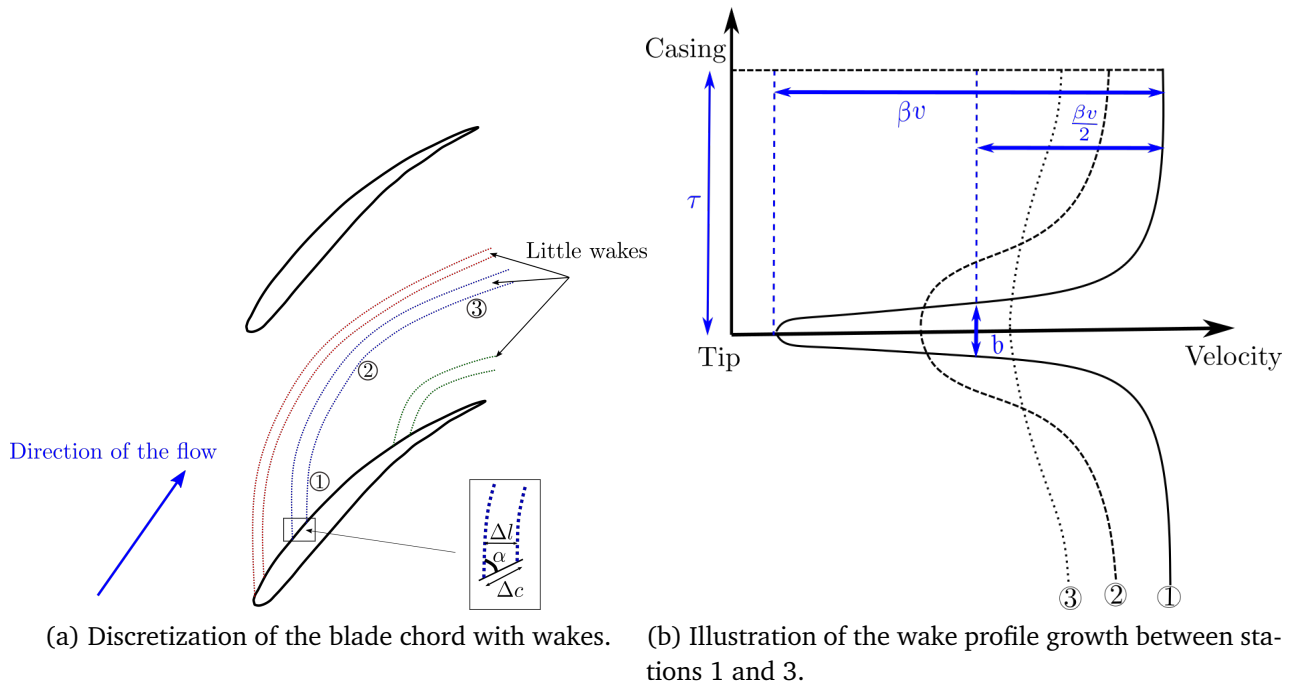


Figure 1.34: Schematic of Khalid's wake TLF model, based on the two-dimensional modelling of Hill.

1. The vorticity ω , more importantly its axial component.
2. The radius of the vortex core.

If one is able to estimate these two parameters at the point of detachment, one can estimate

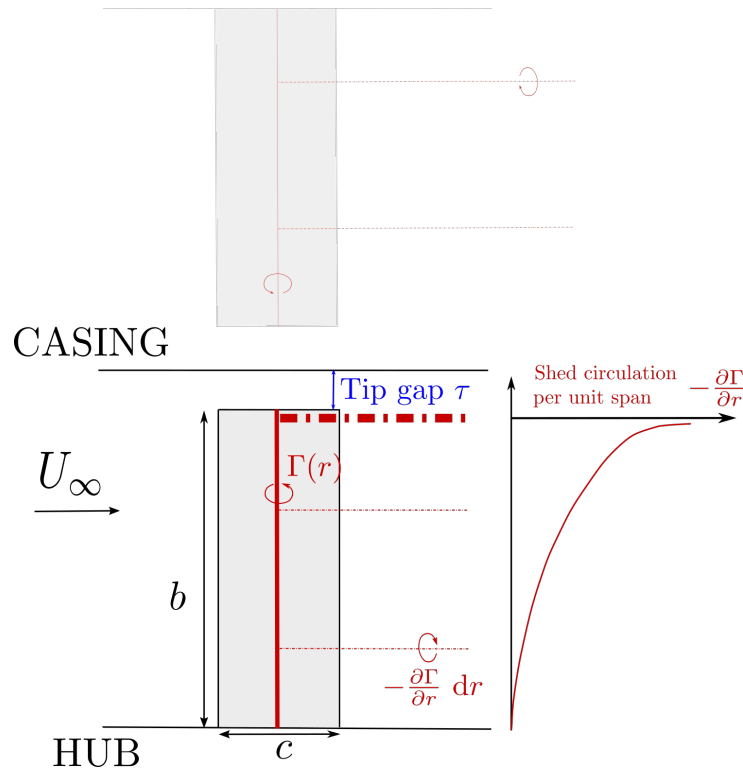


Figure 1.35: Schematic of the lifting line model used by Lakshminarayana and Horlock, the shadowed blade corresponds to the fictive mirror line used in this model.

the evolution of the losses chordwise with analytical vortex models, yielding the axial evolution of the vortex, particularly considering viscosity. The position of the point of detachment can be fairly approximated at the minimum static pressure chordwise, as previously stated. The knowledge of these characteristics allows obtaining the circulation of the vortex at different axial positions. It is then possible to see how this impacts the loading of the blade.

1.4.4.1 Lifting line theory

The model of Lakshminarayana and Horlock [80] is based on a lifting line model derived from Prandtl's theory and applied to a slotted wing, the gap being 2τ . With the existing symmetry condition centered in the middle of the slot, the configuration is similar to the schematic shown in figure 1.35, replicating the presence of a casing and a tip clearance τ . They performed an experiment on that wing varying the gap and compared the results with their model. They identified two cases for their model to be used:

1. For high gap/chord ratios λ , Glauert's type of analysis can be applied.
2. For lower values of λ , viscous effects must be considered.

In the second case, they introduce an empirical coefficient K corresponding to a *retained* vorticity. Indeed, the circulation directly computed from Glauert's theory does not fit with the

experimental measurements. The vortex shed at the tip then has a circulation equal to $(1 - K)\Gamma$, with Γ the shed circulation obtained from the lifting line theory.

Another article of Lakshminarayana [79] relates the circulation calculated with the model to the drag coefficient and the resulting losses. The drag coefficient C_D is expressed for incompressible flows as

$$C_D = \frac{C_L^2(1 - K)}{8\pi AR} f\left(\frac{\tau}{b}\right) \quad (1.14)$$

with AR the aspect ratio of the blade.

Lakshminarayana determines an empirical expression depending on the tip gap size and the pitch s that leads to an expression of the induced drag coefficient as a function of these two parameters and the lift coefficient:

$$C_{Di} = 0.7 \frac{C_L^2}{AR} \frac{\tau}{s} \quad (1.15)$$

These losses are only due to the presence of a potential vortex but they do not account for the energy losses associated to the spanwise flow inside the blade boundary layers. The total pressure loss is therefore divided into two terms as shown below in equation (1.16):

$$\zeta_{\text{tot}} = \zeta_{\text{pot}} + \zeta_{\text{visc}} \quad (1.16)$$

where $\zeta = \frac{\Delta p_0}{p_{01} - p_1}$ represents the total pressure loss.

The first term ζ_{pot} depends on the induced velocities due to the presence of the vortex in the inviscid region and can be calculated with the induced drag coefficient introduced in equation (1.15). The second term ζ_{visc} is due to the spanwise flow in the blade boundary layers: a relation can be derived where the spanwise velocity perturbations w on each side of the blade can be related to the boundary layer displacement thicknesses δ_s^* and δ_p^* .

This approach is able to give the decrease in stage efficiency due to tip-leakage flow. Their results are in quite good agreement with different experimental data.

This model however only provides global losses at the trailing edge of the blade. To have an idea of the decrease of performance due to TLF, this seems to be an interesting approach but a preliminary design of a blade needs a more complete model capturing the blade to blade characteristics of the flow, pitchwise and spanwise. The idea is then to model the chordwise evolution of the vortex: its trajectory, its radius evolution and its intensity.

Prediction of the blade to blade flow In the same article, Lakshminarayana developed a second model [79] to go beyond the limitations of potential vortex theory. The vortex model proposed by Lakshminarayana is based on different experimental observations and is described by three characteristics, as shown in figure 1.36. Assuming the vortex core contains all the shed vorticity, its radius a can be estimated along with its vorticity ω and the location of the vortex in the passage, characterized by b .

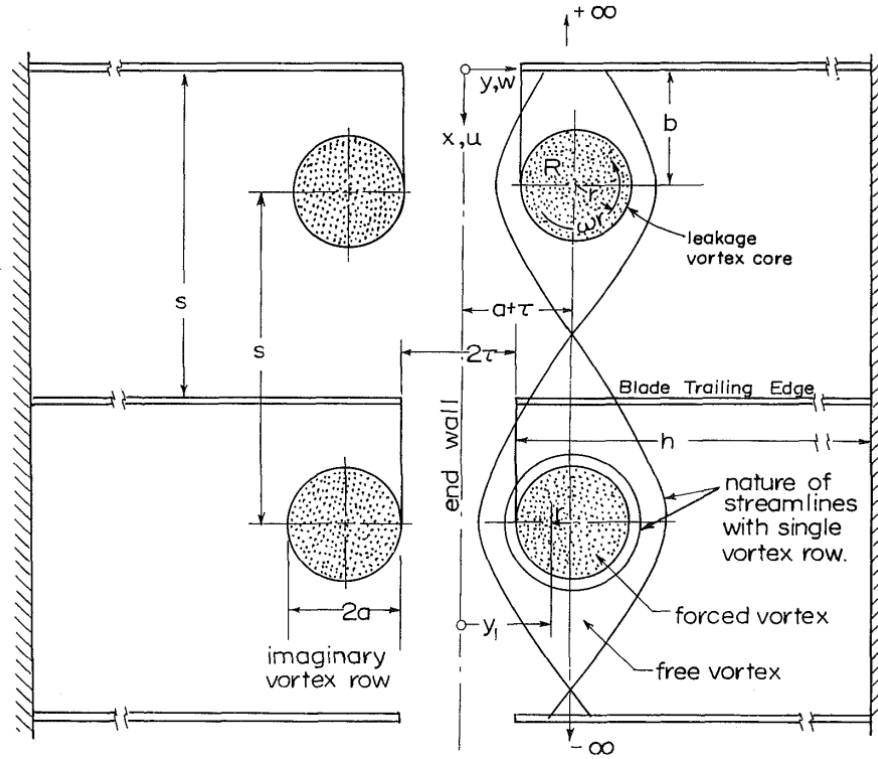


Figure 1.36: Illustration of the vortex characteristics used in Lakshminarayana's model [79].

The radius a is estimated from Rains' theory, relating it to the lift coefficient at the tip C_L , the distance d run by the vortex since its origin where it detached, and the tip gap size τ :

$$\frac{a}{\tau} = 0.14 \left(\frac{d}{\tau} \sqrt{C_L} \right)^{0.85} \quad (1.17)$$

The vorticity ω is a function of the core radius and the circulation Γ of the shed vortex:

$$\omega = \frac{(1 - K)\Gamma}{2\pi a^2} \quad (1.18)$$

The location of the vortex in the passage b tends to increase due to the image vortices, corresponding to moving the vortices in their respective passage farther from the suction side. Starting from vortices at the leading edge, the idea is to calculate the induced flow field due to the image vortices at every axial position along the blade. From that, their position in the passage b can be inferred.

Deviation variations From the characteristics of the vortex, the deviation variations due to the presence of the TLF can be estimated knowing the spanwise distribution of lift C_L .

– Inside the vortex core for $r < a$

$$\tan \Delta \beta_2 = \frac{(1 - K)C_L c r}{4\pi a} \frac{r}{a} \quad (1.19)$$

- Outside the vortex core for $r > a$

$$\tan\Delta\beta_2 = \frac{w}{U_\infty} \quad (1.20)$$

where w is the pitchwise component of the perturbation velocity which can be estimated with the different parameters of the vortex.

1.4.4.2 Nikolos' model

The idea presented in Nikolos *et al.* [101] is to consider that the leakage flow between the pressure and the suction sides is completely converted into the tip leakage vortex (TLV). Their model is presented in two parts:

1. The first part deals with the value of the mass flow rate associated to the leakage flow
2. The second part relates the mass flow rate to the characteristics of the shed vortex at the point of detachment. They also add the vorticity diffusion of the vortex from that point to the trailing edge by considering line vortex models (Lamb and Newman).

Tip-leakage flow - Mass flow rate Following Rains' assumptions presented in section 1.2, their model enables to calculate the mass flow rate through the gap along with the total pressure losses. They improved it by adapting the mass flow rate calculation to the shape of the velocity profile in the gap downstream of the vena contracta. The idea is nonetheless exactly the same and the losses are estimated by computing the energy corresponding to the mass flow rate.

Tip-leakage vortex characteristics From the results obtained in different sets of measurements regarding the characteristics of the vortex [79] [66] [149], Nikolos *et al.* consider the vortex as a solid body rotation structure. The introduction of a retained lift is contested by the authors who propose a new process for the vortex roll-up. The authors assume that the mass flow exiting the gap is wrapped around the existing vortex and supplies its development, increasing both its radius and its intensity. Depending on the value of the velocity at the clearance exit, given by the first part of the model, the circulation and the radius of the vortex forming can be calculated for every streamwise position, adding up to the circulation calculated upstream. The crucial point here is the complete conversion of the clearance mass flow into the formation of the TLV. Improving further the model, the diffusion of the vortex is added, considering line vortex models that account for viscosity. Lamb's [82] and Newman's [99] analytical vortices are compared in the study and give quite good results compared to three experiments, regarding the evolution of the circulation and total pressure losses. The mathematical description of these vortices is given in Appendix .

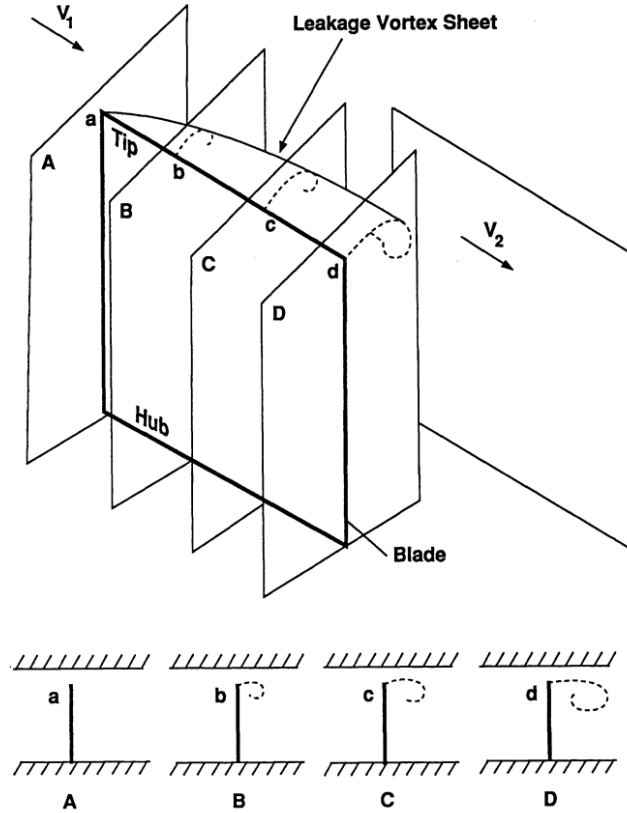


Figure 1.37: Illustration of the evolution of the TLV in the successive crossflow planes, from an unsteady two-dimensional model flow, from Chen's thesis [20].

1.4.4.3 Chen's model

Chen's model [20] is particularly interesting since it analyzes the evolution of the TLV. His idea is to decompose the clearance velocity into independent throughflow and crossflow components according to Rains' assumptions. The generation of the TLV and its roll-up are developed through an unsteady process in successive cross-flow planes, adopting a slender body approximation. The formation of the TLV is reconstructed based on a translation relating time and streamwise position. The values of interest at midspan are gathered into a dimensionless variable t^* for the time increment dt :

$$t^* = \frac{dt}{\tau} \sqrt{\frac{\Delta p}{\rho}} \quad (1.21)$$

The characteristics of the TLV in the different crossflow planes are then recovered from this parameter: two similar TLV correspond to the same value of t^* . For example, the circulation or the position of the vortex core can be obtained from that. The vorticity shed at the tip of the blade is calculated using a two-dimensional unsteady panel method, and is then convected away with the streamwise transformation. The model enables to track the vortex in the crossflow planes as shown in Figure 1.37.

From that, Chen was able to get a correlation on the trajectory of the TLV. This correlation

is a very simple expression relating the dimensionless pitch coordinate of the TLV core to the dimensionless time at midspan:

$$y_c^* = K_{Chen} t^*, \text{ with } K_{Chen} = 0.46 \quad (1.22)$$

This can be rewritten expressed as an angle ε_{TLV}

$$\tan \varepsilon_{TLV} = K_{Chen} \sqrt{\left(\frac{\Delta p}{\rho V_x^2}\right)_{\text{mean}}} \quad (1.23)$$

where V_x is the axial velocity and ρ the density. The quantity inside the square root is averaged over the chord line to estimate the mean trajectory of the TLV. Note that the expression can be used for compressible flows with a variable density over the chord. What is remarkable is that the correlation on the angle of the TLV with respect to the chord line of the blade does not depend on the tip gap size. The values are extracted at midspan where the effect of the tip gap size is negligible on these values. Chen validated his model on different compressor configurations, including that of Inoue *et al.* [66], for tip gaps varying between 0.85% and 4.3% chord length.

Besides, equation (1.23) can be rewritten as a function of the solidity σ , the inlet angle β_1 , the outlet angle β_2 and the mean flow angle β_m at midspan:

$$\tan \varepsilon_{TLV} = K_{Chen} \sqrt{\frac{\tan |\beta_1| - \tan |\beta_2|}{\sigma \cos |\beta_m|}} \quad (1.24)$$

This expression shows two things:

1. For increased incidence (increasing $|\beta_1|$), the angle ε_{TLV} increases, coherently with the literature: the TLV is getting closer to the leading edge of the adjacent blade for increased incidences.
2. If σ is large, typically if the blade pitch s is low (for a high number of blades on the row for example), the TLV core will remain closer to the suction side of the current blade. If σ is low, the variations of the TLV angle will be stronger with the incidence and the TLV will more rapidly get close the leading edge of the adjacent blade. This is consistent with the fact that the solidity usually reinforces the stability of a rotor.

1.5 Synthesis on the literature

Several aspects of tip-leakage flow have been described through this literature review:

- TLF has a major role in compressor performance reduction, in terms of efficiency and surge margin.

- The most frequent topology encountered at the tip of compressor blades consists of two regions: one where the leakage flow across the blade within the clearance develops, the second where mixing with the mainstream flow takes place with the presence of a tip-leakage vortex. This is based on Rains' assumption that the pitchwise pressure gradient is much greater than the chordwise gradient, assumption generally valid for compressor blades.
- The performance is largely affected by the size, the trajectory and the intensity of the TLV.
- The trajectory of the TLV is related to the onset of instabilities and mainly affected by the thickness of the endwall boundary layer and the blade loading: increasing them drives the TLV away from the suction side. The gap size has little effect on the trajectory, but the point of roll-up is farther away along the suction side for large tip gaps.
- The size and the intensity of the TLV generally increase linearly with the tip gap size, and relate directly with the total pressure losses. The circulation of the TLV is a good indicator of the intensity of the TLV.
- Relative motion of the casing strengthens the TLF for compressors.
- The presence of the TLV contributes significantly to the blockage increase in the blade passage at the tip.
- Different viewpoints can be adopted to study the effects of TLF on the performance. These constitute the basis of three types of modelling, each focusing on a specific feature of TLF (mixing, vorticity and blockage).

All these aspects have led to the definition of the present work, whose objective is to clearly understand the role of the tip gap size in driving tip-leakage flow, through the formation and the characteristics of the tip-leakage vortex.

The results introduced in the literature review will be investigated regarding the sensitivity of the TLV characteristics to the tip gap size with the use of a hybrid RANS/LES method (ZDES). First, does it confirm the experimental and numerical results presented here regarding the effects of τ on the TLV trajectory and circulation? Second, how the largest structures in the TLV are resolved with the hybrid approach? How the dynamics of TLF is then impacted depending on the fluctuations within the TLV? In the present work, investigating the influence of the tip gap size on the unsteady behaviour of TLF is of particular interest with the use of the ZDES.

The investigation performed by Riéra [114] showed the benefits of using ZDES on a realistic compressor, capturing the most essential flow characteristics on the first rotor compared to the experiment for a single tip gap size. In the present work, the intention is to study the TLF sensitivity to the tip gap with the same numerical approach and the same compressor, but on the third rotor whose TLF is known to be more intense, and also more unstable [23]. The impact of the tip gap size on the double leakage phenomenon presented in this chapter is of particular interest.

TLF modelling has been presented essentially following three viewpoints. The present work is intended to gauge the capabilities of a method usually applied to external aerodynamics, regarding the influence of the tip gap size on TLF. The intention is to develop a model based on the Vortex Lattice Method (VLM) in order to predict the characteristics of the TLV. The application of VLM to TLF configurations is almost inexistent in the literature, to the author's knowledge: how such a method can capture the essential features of TLF? Is it accurate enough to capture the sensitivity to the tip gap size? Can it run sufficiently quickly to be considered as a possible predesign approach for designers? The originality of the present work lies in the attempt of answering these questions on a simplified TLF configuration (single blade, static) presented in Chapter 5.

Part II

METHODS FOR ANALYZING TIP-LEAKAGE FLOW

STRATEGIES FOR TIP-LEAKAGE FLOW SIMULATIONS

Contents

2.1	Introduction on simulating turbulence	58
2.1.1	The Navier-Stokes equations	58
2.1.2	Strategies for fluid dynamics simulations	59
2.2	Reynolds Averaged Navier-Stokes Equations (RANS)	61
2.2.1	Principle	61
2.2.2	Turbulence modelling	62
2.2.3	Compressible case	63
2.2.4	The Spalart-Allmaras model	63
2.3	Large Eddy Simulation (LES)	63
2.3.1	Strategy and use	63
2.3.2	Subgrid scale models	64
2.3.3	Estimation of the CPU cost	66
2.4	Zonal Detached Eddy Simulation (ZDES)	67
2.4.1	Introduction to hybrid simulations	67
2.4.2	Presentation of the ZDES	69

2.1 Introduction on simulating turbulence

The literature review presented on tip-leakage flow in Chapter 1 showed the complexity of such 3D flows in compressors. If good progress has been made on the comprehension of the impact of TLF on the compressor performance, the behaviour of the tip-leakage vortex can still be further understood with the help of high-resolved computational fluid dynamics (CFD) simulations. These high-resolved simulations have not been so used on wall-bounded configurations such as turbomachinery because of their cost. However, the power of current CPU nowadays offers better possibilities for these simulations to be performed, going beyond the classical RANS turbulence modelling, poorly adapted to secondary flows such as the corner separation [94] or the tip-leakage flow [93].

In the present thesis, a good compromise must be found between flow resolution and computational cost for a simulation applied to tip-leakage flows (TLF). This section is intended to progressively introduce different levels of resolution regarding turbulence in order to choose the most fitted resolution to an acceptable cost. This chapter introduces the simulations investigated in Chapter 4 on a compressor rotor.

2.1.1 The Navier-Stokes equations

The motion of fluids can be characterized by a set of equations, derived by Navier and Stokes. Laminar and turbulent flows can be described by these equations, deriving from the continuity equation, the momentum equations and the energy equation. Five conservative variables are used to describe the flow characteristics on which the set of Navier-Stokes' five equations applies: the fluid density ρ , its momentum vector $\rho\mathbf{u}$ and its total energy E . These equations can be written in a conservative form as ¹:

– Continuity equation

$$\frac{\partial \rho}{\partial t} + \nabla \cdot (\rho \mathbf{u}) = 0. \quad (2.1)$$

– Momentum equations

$$\frac{\partial \rho \mathbf{u}}{\partial t} + \nabla \cdot (\rho \mathbf{u} \otimes \mathbf{u}) = - \underbrace{\nabla p}_{\text{Pressure gradient}} + \nabla \cdot \underbrace{\boldsymbol{\tau}}_{\text{Viscous stress tensor}} + \underbrace{\mathbf{f}}_{\text{Body force}} \quad (2.2)$$

– Energy equation

$$\frac{\partial \rho E}{\partial t} + \nabla \cdot (\rho \mathbf{u} E) = - \nabla \cdot \underbrace{\mathbf{q}}_{\text{Heat flux vector}} + \nabla \cdot [\mathbf{u} \cdot (\boldsymbol{\tau} - p \underbrace{\mathbf{I}}_{\text{Identity matrix}})] \quad (2.3)$$

Fourteen unknowns can be counted in the set of equations and other equations are required to close the system of equations. For a Newtonian fluid with a dynamic viscosity μ evaluated with

¹The vectors and tensors are denoted in bold font

Sutherland's law along with the perfect gas equation and a Fourier conductive equation on the heat flux, one can close the system of equations for the 14 unknowns. These equations are highly non-linear and the possibility of solving them in a general case is still to be proven. Solving them numerically has been in use for decades with the large progress made on computer performance but strategies are needed to reduce the computational time to a reasonable amount.

2.1.2 Strategies for fluid dynamics simulations

The first possibility to solve Navier-Stokes equations is to apply nearly no assumption. The principle of the Direct Numerical Simulation (DNS) is to solve the equations by resolving all the length scales of the flow. The turbulent structures associated to the smallest length scales generally require very refined numerical grids that make the solving impossible in a reasonable amount of time for most practical applications.

Let us denote l_0 the characteristic length scale of the large turbulent structures and η the Kolmogorov length scale, describing the smallest structures of the turbulence. In order to resolve all the turbulent structures, from the size η to l_0 , the number of elements in the x direction of the mesh must be such that:

$$N_x \approx L_x/\eta \approx Re^{3/4}. \quad (2.4)$$

L_x is the maximum size of the grid in the x -direction so as to resolve the largest turbulent structures, therefore with a length scale l_0 . This reasoning is valid in the three directions of the computational domain, the number of elements required evolves as $Re^{9/4}$ [107]. For Reynolds numbers greater than 10^4 , this number can exceed one billion elements. The current CPU power is not sufficient to perform such simulations in a reasonable time. Computers with such power will not be available before 2080 according to the estimations of Spalart [128] for large Reynolds numbers. In turn, the cost of a DNS is prohibitive with the current computational power currently available for Reynolds numbers larger than 10^4 with tridimensional flows.

Strategies have been developed to reduce the computational cost of the simulations. A pyramid, introduced by Sagaut, Deck and Terracol [118], enables to summarize the different possible levels of resolution, showing the degree of modelling and the computational cost associated to all the approaches. This pyramid is displayed in Figure 2.1. The Navier-Stokes equations governing the dynamics of a flow are highly non-linear and their resolution generally passes by the use of turbulence modelling, less costly than resolving all the turbulent structures. The more modelling is put into the resolution, the less costly it is but on the other hand, the accurate prediction of turbulent flows is harder to ensure.

Instead of solving directly the Navier-Stokes equations, operators can be applied to them beforehand. The principle of a Large Eddy Simulation (LES) is to apply low-pass filtering on the equations. The principle is to resolve the largest structures of turbulence, generally the most energetic, and model the behaviour of the small structures. Further, the most used CFD type of simulations are Reynolds Averaged Navier-Stokes simulations (RANS). Instead of the low-pass filter, an ensemble average is applied to the Navier-Stokes equations and the whole spectrum of turbulence is modelled. In the middle, it is possible to use hybrid methods that combine

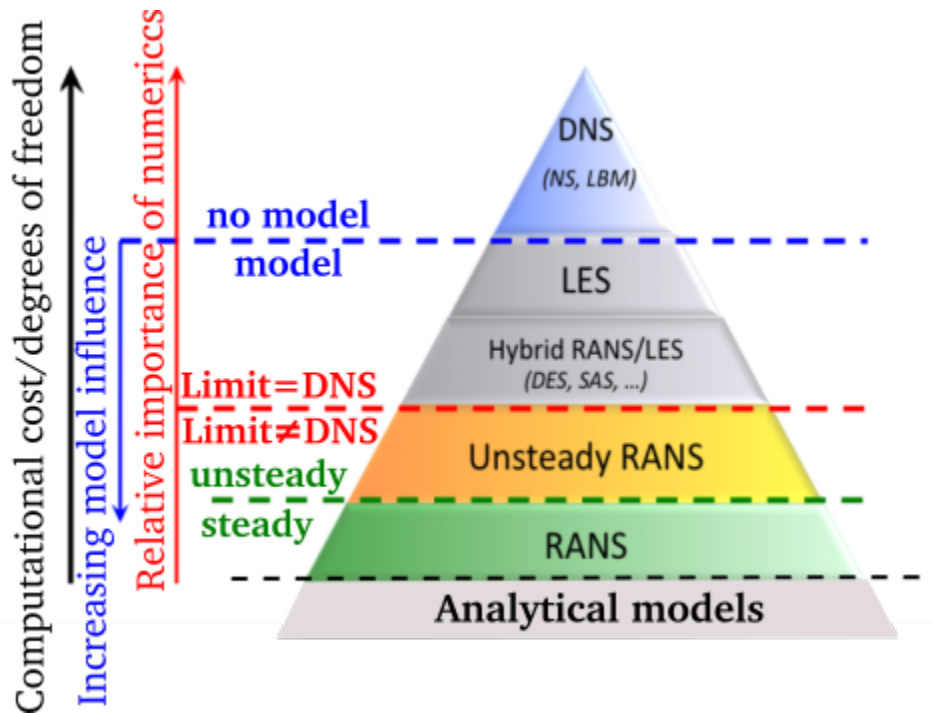


Figure 2.1: Classification of the most common methods used when simulating turbulent flows, adapted from [118].

the strengths of LES and RANS over the computational domain, by resolving the flow regions of interest with LES and loosening the constraints over the rest of the domain with RANS to decrease the overall computational cost.

Simulations with a high resolution aim to resolve most structures present in the flow, contrary to RANS simulations, limited to the mean behaviour of these structures through turbulence modelling. Striking the right balance between modelling and resolving is quite challenging. Modelling heavy turbulent flows is well-adapted to some configurations but poorly to others. On the other hand, resolving all the structures of the flow, from the smallest structure to the largest is so costly that current computers are not capable of processing such resolutions in a reasonable amount of time.

The threshold that defines high-resolved simulations is established for levels higher in the pyramid than unsteady RANS (URANS). For large Reynolds numbers, the turbulent structures are smaller and smaller close to the walls. For that reason, the grid length scale must be adapted to the size of these structures in those regions, which dramatically increases the number of elements to be used to adapt to all the structures. Coherently, the time scale to resolve the unsteady behaviour of these very small structures must be small, as imposed by the numerics consistently with the physics. So, not only does the number of elements to be used over the computational domain requires a larger number of CPU cores to run the simulation but the number of iterations required also significantly increases for a sufficient physical simulation time (> 10 advection times), due to the important reduction of the time step. The number of CPU hours needed for such simulations consequently significantly rises when turbulent structures in

the simulations are partly resolved, especially for wall-bounded flows.

This section introduces the principles of RANS and LES resolutions in more details before going through the hybrid RANS/LES approach used in the present thesis, the Zonal Detached Eddy Simulation (ZDES).

2.2 Reynolds Averaged Navier-Stokes Equations (RANS)

2.2.1 Principle

Resolving all the turbulent structures of the flow for wall-bounded flows with large Reynolds numbers is out of consideration nowadays. In particular, when it comes to turbomachinery applications, industrial designers must resort to simplifications on the Navier-Stokes equations to reduce the computational time. The most widespread way of doing so is to apply the Reynolds averaging of the equations.

Let us first consider the incompressible case, for which the variations of ρ are negligible and $\nabla \cdot \mathbf{u} = 0$. The idea is to separate the instantaneous flow field $f(\mathbf{x}, t)$ at any position \mathbf{x} of the computational domain into a mean flow field \bar{f} and its fluctuations f' by writing

$$\bar{f}(\mathbf{x}, t) = \bar{f} + f' \quad (2.5)$$

The mean flow field can be calculated from an ensemble average defined, on the possible micro-states f_i , by:

$$\bar{f} = \lim_{N \rightarrow \infty} \left(\frac{1}{N} \sum_{i=1}^N f_i \right) \quad (2.6)$$

Following the ergodicity assumption, the ensemble average can be expressed in terms of an average in time:

$$\bar{f}(t) = \lim_{T \rightarrow \infty} \frac{1}{2T} \int_{-T}^T f(t + \tau) d\tau \quad (2.7)$$

The operator defined by equation (2.7) is the Reynolds average operator. This operator has interesting mathematical properties to simplify the averaged Navier-Stokes system of equations: it is linear and is such that $\bar{f}' = 0$ and $\overline{\bar{f}} = \bar{f}$.

Applying the Reynolds operator to the Navier-Stokes equations yields a very similar set of equations on the averaged conservative values. This however generates an additional term in the right-hand side of the momentum equations. This term is referred to as the Reynolds stresses, that writes $\nabla \cdot \mathbf{R}$, where $\mathbf{R} = (R_{ij})_{1 \leq i \leq 3, 1 \leq j \leq 3}$ is the Reynolds stress tensor defined by:

$$R_{ij} = -\overline{\rho u'_i u'_j} \quad (2.8)$$

This tensor is symmetric and generates six new unknowns, which then requires new equations to close the averaged equations. These new equations correspond to where turbulence modelling is added to the system of averaged equations. They are intended to account for the averaged behaviour of turbulence.

2.2.2 Turbulence modelling

A large number of turbulence models use the *Boussinesq assumption*, that consists in relating the Reynolds stresses to the strain-rate tensor.

$$\overline{S_{ij}} = \frac{1}{2} \left(\frac{\partial \overline{u}_i}{\partial x_j} + \frac{\partial \overline{u}_j}{\partial x_i} \right) \quad (2.9)$$

For incompressible flows, this equation writes:

$$R_{ij} = \mu_t \overline{S_{ij}} - \frac{2}{3} \delta_{ij} \rho \overline{k} \quad (2.10)$$

Two unknowns remain in the system of equations: the turbulent kinetic energy (TKE) k and the eddy viscosity μ_t . The TKE is defined as:

$$k = \frac{1}{2} \sum_{i=1}^3 \overline{u'_i u'_i}, \quad (2.11)$$

corresponding to half the trace of the Reynolds stress tensor R_{ij} divided by the density ρ .

As for the eddy viscosity, it can be expressed differently depending on the turbulence model used. The most widespread turbulence models are based on two transport equations in order to close the set of equations on the knowledge of these two unknowns (e.g. the $k - \varepsilon$ or $k - \omega$ models). The $k - \omega$ model for example enables to calculate the eddy viscosity from ω , the specific rate of dissipation of the TKE, as

$$\mu_t = \frac{\rho \overline{k}}{\omega} \quad (2.12)$$

Other RANS models are not based on the Boussinesq assumption: Reynolds Stress Models (RSM) solve the transport equations on the six unknown Reynolds stresses, along with a transport equation on the specific dissipation rate ω .

The ensemble average only offers a steady view of the fluid dynamics but it is also possible to make the approach unsteady by applying a simple average on the field over a period of time T , assumed much greater than the characteristic time scale of the turbulence t_{turbu} . This approach is referred to as unsteady RANS (URANS). The Reynolds operator thus writes

$$\overline{f}(t) = \frac{1}{2T} \int_{-T}^T f(t + \tau) d\tau. \quad (2.13)$$

The URANS approach is well adapted to periodic flows as those encountered in turbomachinery. The idea is to converge towards the mean unsteady behaviour of the flow, as indicated by the Reynolds operator. Rotor-stator interactions are examples where this kind of approach is quite adapted. However, as shown by Riéra [113], URANS is poorly adapted to the tip-leakage flow. As turbulence is modelled, the interaction of the different turbulent structures in the tip-leakage vortex is not well reproduced. Yet, these turbulent structures affect a lot the behaviour of the TLV, and hence the flow in that region, and hence require to be resolved for a better accuracy.

2.2.3 Compressible case

In the context of our study, applied to axial compressors, the variations of ρ are generally not negligible in the flow field. The Favre average is introduced in order to write the averaged Navier-Stokes equations in a similar form as for incompressible flows. The variable f is decomposed into a Favre averaged term \tilde{f} and a fluctuating part f'' as:

$$f = \tilde{f} + f'', \quad (2.14)$$

with $\tilde{f} = \overline{\rho f} / \bar{\rho}$.

The introduction of the Favre operator enables to write the compressible RANS equations in a similar form as the incompressible equations.

The Boussinesq hypothesis on the Reynolds stress tensor $R_{ij} = -\overline{\rho u_i'' u_j''}$ can be expressed as:

$$R_{ij} = -\overline{\rho u_i'' u_j''} = \mu_t \left(\frac{\partial \tilde{u}_i}{\partial x_j} + \frac{\partial \tilde{u}_j}{\partial x_i} - \frac{2}{3} \delta_{ij} \frac{\partial \tilde{u}_k}{\partial x_k} \right) - \frac{2}{3} \delta_{ij} \bar{\rho} \tilde{k} \quad (2.15)$$

2.2.4 The Spalart-Allmaras model

It is also possible to reduce the turbulent equations to only one equation. That is the idea of Spalart-Allmaras' model [129]: the transport equation applies to a pseudo-viscosity $\tilde{\nu}$ as

$$\frac{D\tilde{\nu}}{Dt} = c_{b1} \tilde{S} \tilde{\nu} - c_{w1} f_w \left[\frac{\tilde{\nu}}{d_w} \right]^2 + \frac{1}{\sigma} \left[\nabla \cdot ((\nu + \tilde{\nu}) \nabla \tilde{\nu}) - c_{b2} (\nabla \tilde{\nu})^2 \right] \quad (2.16)$$

The right-hand side divides into three main terms: resp. production, destruction and diffusion of the pseudo viscosity. This pseudo viscosity is convected by the left-hand side.

The eddy viscosity ν_t can be computed from the pseudo-viscosity as follows

$$\nu_t = \tilde{\nu} f_{v1}, \quad f_{v1} = \frac{\chi^3}{\chi^3 + c_{r1}^3}, \quad \chi = \frac{\tilde{\nu}}{\nu} \quad (2.17)$$

with f and c different functions and constants detailed in the article. The second term in the right-hand side, corresponding to the destruction term, is of particular importance for the ZDES introduced afterwards, as it will be explained. The transport equation is also valid for compressible flows, as precised in [4].

2.3 Large Eddy Simulation (LES)

2.3.1 Strategy and use

Contrary to a DNS simulation, a Large Eddy Simulation does not resolve all the turbulent structures of the flow. It aims at describing only the largest and most energetic scales of the turbulence. The smallest scales impose a significant increase of the CPU cost because of the refinement required on the mesh and on the time step. This is particularly critical near the walls, in the

boundary layers. To alleviate the cost increase, the small structures are modelled in LES. The idea is to use the fact that these little structures tend to behave towards an isotropic and homogeneous turbulence, contrary to the large scales. It is then hoped to capture well the physics of these subgrid scale structures with simple models (*Subgrid scale models* or *SGS models*). Besides significantly gaining on the CPU cost compared to a DNS, the precision in the resolution of the Navier-Stokes equations remains high and the physics remains well described.

LES situates in-between DNS and RANS in terms of cost and resolution: instead of applying an average operator, filtering is applied on the Navier-Stokes equations. This filtering is driven by the length of the grid cells in the simulation.

2.3.2 Subgrid scale models

The equations of transport of LES are presented in [105], in their incompressible formulation. They enable to understand how energy is exchanged between the resolved and subgrid scales of the turbulence. The interaction between these two scales can be explained by writing the equations of transport on the double of the resolved kinetic energy, denoted ${}^2\bar{q}^2 = \overline{u_i u_i}$ and the double of the SGS kinetic energy $q_{sgs}^2 = R_{kk}^{sgs} = \overline{u_k^2} - \overline{u_k}^2$. The resolved velocity $\overline{u_i}$ here represents the sum of the mean value $[\overline{u_i}]$ and the fluctuations u'_i . The SGS tensor R_{ij}^{sgs} is defined by

$$R_{ij}^{sgs} = \overline{u_i u_j} - \overline{u_i} \overline{u_j} \quad (2.18)$$

Equation of transport on the resolved kinetic energy

$$\begin{aligned} \frac{\partial \bar{q}^2}{\partial t} + \overbrace{\frac{\partial}{\partial x_j} (\bar{q}^2 \overline{u_j})}^{\text{Advection of } \bar{q}^2} = & -\frac{2}{\rho} \overbrace{\frac{\partial}{\partial x_j} (\overline{p u_j})}^{\text{Pressure diffusion}} + \overbrace{\frac{\partial}{\partial x_j} \left(\nu \frac{\partial \bar{q}^2}{\partial x_j} \right)}^{\text{Viscous diffusion}} - 2 \overbrace{\frac{\partial}{\partial x_j} (R_{ij}^{sgs} \overline{u_i})}^{\text{SGS diffusion}} \\ & - 2 \underbrace{\nu \frac{\partial \overline{u_i}}{\partial x_j} \frac{\partial \overline{u_i}}{\partial x_j}}_{\text{Viscous dissipation}} + \underbrace{2 R_{ij}^{sgs} \overline{S_{ij}}}_{\text{SGS production } -\varepsilon_{sgs}} \end{aligned} \quad (2.19)$$

Equation of transport on the SGS kinetic energy

$$\begin{aligned} \frac{\partial q_{sgs}^2}{\partial t} + \frac{\partial}{\partial x_j} (q_{sgs}^2 \overline{u_j}) = & - \overbrace{\frac{\partial}{\partial x_j} (\overline{u_i u_i u_j} - \overline{u_i u_i} \overline{u_j})}^{\text{Transport term}} - \frac{2}{\rho} \overbrace{\frac{\partial}{\partial x_j} (\overline{p u_j} - \bar{p} \overline{u_j})}^{\text{Pressure diffusion}} + \overbrace{\frac{\partial}{\partial x_j} \left(\nu \frac{\partial q_{sgs}^2}{\partial x_j} \right)}^{\text{Viscous diffusion}} \\ & + 2 \underbrace{\frac{\partial}{\partial x_j} (R_{ij}^{sgs} \overline{u_i})}_{\text{SGS diffusion}} - 2 \nu \underbrace{\left(\frac{\partial \overline{u_i}}{\partial x_j} \frac{\partial \overline{u_i}}{\partial x_j} - \frac{\partial \overline{u_i}}{\partial x_j} \frac{\partial \overline{u_i}}{\partial x_j} \right)}_{\text{Viscous dissipation } \varepsilon_v} - 2 \underbrace{R_{ij}^{sgs} \overline{S_{ij}}}_{\text{SGS dissipation } \varepsilon_{sgs}} \end{aligned} \quad (2.20)$$

² \bar{u} here designates the resolved part of the velocity u (large scales).

The energy exchanges occurring in-between the two scales of the flow can be grasped through this set of two equations. Beyond the transport terms (advection or diffusion) of the energy, the mechanisms describing the transfers are expressed by the SGS diffusion and dissipation terms, identical in the two equations, with an opposite sign.

Most of the SGS models introduce a turbulent viscosity ν_t , similarly to Boussinesq's hypothesis, as

$$R_{ij}^{sgs} - \delta_{ij}/3 R_{kk}^{sgs} = -2\nu_t \overline{S_{ij}} \quad (2.21)$$

with R_{ij}^{sgs} the SGS stress tensor,

and the large-scale strain rate tensor $\overline{S_{ij}} = \frac{1}{2} \left(\frac{\partial \overline{u_i}}{\partial x_j} + \frac{\partial \overline{u_j}}{\partial x_i} \right)$.

The model can be further simplified by imposing an equilibrium assumption on the small scales. In this assumption, the time scales associated to the smaller scales are much lower than those of the larger scales of the turbulence. As a consequence, the SGS structures adapt faster to the perturbations, generally of large scales. In equation (2.20), all terms drop out, except the viscous dissipation ε_v and the SGS dissipation ε_{sgs} , yielding:

$$-R_{ij}^{sgs} \overline{S_{ij}} = \varepsilon_v \quad (2.22)$$

This hypothesis is the basis of Smagorinsky's model [125], that gave rise to numerous other SGS models improving the treatment of the subgrid scales.

Following Taylor's dimensional analysis [137], the viscous dissipation is classically written as

$$\varepsilon_v \approx (q_{sgs}^2)^{3/2}/l, \quad (2.23)$$

with l a length scale associated to the SGS structures.

The eddy viscosity ν_t can be written as the product of a length scale l and a velocity [145], that is,

$$\nu_t \approx l \times q_{sgs} \quad (2.24)$$

For the subgrid scale, the length scale l can be taken as the subgrid length scale $\bar{\Delta}$. Putting equations (2.21), (2.22), (2.23) and (2.24) together, the eddy viscosity writes:

$$\nu_t = (C_s \bar{\Delta})^2 \|\bar{S}\| \quad (2.25)$$

with $\|\bar{S}\| = (2\overline{S_{ij}} \overline{S_{ij}})^{1/2}$ and C_s the Smagorinsky constant, originally evaluated by Lilly [86].

The study of Piomelli *et al.* [106] showed that the assumption made with Smagorinsky's model is only partly realistic for wall-bounded flows. The adaptation time of the smaller scales to the perturbation is indeed lower than for the larger scales, but the equilibrium assumption stating an instantaneous equilibrium is probably too strong. Examples of transitional or relaminarizing flows counter this hypothesis.

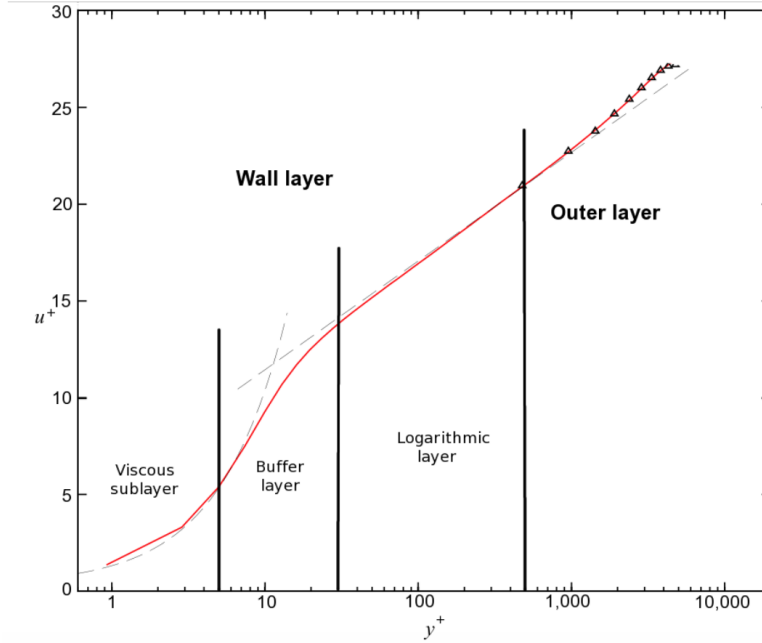


Figure 2.2: Evolution of the normalized mean axial velocity with y^+ for a canonical boundary layer, adapted from [105].

Although relatively simple, this model suffers from several flaws. It is well known that the use of this SGS model near walls yields degraded results compared to other existing SGS models. Volker John summarized the main known flaws related to this algebraic SGS model [69] in an article. Other SGS models are not introduced in the present thesis since the simulations carried out use the ZDES hybrid approach that treats the regions near the walls with RANS.

2.3.3 Estimation of the CPU cost

Let us now focus on the CPU cost of a LES. Chapman was the first to estimate the number of elements required for a structured grid with a LES resolution [18]. The most expensive region of the flow to be correctly resolved by LES is the boundary layer. The wall-normal evolution of the mean velocity normalized by the wall-friction velocity u_τ in a canonical boundary layer is shown in Figure 2.2. Also called shear velocity, u_τ is defined by

$$u_\tau = \sqrt{\frac{\|\tau_w\|}{\rho}}, \quad (2.26)$$

with τ_w the shear stress vector tangent to the wall.

Chapman divided its cost estimate into two regions of the boundary layer. In the external zone of the boundary layer, the number of elements becomes rapidly negligible with respect to the number of elements in the internal zone of the boundary layer. The evolution in the external region, estimates Chapman, varies like $Re^{0.4}$.

Despite the extreme fineness of the internal region of the boundary layer (representing sometimes less than 1% of the boundary layer thickness), the number of elements required in that zone surges with the increase of the Reynolds number. Robinson *et al.* showed that the dynamics of this region is dominated by quasi-streamwise vortices (QSV), very small structures thus imposing a very small size to the grid cells populating the internal region of the boundary layer. In the three directions of the structured mesh, the grid cells must satisfy the criteria for the wall-resolved LES (WRLES) summarized in Table 2.1 in wall units. Chapman shows that the number of elements required in the internal region can write

$$(N_x N_y N_z)_{\text{internal region}} \propto C_f Re^2 \quad (2.27)$$

The evolution of the friction coefficient of a boundary layer, proposed by Schlichting [119],

$$C_f \propto Re^{-0.2}, \quad (2.28)$$

enables to directly relate the number of elements required to the Reynolds number following

$$(N_x N_y N_z)_{\text{internal region}} \propto Re^{1.8}. \quad (2.29)$$

	Δx^+	y^+	Δz^+
RANS	500	1	1000
WMLES	200	1	100
WRLES	50	1	15

Table 2.1: Criteria on the wall grid size expressed in wall units for three resolutions [118].

The resolution of the turbulent structures near the wall dramatically increases the CPU cost compared to a large-eddy simulation where the flow near the walls is modelled with a wall-layer model (Wall-modelled LES or WMLES) or a RANS turbulence model. Table 2.1 sums up the specifications on the grid refinement for three different flow resolutions (RANS, WMLES and WRLES) in wall units, recommended by Sagaut *et al.*. The wall unit is obtained by normalizing the grid size by $l_\tau = \nu/u_\tau$. The table enables to grasp the significant cost excess involved by the use of a higher resolution like WRLES compared to RANS. According to these criteria, the WMLES resolution is about 25 more costly than the RANS. Further, if the boundary layer is completely resolved with LES, a factor 25 applies again.

2.4 Zonal Detached Eddy Simulation (ZDES)

2.4.1 Introduction to hybrid simulations

Contrary to WRLES, hybrid methods seeks to reduce the number of elements of the grid by not resolving the turbulent structures in some regions of the computational domain. Spalart's

Detached-Eddy Simulation [123] (DES) is here introduced. It aims at modelling the behaviour of the structures in the boundary layer to gain CPU cost instead of resolving them, more particularly in the internal region.

The philosophy of hybrid RANS/LES methods is to use LES where it is really necessary, that is, where (U)RANS methods are known to be inaccurate (separated boundary layers, secondary flows). RANS and filtered LES Navier-Stokes equations have the same form and in particular generate a similar additional term corresponding to the Reynolds stress tensor R_{ij} or the SGS stresses R_{ij}^{sgs} , depending on the resolution. Let us illustrate that in the incompressible form of the momentum equations:

$$\frac{\partial \bar{u}_i}{\partial t} + \frac{\partial}{\partial x_j} (\bar{u}_i \bar{u}_j) = -\frac{1}{\rho} \frac{\partial \bar{p}}{\partial x_i} + \overbrace{\frac{\partial R_{ij}^{sgs}}{\partial x_j}}^{\text{SGS stresses}} + \frac{\partial \bar{\tau}_{ij}}{\partial x_j} \quad (2.30)$$

$$\frac{\partial U_i}{\partial t} + \frac{\partial}{\partial x_j} (U_i U_j) = -\frac{1}{\rho} \frac{\partial P}{\partial x_i} + \underbrace{\frac{\partial R_{ij}}{\partial x_j}}_{\text{Reynolds stresses}} + \frac{\partial T_{ij}}{\partial x_j} \quad (2.31)$$

The equations are written with the Einstein convention, the upper bar designates the low-pass filter operator, the upper-case letters the averaged values in these two equations. The code based on these equations for a hybrid RANS/LES method can therefore come down to a single equation. The character of the solution (RANS or LES) is determined by the grid, the time advancement and the stress model (SGS or turbulence).

DES consists in playing on the stress model by transforming the transport equation of the turbulent variable $\tilde{\nu}$ in Spalart-Allmaras RANS model (RANS-SA) [130] into a subgrid-scale equation of a LES in some regions. The transport equation writes:

$$\frac{D\tilde{\nu}}{Dt} = P_{\tilde{\nu}} - D_{\tilde{\nu}} + \text{Diff}_{\tilde{\nu}} \quad (2.32)$$

where $P_{\tilde{\nu}}$ is the production term, $D_{\tilde{\nu}}$ the destruction term and $\text{Diff}_{\tilde{\nu}}$ designates the diffusion term on the pseudo eddy viscosity $\tilde{\nu}$. The second term depends on the distance to the wall d_w and writes

$$D_{\tilde{\nu}} = c_{w1} f_w \left(\frac{\tilde{\nu}}{d_w} \right)^2 \quad (2.33)$$

The strategy of DES is to modify that distance in order to switch from RANS to LES by destroying more eddy viscosity. By redefining the length scale in the destruction term, the idea is to increase the importance of this term in order to generate an eddy viscosity of the same order of magnitude as that given by a Smagorinsky SGS model in LES, outside the zones where the boundary layer is attached. By changing the length scale, the production and destruction terms are balanced, satisfying the equilibrium hypothesis mentioned before.

In the DES97 [131], the new length scale is defined as

$$\tilde{d} = \min(d_w, C_{DES} \bar{\Delta}), \quad (2.34)$$

with $\bar{\Delta} = \max(\Delta x, \Delta y, \Delta z)$, applying to every cell of the mesh, in Spalart's formulation. The constant C_{DES} is based on the calibration of Shur *et al.* [123] on a homogeneous isotropic turbulence case, based on the experiment of Comte-Bellot and Corrsin [22].

Through a single general equation, Spalart's formulation thus enables to process the zones of interest farther from the walls with LES, while reducing significantly the number of elements of the grid by modelling the boundary layer with RANS. The function f_w in equation (2.33) has been calibrated to obtain a rapid decrease towards 0 on the difference between the production and the destruction terms on $\tilde{\nu}$.

In the RANS zones, Reynolds stresses are modelled and depend on the eddy viscosity ν_t following Boussinesq's assumption. This is generally well-adapted for attached boundary layers. In the LES zones, the Reynolds stresses are resolved at the same time as the eddy viscosity ν_t has dropped. The activation of these resolved stresses correspond to the formation of turbulent structures in the flow with a length scale larger than the subgrid scale $\bar{\Delta}$. The interest of the DES precisely lies in the former point: RANS is poorly adapted to separated flows and DES allows a rapid switch to LES as soon as the boundary layer separates.

Table 2.1 shows the important difference on the number of elements required between a WRLES and a hybrid approach like DES or WMLES: there is a factor 27 on the grid refinement between the two approaches. As an illustration, a mesh that would require 100 million elements for a DES, 3 billion would be necessary with the WRLES, which is hardly achievable with the current CPU power.

The hybrid approach nonetheless suffers from two major flaws that the Zonal Detached Eddy Simulation introduced in the next section addresses:

1. In DES approach, the RANS/LES switch directly depends on the grid itself. This may lead to separations that are completely numerical and not physical, that is, induced by the grid (Grid Induced Separation or GIS). This phenomenon is in general caused by a Model Stress Depletion (MSD) where the resolved Reynolds stresses are not sufficient to compensate the decrease in the modelled Reynolds stresses due to the destruction of ν_t , from the moment the switch occurs.
2. There is a delay between the position of the switch and the formation of coherent turbulent structures when passing from RANS to LES. This generally originates from the slow decrease of the eddy viscosity ν_t .

Uribe's thesis [139] and the article of Marty and Uribe [89] tackle these two issues with their ZDES simulations.

2.4.2 Presentation of the ZDES

The Zonal Detached Eddy Simulation of Deck *et al.* [35] derives from Spalart's DES formulation but mainly differs on the choice of the length scale \tilde{d} , the subgrid scale $\bar{\Delta}$ and the near-wall treatment of the flow.

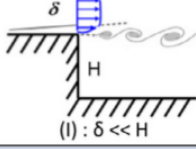
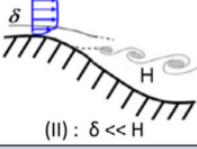
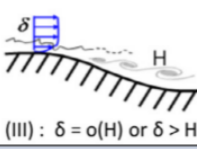
Zonal Detached Eddy Simulation (ZDES)			
	Mode 1	Mode 2	Mode 3
Flow category	 (I) : $\delta \ll H$	 (II) : $\delta \ll H$	 (III) : $\delta = o(H)$ or $\delta > H$
Applications	Base flow, free shear flows, spoilers, steps, slat/flap cove, etc.	Buffet, flaps, duct flows, nacelle intake, etc.	Corner flows, turbulent boundary layer, separation onset on high lift devices, shallow separations, etc.
Hybrid length scale	$\tilde{d}_{ZDES}^I = \begin{cases} d_{wall} & \text{in RANS areas} \\ \min(d_{wall}, C_{DES} \Delta_{ZDES}^I) & \text{in DES areas} \end{cases}$	$\tilde{d}_{ZDES}^{II} = d_{wall} - f_d \max(0, d_{wall} - C_{DES} \Delta_{ZDES}^{II})$	$\tilde{d}_{ZDES}^{III} = \begin{cases} d_{wall} & \text{if } d_{wall} < d_{interface} \\ \min(d_{wall}, C_{DES} \Delta_{ZDES}^{III}) & \text{otherwise} \end{cases}$
Subgrid length scale	$\Delta_{ZDES}^I = \Delta_{vol} \text{ or } \Delta_{\omega}$ $-f_{v1}=1, f_{v2}=0, f_w=0$ in LES areas	$\Delta_{ZDES}^{II} = \begin{cases} \Delta_{max} & \text{if } f_d < f_{d0} \\ \Delta_{vol} \text{ or } \Delta_{\omega} & \text{if } f_d > f_{d0} \end{cases}$	$\Delta_{ZDES}^{III} = \Delta_{vol}$

Figure 2.3: Summary on the three modes of the zonal approach ZDES.

As summarized by Figure 2.3, three modes can be distinguished in the use of ZDES. Each mode is well adapted to certain types of flow configurations to be simulated. The first and second modes are quite effective for flows with massive separations:

1. The first mode is similar to Spalart's DES97 and can be used for configurations where the flow separation is induced by an abrupt change in the geometry.
2. The GIS is handled by the second mode by introducing a protection function f_d that modifies the ZDES length scale \tilde{d} and guarantees the treatment of the entire boundary layer of thickness δ with RANS. This mode is adapted to configurations where the adverse pressure gradient is smooth. Besides, the position of the separation point is not known *a priori*. This mode is similar to the DDES of Spalart (Delayed Detached Eddy Simulation) [132]. New enhancements of the protection of attached boundary layers have been published recently by Deck and Renard [37] but the original f_d expression [35] is used in the present thesis.
3. Finally, the third mode enables the user to fix the RANS/LES interface manually at a distance $d_{interface}$ from the wall. Deck *et al.* [38] showed that setting the interface at 10% of the boundary layer thickness yields very good results regarding the friction coefficient. This formulation can be identified as a WMLES that does not model the entire boundary layer. In order to restore the missing stresses in the resolved part of the boundary layer, turbulent structures must be injected upstream, at least in the external region of the boundary layer. For example, the Synthetic-Eddy Method (SEM) can be used to generate synthetic turbulent structures that develop and reorganize in the boundary layer to recover a more physical friction coefficient based on larger Reynolds stresses. Pamiès [103] or Jarrin's [68] SEM are particularly interesting since they go beyond the traditional homogeneous and isotropic turbulence in the injection. The adaptation time of the turbulent structures when they reorganize in the flow following their injection is in particular shorter with

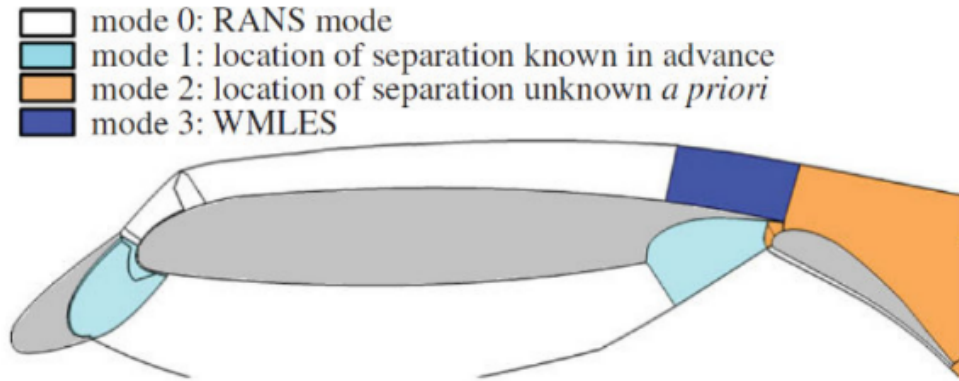


Figure 2.4: Example of use of the zonal strategy on a three-element airfoil [36].

SEM, by injecting non-homogeneous and non-isotropic turbulence near the walls, closer to what can actually be found in a boundary layer.

The main difference with DES or DDES lies in the possibility to apply the different modes locally. Figure 2.4 shows an example of how the zonal strategy can be used: on the airfoil exhibited, four different treatments coexist over the same solid walls, chosen depending on the criteria mentioned above. In order to correct the flaws of the DES97, the choice of the subgrid scale is also adapted in the method. Deck *et al.* have introduced two other subgrid scales among which the user can choose when using the ZDES:

1. The first length scale is defined by the volume of the cell considered $\Delta_{vol} = (\Delta x \Delta y \Delta z)^{1/3}$,
2. The second, introduced by Chauvet *et al.* [19], uses a definition based on the vorticity. It gives very good results regarding the formation of the resolved structures, quicker than with the DES subgrid scale $\bar{\Delta}$.

The second mode of the ZDES is used in the present thesis because it represents a very good compromise between cost and flow resolution, especially for turbomachinery configurations, well-known application of internal flows (with solid walls), and where the Reynolds number is generally close to 10^6 . The subgrid scale used is the former, Δ_{vol} . Besides, as mentioned in the literature review in Chapter 1, the approach has been assessed on a compressor rotor by Riéra [114] and brought very interesting results regarding tip-leakage flow.

VALIDATION OF THE VORTEX LATTICE METHOD AND
APPLICATION TO TIP-LEAKAGE FLOW

Contents

3.1	Introduction	74
3.2	Singularity methods	75
3.2.1	Potential flow theory	75
3.2.2	The problem of the wing	77
3.2.3	Application to three-dimensional bodies	81
3.2.4	Development of the module <i>PyLiSuite</i>	88
3.3	Validation of <i>PyLiSuite</i>	88
3.3.1	Two-dimensional validation	88
3.3.2	Three-dimensional validation	90
3.3.3	Influence of the HSV angle	92
3.4	Application to tip-leakage flow	96
3.4.1	Influence of the endwalls	97
3.4.2	Grid criterion on the tip gap size	100
3.4.3	Implementation of the symmetry condition	101
3.4.4	Generation of casing	102
3.4.5	Periodicity	105
3.4.6	Compressibility correction	108
3.5	Summary on the method	109

3.1 Introduction

With the advent of more and more advanced computer processors and cores, large and costly simulations have become more feasible. As explained in chapters 2 and 4, the use of the hybrid RANS/LES approach for hundreds of million elements for the grid is now accessible for more advanced research on phenomena that RANS is known to reproduce badly. For industrial designers however, adapting this kind of methods to their design process is still challenging nowadays for the cost and the difficulty linked to the setup of a large-eddy simulation, for which finding solid criteria valid for different sets of configurations is still a challenging task [108]. Beyond this fact, the need for simple and quick methods for designers is crucial when it comes to predesigns. More resolved simulations take part of the process around its end, when most of the blade design features have already been set and only require adjustments. This section introduces a low-resolution method based on a potential approach, to be applied on compressor blades regarding the prediction of the tip-leakage flow. The main objective is to assess the capabilities of the code developed on this approach. Assumptions are made in this approach and the results obtained also guide better models to be built in order to capture the physics of the flow, in relation to what is obtained with a high resolution simulation, close to the actual physics of the flow.

The method studied in the present thesis is a singularity method, which has become widely used in the aerospace industry in the 1960s. Compared to more developed CFD simulations, the idea is to discretize the aerodynamic objects considered into elementary solutions of the potential flow problem. Thanks to the linearity of Laplace's equation characterizing potential flows, the general solution consists of the sum of all the solutions depicted by the different sources and vortices discretizing the aerodynamic object. Although it is possible to extend the solutions to more general types of flows, potential flow theory has been developed for incompressible and inviscid flows and will be first explained in this framework.

Historically, this kind of methods has been particularly applied to external flow aerodynamics, such as aircrafts, rockets or missiles. Figure 3.1 shows an example of discretization of an aircraft with panels, from Katz and Plotkin [72]. The panel and collocation points are defined in the next section. The use of this kind of method on internal flows is far less common. The objective of this work is to investigate the use of a singularity method for internal flows, in particular for tip-leakage flow configurations.

Objectives

The chapter is organized in three main sections:

1. The first section goes through potential flow theory and the principle of the methods with singularities. It then presents the *Vortex Lattice Method*, also known as VLM, developed in the code used for the study, with the main assumptions made.
2. The second section deals with the main validations of the module on classical aerodynamic configurations.

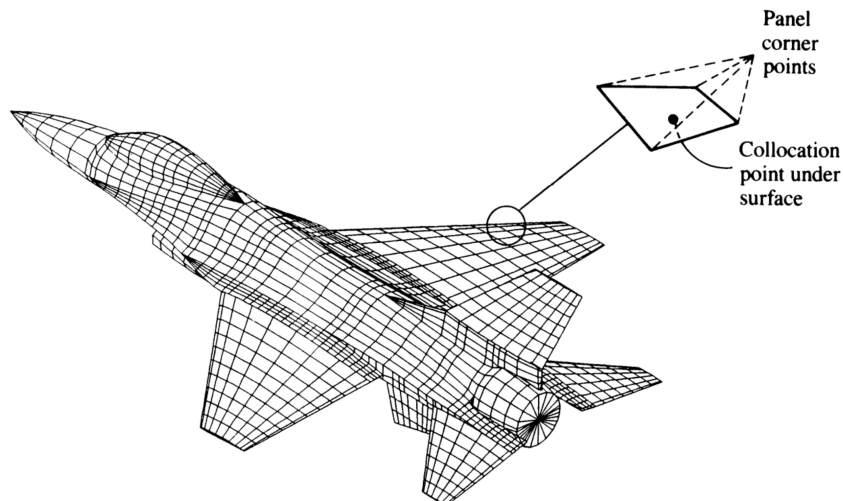


Figure 3.1: Discretization of an aircraft into source panels, from Katz and Plotkin [72].

3. Finally, the third section investigates the important parameters of the approach developed: parametric studies on the discretization and the implementation of other features (symmetry condition, periodicity, low-compressibility correction) are treated. These parameters are fixed for the study on TLF in Chapter 5.

3.2 Singularity methods

3.2.1 Potential flow theory

A classical simplification made in fluid dynamics is to consider the fluid as incompressible, inviscid and irrotational. The first assumption enables to simplify the Navier-Stokes continuity equation to

$$\nabla \cdot \mathbf{U} = 0 \quad (3.1)$$

The flow being irrotational, another identity can be written on the velocity

$$\nabla \times \mathbf{U} = 0 \quad (3.2)$$

The classical operator identity on any scalar A

$$\nabla \times \nabla A = 0, \quad (3.3)$$

allows introducing a *potential* Φ such that the velocity \mathbf{U} be reexpressed

$$\mathbf{U} = \nabla \Phi \quad (3.4)$$

Substituting (3.4) into (3.1) leads to the linear Laplace equation

$$\nabla^2\Phi = 0 \tag{3.5}$$

whose elementary solutions are known and discussed afterwards. The main benefit of using this approach is the linearity of the problem, which allows a superposition of elementary solutions to solve a more general potential flow problem.

Let us now consider a body immersed into a fluid with an undisturbed velocity U_∞ . The presence of the body induces a disturbance u of the velocity, and the potential problem must be completed with the following boundary conditions:

1. On the body surface

$$U \cdot n = 0 \text{ on the body surface } S_B, \text{ with } U = U_\infty + u \tag{3.6}$$

2. Far from the body

$$U = U_\infty \tag{3.7}$$

simply describing the decay of the disturbance when the distance from the body r tends towards infinity, where the flow is not affected by the presence of the body anymore.

Figure 3.2 offers a clearer view of the problem with the notations introduced above. The potential field and hence the velocity field is to be calculated at the point P , where the lower case letters designate the components of the perturbation due to the presence of the body. The vector n in the figure is normal to an unspecified point of the body surface.

The most classical singularities are the source, the doublet and the vortex presented in Appendix B. It is possible to reformulate the potential flow problem on a combination of these elementary solutions, which paves the way to solving body problems with complex geometries. The reformulation from Laplace's equation to the use of the elementary solutions is thoroughly derived and explained in Katz and Plotkin [72]. The main principle of the singularity methods is therefore to distribute singularities of unknown strengths over the surface of the body. Thanks to the linearity of the problem, the complete solution can be found by superimposing the solutions associated to the singularities. The resolution of the problem then consists in finding the strengths of the singularities distributed over the body. From that, the velocity field in the whole domain can be retrieved. The advantage of the method in terms of computational costs compared to a classic 3D CFD approach is already clear at this point: instead of having a three dimensional grid over the whole computational domain, the grid is limited to the two dimensional surface of the body. The strengths of the singularities are sufficient to calculate the flow characteristics over the 3D domain.

So, very complex geometries can be discretized by singularities with this potential approach. Now, the question is how. Indeed, there exists an infinite set of possibilities of tackling the problem [30], with various singularities and distributions. For example, a combination of sources and vortices can be applied to simulate the flow around an airfoil. The case of the airfoil is of particular interest in the present thesis.

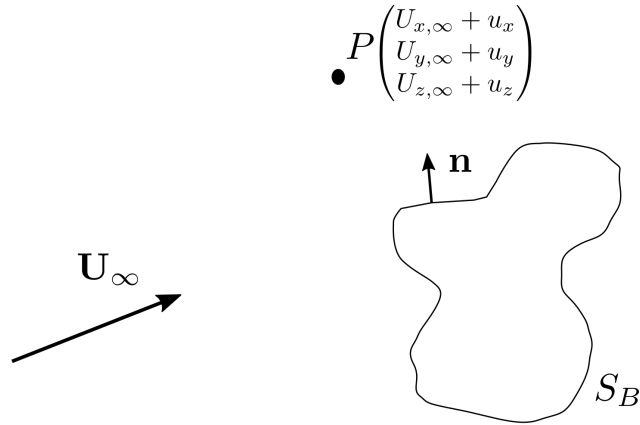


Figure 3.2: Illustration of the potential flow problem, where the velocity components are to be calculated at point P .

3.2.2 The problem of the wing

Before being applied to complete aircrafts, one of the first applications of this kind of approach was the three-dimensional wing. Initially, the method was developed for a 2D approach on airfoils and extended to 3D applications. The theory is here first set out for a 2D airfoil, where the thin airfoil theory is briefly explained, before going through the three-dimensional method. The objective of this part is to show which singularities should be employed on the airfoil.

Figure 3.3 shows a classical wing airfoil, mathematically defined by

$$z = \eta(x) \tag{3.8}$$

The upper and lower sides are denoted respectively by η_u and η_l , while η_c and η_t denote the camber and the thickness of the airfoil. The camber and the thickness can be expressed as functions of the upper and the lower surface functions:

$$\eta_c = \frac{1}{2}(\eta_u + \eta_l) \tag{3.9}$$

$$\eta_t = \frac{1}{2}(\eta_u - \eta_l) \tag{3.10}$$

The idea of the thin airfoil theory is to consider that the perturbations induced by the presence of the airfoil are much lower than the freestream velocity ($u \ll U_\infty$). Two other assumptions are made: on the shape of the airfoil ($\eta \ll c$) and on the angle of attack (α remains low). In these conditions, the boundary condition can be reduced to a simple form on the body surface [30] [72] [100]

$$\frac{\partial \Phi}{\partial z}(x, \eta) = U_\infty \left(\frac{\partial \eta}{\partial x} - \alpha \right) \quad (3.11)$$

By writing a first-order Taylor expansion, the boundary condition can be transferred to

$$\frac{\partial \Phi}{\partial z}(x, \eta) = \frac{\partial \Phi}{\partial z}(x, 0) \quad (3.12)$$

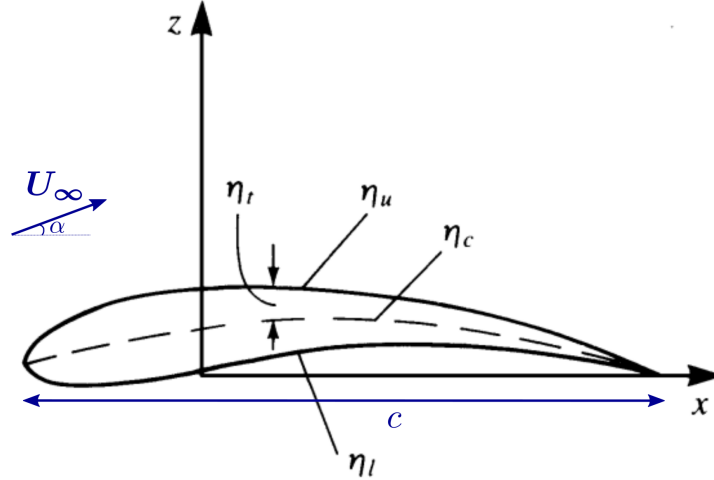


Figure 3.3: Basic definitions and notations for the wing airfoil, adapted from Katz and Plotkin [72].

Let us now decompose the potential function into a symmetric and an asymmetric part

$$\Phi(x, z) = \Phi_s(x, z) + \Phi_a(x, z) \quad (3.13)$$

with

$$\Phi_s(x, -z) = \Phi_s(x, z) = \frac{1}{2}[\Phi(x, z) + \Phi(x, -z)] \quad (3.14)$$

and

$$\Phi_a(x, -z) = -\Phi_a(x, z) = \frac{1}{2}[\Phi(x, z) - \Phi(x, -z)], \quad (3.15)$$

the boundary condition equation (3.11) can be decomposed for the two potentials Φ_s and Φ_a as follows

$$\frac{\partial \Phi_s}{\partial z}(x, 0^\pm) = \mp \frac{1}{2} U_\infty \left(\frac{\partial \eta_u}{\partial x} - \frac{\partial \eta_l}{\partial x} \right) = U_\infty \frac{\partial \eta_t}{\partial x} \quad (3.16)$$

$$\frac{\partial \Phi_a}{\partial z}(x, 0^\pm) = \frac{1}{2} U_\infty \left(\frac{\partial \eta_u}{\partial x} + \frac{\partial \eta_l}{\partial x} - 2\alpha \right) = U_\infty \left(\frac{\partial \eta_c}{\partial x} - \alpha \right) \quad (3.17)$$

Within the thin airfoil theory, this divides the initial problem into two problems that, by linearity, can be solved independently and superimposed afterwards:

1. A problem on a symmetric profile of thickness $\eta_t(x)$, for a zero degree incidence.
2. A problem on the mean-camber line $\eta_c(x)$, with no thickness, for an angle of attack α .

Figure 3.4 summarizes the decomposition. The first problem cannot be responsible for the generation of lift due to the symmetry of the problem, which leaves the complete lift generation to the mean-camber line problem. Hence, the lift is only due to the camber of the profile and the angle of attack in the thin airfoil theory. The thickness problem is interesting when the pressure distribution along the blade is aimed for in separation or cavitation problems [100]. In the former case, discretizing the blade with sources, over the thickness, is a good way to include the boundary layer in the formulation (using the displacement thickness δ^*).

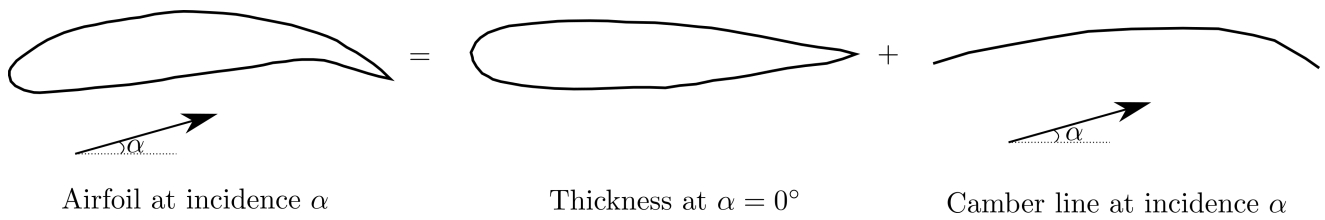


Figure 3.4: Decomposition of the thin airfoil problem into a thickness and a lifting problem.

Now that we have decomposed the problem, still remains the question of which singularities are best to be used depending on the configuration. This decomposition is particularly helpful in that regard. The use of vortices as singularities is particularly interesting regarding the lifting problem since:

1. Kutta-Jukowski's theorem induces the existence of a circulation γ_{tot} around the profile for the generation of lift. The lift per unit span, l , is expressed as a function of the density ρ , the freestream velocity U_∞ and the circulation γ_{tot} per unit length:

$$l = \rho U_\infty \gamma_{tot} \tag{3.18}$$

If a distribution of vortices is used, each represents a part of the total circulation.

2. With the small-disturbance assumption, the pressure coefficient difference can be expressed as a function of the circulation per unit span $\gamma(x)$ as follows ¹

$$\Delta c_p = 2 \frac{\gamma}{U_\infty} \tag{3.19}$$

Equation (3.19) is a direct indicator of how the circulation contributes to the lift generation, since the total lift directly depends on the pressure difference across the blade, here across the mean-camber line approximating it.

¹[72]: see paragraph 5.2., dealing with a zero-thickness airfoil at Angle of Attack

3.2.2.1 The Kutta condition

The potential flow problem formulated as such therefore only consists in finding the right combination of singularities replicating the presence of the body by making sure the non-penetration boundary condition is satisfied on the body surface. However, an infinite number of total circulations γ_{tot} around the wing airfoil can be selected and satisfies the boundary condition. Another condition is necessary to guarantee the uniqueness of the solution: this is the Kutta condition. Depending on the value of the circulation γ_{tot} , the fluid can leave the trailing edge quite differently. The right amount of circulation, as Kutta was the first to state it [78], corresponds to the physical case where the fluid leaves the sharp trailing edge smoothly with a finite velocity. This condition can only be ensured with a zero pressure difference at the trailing edge, which can be expressed with the circulation γ at the trailing edge

$$\gamma_{t.e.} = 0 \quad (3.20)$$

3.2.2.2 Summary of the formulation

In the present thesis, two formulations of the problem are considered:

1. Distributing the vortices over the thickness of the body itself. For example, if a compressor blade is treated, the vortices will be distributed over the pressure and suction sides. This is what we call the *surface formulation*.
2. Distributing the vortices over the mean camber line of the airfoil. This is called the *camber formulation*.

The configurations studied will only be considered through a lifting problem. In summary, the formulation of the potential flow problem used in the thesis requires:

1. An inviscid, incompressible and irrotational flow.
2. Small angles of attack for which the actual boundary layer, not resolved with an inviscid view of the flow, does not separate.
3. The non-penetration condition over the body surface: $\mathbf{U} \cdot \mathbf{n} = 0$.
4. The Kutta condition: $\gamma_{t.e.} = 0$.
5. The unknown of the problem is the distribution of circulation $\gamma(x)$. The one and only solution to the problem satisfies all the previous conditions.

Extensions of the formulation will be considered in the rest of the thesis when applied to TLF, but the validation of the module sticks to these assumptions.

3.2.3 Application to three-dimensional bodies

The formulation developed before is 2D, and applied in particular to the case of the airfoil. The problem can be extended to a 3D vision by discretizing the span and the chord of the object with vortices. Based on that, a major difference lies between 2D and 3D formulations: with the 3D formulation, variations of the circulation are allowed spanwise.

Helmholtz's theorems indeed state that:

1. The total circulation must remain constant.
2. A vortex filament cannot end in a fluid.
3. In the absence of rotational external forces, a fluid initially irrotational remains irrotational.

Due to these theorems, a spanwise variation of the circulation spanwise induces the shedding of axial vorticity downstream of the blade. The existence of a wake in the 3D formulation must therefore be considered. This section deals with the implementation of the 3D approach, going through the equations used to solve the problem, the link between the bound and the free vorticities, and where the vortices are actually distributed over the surface, as well as the points of application of the boundary conditions. The Vortex Lattice Method (VLM) is here explained in details.

3.2.3.1 The lifting line theory

Before presenting the conventional VLM that is used through the thesis, let us go through a simpler and classical method. The chordwise distribution of circulation is here not discretized but replaced by a concentrated circulation $\Gamma(y)$. The object is replaced by a spanwise line of concentrated circulation, giving its name to the method. The major assumption made with the lifting line theory concerns the span length that is required to be much greater than the chord length

$$b \gg c \tag{3.21}$$

The most basic element of the model is the horseshoe vortex, represented in Figure 3.5 to model a wing of span b . The horseshoe vortex consists of a line segment of constant bound vorticity Γ spanwise (y axis) and two legs of trailing vortices shed to infinity downstream (x axis) with a circulation $\pm\Gamma$ for each.

The lifting line method consists in distributing horseshoe vortices spanwise to model the wing. This goes further than the simple horseshoe model since it considers variations of the circulation spanwise with the condition that the circulation must be zero at the tips of the wing (from second Helmholtz's theorem). For every element dy of the line, a concentrated vortex with a strength $\Gamma(y)$ exists and a vortex of circulation $-\frac{d\Gamma}{dy}dy$ is shed downstream, compensating the variation $+\frac{d\Gamma}{dy}dy$ on the blade. Figure 3.6 illustrates the lifting line theory, first developed by Prandtl [109], which has been quite used due to the simplicity of the approach. The distribution of these horseshoe vortices enables to find the distribution of bound vorticity attached to the

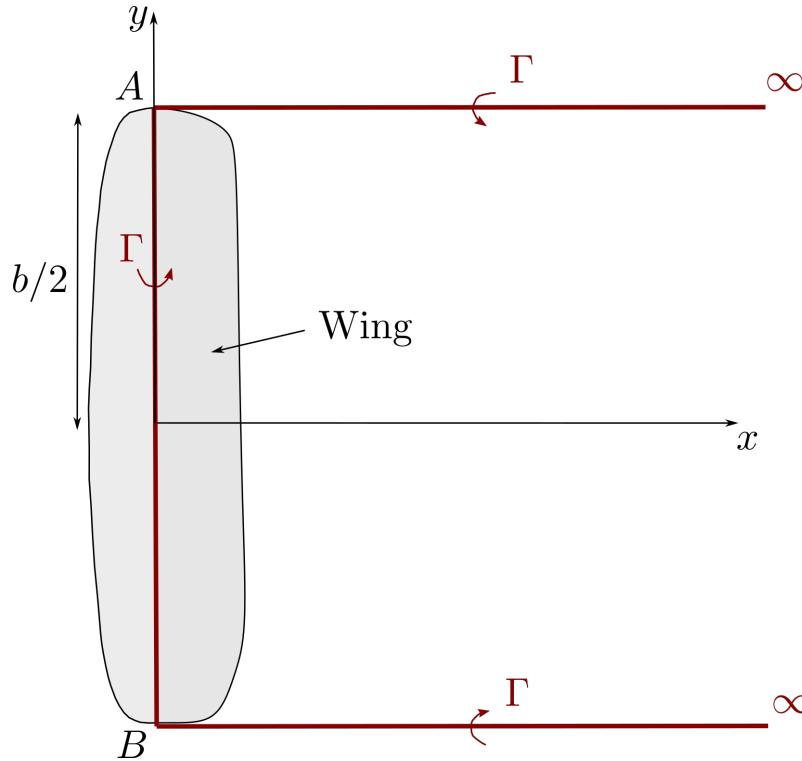


Figure 3.5: The horseshoe vortex (in red) modelling a wing of span b . Points A and B are at each tip of the wing.

wing and the intensity of the wake shed downstream, consisting of the trailing vortices indicated in the figure.

In terms of aerodynamic forces, such an approach allows calculating the lift thanks to the bound circulation Γ , but also the induced drag due to the rotation of part of the lift, because of the presence of the trailing vortices (see Appendix B). These vortices are responsible for the existence of a downwash w_i , that transforms part of the lift into drag. The local aerodynamic force at the span position y can be expressed as follows in the frame of coordinates of Figure 3.7:

$$\mathbf{F} = \underbrace{\rho U_\infty \Gamma(y) \mathbf{e}'_z}_{\text{Lift}} + \underbrace{\rho U_\infty \Gamma(y) \tan \alpha_i \mathbf{e}'_x}_{\text{Induced drag}} \quad (3.22)$$

The angle α_i is the induced angle and is defined by

$$\tan \alpha_i = \frac{-w_i}{U_\infty} \quad (3.23)$$

Figure 3.7 shows the decomposition of the angle of attack with the effective angle and the induced angle. The induced drag d_i is also indicated. The downwash can be calculated from Biot-Savart's law as a function of the circulation, and a differential equation on the circulation Γ can be derived. This differential equation can be solved numerically, for example by decomposing the circulation into a Fourier series. The differential equation is derived in Appendix B and

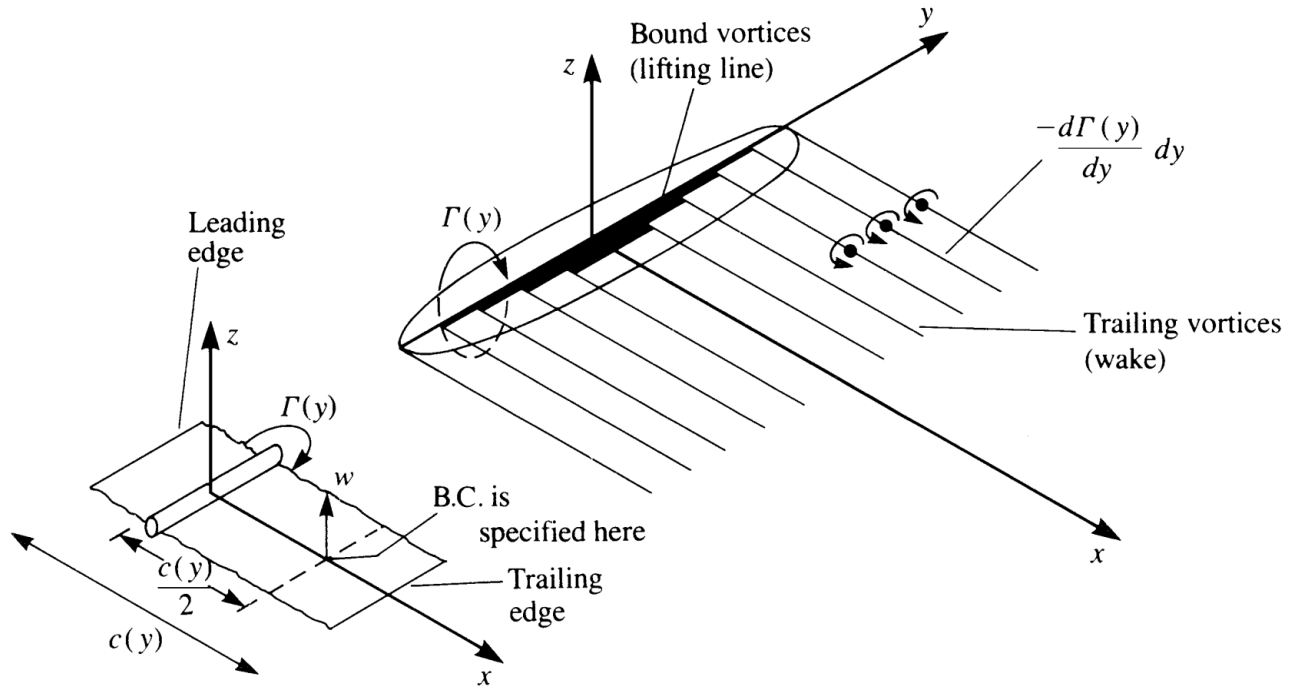


Figure 3.6: Illustration of the lifting line approach as developed by Prandtl, from [72].

the numerical resolution of the equation briefly explained. Classical cases such as the elliptic or the parabolic wings are very good examples of the application of the method, which fits quite well the actual results. In particular, the circulation distribution is well predicted by Prandtl's method.

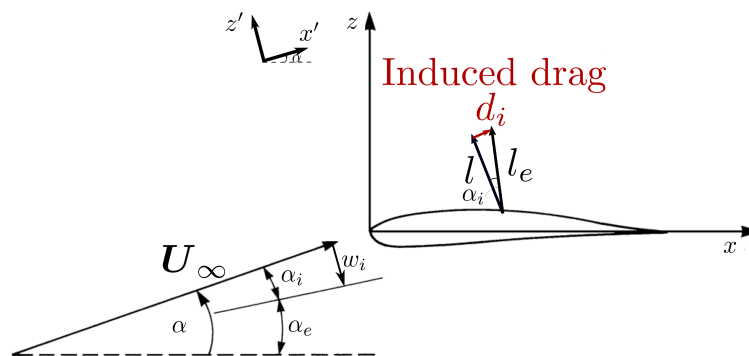


Figure 3.7: Decomposition of the angle of attack α as a function of the effective angle α_e and the induced angle α_i .

3.2.3.2 The Vortex Lattice Method formulation

The assumption $b \gg c$ for lifting line theory may be suitable for a wing, but can hardly be applied to compressor blades, which rather present an aspect ratio $AR = \frac{b^2}{S}$ of the order of magnitude 1. S is the wet surface area of the object considered. The assumption made on the span-to-chord

ratio is in that case probably too strong. Another reason why the chord should be discretized is the gap itself. Indeed, the tip gap introduces a length scale, usually two orders of magnitude smaller than the chord length, which contradicts the description of the blade as a spanwise line. The VLM is precisely an extension of the lifting line theory to a lifting surface. The surface is therefore also discretized chordwise.

Instead of mimicking the surface by a discrete line of vorticity, the surface is discretized by a 2D distribution of horseshoe vortices whose circulations are the unknowns of the problem. The non-penetration boundary condition introduced in section 3.2.2 is here applied on the surface so that the normal component of the velocity on the surface be zero. Let us go through the steps of the construction of the system of equations to be solved in order to find the circulation distribution over the surface.

Construction of the system of equations As explained in the lifting line theory, the velocity at a point $P(x, y, z)$ can be expressed as a function of the circulation Γ with Biot-Savart's law. The general expression at P due to the horseshoe vortex in Figure 3.8 can be written as the sum of three contributions:

$$\mathbf{V}_P = \mathbf{V}_{AB} + \mathbf{V}_{A\infty} + \mathbf{V}_{B\infty}, \quad (3.24)$$

one from the finite vortex segment AB (the *head*) and two from the semi-infinite trailing vortices (the *legs*).

The expression of the velocity at P due to the finite vortex segment can be written

$$\mathbf{V}_{AB} = \frac{\Gamma_{AB}}{4\pi} \frac{\mathbf{AP} \times \mathbf{BP}}{\|\mathbf{AP} \times \mathbf{BP}\|^2} \left(\mathbf{AB} \cdot \frac{\mathbf{AP}}{\|\mathbf{AP}\|} - \mathbf{AB} \cdot \frac{\mathbf{BP}}{\|\mathbf{BP}\|} \right) \quad (3.25)$$

Denoting \mathbf{e} the normal vector directing the trailing vortices of the horseshoe vortex and θ_0 the angle between vectors \mathbf{AP} and \mathbf{e} , the expression of the velocity due to one leg can be written

$$\mathbf{V}_{A\infty} = \frac{\Gamma_{AB}}{4\pi} (1 + \cos \theta_0) \frac{\mathbf{AP} \times \mathbf{e}}{\|\mathbf{AP} \times \mathbf{e}\|^2} \quad (3.26)$$

The same can be applied to the leg leaving from B . Overall, the velocity at point P can simply be expressed by the following expression:

$$\mathbf{V}_P = \mathbf{C}_{AB} \Gamma_{AB} \quad (3.27)$$

where \mathbf{C}_{AB} is a vector gathering the expressions developed above.

This is easily generalizable with a distribution of vortices Γ_{mn} , with m vortex elements chordwise and n spanwise. By linearity, the velocity at P is the sum of the contributions of all the vortex elements and is given by

$$\mathbf{V}_P = \sum_{i=1}^m \sum_{j=1}^n \mathbf{C}_{ij} \Gamma_{ij} \quad (3.28)$$

Applying the non-penetration condition over the surface, at $m \times n$ collocation points (in blue in Figure 3.8), yields the same number of equations as unknowns Γ_{ij} . Let P be a collocation point, the boundary condition can be written

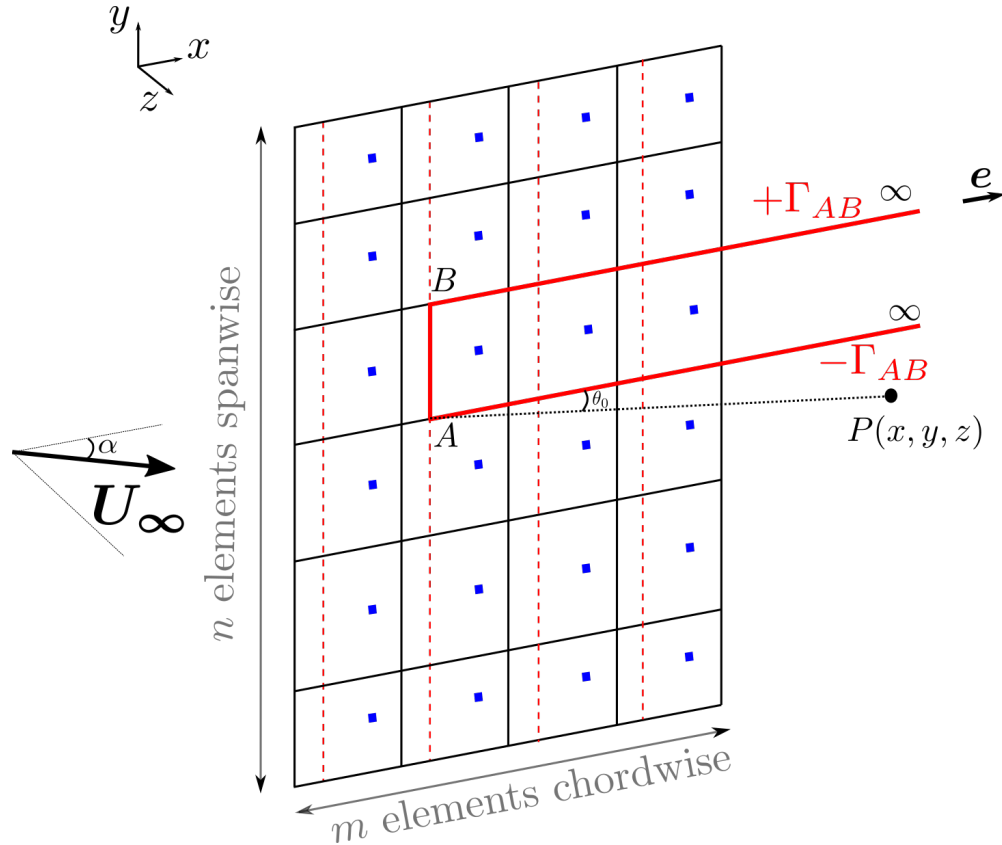


Figure 3.8: Illustration of the Vortex Lattice Method (VLM) for a flat plate. The flat plate is discretized by horseshoe vortices in red. The collocation points are indicated by the blue squares.

$$(\mathbf{V}_P + \mathbf{U}_\infty) \cdot \mathbf{n}_P = 0 \quad (3.29)$$

This can be transformed into a linear system that can be solved with a Gauss-Seidel method, for example, yielding the strength of all the vortex elements.

Location of the vortex and collocation points A special word is needed on the location of the vortex elements and collocation (or control) points. The Kutta condition presented in the previous section must be satisfied at the trailing edge to close the problem along with the singularity at the leading edge (square root singularity). To that end, the locations of the singularities and the control points are crucial. To guarantee the Kutta condition, the vortex segments are placed at $1/4$ length of each panel, chordwise, and the control points are placed at $3/4$ of the same length on each panel, halfway between the two legs of the horseshoe vortex. Figure 3.9 shows a discretization of a flat plate. A vortex element is indicated in red, whose head is located at $1/4$ length of the panel. In blue, the collocation points are shown.

A simple way of understanding the reason of these locations is summarized in Katz and Plotkin [72] on a single vortex element. The position of the vortex element derives from the application point of the lift: for a flat plate, the center of pressure is located at the quarter chord.

And if the flat plate is only represented by a single vortex with a circulation Γ , the collocation point position $x = kc$ is obtained by applying the zero normal component boundary condition, which yields $k = 3/4$. A more general proof of this is done by James *et al.* [67] for an arbitrary discretization. Positioning the points elsewhere changes the singularity positions and leads to an inaccurate definition of the problem to be solved.

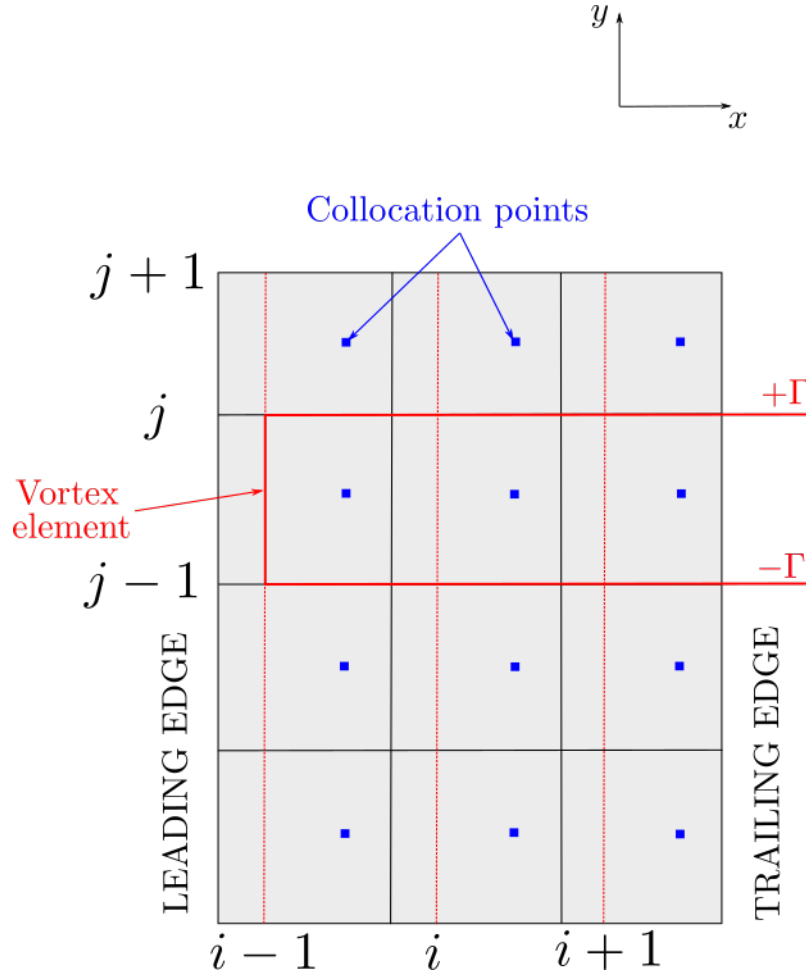


Figure 3.9: Illustration of the Vortex Lattice Method (VLM) for a flat plate. The flat plate is discretized by horseshoe vortices in red.

Formulation of the wake It is important to note that the lift is only generated by the *bound* vortices, that is, those populating the surface. The wake model used is a prescribed wake approach: in practice, this means that the wake is flat. The wake does not contribute to any lift generation. The aerodynamic force can indeed be expressed as follows

$$\mathbf{F} = \rho \mathbf{U}_\infty \times \mathbf{\Gamma} \quad (3.30)$$

Assuming the freestream velocity $\mathbf{U}_\infty = \begin{bmatrix} U_\infty \cos \alpha \\ 0 \\ U_\infty \sin \alpha \end{bmatrix}$ is the primary contributor to the lift,

the force induced by one trailing vortex of circulation $\Gamma = \begin{bmatrix} \Gamma \cos \theta_{HSV} \\ 0 \\ \Gamma \sin \theta_{HSV} \end{bmatrix}$ is

$$\mathbf{F} = \begin{bmatrix} 0 \\ \rho \Gamma U_\infty (\cos(\theta_{HSV}) \sin \alpha - \sin(\theta_{HSV}) \cos \alpha) \\ 0 \end{bmatrix} \quad (3.31)$$

where θ_{HSV} is the angle between the legs of the horseshoe vortices (HSV) and the axis x . To make sure that no lift is generated, the x and z components must be zero, which is the case with the wake defined as such. The choice of the angle θ_{HSV} is discussed in the section dedicated to the validation of the module. Figure 3.10 shows the trailing vortices at a fixed span position. Here, the lift is assumed to be only due to the freestream velocity. More advanced formulations also account for the velocity perturbations in the generation of the lift. In that case, in order to ensure no lift is generated by the trailing vortices, the wake deformation is allowed, giving degrees of freedom to it. These formulations are called *free vortex* formulations. They will not be used in the present thesis, but interesting perspectives are to be mentioned with this approach, more complicated to implement. The main idea is that an interaction is made possible between the trailing vortices in the wake, which is not the case with the prescribed wake formulation.

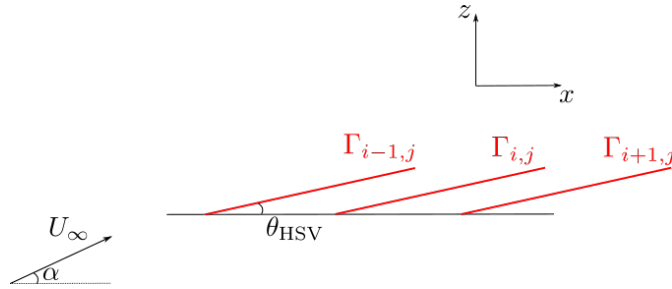


Figure 3.10: Illustration of the Vortex Lattice Method (VLM) for a flat plate. Trailing vortices are shed to infinity with an angle θ_{HSV} with the x -axis.

3.2.3.3 Summary on the use of the method

The use of the classical Vortex Lattice Method on blades can be summarized by the following items [30]:

1. Discretize the surface of the blade spanwise and chordwise. The camber and the thickness of the profiles can vary spanwise as it is the case for a compressor blade.
2. Distribute a horseshoe vortex on each panel at 1/4 of its length.
3. Apply the non-penetration boundary condition at 3/4 length of each panel.
4. Solve the linear system constructed, where the unknowns are the circulations Γ_{ij} corresponding to each vortex element.

5. The wake is assumed to be flat and no deformation is allowed. This corresponds to a horseshoe vortex angle $\theta_{HSV} = 0$ for the flat plate. More advanced criteria are developed in section 3.4 to guarantee the flatness condition.

3.2.4 Development of the module *PyLiSuite*

The VLM has been developed in the module called *PyLiSuite*, based on this formulation. Compared to existing codes in the literature, the formulation is only based on vortex singularities. Other codes are also developed with a combination of sources and vortices when discretizing a whole aircraft for example, or with a mixture of doublets and sources. For example, the code *xfoil* [47] is based on a mixture of sources and vortices. The sources allow to account for the thickness in the inviscid problem. Using sources also enables to approximate the development of the boundary layer over the airfoil. For compressor blades, the use of a single type of singularities on a lifting problem is justified by the fact that the loading in potential flows is mostly due to the camber of the blade. The thinness of compressor blades adds up to this consideration.

The architecture of the code is in *Python* but the construction of the linear system and its solving depend on low-level languages:

- The linear system construction is coded in *Fortran*.
- The linear system is solved with the *linalg* library from *Python*. The function *lstsq* is coded in *C*.

With a linear system construction based on *Python*, the computational time is multiplied by a factor at least 500 compared to the *Fortran* version of the routine. The validation of the code relies on classical external aerodynamic two-dimensional and three-dimensional cases that are presented in the next section.

3.3 Validation of *PyLiSuite*

Before adapting the code to turbomachinery configurations with TLF, *PyLiSuite* is validated on classical configurations of external aerodynamics. The validation process is done in two phases, first without accounting for the 3D effects, second on 3D configurations where the variation of the circulation spanwise is allowed.

3.3.1 Two-dimensional validation

So that the 3D effects be neglected, the VLM must be applied to very slender bodies, with a large aspect ratio. The circulation calculated at midspan of the surface considered must in that case be close to results given by the thin airfoil theory, a 2D panel method, or, in the case of the flat plate, close to the analytical results. The validation relies on the comparison of the lift coefficient, the pressure coefficient difference Δc_p and the circulation distribution spanwise (when 3D effects are considered).

3.3.1.1 The flat plate

The first validation case concerns the basic flat plate configuration illustrated in Figure 3.11. In potential flow, an analytical solution can be determined for the pressure coefficient difference with the Thin Airfoil Theory, given by the following expression:

$$\Delta c_p = 4\alpha \sqrt{\frac{1 - x/c}{x/c}} \quad (3.32)$$

The circulation on the flat plate is computed with the VLM over a 37×37 grid. A more detailed grid convergence is carried out in section 3.4 when applied to TLF configurations. The grid obtained with the grid convergence has been used for the 2D validation of the module as well.

This can be compared with VLM by applying equation (3.19). This is done in Figure 3.12 for an angle of attack $\alpha = 5^\circ$. The results from VLM fit perfectly the analytical solution in equation (3.32). The application of the Kutta condition to the flat plate problem yields the analytical expression of the total circulation Γ and hence the lift coefficient from equation (3.18)

$$c_l = \frac{l}{1/2\rho U_\infty^2 c} = 2\pi \sin \alpha \approx 2\pi\alpha. \quad (3.33)$$

The evolution of the lift coefficient c_l is given in Figure 3.12 as a function of the angle of attack and shows a very good comparison between the results obtained with *PyLiSuite* and the analytical expression of the coefficient.

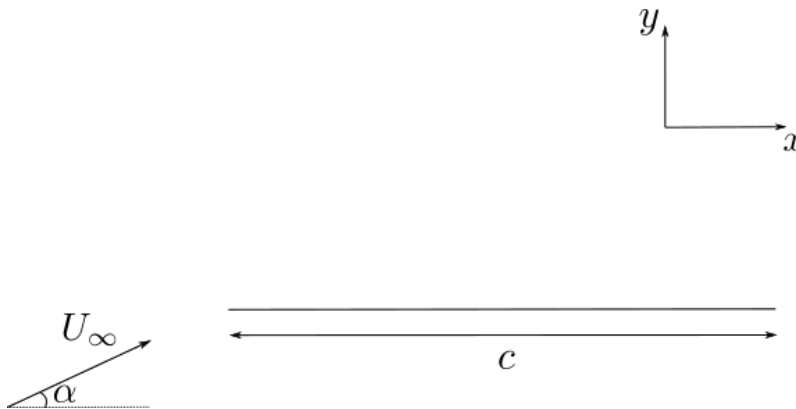


Figure 3.11: Flat plate configuration in two dimensions.

When thickness is neglected, the validation here displayed applies to all symmetrical airfoils, for which the camber line is the flat plate section line.

3.3.1.2 The NACA0012 airfoil

It is interesting to consider the case of the NACA0012 airfoil, for its axial symmetry. The camber line is indeed the same as the flat plate. The surface formulation is here compared to the camber formulation and the thin airfoil theory presented before with the flat plate. The grid uses 37×37

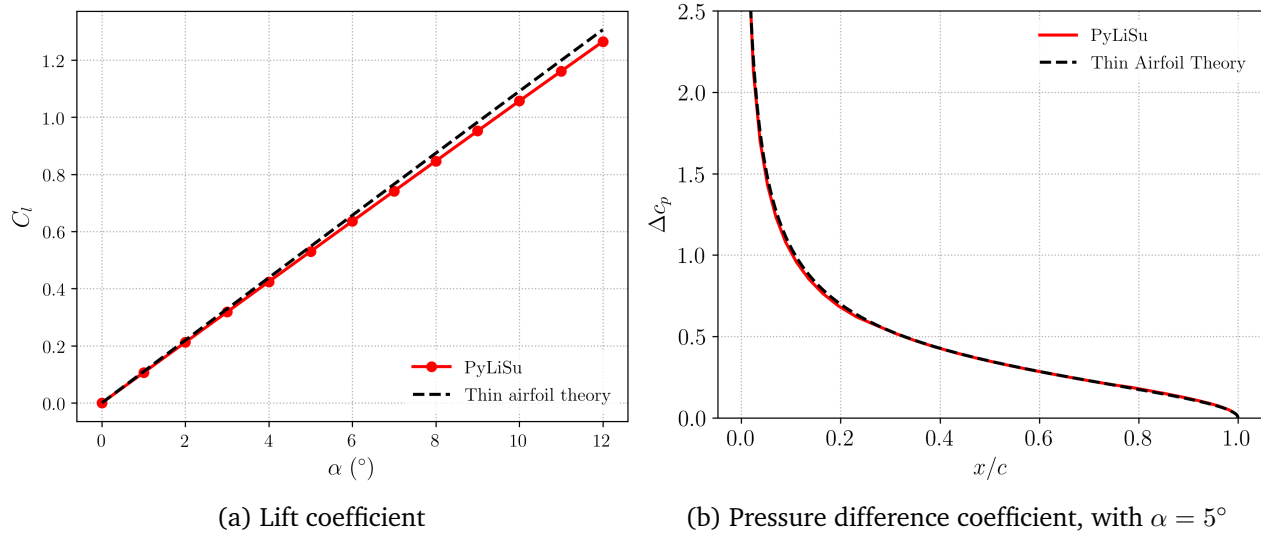


Figure 3.12: Validation of the *PyLiSuite* VLM on the lift and pressure difference coefficients c_l and Δc_p , for a flat plate. Aspect ratio $AR = b/c = 1000$.

points over the pressure and suction sides of the NACA0012 blade in the surface formulation, and 37×37 points on the camber line (which is a flat plate) with the camber formulation.

Figure 3.13a shows the evolution of the lift coefficient with the angle of attack for the two formulations. The results obtained with the panel method from *xfoil* [47] are also presented in the figure. With the surface formulation, the results fit very well with *xfoil* and exhibit a larger value of the lift coefficient, compared to the camber formulation and the thin airfoil theory. This indicates that the thickness problem is not completely negligible with this geometry. Figure 3.13b shows the pressure difference coefficient extracted at midspan from *PyLiSuite* with the two formulations. The surface formulation is in better agreement than the camber formulation, coherently with the lift evolution. The lift can indeed be calculated by integrating Δc_p along the chord.

3.3.2 Three-dimensional validation

The variations of the circulation spanwise are crucial in the generation of the vorticity driving the TLF. A good working of the module on 3D cases therefore needs to be achieved. The idea is to check the circulation distribution over the span. This is done on the flat plate and on the classic case of the elliptical wing.

3.3.2.1 The flat plate

The 3D validation is based on another VLM code from Tuck [138]. The circulation distribution spanwise is compared with his results for three aspect ratios: $AR = b/c = 1, 4$ and 20 . For these aspect ratios, the 3D effects can no longer be neglected. The grid used for the three cases is the same as that used for the 2D validation on the flat plate. Figure 3.14 validates the spanwise

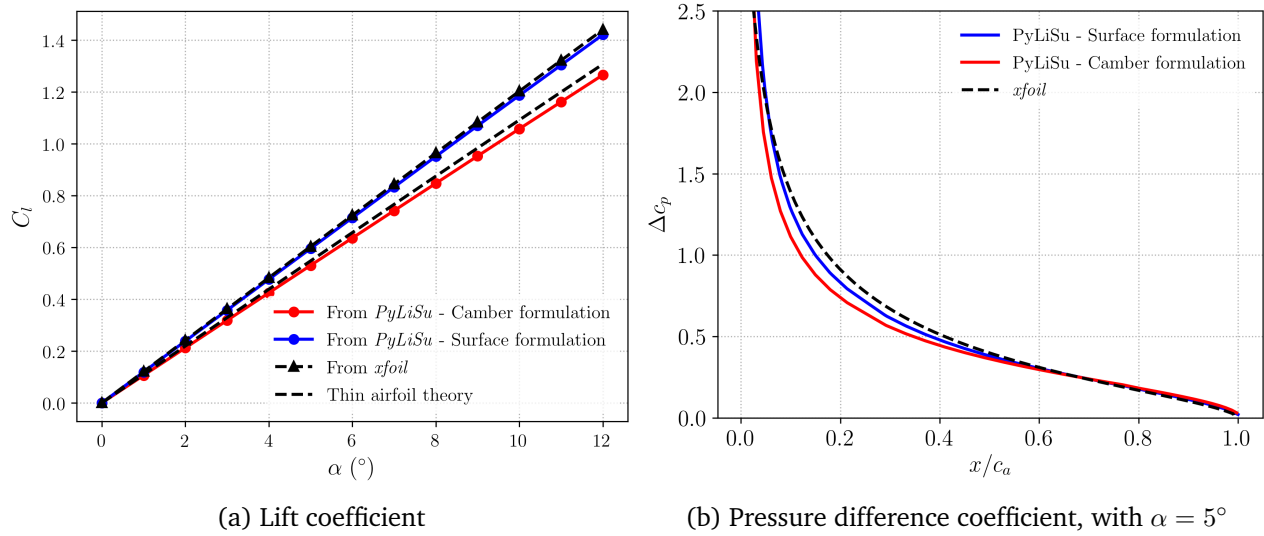


Figure 3.13: Validation of the *PyLiSuite* VLM on the NACA0012 airfoil with $AR = 1000$.

evolution of $\Gamma(y)/\Gamma_0$, with $\Gamma_0 = \pi\alpha U_\infty c$: the evolution of the normalized circulation matches Tuck's for the three aspect ratios tested.

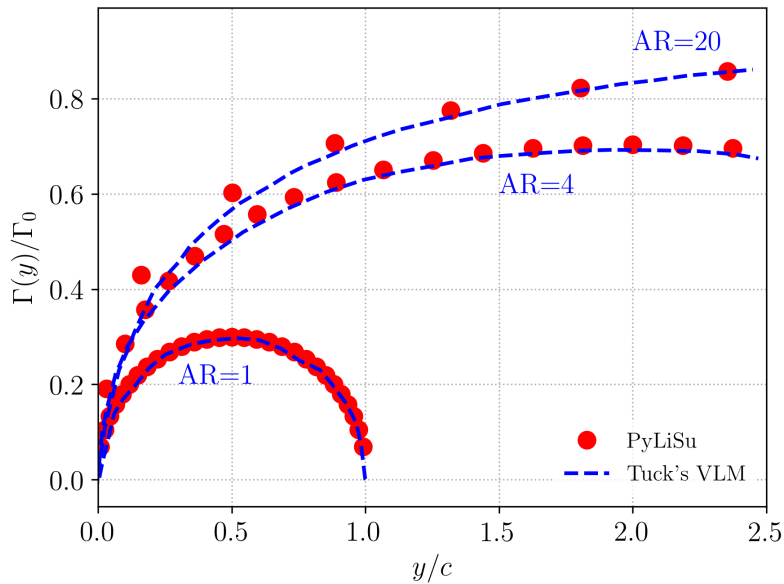


Figure 3.14: Validation of the VLM module *PyLiSuite* on the spanwise normalized circulation distribution.

3.3.2.2 The elliptical wing

The elliptical wing is known for its optimized shape in terms of induced drag generation, according to lifting line theory. The corresponding circulation distribution can be derived analytically

with this approach, explained in section 3.2.3.1, and writes ²

$$\Gamma(y) = \Gamma_{\max} \left[1 - \left(\frac{y}{b/2} \right)^2 \right]^{1/2} \quad (3.34)$$

This corresponds to a spanwise distribution of chord

$$c(y) = c_0 \left[1 - \left(\frac{y}{b/2} \right)^2 \right]^{1/2}. \quad (3.35)$$

for which the aspect ratio is

$$AR = \frac{b^2}{S} \text{ with } S = \pi \frac{c_0}{2} \frac{b}{2} \quad (3.36)$$

The shape of the wing is shown in Figure 3.15a. Its main advantage is the optimized amount of induced drag generated, directly related to the lift coefficient as

$$C_{D_i} = \frac{1}{\pi AR} C_L^2, \quad (3.37)$$

with

$$C_L = \underbrace{\frac{2\pi}{1 + 2/AR}}_{C_{l_\alpha}} (\alpha - \alpha_0), \quad (3.38)$$

α_0 corresponding to the zero-lift angle of attack.

Figure 3.15b shows the spanwise distribution of circulation for an aspect ratio $AR = 100$, comparing the analytical expression of the circulation from equation (3.34), the result from lifting line theory using Glauert's method, as described in Appendix B, and the result from VLM. The agreement is very good between the three curves, although Γ_{max} predicted by the lifting line theory is a bit underestimated.

Figure 3.16 shows the evolution of the coefficient C_{l_α} with the aspect ratio, comparing the three evolutions as well, showing a good fit between all of them.

3.3.3 Influence of the HSV angle

As presented in section 3.2.3.2, the VLM formulation is based on a prescribed wake. This means that the legs of the horseshoe vortices (HSV) extend to a prescribed and unique direction. This also implies that the trailing vortices do not interact with each other. It was shown that keeping the HSV in the (x, z) plane prevents the generation of an aerodynamic force that would add up to the drag or the lift. A residual force is generated in the span direction if the angle $\theta_{HSV} \neq \alpha$, i.e. whenever the trailing vortices are not aligned with the freestream direction. Nonetheless, fixing $\theta_{HSV} = \alpha$ contradicts the flatness of the wake of a classical VLM with a prescribed wake, that can only be obtained for trailing vortices aligned with the axial direction x and $\theta_{HSV} = 0$.

²See section 8.1. in Katz and Plotkin [72].

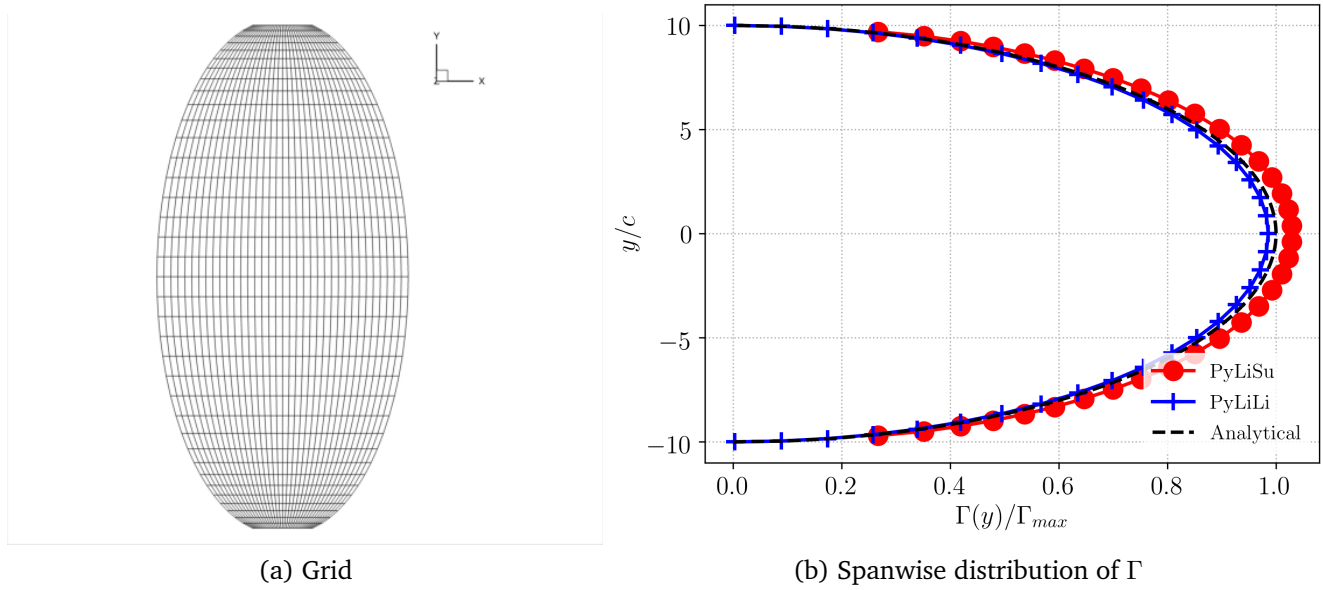


Figure 3.15: Grid of the elliptical wing used for VLM, and comparison with the lifting line theory results. The blue line corresponds to the results from the lifting line theory coded numerically in *PyLiSuite*, the black dashed line is the analytical result from lifting line theory.

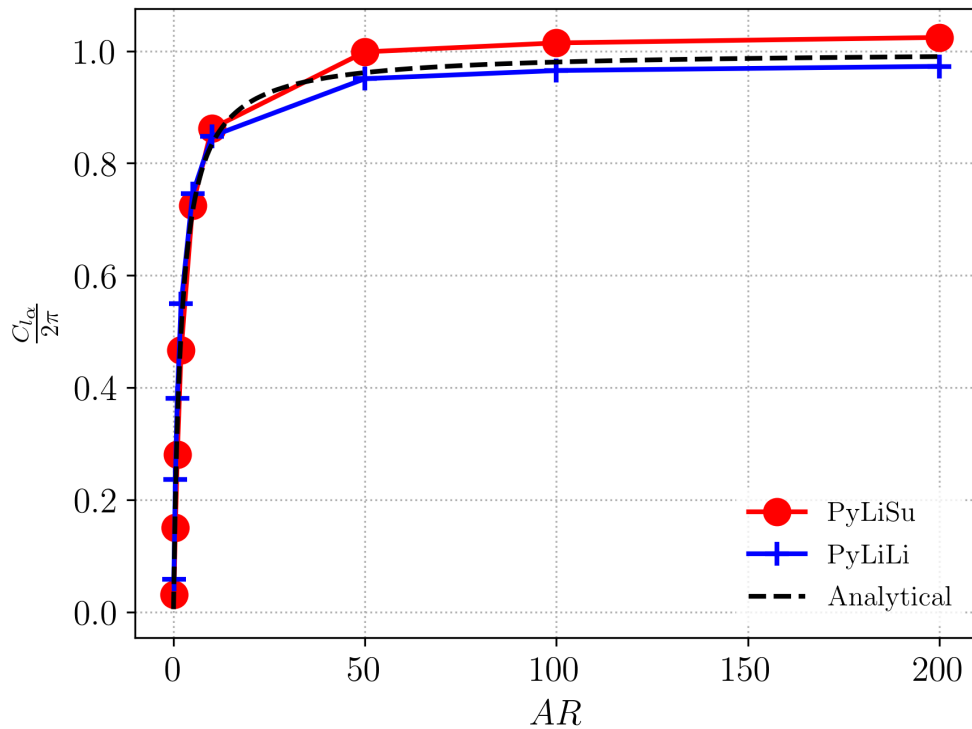


Figure 3.16: Evolution of C_{l_α} with the aspect ratio AR for the elliptical wing, from the analytical expression, numerical lifting line theory (*PyLiLi*) and VLM (*PyLiSu*).

This section investigates the influence of the HSV angle on the circulation and the lift generated, comparing the two values $\theta_{HSV} = \alpha$ and $\theta_{HSV} = 0$.

The flat plate is again treated with $\alpha = 5^\circ$, the same grids as before, and the two HSV angles. The influence of the HSV angle θ_{HSV} is investigated through the evolution of the lift coefficient, by varying two parameters:

1. The aspect ratio AR , to compare the relative error ε_{C_L} between the two values $\theta_{HSV} = \alpha$ and $\theta_{HSV} = 0$, $\theta_{HSV} = 0$ being the reference as validated on Tuck's VLM before.
2. The HSV angle for a fixed aspect ratio $AR = 1$.

Figure 3.17 displays the shedding of the vortices along the flat plate with an angle θ_{HSV} . The width t_w of the wake, formed by the elementary vortices is defined at the trailing edge and indicated in the figure.

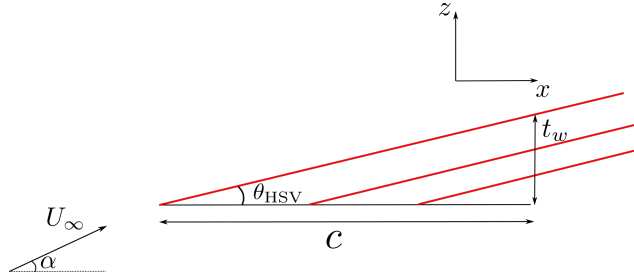


Figure 3.17: Wake thickness in the airfoil plane due to the HSV angle.

The idea is to build up a criterion on the wake width-to-span ratio at the trailing edge

$$w_{wake} = \frac{t_w}{b} = \frac{c \tan \theta_{HSV}}{b} = \frac{\tan \theta_{HSV}}{AR} \quad (3.39)$$

ensuring a sufficiently low relative error on the lift. The VLM based on a prescribed wake formulation indeed relies on the fact that the wake must be flat. The interaction of the trailing vortices is not accounted for in this formulation and allowing them to have a different pitch direction, giving a thickness to the wake, does have an influence on the bound vorticity calculated on the blade. To this end, w_{wake} must remain much lower than 1.

Figure 3.18 shows the distribution of the trailing vortices in a plane right downstream the trailing edge of the flat plate for the two angles. The colour of the disks corresponds to the position from which the vortex is shed, and their size to the intensity of the shed vortex. The wake width for $\theta_{HSV} = \alpha$ is quite important and as it is shown afterwards, the influence on the lift coefficient is major.

Figure 3.19 shows the evolution of the relative error

$$\varepsilon_{C_L} = \frac{|C_{L_{ref}} - C_{L_{\theta_{HSV}}}|}{C_{L_{ref}}} \quad (3.40)$$

as a function of the wake width-to-span ratio w_{wake} , for $\alpha = 5^\circ$. w_{wake} can be varied either with AR or with θ_{HSV} , and the figure shows consistent evolutions. The relative error remains

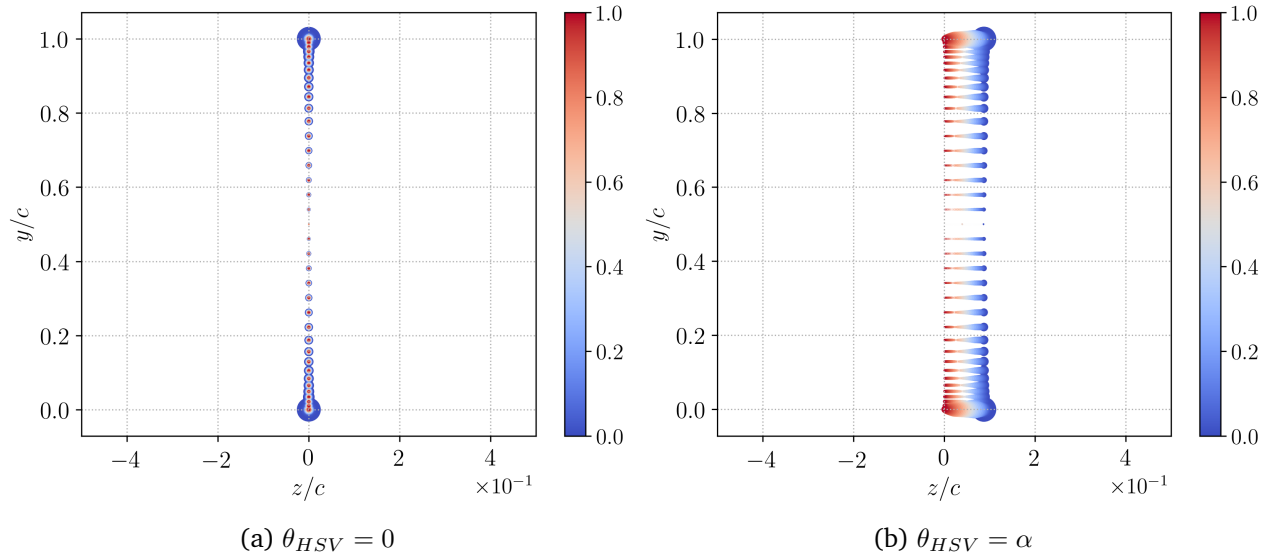


Figure 3.18: Impacts of the trailing vortices in the plane $x = 1.05c$, right downstream the trailing edge of the flat plate. Comparison between two HSV angles for $\alpha = 5^\circ$ and $AR = 1$. The contour colours correspond to the positions from which the legs of the HSV are shed (0: leading edge to 1: trailing edge) and the size of the disks relates to the intensity of the vortices.

lower than 5% for a wake width-to-span ratio of 2%, corresponding to $AR > 5$ or $\theta_{HSV} < 1^\circ$. The following criterion

$$w_{wake} < 2\% \quad (3.41)$$

is kept for the rest of the thesis.

The flatness of the wake therefore seems to have a big impact on the bound circulation. It may be due to the fact that if the vortices are shed along the chord with a thick wake, the Kutta condition at the trailing edge is no longer satisfied.

For the flat plate, the flatness is perfectly guaranteed with trailing vortices following the axis. Nevertheless, for cambered blades, the flatness of the wake cannot be ensured and this criterion is crucial. The same consequence applies when the surfaces are discretized with vortices, as shown in Figure 3.20. The wake width t_w then corresponds to the maximal thickness of the airfoil.

For example, with the NACA0012 airfoil, the solution with the surface formulation will be acceptable for aspect ratios $AR > 6$, based on criterion (3.41).

In the case of compressor blades ($AR \sim 1$), of interest in this thesis, the camber and the thickness generally remain small ($t_w = 1\% c$, yielding $w_{wake} \sim 1\%$) and the use of VLM with a prescribed wake is justified. In order to minimize as much as possible the wake thickness t_w , the angle θ_{HSV} is fixed at 0° for the rest of the thesis, since the application of the method to TLF sticks to unstaggered airfoils.

Note that for a blade airfoil that is staggered with an angle γ (with a low camber), the thickness t_w remains low for $\theta_{HSV} = \gamma$. In the case of a compressor blade, γ is generally not

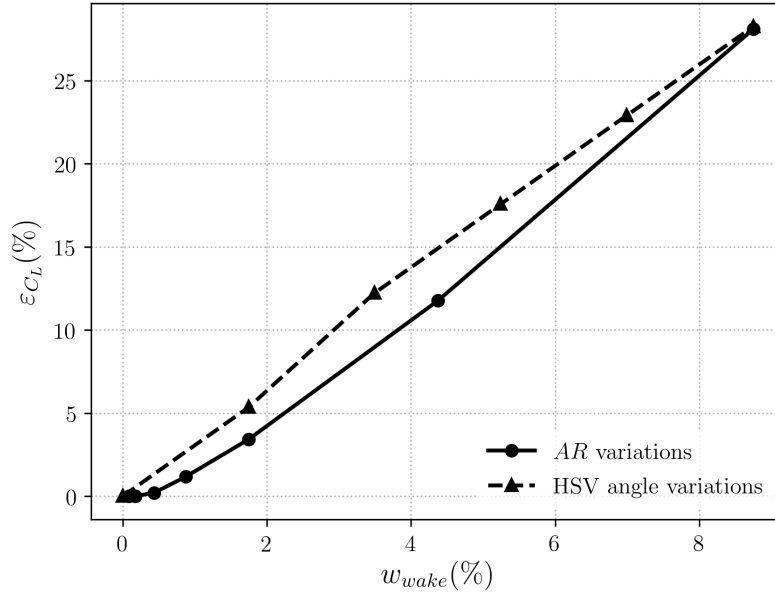


Figure 3.19: Evolution of the relative error on the lift coefficient on the flat plate with $\alpha = 5^\circ$, with the reference case at $\theta_{HSV} = 0^\circ$, as a function of the wake width-to-span ratio w_{wake} .

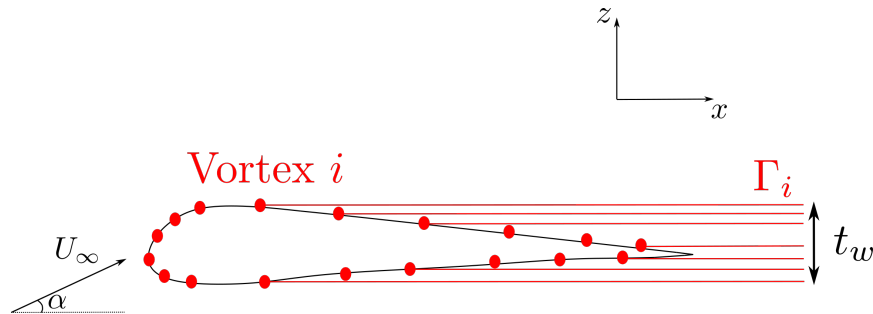


Figure 3.20: Wake thickness in the airfoil plane generated by a surface distribution of vortices.

null. The application of the method to a compressor rotor is discussed in section 5.5.3.

3.4 Application to tip-leakage flow

The VLM has now been validated on external aerodynamics cases. The present thesis deals with TLF and the method has to be applied to configurations with endwalls. This section shows how the endwalls (hub and casing) are accounted for. The evaluation of the results on tip-leakage flow configurations is presented in chapter 5. Some criteria on the discretization to be used as a function of the tip clearance size are also presented along with the influence of the horseshoe vortices, whose angle between the legs and the streamwise axis can be varied.

3.4.1 Influence of the endwalls

The presence of the endwalls must be described in *PyLiSuite* to account for the presence of a casing and a hub. There are two possibilities with VLM:

1. Applying the same mirror symmetry condition as Lakshminarayana and Horlock did for their slotted wing [81] for replicating the presence of a casing and hence of a tip clearance. Moreover, a mirror blade is also generated symmetrical with respect to the root of the current blade to replicate the presence of the hub. The idea is to ensure that the circulation slope is zero at this position (no shed vorticity).
2. Generating the surfaces associated to hub and casing, with panels.

The second solution is investigated at the end of the section, but we here focus on the first possibility.

Four cases of reference are considered to deal with tip-leakage flow configurations. The idea is to show the impact of the two mirror conditions in configuration 11, compared to the three other cases. Figure 3.21 shows a sketch of the four cases considered:

- Case 00 is the external aerodynamic case treated before, with no endwall and a single blade.
- Case 01: two mirror conditions are applied with a gap 2τ between the two tips of the blade (in solid line) and the mirror blades.
- Case 10: two mirror conditions are applied with no gap on both sides of the blade.
- Case 11: the tip-leakage flow configuration, with a mirror blade in contact with the blade at the equivalent hub, and another, symmetric to the resulting $2b$ span blade, distant from 2τ from the tip, to mimic the presence of the casing.

The results are presented for the flat plate configuration with a large gap size $\tau/c = 13\% c$ and a bigeometric distribution chordwise and spanwise for the grid. The angle of attack is set to $\alpha = 5^\circ$. The aspect ratio is fixed at $AR = 1$. Except when mentioned explicitly in the rest of the chapter, these conditions will be used for the different tests performed on *PyLiSuite*.

3.4.1.1 Grid convergence

Criteria on the grid refinement to be used are of great importance in terms of computational time and resolution of the results. A grid convergence is therefore carried out to optimize the refinement for a sufficient resolution. The grid is generated through two parameters in the two directions (spanwise and chordwise): the first grid size Δ_0 and the growth ratio g . A bigeometric evolution of the cell size is applied in both directions according to

$$\Delta l_n = \Delta_0 g^n, \text{ for the } n^{\text{th}} \text{ cell} \quad (3.42)$$

such that

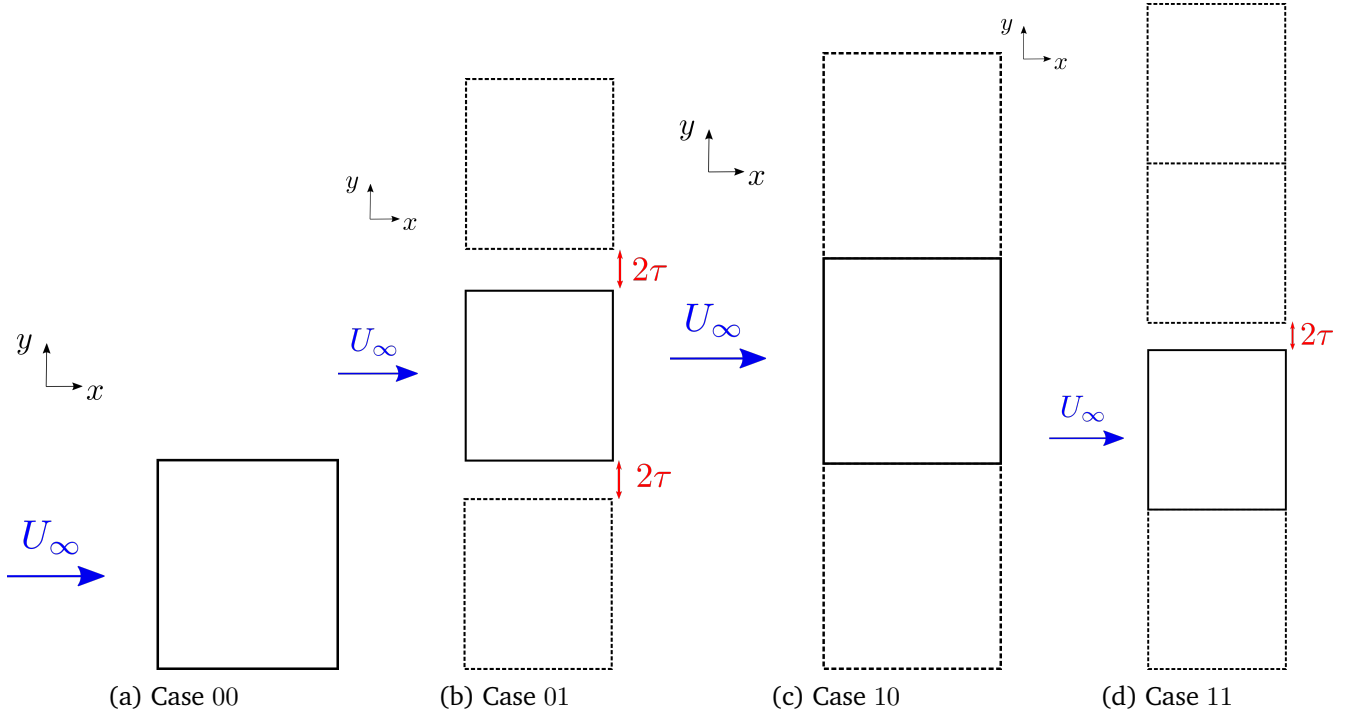


Figure 3.21: Sketches of the four cases of reference regarding the two conditions of symmetry. The dashed lines indicate that the surface is a mirror blade. The TLF configuration corresponds to case 11.

$$c/2 = \Delta_{0,c} \frac{1 - g^{\lfloor N_{pts}/2 \rfloor}}{1 - g} \quad (3.43)$$

with N_{pts} the overall number of points in the chord direction. Likewise with the span. Figure 3.22 shows the evolution of the lift coefficient with N_{pts} . The convergence is quickly obtained in the four cases from about 30 points in the two directions. Here, the same number of points is applied on both directions for sake of simplicity for the presentation of the results. Besides, the computational time really starts augmenting for a grid with more than 10000 points, because of linear system solving, very costly for big matrices.

Regarding the value of the first cell size $\Delta_{0,c}$, the ratio $c/\Delta_{0,c}$ is plotted in Figure 3.23. The grid refinement to be applied for smaller gaps is investigated afterwards in case 11.

A comparison of the spanwise evolution of the bound circulation Γ_b between the four cases is done in Figure 3.24. For each case, the circulation is plotted over the span of the solid blade generated in the module, in solid line in Figure 3.21. Case 10 presents the largest bound circulation, with slight variations over the span. There is no gap in this configuration and the extension of the blade on both sides rejects the vortex shedding to the tips of the mirror blades, where the variation of the circulation is strong. The main point is therefore that nearly no vorticity is shed in case 10 on the central blade. In case 11, the TLF configuration, the slope is null near the hub at $y/c = 0$ and the bound circulation decreases to zero when approaching the tip. The slope of the circulation is largest at the tip, where most of the vorticity is shed.

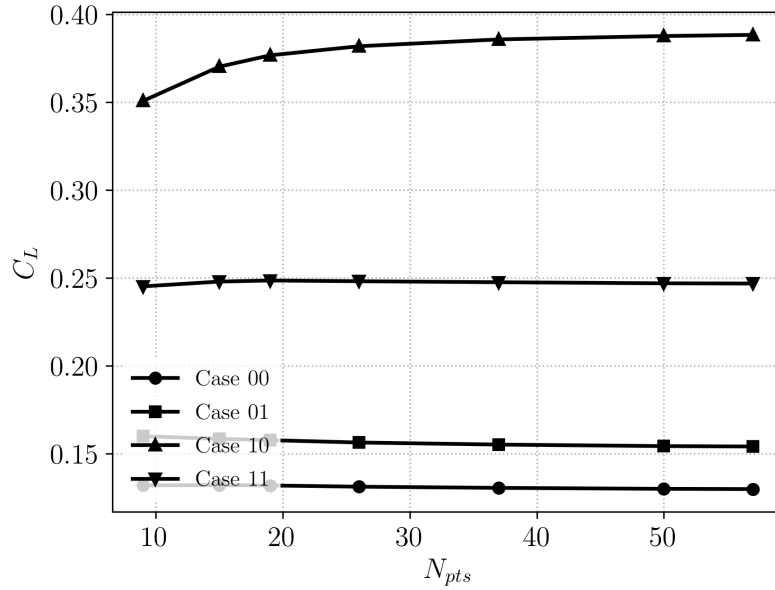


Figure 3.22: Grid convergence on the lift coefficient. N_{pts} represents the number of points chordwise and spanwise, with a constant growth ratio $g = 1.05$.

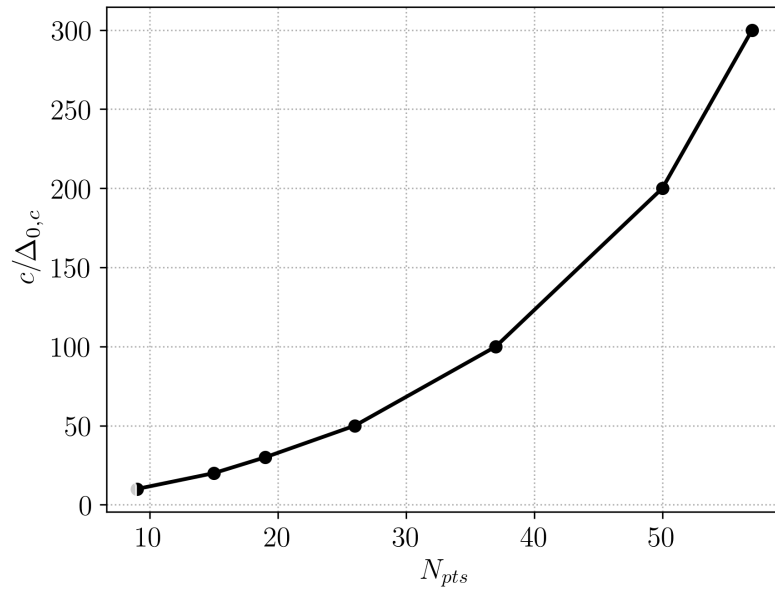


Figure 3.23: Evolution of the ratio $c/\Delta_{0,c}$ with the number of points used on a bigeometric distribution, with a constant growth ratio $g = 1.05$.

Regarding cases 00 and 01, the bound circulation is even smaller because vorticity is shed at both tips of the blade. Coherently, more vorticity is shed for the infinite tip clearance (case 00), which induces a lower bound vorticity on the blade, compared to case 01. That case indeed presents a finite tip clearance at both tips and is responsible for less shed vorticity.

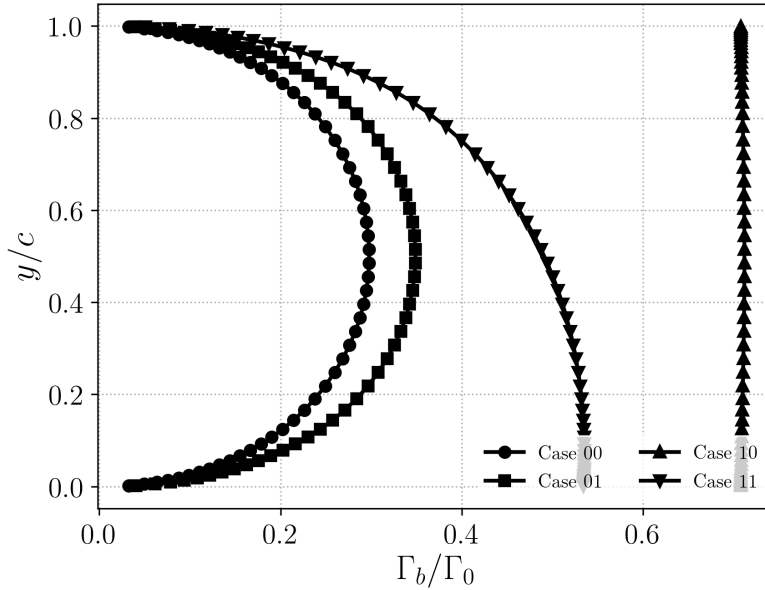


Figure 3.24: Spanwise circulation distribution for the four cases, with the 37×37 converged grid.

3.4.2 Grid criterion on the tip gap size

The present thesis deals with TLF configurations and before comparing the capabilities of the VLM module, it is necessary to establish a criterion on the grid with respect to the tip gap size. Indeed, for small gaps about $\tau = 1\% c$, the grid may require a significant refinement compared to $\tau = 13\% c$. A grid convergence is done in this section to set a grid criterion for TLF configurations in *PyLiSuite*. Figure 3.25 presents the evolution of the lift coefficient for the NACA0012 and the NACA4412 airfoils, with an aspect ratio $AR = 1$, for four different tip gap sizes. The formulation used is based on the camber, and the surface generated for the NACA0012 airfoil is therefore a flat plate. The convergence is quickly obtained in all cases around this criterion:

$$\tau/\Delta_{0,b} > 2 \quad (3.44)$$

where $\Delta_{0,b}$ is the first grid size at the tip. The grid is still based on a bigeometric distribution spanwise, with an expansion ratio $g = 1.05$. The chordwise distribution has been set to 37 points following previous results from section 3.4.1. With this criterion, the number of points spanwise in the worst case (the smallest gap) is about 90 points, which is reasonable. For a compressor rotor, the order of magnitude of the tip gap is about $1\% c$. The module runs in 10 seconds, on a single core of a standard computer.

Besides this criterion, it is interesting to notice the influence of the gap size on the lift. Considering the converged C_L , the lift decreases as the tip gap size increases. This is coherent with the observations done on the four cases of reference: for a larger gap, more vorticity is shed and from Helmholtz's conservation of the circulation in potential flows, the bound circulation decreases, explaining the tendency obtained for C_L .

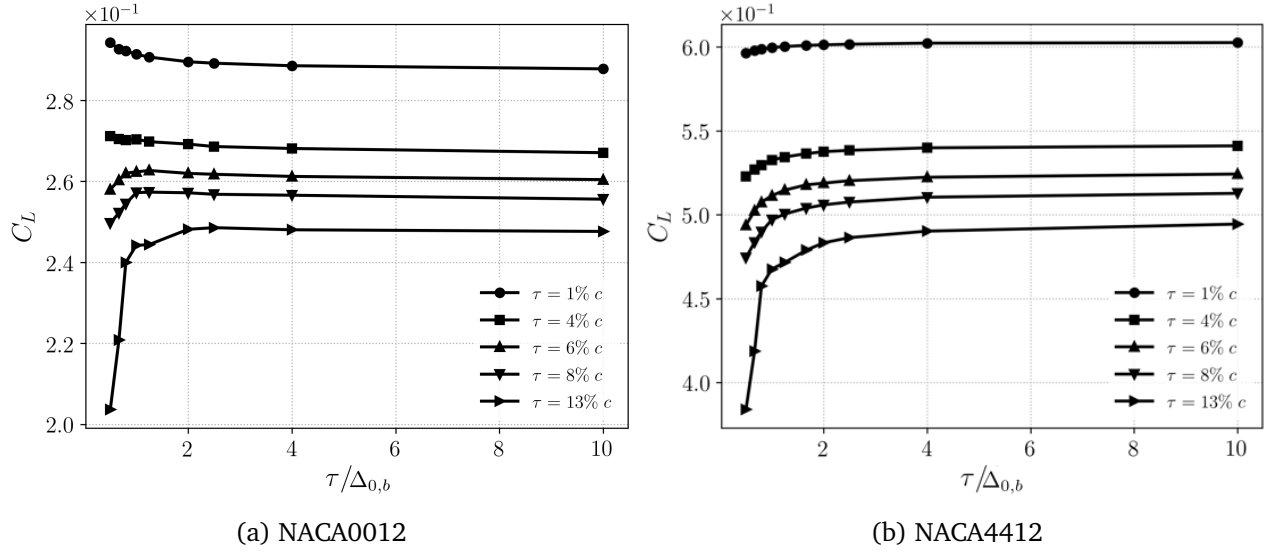


Figure 3.25: Evolution of the lift coefficient obtained with *PyLiSuite*, with the camber formulation, on the NACA0012 and NACA4412 airfoils, with an aspect ratio $AR = 1$ and $\alpha = 5^\circ$. Five different tip gap sizes are tested for configuration 11.

3.4.3 Implementation of the symmetry condition

A mirror condition has been applied to case 11, as shown in the previous sections, by satisfying the non-penetration condition over all the surfaces generated, including the mirror blade. It is however possible to reduce the number of elements of the linear system to the blade of span $2b$ with $m \times n$ points, by stating that the circulation is the same on the mirror fictive blade. The velocity calculated at any point P of the field can therefore be computed as

$$\mathbf{V}_P = \sum_{i=1}^m \sum_{j=1}^n (C_{ij} + C_{ij}^*) \Gamma_{ij} \quad (3.45)$$

instead of

$$\mathbf{V}_P = \sum_{i=1}^m \sum_{j=1}^n (C_{ij} \Gamma_{ij} + C_{ij}^* \Gamma_{ij}^*) \quad (3.46)$$

where Γ_{ij} and Γ_{ij}^* are respectively the circulations on the real and fictive blades, at the same position. This simplification allows a reduction of the number of unknowns Γ_{ij} by a factor 2.

Figure 3.26a compares the circulation distribution over the flat plate for case 11, with and without the system reduction, for a gap size $\tau = 13\% c$. A perfect fit is observed.

Theoretically, accounting for the hub and casing requires a symmetry condition with an infinite number of fictive blades spaced with a 2τ gap with one another. The idea of the system reduction is the same applied to k blades, reducing the number of unknown vortex intensities from $k \times m \times n$ to $m \times n$. The same idea is also developed in section 3.4.5, for implementing the

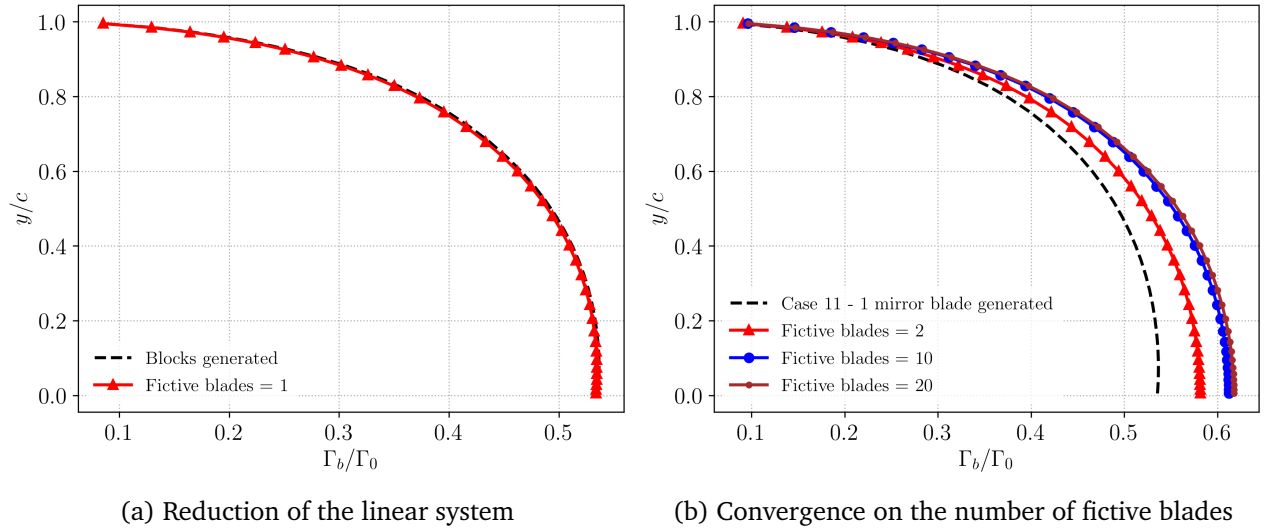


Figure 3.26: Evolution of the normalized bound circulation with the span comparing the reduced system to the complete linear system in case 11. The convergence to the theoretical symmetry condition is obtained in the second figure with 5 blades on each side of the central blade (total: 10 blades).

periodicity condition. Figure 3.26b shows the convergence of the circulation distribution with the reduced system, from 1 fictive blade on each side of the central blade to 10 fictive blades.

3.4.4 Generation of casing

In the previous section, the tip clearance has been taken into account with a symmetry condition. With annular geometries, this condition is no longer applicable. Another possibility to account for the tip clearance is to distribute horseshoe vortices over the casing surface. Figure 3.27 shows an example of the grid generated for the simulation of a tip-leakage configuration with a plate replicating the casing. The casing generated is a square of length L_{casing} , divided into N_{casing} points streamwise and pitchwise. These two parameters are varied to compare this formulation of the problem with the symmetry condition.

The grid convergence is studied in two steps:

- First, the extension of the casing is set to $L_{casing} = 6c$ and the number of points N_{casing} is varied. Figure 3.28a shows the evolution of the lift coefficient as a function of the ratio $\tau/\Delta L_{casing}$, with $\Delta L_{casing} = L_{casing}/N_{casing}$.
- Second, the extension of the casing is varied, based on the criterion

$$\tau/\Delta L_{casing} = 1 \quad (3.47)$$

obtained with the first item. The idea is to check the convergence of the lift coefficient depending on L_{casing} , as shown in Figure 3.28b. The evolution is compared to the reference

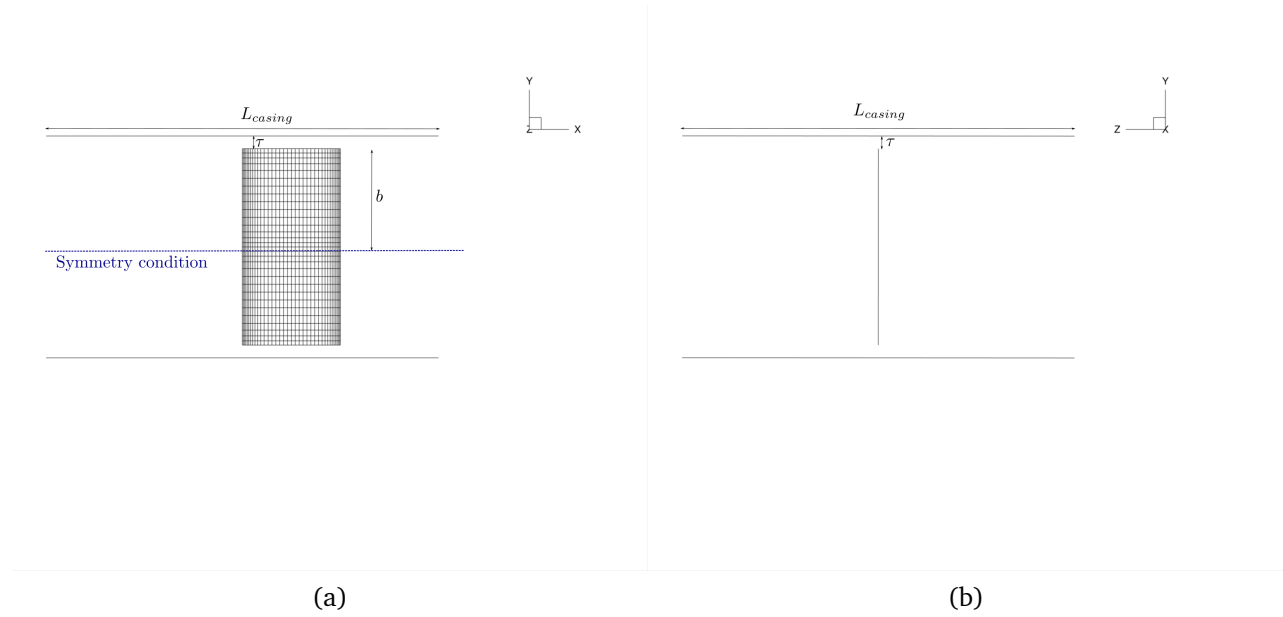


Figure 3.27: Views of the configuration with a plate generated for modelling the presence of a casing.

value from the symmetry condition, described in the previous section. The convergence is not completely achieved for $L_{casing}/c = 12$ but the slope is nearly flat and the resulting lift coefficient close to the lift coefficient obtained with the symmetry condition.

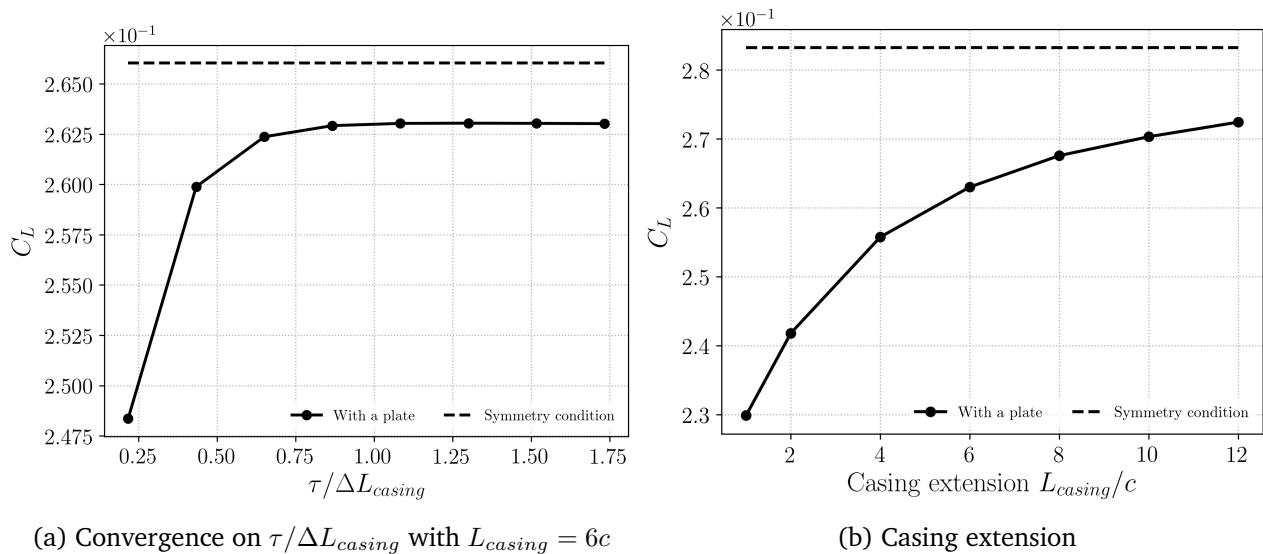


Figure 3.28: Grid convergence on the lift coefficient with a plate generated for casing, in the case of a flat plate blade. Comparison with the case of reference 11 with a symmetry condition.

Figure 3.29a shows the circulation distribution associated to the lift coefficient, with an extension $L_{casing} = 12c$, compared to that from the application of the symmetry condition.

Coherently with Figure 3.28, the bound circulation is underestimated with the plate replicating the casing. The augmentation of the casing extension makes the circulation tend towards the circulation got from the symmetry condition. The problem with such a choice is the number of points and the subsequent CPU time required to solve the linear system. The advantage of the symmetry condition is that only the main blade is generated, with a reasonable number of points. Figure 3.29b shows the CPU time against casing extension, for a given grid step size. It increases significantly from $L_{casing} = 10c$ and reaches about 20 minutes with the $12c$ extension.

This is critical since the method is expected to run in less than 10 minutes to get the results. The CPU evolution was obtained for the most favourable case with $\tau/c = 13\%$. For a gap of the order of magnitude of an actual compressor blade ($1 - 2\% c$), this would take hours, even risking the memory saturation of the processor. Figure 3.30 indicates the total number of points required based on the two criteria, (3.44) and (3.47), for a fixed casing plate extension. For 10^4 points, the CPU time already reaches 20 minutes. For lower gaps, the method is simply not relevant anymore with this discretization of the casing.

The grid could be optimized with a geometric evolution from the center to the edges of the casing plate, but the symmetry condition is here retained as it is clearly optimal in terms of CPU. The study will keep the symmetry condition to account for the gap out of simplicity, but the discretization of the casing plate remains an interesting feature as it could be used for annular configurations where the symmetry condition is not relevant. This is not considered in this thesis.

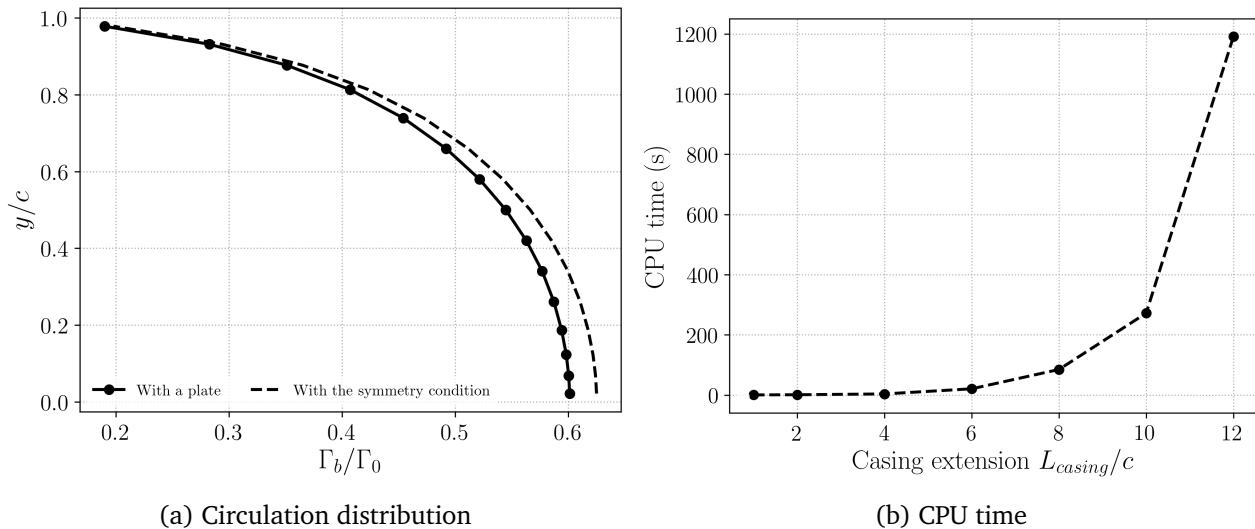


Figure 3.29: (a) Comparison of the circulations from the symmetry condition and the application of a casing plate, with $L_{casing} = 12c$. (b) CPU time indicated as a function of the extension of the casing.

Regarding the discretization of a plate replicating the hub, the proximity of the control points of the hub plate to the legs of the horseshoe vortices from the root of the blade makes it impossible to work correctly, the velocity at the control points surging very quickly. The application

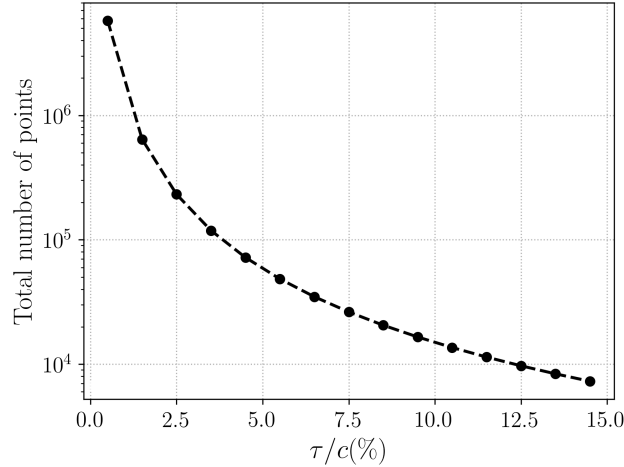


Figure 3.30: Total number of points for $L_{casing}/c = 12$ with the grid criteria applied on the blade ($AR = 1$) and the casing plate, as a function of the tip gap size.

of the non-penetration condition cannot be guaranteed and the solving of the linear system subsequently either.

3.4.5 Periodicity

Implementation for linear cascades

So far, the TLF configurations studied only concern single blades. The implementation of a periodicity condition is crucial with the objective of approaching a representative compressor configuration with VLM. The first naive idea consists in generating all the blades. For example, let us consider a 15-blade linear cascade. The first idea would simply be to solve the linear system composed of the HSV distributed over the 15 blades. Such a formulation is however rapidly costly since the size of the linear system to be solved is 15 times larger than for a single blade. Moreover, the construction of the linear system also takes more time.

Instead, the idea behind the periodicity condition to be implemented is that the spanwise distribution of Γ is the same over all the blades of the cascade. In the case of the 15-blade cascade, assuming the periodicity, the system to be solved reduces from $15 \times N_{pts}$ to N_{pts} , N_{pts} being the number of grid elements over a single blade. Getting back to equation (3.28) for the calculation of the velocity at a point P of the domain, distributing the unknown circulations over N_{blades} yields for the perturbed velocity

$$V_P = \sum_{k=1}^{N_{blades}} \sum_{i=1}^m \sum_{j=1}^n C_{ij}^{(k)} \Gamma_{ij}^{(k)} \quad (3.48)$$

with a non-penetration condition applied to all the control points of the N_{blades} blades. Applying the periodicity condition, equation (3.48) simplifies to

$$\mathbf{V}_P = \sum_{k=1}^{N_{blades}} \sum_{i=1}^m \sum_{j=1}^n C_{ij}^{(k)} \Gamma_{ij} \quad (3.49)$$

with the non-penetration condition only applied to the middle blade of a linear configuration, as that shown in Figure 3.31. Theoretically, for a linear cascade, the periodicity can only be obtained for an infinite number of blades. In practice, more than 15 blades is sufficient to guarantee that adding more blades to the sides of the cascade will not affect the circulation distribution over the blade in the middle. Figure 3.31 shows a linear cascade, tested with the module to validate the periodicity condition. Blade 0 designates the blade in the middle of the cascade³. The other blades are numbered increasingly up to $\lfloor N_{blades}/2 \rfloor$ towards the larger pitchwise positions, and down to $-\lfloor N_{blades}/2 \rfloor$ on the other side of blade 0.

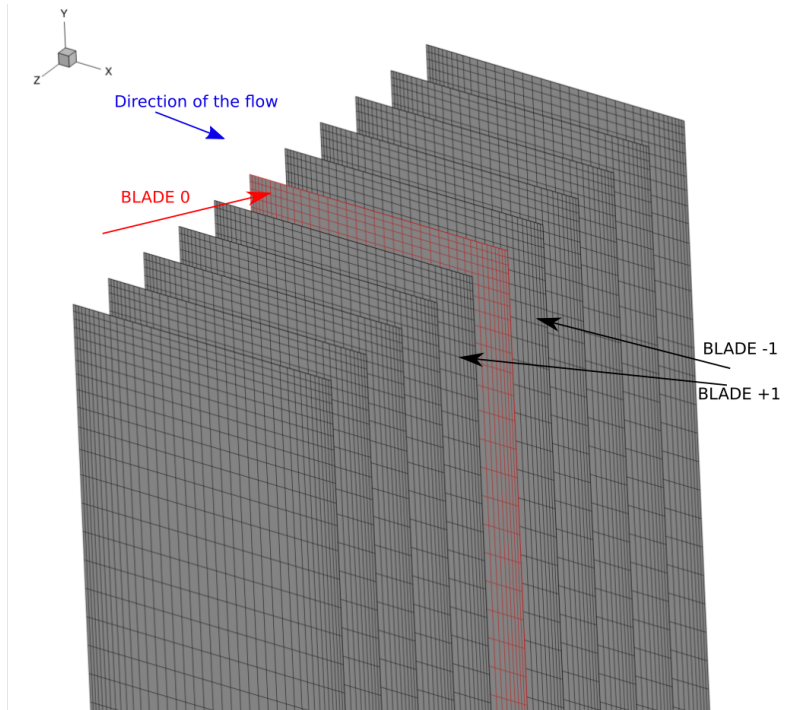


Figure 3.31: Sketch of a 11-blade linear cascade generated with *PyLiSuite*.

Figure 3.32a shows the distribution of circulation over blade 0 for several numbers of blades, with a constant pitch $s = c$ (hence a solidity $\sigma = c/s = 1$). The idea is to check from what number of blades the circulation is unchanged when adding new blades. For this case, the whole linear system is solved and the periodicity condition is not applied. Here, nine blades is a good fit. Figure 3.32b verifies the periodicity condition implemented in the module, based on the circulation calculated by solving the whole linear system. The red curve distribution was obtained with the periodicity condition and superimposes perfectly to the black curve (whole linear system).

³Only odd numbers of blades N_{blades} are considered here, to ensure the same number of blades to the right and to the left of blade 0.

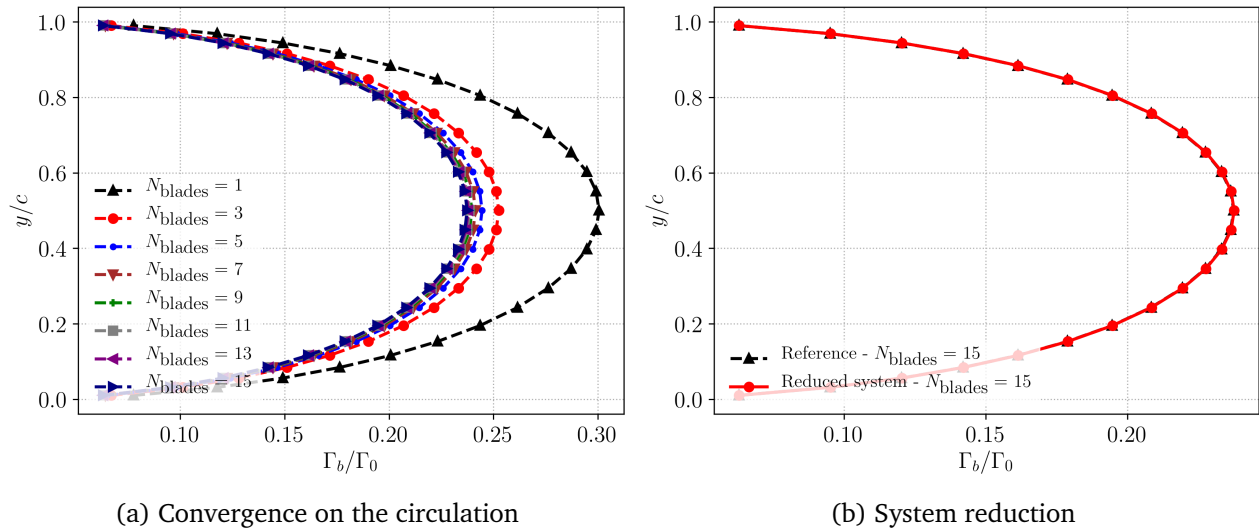


Figure 3.32: Test of the periodicity and the periodicity condition with *PyLiSuite* on case 00.

The same verification is done when a finite gap is considered, on case 11. In Figure 3.33a, the evolution of the circulation distribution depending on the number of blades shows a convergence on blade 0 for $N_{blades} = 13$, slightly more than for case 00. One can notice that the bound circulation overall diminishes with the number of blades. Looking at the blade in the middle, the potential influence of the other blades seems to unload it and redistribute this loading over all the blades. The fit is also very good between the reduced system and the reference in Figure 3.33b.

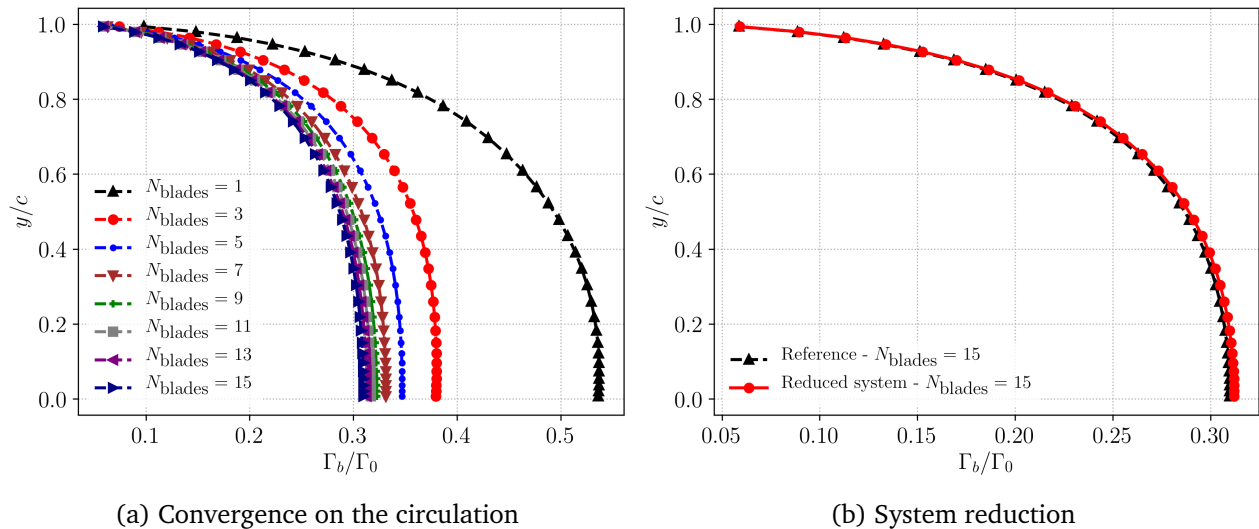


Figure 3.33: Test of the periodicity and the periodicity condition with *PyLiSuite* on case 11.

The good working of the periodicity condition makes the module *PyLiSuite* performance much better. For instance, if for one blade, the solver runs in 10 seconds, with 15 blades,

the solver requires 2.5 minutes to run without the periodicity condition. With the periodicity condition, the CPU time reduces to barely more than 10 seconds with the converged grid.

3.4.6 Compressibility correction

Up to this point, all the validations have been made on the assumption that the flow is incompressible. Keeping the assumption of small disturbances and steady flow, the method can be extended to compressible flows up to where the transonic effects start appearing. Usually, the threshold Mach number for this extension is set at $M_\infty = 0.6$. Below that, the compressibility effects are small enough for the simple correction that is introduced here to be adapted.

Assuming the velocity perturbations are small and the free-stream velocity is oriented stream-wise ($\mathbf{U}_\infty = U_\infty \mathbf{e}_x$), the velocity components can be written as a function of the potential Φ as

$$\begin{aligned} u &= U_\infty + \frac{\partial \Phi}{\partial x} \\ v &= \frac{\partial \Phi}{\partial y} \\ w &= \frac{\partial \Phi}{\partial z} \end{aligned} \quad (3.50)$$

The potential equation can be written

$$(1 - M_\infty^2) \frac{\partial^2 \Phi}{\partial x^2} + \frac{\partial^2 \Phi}{\partial y^2} + \frac{\partial^2 \Phi}{\partial z^2} = 0 \quad (3.51)$$

Equation (3.51) can now be transformed by using the Prandtl-Glauert transformation, introducing the new variables

$$x_M = \frac{x}{\sqrt{1 - M_\infty^2}}, y_M = y, z_M = z, \quad (3.52)$$

to recover the Laplace equation.

From that, the results presented for incompressible flows are applicable to the reduced Laplace equation in compressible conditions. Relations can be derived between the incompressible and the corrected lift and pressure coefficients for two-dimensional cases, by simply applying Prandtl-Glauert's coefficient:

$$\begin{aligned} C_L(M > 0) &= \frac{C_L(M = 0)}{\sqrt{1 - M_\infty^2}}, \\ c_p(M > 0) &= \frac{c_p(M = 0)}{\sqrt{1 - M_\infty^2}}. \end{aligned} \quad (3.53)$$

The case $M = 0$ corresponds to the reference incompressible case where $x_M = x$.

The correction (3.52) has been added to the VLM module *PyLiSuite*: the grid is deformed before the linear system construction according to that rule. The validation presented in Figure

3.34 compares the lift coefficient evolutions for the two airfoils NACA0012 and NACA4412, with the camber and the surface formulations, for $M_\infty = 0.5$ and an aspect ratio $AR = 1000$. The fit between the left-hand side and the right-hand side of equation (3.53) is very good and validates the implementation of the correction in the module for two-dimensional cases.

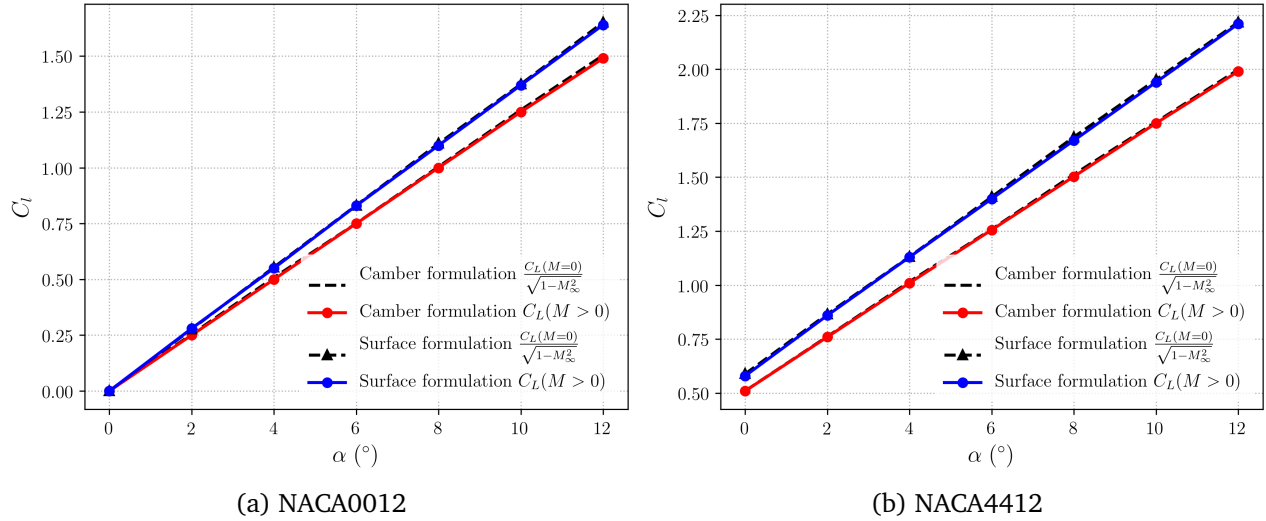


Figure 3.34: Lift coefficient C_L with the Prandtl-Glauert correction, for the two VLM formulations.

For three-dimensional cases, the same transformed geometry can be used (x_M, y_M, z_M) to compute the pressure coefficient c_p with Göthert's rule [55]. The resulting forces and moments can subsequently be calculated. Note that Prandtl-Glauert's correction on the lift coefficient cannot be used as in equation (3.53).

3.5 Summary on the method

This chapter was intended to validate the Vortex Lattice Method developed through the present thesis and apply it to tip-leakage flow configurations. Some criteria have been put forward and the capabilities of the module to be applied to TLF configurations have been assessed. The most important points to be retained for the rest of the study are:

1. The tip gap is accounted for by a symmetry condition, reducing the linear system from dozens of blades to ensure a convergence on the circulation, to one blade. This is done by assuming the circulation is the same over all the fictive blades, spaced with a 2τ gap from one another. The reason of applying this symmetry condition, replicating an infinite number of blades is due to the double endwall influence, with both the casing and the hub to be taken into account. The zero slope of the circulation is obtained at the hub by simulating a blade of span $2b$ ensuring the slope at midspan is zero. This blade is mirrored several times to model the presence of the casing with the fictive blades.

2. The VLM developed runs in less than 20s for a converged grid on the lift coefficient, for all the gap sizes considered (from $0.5\%c$), based on criterion (3.44).
3. The flatness of the wake is crucial and ensured thanks to criterion (3.41), which estimates the maximum wake width-to-span ratio acceptable for the method.
4. A discretization of the casing is possible but requires more computational time than the application of the symmetry condition. This will not be used in the present thesis, but this result is interesting if the method is extended to annular configurations, for which the application of the symmetry condition is no longer relevant.
5. A periodicity condition has been coded and validated, on the same idea as the symmetry condition, applying the same circulation distribution over fictive blades regularly spaced from one another in the pitch direction. This feature is of interest for linear cascade configurations.
6. The VLM module can be applied to low compressible flows with the Prandtl-Glauert correction, validated in this chapter.

Main developments (+)	-
<ul style="list-style-type: none"> - Chordwise discretization - Blade camber effects (compressor blade camber $\sim 1\% c$) - Development to account for casing (symmetry, plate) - Linear periodicity - Low-compressibility effects ($M_\infty < 0.6$) 	<ul style="list-style-type: none"> - Blade thickness - Generalized inflow profiles - Cylindrical geometries - Transonic/supersonic effects

Table 3.1: Main developments (left-hand column) and possible future improvements (right-hand column) of the VLM developed in the present thesis regarding TLF.

Table 3.1 summarizes the main developments of the present VLM and the potential improvements to be envisaged in the future. In any case, such a module is already mature enough to be evaluated on a simplified TLF configuration with a reasonable CPU time. The experimental single-blade TLF configuration is presented in Chapter 5 and the VLM developed here compared to the experimental results, concerning the three TLV characteristics previously introduced in Chapter 1. The extension of the method to simulate a compressor rotor is discussed at the end of Chapter 5, especially considering the items of the right-hand column of Table 3.1.

Part III

INFLUENCE OF THE TIP GAP SIZE ON TIP-LEAKAGE FLOW

ZDES INVESTIGATION OF TIP-LEAKAGE FLOW ON A HIGH-PRESSURE COMPRESSOR

Contents

4.1	Definition of the configuration	114
4.1.1	Experimental setup	114
4.1.2	Computational domain	116
4.1.3	Numerical setup	118
4.1.4	Boundary conditions	119
4.2	Parametric study on the tip clearance size	120
4.2.1	Presentation of the study	120
4.2.2	Performance	121
4.2.3	Radial profiles	122
4.2.4	Tip flow analysis	124
4.2.5	Mean tip-leakage vortex analysis	128
4.2.6	Unsteady analysis	135
4.2.7	The vortex wandering	144
4.3	Conclusions	147

As explained in the previous sections, the understanding of secondary flows requires a better resolution of the flow mechanisms. RANS simulations do not offer a sufficient accuracy to conclude on the behaviour of three-dimensional flows such as tip-leakage flow. Although sensitivity studies found in the literature have enabled great progress, the need for a resolution which depicts the largest turbulent eddies is essential to go further than RANS modelling. In this chapter, the main objective is to understand how the size of the tip clearance affects the flow behaviour around a rotor of a 3.5-stage high-pressure compressor.

This is done on a single rotor, with the ZDES approach, keeping the same boundary conditions between the simulations. Because such simulations are restrained to a single rotor, the complexity of the flow resulting from the different compressor stages cannot be captured accurately. In fact, the objective of the present chapter is to study the sensitivity to the tip gap size on the third rotor with the ZDES resolution. The calibration of the inflow and outflow boundary conditions and the preliminary RANS study are presented in Appendix C.

The first section presents the experimental configuration and the numerical setup. In the second section, the results of the sensitivity study conducted on the tip gap size are presented: three ZDES simulations are performed for three different tip gap sizes. The main features of the TLV are emphasized and compared, such as the detachment of the TLV from the suction side of the rotor blade, its trajectory and its size and intensity. The influence of the tip gap size on the double-leakage phenomenon, introduced in Chapter 1, is also investigated in the unsteady analysis of this chapter.

4.1 Definition of the configuration

The choice of the computational domain for the simulations to be carried out on tip-leakage flow is described in this section.

4.1.1 Experimental setup

4.1.1.1 The research compressor CREATE

The compressor CREATE is a 3.5-stage high-pressure compressor on which several test campaigns have been led over the past fifteen years. The instrumentation of the rig have enabled refined analyses of the flow, very interesting for its similarity to that encountered for an actual compressor of a turbofan. A picture of the rig is displayed in Figure 4.1.

Figure 4.2 shows a meridian view of CREATE, from the Inlet Guide Vane (IGV) to the outlet plane 300. The number of blades per row is specified in Table 4.1. Note that the machine has a $2\pi/16$ (22.5°) circumferential periodicity. This enables to distribute the measurements over this periodicity sector for stable operating points, ensuring that all the spatial information is well captured.

The campaign considered in the present thesis presents a conventional tip gap size on the first rotor and enlarged tip gaps on the two rear rotors, especially on the third ($\tau/c_a > 2.5\%$). Stronger effects due to the enlargement of the tip gap are sought concerning the behaviour of the



Figure 4.1: Picture of the compressor CREATE.

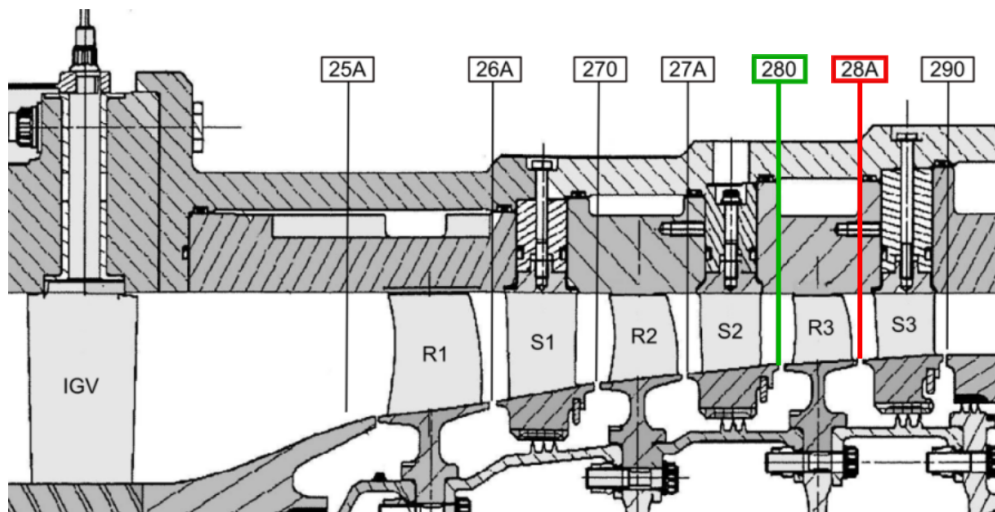


Figure 4.2: Meridian view of CREATE.

Row	IGV	R1	S1	R2	S2	R3	S3
Number of blades	32	64	96	80	112	80	128

Table 4.1: Number of blades per each row of CREATE.

tip-leakage vortex at different operating points. The third rotor is of particular interest for TLF because the strongest aerodynamic phenomena have been observed on this rotor by Courtiade [23]. In particular, the onset of instabilities has been detected on this rotor, even showing a very disturbed flow in the tip region at the peak efficiency operating point. The blockage is already strong in that region, presenting reverse flow zones at some locations near the tip.

Inter-row planes 280 and 28A are emphasized in Figure 4.2, resp. in green and red, as this work focuses on the third rotor of CREATE. The results of our simulations will be compared to the experimental measurements obtained in these two planes, upstream and downstream the third rotor, in section C.2.

4.1.1.2 Available measurements

Several types of measurements have been performed on CREATE, based on different criteria of frequential resolution and non-intrusiveness. Table 4.2 summarizes those used in the present thesis for the comparisons with the simulations performed.

Measurement type	Intrusive	Frequential resolution	Location
Pneumatic probes (P_s, P_t, T_t)	Yes	Steady	Inter-row over the whole span except in the 5% near the walls
Laser Doppler Anemometry (V_x and V_θ)	No	20 kHz	Inter-row between 15 and 98% height and in the tip region of rotor 3 (five axial planes between 73.5 and 98% height)

Table 4.2: Summary on the different types of measurements carried out on CREATE, used in the present thesis.

The steady probes are regularly placed over a 22.5° azimuthal sector for each inter-row plane (280 and 28A in particular). The radial profiles obtained from these measurements on the total values use a pitchwise average weighed by the mass flow rate. For example, on the total pressure, this writes for all the radial position r_j :

$$\bar{P}_t(r_j) = \frac{\sum_{i=1}^{N_\theta} \rho(r_j, \theta_i) V_x(r_j, \theta_i) P_t(r_j, \theta_i)}{\sum_{i=1}^{N_\theta} \rho(r_j, \theta_i) V_x(r_j, \theta_i)}, \quad (4.1)$$

with N_θ the number of probes pitchwise.

A simple pitchwise average is applied on the static pressure.

The data acquisition by the pneumatic probes was only done on operating points sufficiently far from surge. Indeed, near surge, a slight perturbation may easily trigger the instability. With intrusive measurements like the probes, the starting point of the surge would be biased. In any case, the present study only focuses on TLF on the nominal operating point. At this operating point, the experiments of Courtiade [23] put in evidence intense aerodynamic phenomena in the tip region. Due to the presence of a strong TLV, the blockage is important and the tip region even presents zones of reversed flow.

The laser measurement technique (LDA) allows measuring two components of the velocity (axial and tangential) in the inter-row planes and in several planes perpendicular to the axial direction along the chord of rotor 3.

The velocities are normalized by the tip velocity $U_{tip} = r_{tip}\omega$.

Details on the measurement techniques and their complete distribution over the compressor are given in Courtiade's thesis [23].

4.1.2 Computational domain

For the purpose of a reasonable number of elements for the parametric study to be carried out on the tip gap size, the choice of the computational domain is crucial. The objective is to keep a

4.1. DEFINITION OF THE CONFIGURATION

grid sufficiently refined to capture the structures of the TLV in the tip region while maintaining a reasonable CPU time for the simulations.

The ZDES simulations of Riéra [113] were performed over two passages of the first rotor of CREATE, each passage being meshed with 44 million elements. Two passages of the rotor (64 blades) were necessary to account for the passing wakes of the IGV upstream (32 blades). The region upstream of the row was simulated with the Spalart-Allmaras RANS model, the rest of the domain with the second mode of ZDES. As mentioned in the literature review, the study permitted to validate the ZDES approach on the compressor rotor at peak efficiency and near surge.

The present work is a follow-up to Riéra's thesis and aims at investigating the influence of the tip gap size on the TLF topology and dynamics in the tip region of the third rotor, where the stronger aerodynamic phenomena were experimentally observed. To make sure that the number of elements does not exceed 100 million, the computational domain is restricted to one passage of the third rotor, with an elongated domain upstream and downstream. The passing wakes are not considered in the present study and a steady boundary condition at the inlet is set for the simulations. This is further detailed in sections 4.1.4 and C.1.

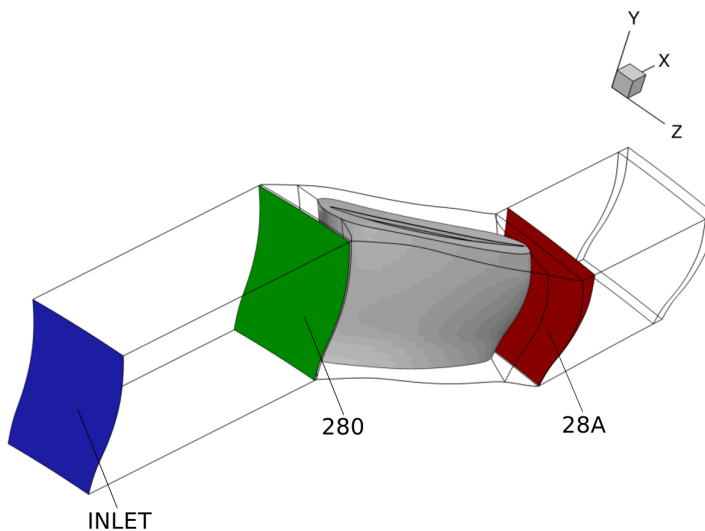


Figure 4.3: Screenshot of the computational domain used for the study. The inlet plane and two planes of reference (280 and 28A) from the experiment are indicated.

Figure 4.3 shows the computational domain chosen in the study. The domain is elongated upstream to avoid forcing the behaviour of the flow around the row if the inflow is placed too close to the row. This requires the calibration of the boundary conditions, especially for a rotor located at the rear of the compressor. That is explained in details in section C.2. The domain is also extended downstream to avoid any numerical reflection at the outlet. The inlet boundary

condition is located $1.5c_a$ upstream of plane 280 and the outlet is placed $1.5c_a$ downstream of plane 28A.

4.1.3 Numerical setup

Given the good compromise achieved by hybrid resolutions, the parametric study on the tip gap size presented in section 4.2 is carried out with ZDES. The second mode is applied on the whole computational domain for an overall number of elements of 100 million.

Figure 4.4 illustrates the idea of using the zonal approach on the compressor rotor. Three main zones are materialized in the figure: the URANS zone in the casing boundary layer, the grey zone, transitional region where the turbulent viscosity levels decrease down to SGS levels ($\mu_t/\mu \sim 1$) while the resolved eddies are formed, and finally the LES region where the largest structures of turbulence are resolved. In the sketch, the boundary layer does not completely immerse the tip gap but this is not general. On the third rotor of CREATE in particular, the casing boundary layer has thickened (about 30 % height upstream of rotor 3 [23]) after passing through the upstream stages and completely immerses the gap. Besides, the boundary layer on the blade skin is not represented in this view but is also treated with URANS.

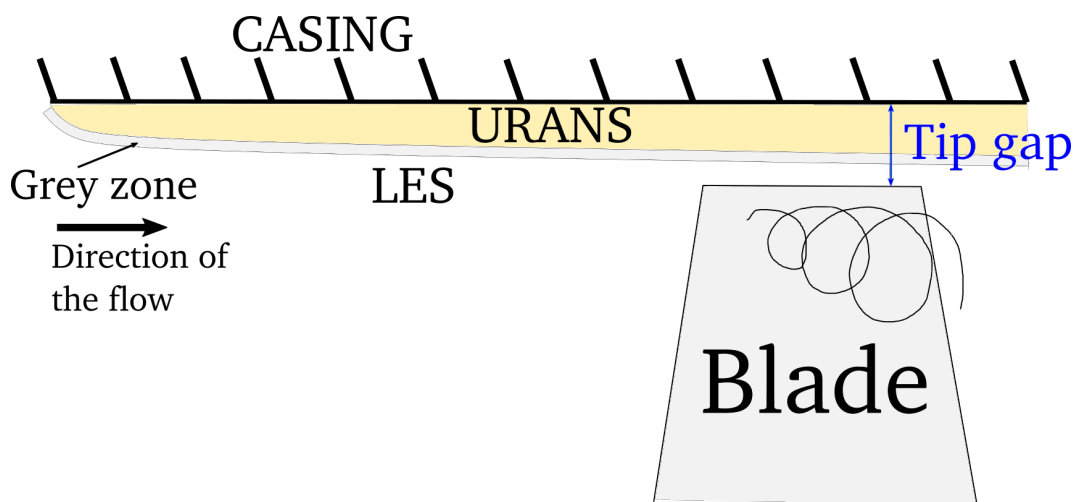


Figure 4.4: Explanation of the use of the second mode of ZDES applied on a compressor rotor.

The numerical simulations have been performed with *elsA*, a software developed by ONERA and co-owned by Safran and Airbus [16]. The Navier-Stokes equations are solved on multi-block structured grids with a cell-centered finite volume approach. The RANS simulations use a Jameson scheme for the inviscid fluxes. In order to reduce the artificial dissipation in the ZDES simulations, the AUSM+P scheme [117] is used for the inviscid fluxes. The viscous fluxes are discretized with a second-order centered formulation. The time discretization relies on the second-order Gear scheme [52] [53] with 15 subiterations, to ensure a decrease of more than one order of magnitude on the residuals for each physical time step, which is set to $\Delta t = 0.7 \mu s$. This represents about 100 iterations per blade passing period T_{bp} , meaning a complete revolution is achieved within 8000 iterations. The unsteady fields are time-averaged over 20 blade

N_{blades}	80
Revolution speed ω	11543 <i>rpm</i>
Blade passing period T_{bp}	65 μs
Advection time T_{adv}	$\sim T_{bp}$
Time step Δt	0.7 μs
Number of iterations per revolution	~ 8000

Table 4.3: Summary of the main numerical parameters for the ZDES simulations on the third rotor of CREATE.

passaging periods, also representing about 20 advection periods $T_{adv} = c_a/U_{tip}$ (calculated on the axial chord c_a and the tip speed $U_{tip} = r_{tip} \omega$), for a sufficient convergence of the first and second order statistics of the conservative variables. The parameters are summarized in Table 4.3 for more clarity.

4.1.4 Boundary conditions

The choice of the boundary conditions is crucial to correctly replicate the flow conditions corresponding to the right operating point on the rotor. It is all the more complex when it applies to the third rotor of the compressor, where the flow has already undergone a lot: the boundary layer has a long history and is thick, the flow is sheared and the rotor-stator interactions from the other stages can hardly be accounted for through a steady boundary condition.

For sake of simplicity, because the aim is to focus on the tip gap influence, time-averaged and steady boundary conditions at the inlet and the outlet are used in the study. As it is explained in the preliminary study of section C.1, these boundary conditions are extracted from a three-stage RANS-SA simulation calibrated on the experimental peak efficiency operating point.

Inlet boundary conditions The boundary condition at the inlet is based on the injection of the following five values in the absolute frame of reference: total pressure, total temperature, pitchwise fluid angle α , meridian fluid angle φ , and turbulent value $\tilde{\nu}$ of the SA model. With the software used, they are correspondingly imposed with the total pressure and the total enthalpy, and the direction of the velocity is given in the boundary condition as three components of a unit vector. Additionally, the turbulent variable $\tilde{\nu}$ is also imposed.

Outlet boundary condition Static pressure is imposed on the outlet with a radial equilibrium condition. The radial equilibrium is based on two main assumptions: (i) the radial component of the velocity is zero and (ii) the flow is axisymmetric. The idea of the radial equilibrium on axial compressors is to consider that if there is a radial flow, it may only occur within a blade row [126]. The flow outside the row thus is in a radial equilibrium state and follows the simplified radial equilibrium equation

$$\frac{\partial p}{\partial r} = \rho \frac{V_\theta^2}{r} \quad (4.2)$$

In the simulation, a pivot pressure p_{pivot} is set at a pivot radius r_{pivot} and the static pressure variation along the span is recovered by integrating equation (4.2) at every spanwise position. Thanks to the axisymmetry, the pressure distribution over the outlet plane can be inferred.

Other boundary conditions An adiabatic no-slip condition is applied to the casing wall and the blade skin. A slip condition is applied on the hub wall upstream of plane 280, and the same adiabatic no-slip condition is applied downstream from that position to the outlet. This was chosen so as to avoid an important corner separation at the hub. Indeed, between the inlet plane and plane 280, the no-slip condition would thicken the hub boundary layer, developing the corner separation, and limiting the stability of the simulation.

A periodicity condition is imposed on the sides of the domain.

4.2 Parametric study on the tip clearance size

The analysis of the results on CREATE A with RANS and ZDES confirmed the benefits of the hybrid approach already shown in the literature. The differences have been analyzed through a steady analysis, with a time-averaged ZDES field. The objective of the study remains to tackle the topic of the tip gap size itself. This section is intended to go through the results given by three simulations on the same row, with the same boundary conditions, only modifying the tip clearance size. A mean flow analysis is first carried out, based on a time average of the flow over $20T_{bp}$ as explained in section 4.1.3. Second, the analysis concerns the unsteadiness of TLF.

4.2.1 Presentation of the study

The motivation of this study concerns the effects of the tip clearance size on a representative high-pressure compressor. Given the value of the clearance on the third rotor ($> 2.5\% c_a$), according to the study of Courtiade [23], the structures are strong and energetic, even at nominal point. Two other gaps are investigated in the present thesis to lead a parametric study on the tip gap size, with the benefits of a higher resolution given by the second mode of ZDES. The values of the gaps are summarized in Table 4.4, normalized by the larger tip gap size. CREATE A is the configuration studied in the previous section, based on the experiments of Courtiade. Different versions of CREATE were tested to investigate different technological effects on the flow aerodynamics. The tip gap value for CREATE B corresponds to an older version of CREATE A, with lower tip gaps on rotors 2 and 3. The experimental measurements from CREATE B are not used in the present thesis. This case is fully numerical and compared to the simulations and experiments on CREATE A. Finally, the tip gap size for the third case, that we call CREATE C in the present work, has been chosen to be lower than $1\% c_a$. The possible occurrence of a casing corner separation, as observed by Hewkin-Smith *et al.* [62] and described in Chapter 1, is also sought with such a choice.

	CREATE A	CREATE B	CREATE C
Normalized tip gap	1	0.77	0.27
Number of elements in the clearance	49	49	33
Wall element size	$1 \mu m$	$1 \mu m$	$1 \mu m$
Grid expansion ratio	1.15	1.13	1.17

Table 4.4: Tip gap values normalized by the largest gap value, for the parametric study.

The numerical simulations all use the same boundary conditions, as described in section C.1.1, at the inlet and the outlet. On the walls, an adiabatic no-slip condition is applied and a periodicity condition is used on the sides of the computational domain. In the tip clearance, the grid resolution is the same streamwise and pitchwise for the three cases, following the ZDES grid requirements. Spanwise, the modification of the gap value induces a modification of the grid, summarized in Table 4.4 with the main parameters of the grid within the clearance.

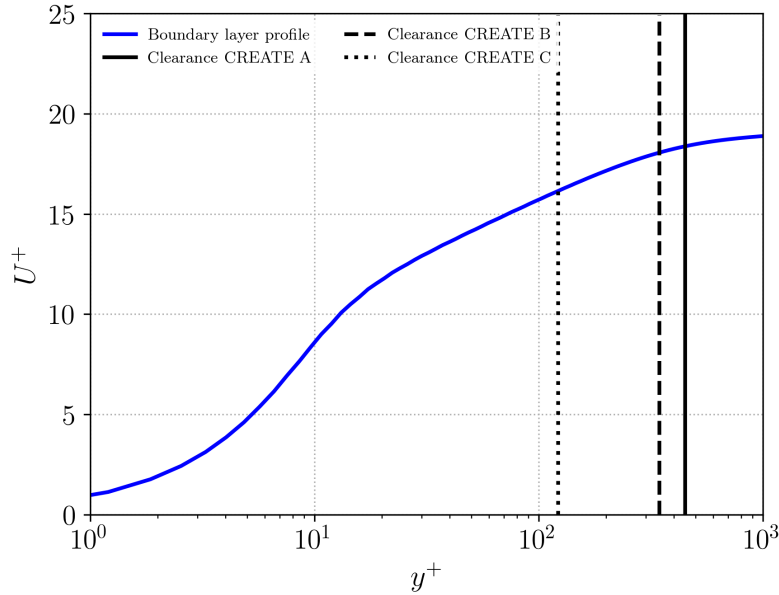


Figure 4.5: Boundary layer profile at casing in plane 280, upstream the rotor.

Figure 4.5 shows the boundary layer profile at casing in plane 280, identical for the three tip gap sizes at this position. As indicated in the figure, the three tip gap sizes are immersed by the boundary layer and located in the logarithmic layer, between $y^+ = 100$ for the small gap and $y^+ = 500$ for the large one.

4.2.2 Performance

The first investigations are related to the performance of the single rotor for the three different gaps. How does reducing the tip gap size affect the time-averaged mass flow rate, the compression ratio and the efficiency?

	CREATE A	CREATE B	CREATE C
Mass flow rate	1.10	1.11	1.13
Compression ratio	0.978	0.979	0.977
Isentropic efficiency	1.067	1.074	1.083

Table 4.5: Performance recap for the three different gaps of the study, normalized by the values of the nominal operating point from the experiment on CREATE A.

Table 4.5 summarizes the performance obtained with the three gaps. The mass flow increases when the tip gap is decreased, keeping the boundary conditions identical between the three cases. We will see in the next sections that it is consistent with the fact that the TLF is less intense with smaller gaps and thus induces less losses. On the contrary, with the larger gap, the presence of the strong vortex generates much more vorticity, which increases the blockage in the passage and reduces the mass flow rate (see section 4.2.3). The overall compression ratio slightly rises with the tip gap increase. We will see in the next section that there are differences on the compression ratio profile near casing but the difference is hardly observable with the only value of the overall compression ratio. Finally, the smaller gap shows a better efficiency, which decreases with the gap size increase.

4.2.3 Radial profiles

The first analyses can be done on the radial profiles, which give a good overview of how the tip gap size influences the pitch- and time-averaged flow. The gap sizes are given with respect to that of CREATE A, set to 1 and designating the largest gap. Figure 4.6 shows the stagnation pressure and temperature ratios radial profiles for the three gaps compared with the pneumatic measurements on CREATE A. The largest gap induces the largest total pressure deficit in the tip region. With the smaller gap, the compression ratio achieved by the blade in the last 10% height near casing is greater than for the two other gaps. The influence of the gap size on the compression ratio spans down to about 60% height while the rest, down to the blade root, is unaffected. Between 70 and 85% height however, the intermediate tip clearance yields a better compression ratio than the two other sizes, with a maximum of 4% rise around 80% height. Looking at the stagnation temperature ratio, the profiles are almost the same between CREATE A and B up to 90%, with a maximal relative difference less than 0.5%. This indicates a comparable work in both cases up to 90% height. In the last 10%, case A is more loaded than the others. The mass flow rate increase with the decrease of the gap in Table 4.5 also illustrates this behaviour: the boundary conditions being the same for the three cases, the TLF is less intense for the smaller gap and the incidence angle at the tip subsequently lower. Hence, the blade loading is lower for the small gap.

Finally, the slope discontinuity already mentioned on CREATE A is encountered again in cases B and C at the same position, around 65% height. Again, this change in slope is due to the RANS to LES switch occurring at this position. Indeed, the inlet conditions used for the three simulations are the same and the incoming boundary layer at casing is therefore similar

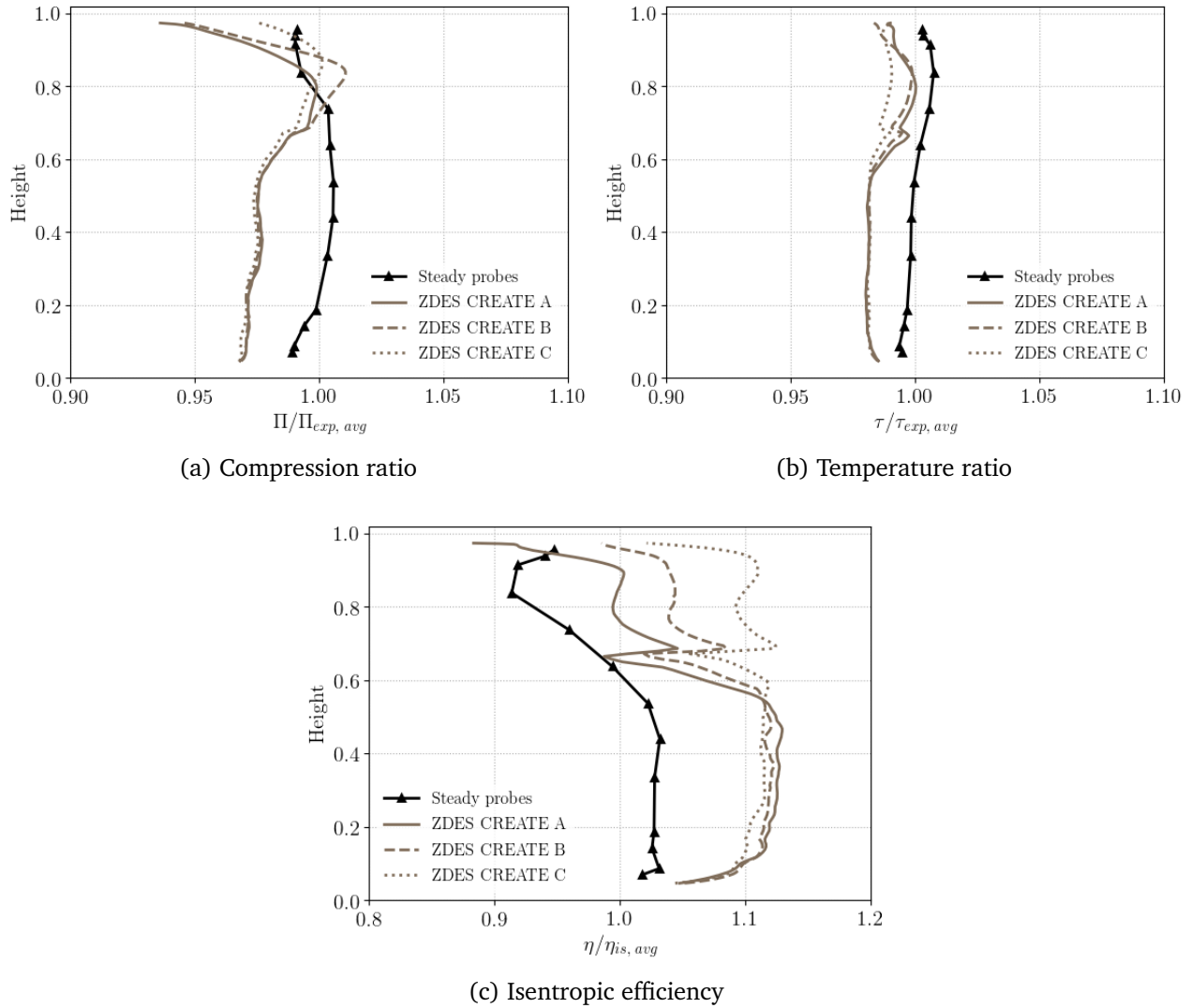


Figure 4.6: Compression and temperature ratio distributions between planes 28A and 280.

for the three configurations. Figure 4.6 c shows the radial profile of the isentropic efficiency for the three gaps. The slope discontinuity already seen in the temperature ratio profile is here emphasized around 70% height for the three gaps. The figure is interesting to observe the performance evolution with the tip gap size. The smaller gap yields a better efficiency in the tip region, from 70% height to casing, by nearly 10% compared to the larger gap. The region is treated partly by RANS and LES, as shown in section C.2.3. For lower heights, the efficiency for the three gaps is comparable, confirming the major influence of the tip gap size in the tip region.

Plane 280 Figure 4.7 shows the axial velocity and relative fluid angle profiles in plane 280, comparing the three gap sizes and the laser measurements on CREATE A. It is recalled that the absolute conditions are kept constant in the three cases. From Figure 1.3, if the absolute fluid angle α is kept constant, increasing V_x yields a decrease for $|\beta|$, absolute value of the relative

fluid angle.

The difference in the incidence between the smaller and larger gaps is about 1° near the tip due to the different adaptation of the flow to the row with the modified clearance. This has a direct impact on the axial velocity profiles, which are shifted to the left when increasing the gap, all the more in the last 20% height. The gradients, both for the velocity and the fluid angle, are the same for the three gaps. This indicates a relative homogeneous redistribution of the flow spanwise with the modified tip clearances compared to CREATE A, which has been investigated against experimental measurements in the previous section.

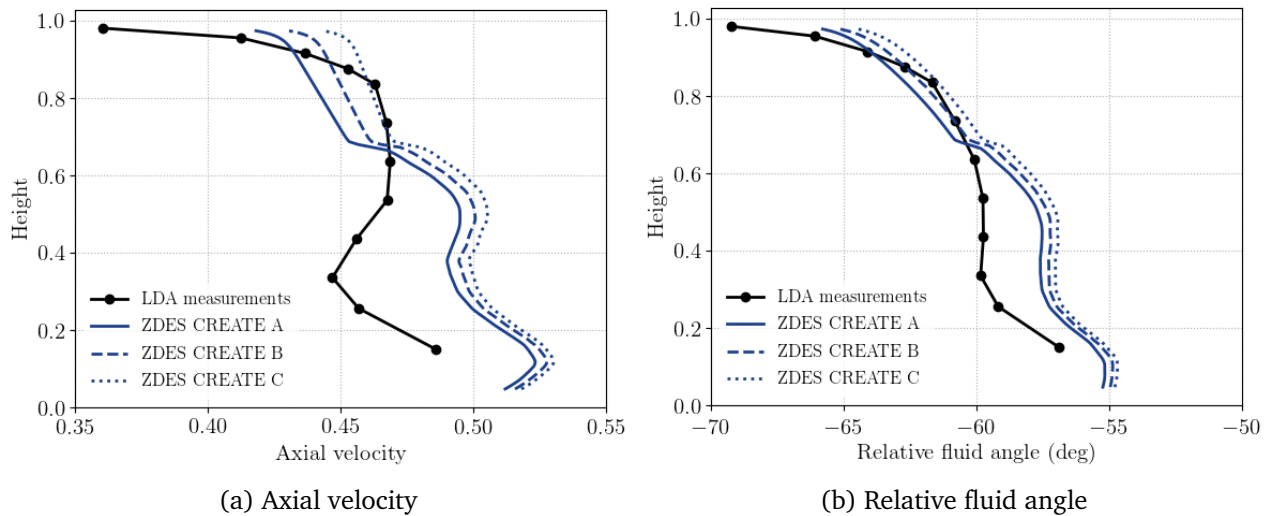


Figure 4.7: Radial distributions of normalized axial velocity and relative fluid angle β in plane 280.

Plane 28A Let us now have a look at how the radial profiles are affected by the clearance modification downstream of the row, in plane 28A, showed in Figure 4.8. For decreasing gap values, the axial velocity is larger in the last 20% height, corresponding to a lower blockage in the tip region. In comparison, at 90% height, the axial velocity for CREATE C is more than 20% greater than for CREATE A. The relative fluid angle is the same from root to 60% height. In the tip region, case C shows a better deviation with a lower value of the outlet relative fluid angle, which is certainly caused by the lower intensity of the TLV.

4.2.4 Tip flow analysis

4.2.4.1 Numerical resolution

The resolution of the field is illustrated in Figure 4.9 with the isolines of f_d and the contours of the eddy-to-molecular viscosity. Comparing figures 4.9 and 4.19, the LES regions correspond to the TLV locations in the different planes. The contours of the eddy viscosity are coherent with the isolines of f_d , since the eddy viscosity rapidly decays in the LES regions confined by

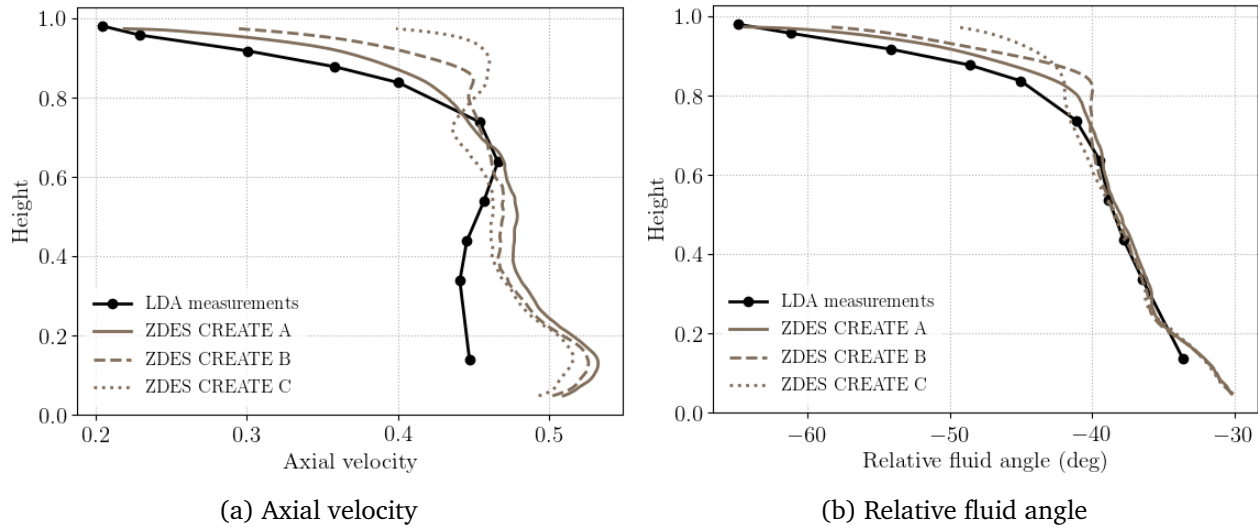


Figure 4.8: Radial distributions of normalized axial velocity and relative fluid angle β in plane 28A.

the dashed lines in the figure, corresponding to the destruction of the pseudo viscosity $\tilde{\nu}$ in the turbulence equation. For the larger gap, its extension is larger and the LES region is wider near the tip of the blade, pitchwise and spanwise. In comparison, for case *C*, the LES region is restricted to a small region related to the small value of the clearance. Generally, the core radius and the vorticity of the TLV decrease with the tip gap size. Also, the contours of the eddy viscosity are more developed in the passages than for the two other clearances (cases *A* and *B*), showing a wider RANS region. Finally, one can notice that upstream of the row, the tip region is completely modelled by RANS, due to the very thick casing boundary layer that could be seen in the radial profiles previously.

4.2.4.2 Topology of the flow

The tip flow structures are visible in Figure 4.10 for the three gaps. For all cases, the presence of the TLV and the induced vortex is observable. As explained in section 1.2.2, the interaction of the TLV with the boundary layer generates another vortex with an opposite sense of rotation or helicity. Downstream, the TLV is supplied by a vortex sheet all along the chord, more and more energetic with the increasing value of the gap. Although most of the TLV intensity seems to be gained in the first 50% chord, the leakage flow continues affecting its development down to the trailing edge. The small eddies resolved by LES can be observed in the three cases, but more clearly for the larger gap. More interestingly, it seems that the bigger TLV obtained with the bigger gap undergoes a vortex fragmentation around 40% chord, where the TLV structure suddenly divides into small structures. The fragmentation is indicated by the white cross in the figure. In the two latter cases, the TLV keeps its shape all along its trajectory in the passage. A strong unsteadiness of the vortex can be the cause of such a fragmentation and will be regarded in the next sections. As for the induced vortex trajectory, it looks different in the smaller gap case

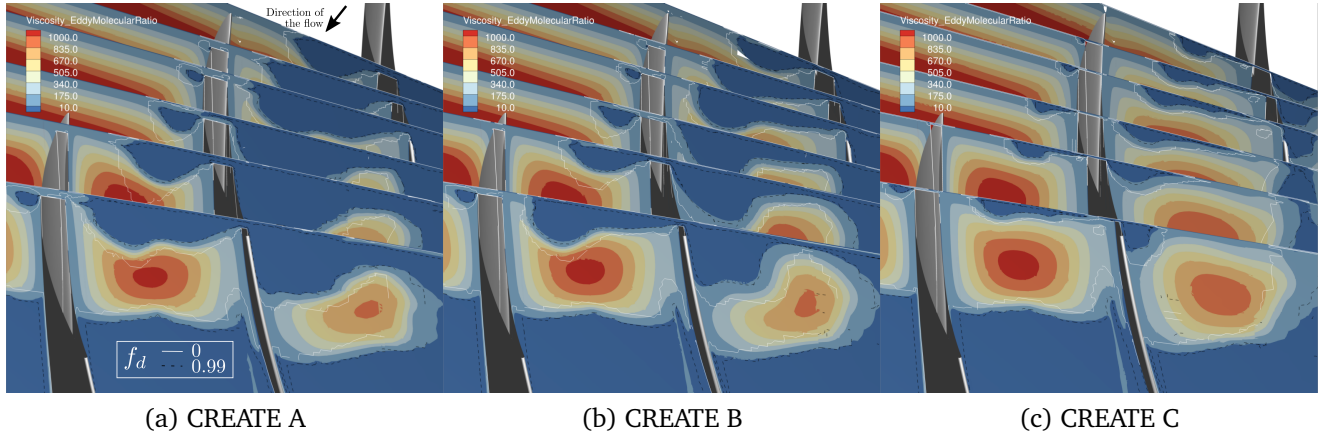


Figure 4.9: Eddy-to-molecular viscosity ratio contours for the three tip gap sizes. Isolines represent the two values of the sensor f_d indicated in the legend. A LES resolution corresponds to $f_d = 1$ and a RANS resolution to $f_d = 0$. The locations of the cutting planes are the same as in Figure C.19.

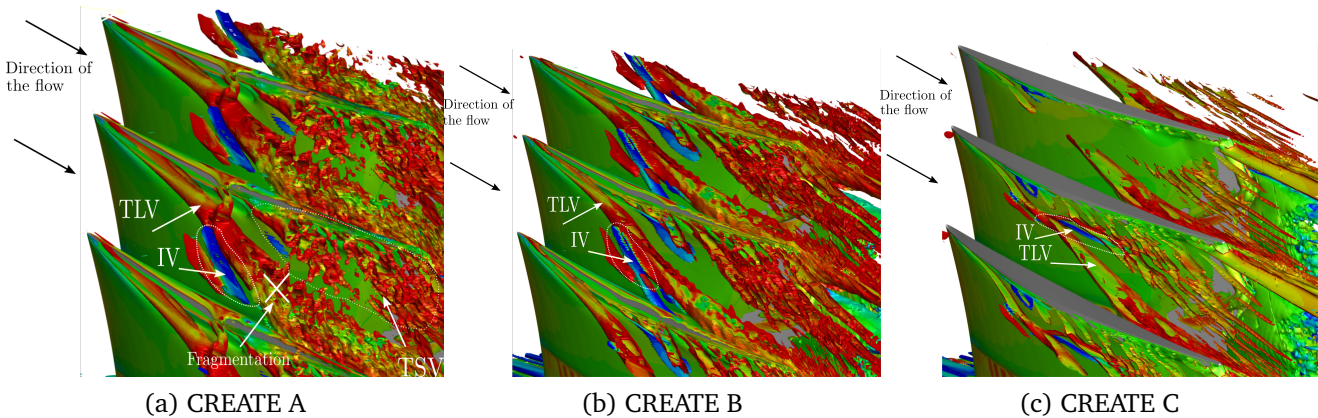


Figure 4.10: Isosurfaces of Q-criterion colored by normalized helicity from -1 (blue) to 1 (red).

where the vortex turns rapidly towards the suction side and deviates from the TLV trajectory, whereas for the two larger gaps, they follow a similar trajectory.

4.2.4.3 Loss analysis

The comparison of the entropy distribution in the passage for different heights is interesting to visualize the actual losses due to the TLV trajectory and growth. Two blade-to-blade plots are here shown in Figures 4.11 and 4.12, respectively at 94% and 97% height, with the same scale for the six subfigures. Two heights are plotted since the spanwise extension of the TLV is different between the three cases.

For example, the TLV track is not visible for case *C* in the first 50% axial chord at 94% height. That is because the position looked at corresponds to a position underneath the TLV core. The losses are much more important for case *A* at 94% height, indicating a larger extension of the

TLV spanwise than for the two other gaps. The losses are significantly greater in that case and decrease with the gap value at that height. Regarding the pitchwise extension, considering the intense losses are coloured in red, the blockage due to the TLV is massive for case A. More concentrated in case B at this height, the losses are essentially larger than for the smaller gap, especially in the portion between midchord and 75% chord.

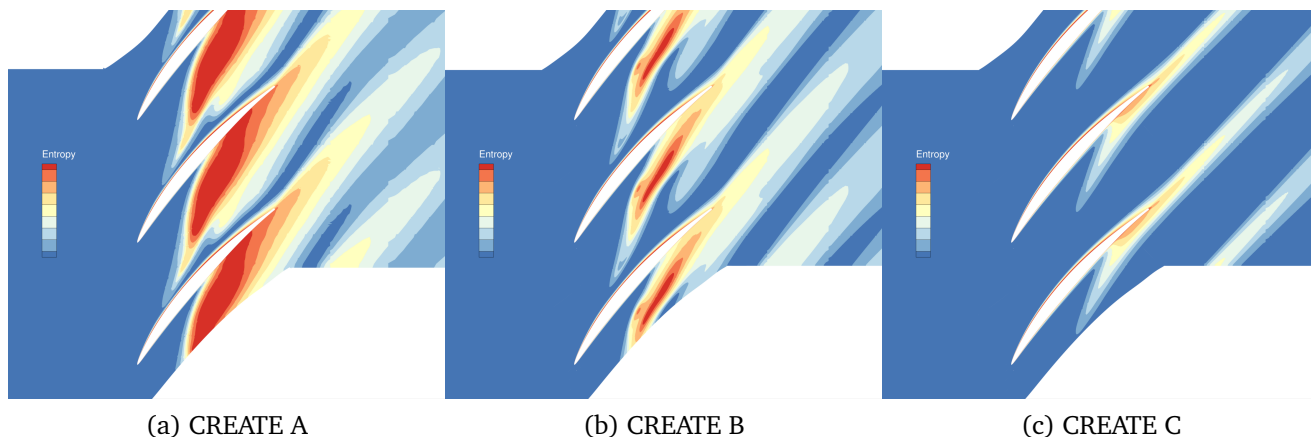


Figure 4.11: Entropy contours at 94% height for the three different gaps.

Closer to casing, at 97% height, the losses are spread over the whole passage from midchord to the trailing edge with CREATE A. In the core of the vortex, the entropy variations are more important for case C than case B but they are much more concentrated and localized. In case B, the maximum value in the TLV is lower than in case C, but the pitchwise extension of the yellow to orange entropy intensities spread over the whole passage.

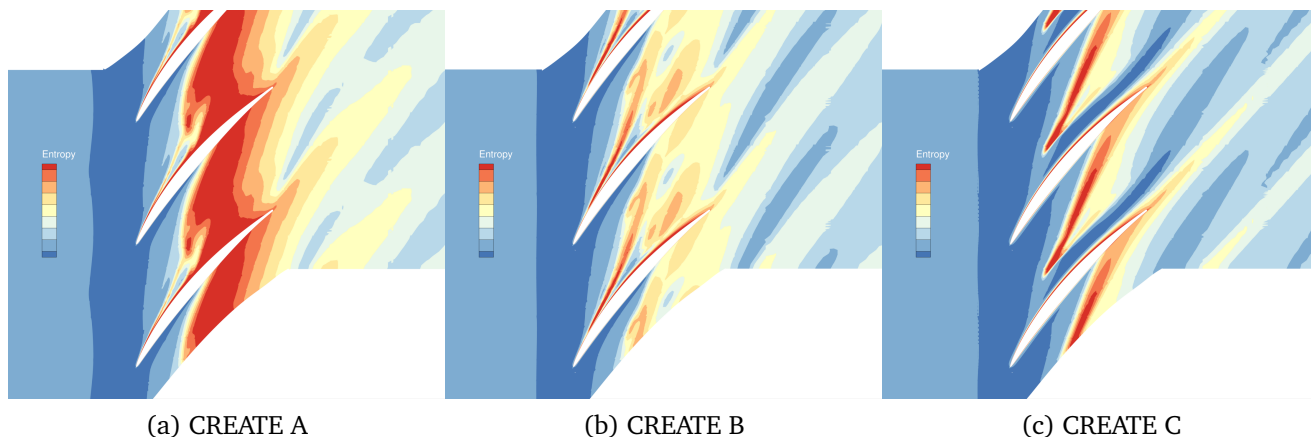


Figure 4.12: Entropy contours at 97% height for the three different gaps.

4.2.5 Mean tip-leakage vortex analysis

Three main features of the TLV are analyzed through this section: where it detaches from the suction side of the blade, its trajectory and the evolution of its circulation streamwise for the three tip gaps considered in the study. These are fundamental features of the TLV whose variations can have a massive impact on the performance of the rotor, as reviewed in Chapter 1.

4.2.5.1 Detachment of the TLV

As seen in the literature review, the point of detachment of the TLV is a crucial input for some models relying on the TLV evolution through the passage. Physically, following the separation, the losses surge due to the development of the vortex all along its trajectory. For example, applying a diffusion model on the circulation to replicate the evolution of the TLV in the passage requires the position of the detachment point. In the literature, most authors found that the maximum pressure difference at the tip corresponds to where the TLV usually detaches, with a velocity on the suction side also maximal. The leakage mass flow rate is the highest at this point and the adverse pressure gradient leads to the separation of the vortex. Here, the results with the three gaps are analyzed regarding this criterion. Do they follow the same behaviour and if not, which simplifications are made?

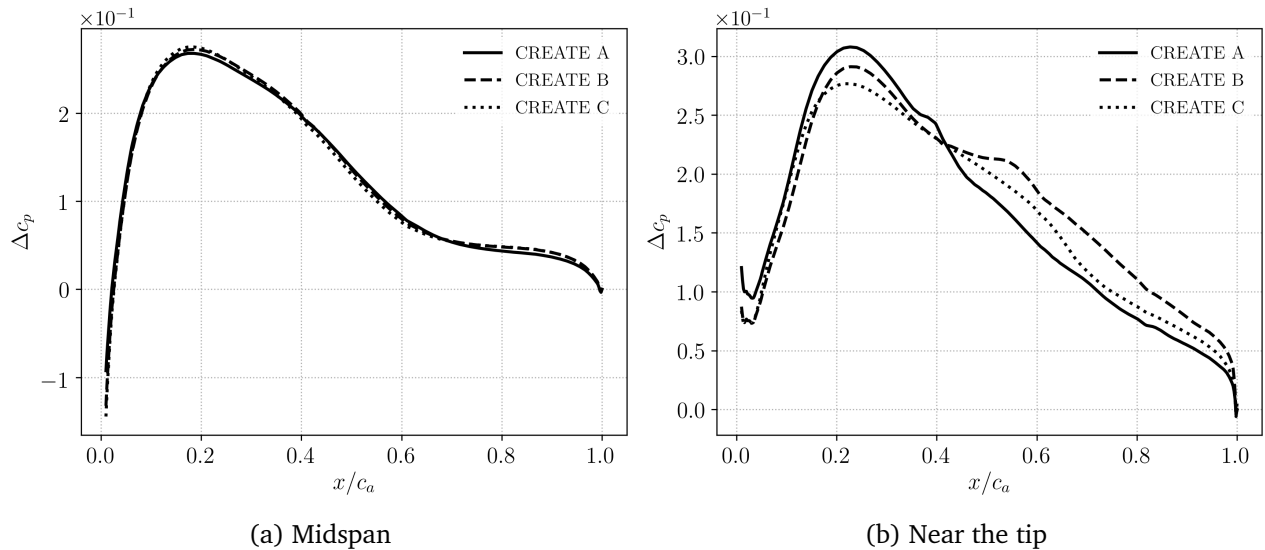


Figure 4.13: Pressure difference coefficient at midspan and at the tip (99% blade span).

Figure 4.13 shows the pressure difference coefficient Δc_p at midspan and at the tip. The reference pressure for normalizing the static pressure difference is the mass-averaged total pressure P_{ref} in plane 280. The pressure difference coefficient is shown at 50% span and 99% span, near the tip. Far from the tip, at midspan, the pressure difference can be considered the same for the three gaps, which remains coherent with the figures showing vorticity and the influence of the TLV down to 90% span. Near the tip, the profiles differ from one another depending on the tip gap. The largest gap corresponds to the largest pressure difference up to 40% chord. With

exactly the same incidence near the tip for the three gaps, it could be expected that the order be inverted. Indeed, the larger TLV is shed for the larger gap, which corresponds to a bigger unloading of the blade in the tip region. However, Figure 4.8 showed that with the boundary conditions used, the incidence was reduced for decreasing values of the clearance, which results in the unloading of the blade for the smaller gap. More downstream however, the pressure difference of case A becomes lower than for the two other gaps, case B being the most intense. The intensity of the TLV for the larger gap could explain this behaviour: the blade is unloaded more abruptly than for cases B and C. Regarding the maximum pressure difference, the position is relatively the same for the three cases, at 22% axial chord for cases A and B and slightly closer to the leading edge for case C, at 20% axial chord.

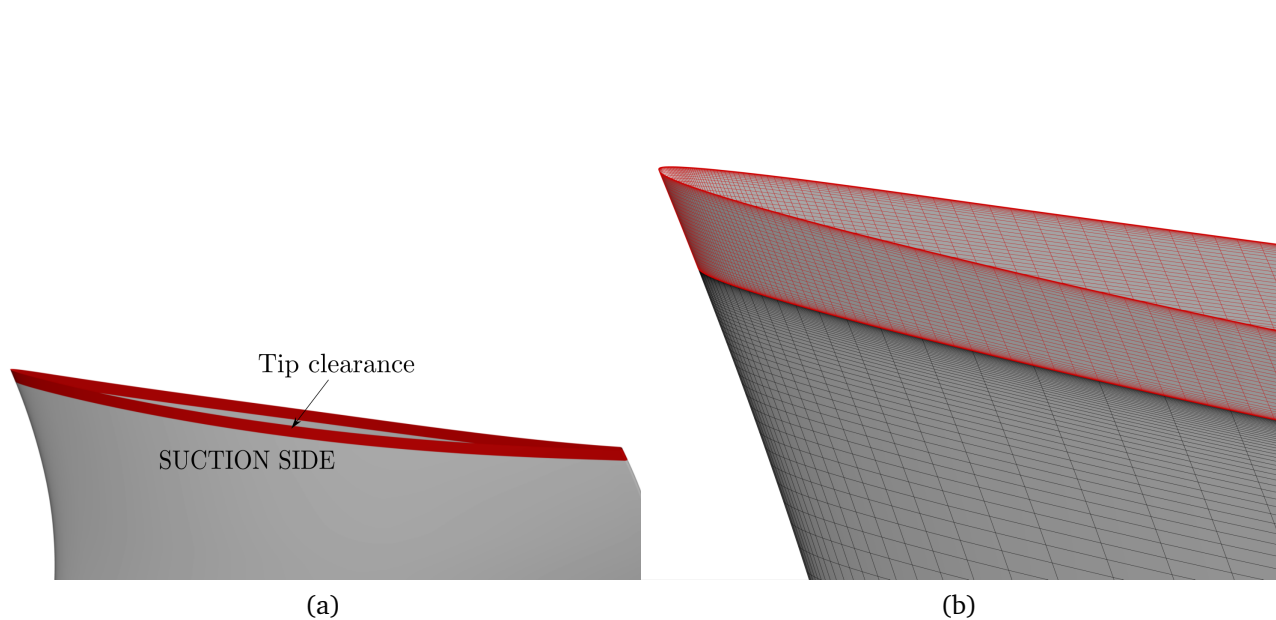


Figure 4.14: (a) Screenshot of the blade and clearance for CREATE A (clearance in red). (b) Zoom in the clearance near the leading edge on the suction side of the blade.

The chordwise evolution of the tangential component of the relative velocity is averaged over the whole span of the clearance, yielding the leakage velocity. The velocity profiles have been extracted on every line of the grid in the clearance and averaged afterwards. Spatially, the average is done in the continuation of the suction side over the red zone indicated in Figure 4.14. The velocity is negative by convention since the velocity is opposed to the rotation of the rotor. The resulting profiles are shown in Figure 4.15. It compares the axial evolution of these profiles depending on the tip gap size. Coherently with the pressure difference near the tip, the leakage velocity is the largest around 22% axial chord, at the same position as the maximal pressure difference. For the smaller gap, that position is shifted upstream, around 15% axial chord in our case. The influence of the viscosity in the leakage flow may be of importance since the gap is much smaller. Generally, the leakage velocity level is lower for the smaller gap, consistently with the pressure difference. The positions of the maxima are indicated by red squares.

A slope break can be observed downstream in cases A and B, indicated by the green dots.

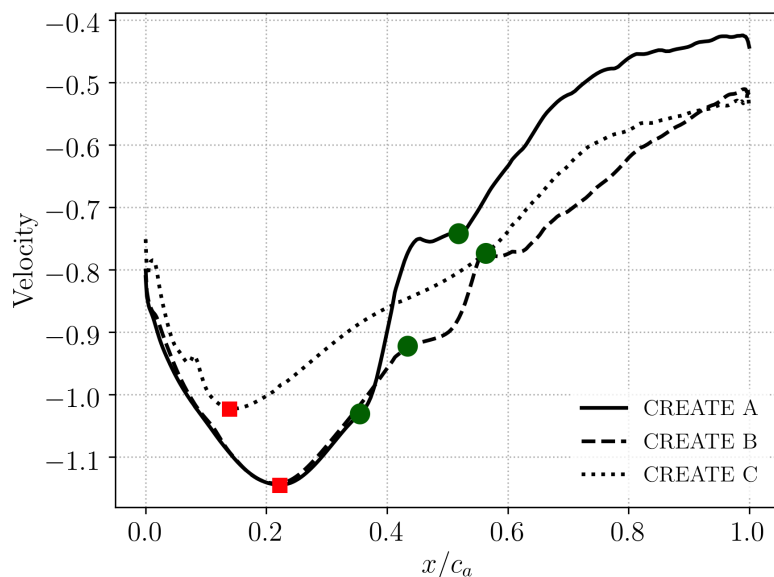


Figure 4.15: Normalized leakage velocity profiles in the clearance of each case, in the prolongation of the suction side of the blade. The red squares indicate the respective position of the maximal magnitude of leakage velocity. The green dots indicate the positions of the slope breaks for CREATE A and B.

The slope first breaks with a sudden diminution of the leakage velocity, before recovering the slope from near the leading edge. This is discussed in section 4.2.6.3.

Figure 4.16 shows the streamlines in the rotor frame of reference for the three cases, along with the contours of static pressure over the suction side of the blade in the tip region. A convergence of the streamlines is observed in the three cases. Two regions, upstream and downstream the convergence point indicated in the figure, are distinguished for the three cases:

1. Upstream the convergence point, the streamlines are deformed near the tip due to the presence of the TLV forming and strengthening before detaching.
2. Downstream the convergence point, they are deformed as well over a lower area near the tip. This time, the flow topology shown in the Q-criterion explains this deformation by the TSV observed all along the chord after the detachment of the TLV. Separation at the tip is clearly shown by the backflow streamlines.

In the middle, the convergence point of the streamlines corresponds to where the TLV detaches and can be directly related to the maximal leakage velocity described in Figure 4.15 in the clearance. For the three gaps, the positions of the maximal transverse velocity and the convergence point fit quite well.

Regarding the differences between the three cases, the deformation region upstream the convergence point is less marked for the smaller gap, illustrating the lower intensity of the TLV for this case. The same applies to the TSV downstream, whose influence on suction side is only observed up to 40% c_a for case C. For the two larger gaps, the topology is quite similar on the suction side of the blade.

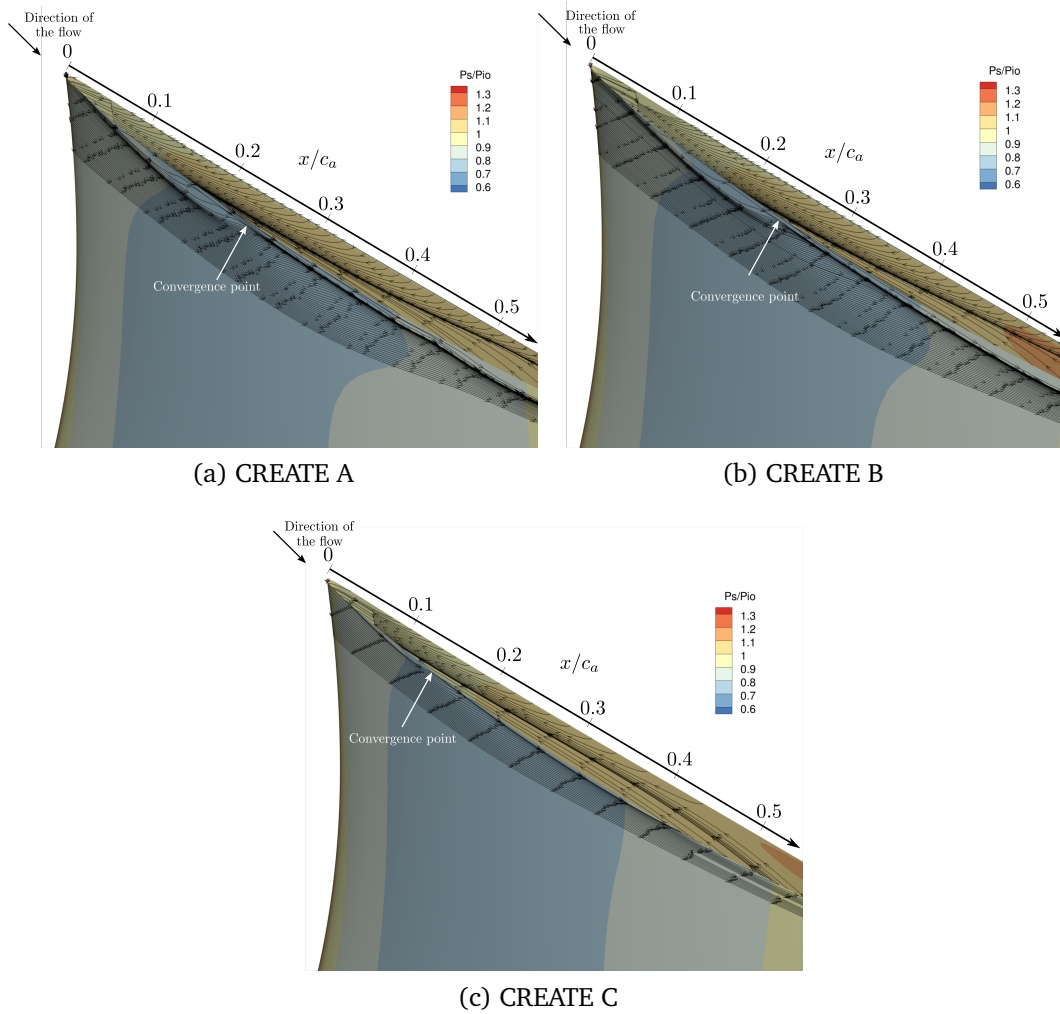


Figure 4.16: View on the suction side and tip of the blade. Time averaged streamlines at the tip of the blade and contours of the normalized static pressure on the blade skin.

4.2.5.2 Trajectory of the TLV

The TLV trajectory is one of the major features of TLF. As seen in the literature review, the pitchwise position of the TLV in the passage is strongly related to the loading of the blade. In particular, a more loaded blade induces a TLV trajectory getting farther from the suction side and closer to the leading edge of the neighbouring blade. Here, the tip gap size is varied and the impact on the TLV trajectory is investigated. The correlation developed by Chen in his thesis is compared to the results obtained with the simulations.

The estimate of the TLV angle is done graphically from density contours plotted at two constant relative heights. The core of the vortex is followed in Figures 4.17 and 4.18 through the minima of the density, which roughly give the trajectory of the TLV. The angle ε between the straight line, approximating the TLV trajectory, and the horizontal axis is estimated graphically, and the angle ε_{TLV} , of the TLV relative to the blade, inferred by removing the stagger angle γ :

$$\varepsilon_{TLV} = \varepsilon - \gamma \quad (4.3)$$

Here, the angles determined graphically varied within 3° . The conclusion on whether this is due to the graphic determination or to the tip gap size is not possible to draw, but the assumption of Chen that the trajectory does not depend on the gap size seems to be reasonable.

The experimental data used in Chen's thesis covers a large range of clearances for cascade or compressor experiments. Let us compare the angle obtained with Chen's model with what is obtained using the equation below

$$\tan \varepsilon_{TLV} = K_{Chen} \sqrt{\frac{\Delta c_{p,m}}{2}}, \quad (4.4)$$

$\Delta c_{p,m}$ here designates the average value of the quantity $\frac{\Delta p}{0.5\rho V_x^2}$ at midspan. The density ρ is therefore not fixed and the correlation is derived with compressible flows. The axial velocity V_x is a constant in the definition of $\Delta c_{p,m}$ and is extracted at midspan in the inlet plane. K_{Chen} is an empirical constant determined from his numerical method, explained in the literature review. Far from the tip, the influence of TLF on the blade loading is negligible: according to Chen's model to consider, the TLV angle is virtually not affected by the tip gap size. Table 4.6 shows the results obtained with the graphical estimation and with Chen's model, using the mean value $\Delta c_{p,m}$ at midspan.

	From the density contours	From Chen's model
ε_{TLV}	$17 \pm 3^\circ$	20°

Table 4.6: Estimation of the TLV angle based on the density contours and Chen's correlation.

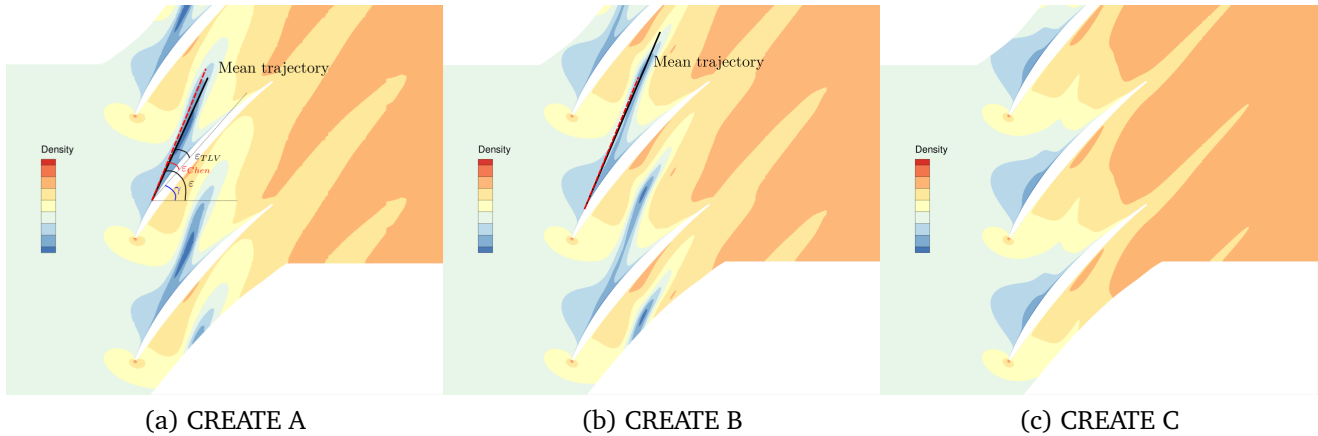


Figure 4.17: Contours of the density at 94% height for the three cases. The mean trajectory of the TLV, determined graphically, is indicated by the black line if possible to be identified clearly. The red dashed line shows the mean trajectory from Chen's correlation.

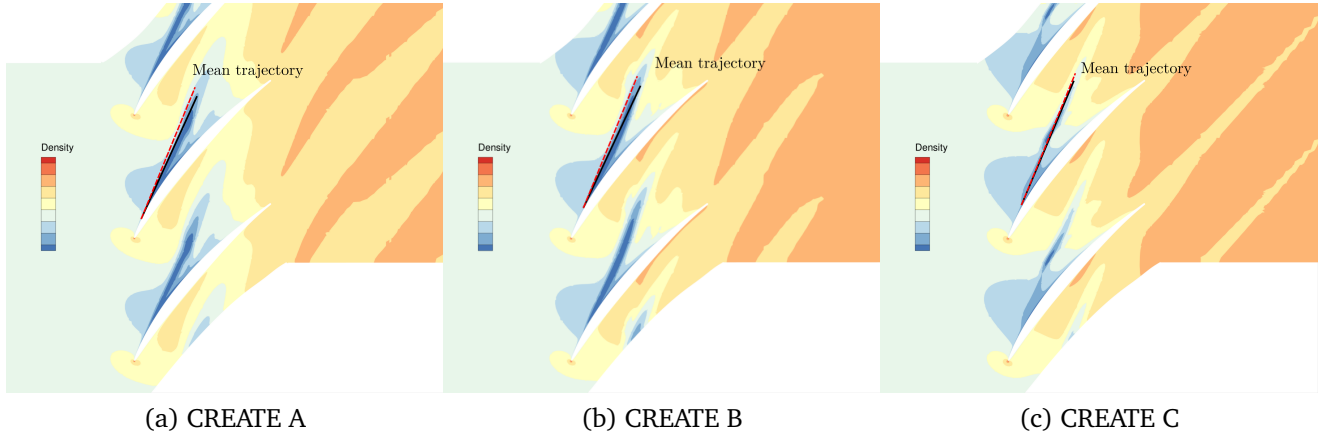


Figure 4.18: Contours of the density at 97% height for the three cases. The mean trajectory of the TLV, determined graphically, is indicated by the black line if possible to be identified clearly. The red dashed line shows the mean trajectory from Chen's correlation.

In reality, the TLV does not follow exactly the straight line as it can be seen in the figures. Progressing through the passage, its trajectory is disturbed by the presence of the endwall boundary layer and the relative motion of casing. However, the prediction based on Chen's model is quite reasonable: the mean trajectory determined graphically fits quite well with that from Chen's correlation. The spanwise extension of the TLV for the smaller gap is much smaller than for cases A and B and the trajectory is only slightly visible at 94% height. The peaks in Figure 4.17c seem to indicate the TLV track but the core is situated closer to the casing. Nonetheless, the trajectory is captured in the three cases at 97% height.

4.2.5.3 Circulation analysis

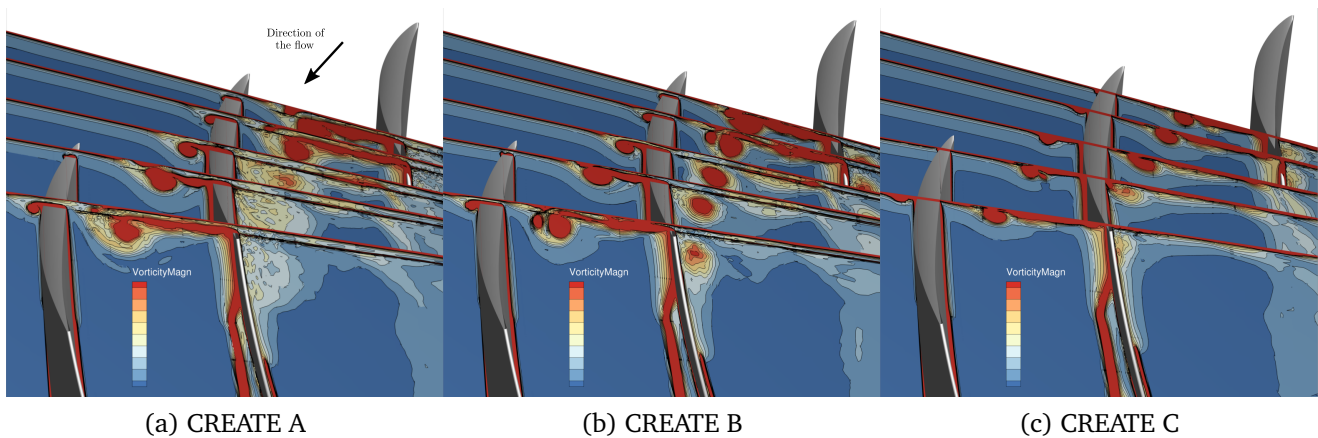


Figure 4.19: Evolution of the mean vorticity magnitude through cutting planes perpendicular to the suction side of the blade (at 10, 21, 40, 61, 95 % c_a), for the three gap sizes. The same scale is used for the vorticity magnitude in the three figures.

The generation of the vorticity in the tip region is compared between the three cases. Figure 4.19 focuses on the development of the vortex through the passage, its intensity and its core radius, depending on the tip clearance size. The observations follow what was already observed with the Q-criterion: in case C, the vortex core diameter is smaller than with the two bigger gaps. Downstream the trailing edge, it is rapidly dissipated and generally seems less energetic than for cases A and B. The vortex fragmentation observed with the Q-criterion is particularly visible here right downstream the trailing edge for CREATE A, where the core of the vortex spreads over a larger radius and consists of smaller and less concentrated structures. Qualitatively, the size of the main structures evolves with the tip clearance size, with more intense structures for the larger gaps. However, the dynamics of the TLV for the bigger gap seems to trigger a collapse of the global structure, which has to be investigated further in the next sections. In comparison, at the same position for CREATE B, the vortex shape is still round and structured.

The radial distribution of Γ is calculated around the blade as

$$\Gamma(r) = -s(r)\Delta V_\theta, \quad (4.5)$$

with $s(r) = \frac{2\pi r}{N_{blades}}$ the blade pitch. Appendix D shows how equation (4.5) is obtained but also proposes a fragmentation of the circulation at the tip, to account for the TLV presence, which influences the resulting deflection.

Using Euler's equation, it is possible to directly relate the circulation around the blade to the blade loading $\Delta h_0(r)$ for any radius, following:

$$\Gamma(r) = -\frac{2\pi r}{N_{blades}} \frac{\Delta h_0(r)}{r\omega} = -T_{bp} \times \Delta h_0(r) \quad (4.6)$$

The spanwise distribution of circulation is shown in Figure 4.20 for the three tip gap sizes with ZDES and compared with the experimental results from LDA on the largest gap.

The ZDES results are in good agreement with the experiment on CREATE A (solid line), consistently with what was observed in section C.2 when comparing the different radial profiles. The gradients are well captured from hub to 80% height, with a good prediction of the blade loading, and an error less than 4%. Looking at the radial evolution of circulation in absolute value, it increases more and more near the tip of the blade, which corresponds to an increase of the blade loading. The deficit observed at 30% height for the three gaps is due to the corner separation. In the region of interest, near the tip, the results indicate a more significant difference between the three gaps. Case A, the larger gap, is clearly more loaded than the two other cases, which was previously observed through the temperature ratio profiles in Figure C.7b. The behaviour of cases A and C in terms of gradients in the tip region is quite similar. Case B does not follow the same gradients: close to the distribution of CREATE A around 80% height, Γ rapidly increases and fits the smallest gap values at casing.

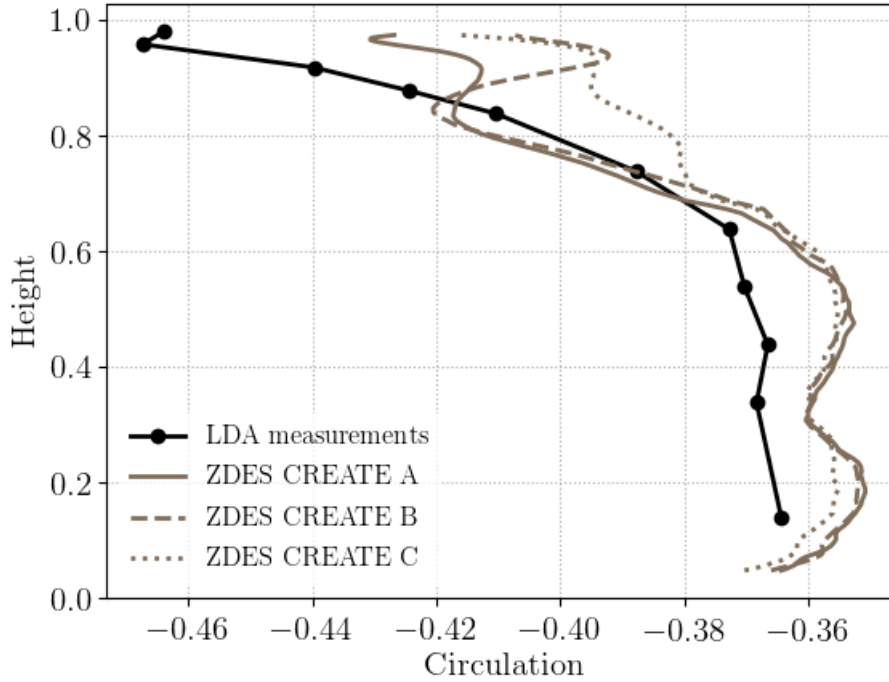


Figure 4.20: Radial distribution of the normalized circulation $\Gamma(r) = -s(r) \frac{\Delta V_\theta}{U_\infty c_a}$ for the three gap values, compared with the LDA measurements on CREATE A.

4.2.6 Unsteady analysis

4.2.6.1 Spectral analysis

Up to this section, the analyses have remained focused on the time-averaged behaviour of TLF to compare the three gap values. The unsteadiness of TLF has a major role in the development of instabilities and this effect has to be considered in the sensitivity study. Given the ZDES approach, by definition unsteady, the study cannot stay limited to a behaviour in average, although it has already shown important differences between the three cases. The motion of the turbulent structures populating the field is by nature unsteady and resolving the TLV with LES is a good opportunity to investigate the differences in the overall unsteady behaviour of the TLV.

The power spectral density (PSD) of some values can be plotted in order to quantify the energy related to the frequencies of the time signal. The probe, called probe 0 in the rest of the study, is located at the blade tip, near the trailing edge. Figure 4.21 shows the PSD of the axial velocity, plotted based on equation (4.7) for the generic variable ξ and the corresponding reference value ξ_{ref} . The signals were processed using Welch's method [144] described in section 2.4 with ten windows and an overlap of 50 %. The spectra illustrate the energy scale order between the three cases, following the order in terms of gap sizes: the larger gap induces the generation of the most energetic TLV at the trailing edge of the blade in the tip region over the whole range of frequencies. The turbulence decay starts around 100 kHz and follows the classical Kolmogorov's cascade with the $-5/3$ slope for the axial velocity.

$$G_{dB} = 10 \log_{10} \left(\frac{PSD(\xi)}{\xi_{ref}^2} \right) \quad (4.7)$$

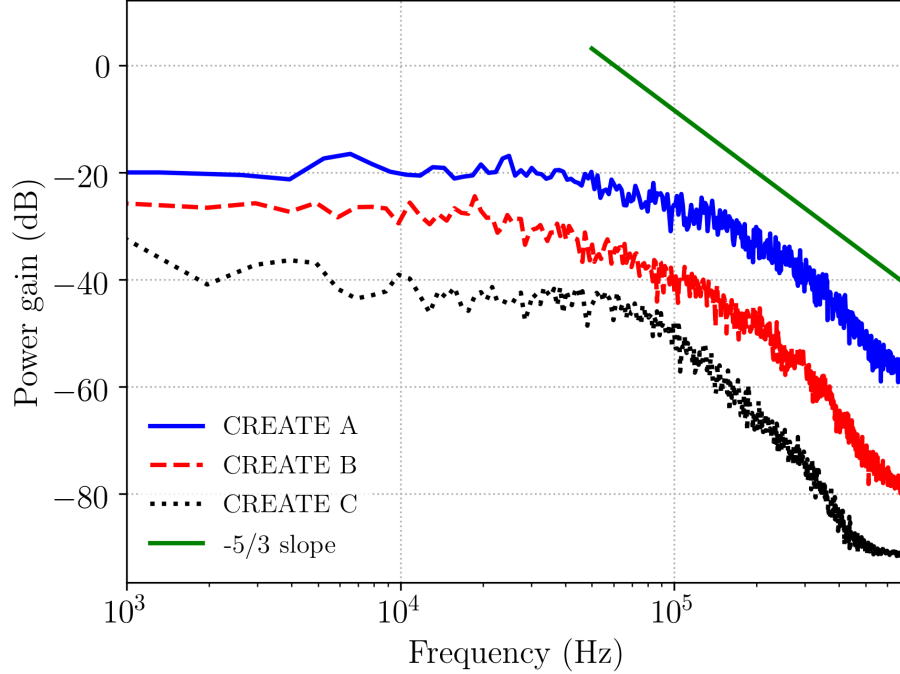


Figure 4.21: Power spectral density of the axial velocity expressed in dB as a function of the frequency. The reference velocity for the gain calculation is set to $U_{ref} = 1 \text{ m/s}$.

Figure 4.22 shows the static pressure spectra with two different scales for the abscissa in subfigures (a) and (b). First, the distributions are similar and follow quite well the $-7/3$ slope on the spectrum decrease. It was analytically shown by George *et al.* [54] that the turbulent pressure fluctuations decrease with that slope in the inertial subrange. Second, a slight bump can be observed on spectra of cases A and B, with a maximum at 40 kHz for case A and 30 kHz for case B. The maximum is more intense for the larger gap. As for case C, a bump can be observed around 80 kHz, however much less energetic than for the two other gaps. Expressed in terms of a Strouhal number normalized with the tip gap size τ

$$St_{\tau} = \frac{f\tau}{r_{tip}\omega}, \quad (4.8)$$

the bump is observed for $St_{\tau} = 0.1$ for the two larger gaps, slightly more energetic for CREATE A. This suggests an unsteadiness driven by the tip gap length scale. For case C, the bump is shifted to $St_{\tau} = 0.06$.

4.2.6.2 Turbulence levels

The resolved turbulent kinetic energy $k = \frac{1}{2} (u'^2 + v'^2 + w'^2)$ indicates the levels of energy due to the turbulent fluctuations of the flow. In the TLV, these fluctuations are intense and are

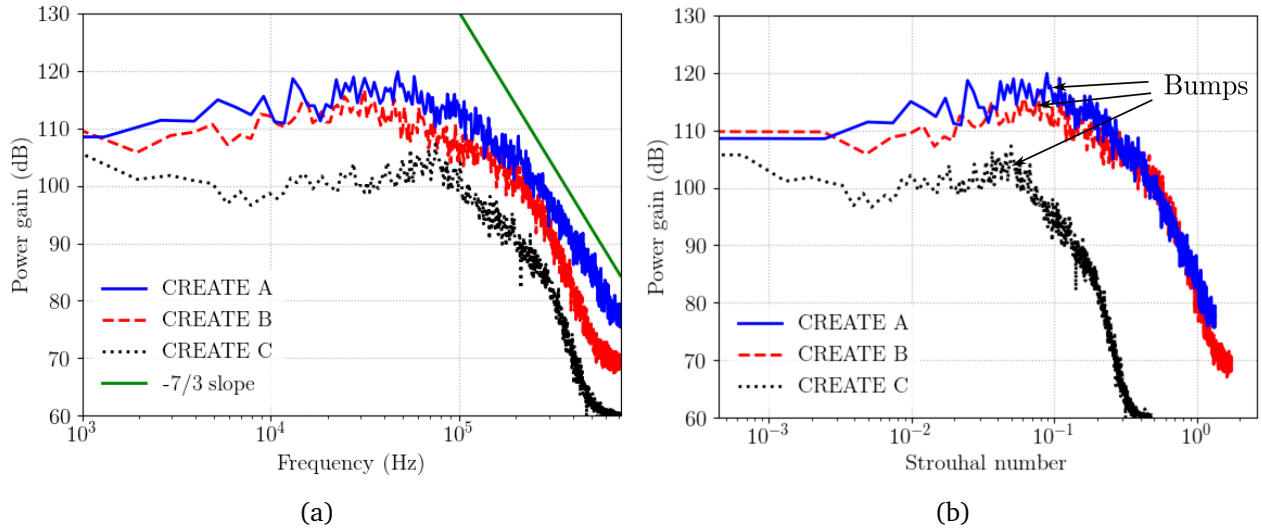


Figure 4.22: Power spectral density for the static pressure expressed in dB as a function of the frequency and the dimensionless Strouhal number, based on the respective tip gap size of each case. The reference pressure is set to $p_{ref} = 2 \times 10^{-5}$ Pa.

responsible for a significant part of the losses. The total pressure increase aimed for with the rotation of the blade and the deviation of the fluid is reduced due to these fluctuations in the vortex, which also relate to the vorticity shown before. These levels of energy can be estimated in terms of a turbulence level, by computing the ratio of the fluctuations with the tip velocity U_{tip} . The turbulence level can be defined as

$$Tu = \frac{\sqrt{2/3 k}}{U_{tip}} \quad (4.9)$$

Figure 4.23 shows the turbulence level contours comparing the three cases, corresponding to the resolved fluctuations. It is recalled that the f_d sensor indicated a complete LES treatment in the TLV, which allows restricting the turbulence level due to the presence of the TLV to the resolved fluctuations with this hybrid approach. The modelled TKE cannot be calculated with the Spalart-Allmaras turbulence model since the knowledge of the one and only turbulent variable in the model is not sufficient to get the TKE. In any case, the modelled part is essentially reduced to a negligible part of the TKE in the TLV regions. Indeed, as shown in Figure C.14, the levels of μ_t/μ are about 1 in that region, typical of SGS levels and therefore not energetic, as explained in Chapter 2.

In the three cases, the vortex sheet supplying the development of the TLV down to the trailing edge can be seen: large levels of turbulence are to be noticed between the suction side and the core of the vortex near casing. This is actually due to the tip separation vortices feeding the TLV that were already visible in the Q criteria shown before. The larger gap induces a large turbulence intensity (more than 30%), indicating strong fluctuations in the vortex core, with a large extension. Decreasing the gap has an impact on both the intensity and the extension of the fluctuations, which are importantly reduced with the smaller gap.

The impact of the neighbouring TLV on the blade has a strong influence on the development of the TLV of the considered passage, driving differently the leakage flow in the clearance. One can observe the turbulence intensity within the clearance: before the impact of the neighbouring TLV, the resolved fluctuations are virtually zero and they significantly increase at the impact and downstream.

Returning to Figure C.14, this corresponds to the RANS to LES switch within the clearance. Essentially treated by RANS in case A upstream of 40% axial chord, the rest is resolved with LES, as indicated by the f_d sensor. Here, the conclusion is that the interaction between the TLV and the blade changes the numerics within the clearance with this hybrid approach: the resolved turbulent fluctuations of the TLV of the adjacent blade are sucked up into the clearance. In case B, this impact is visible at 60% axial chord and it is not visible for the smaller gap. Given the trajectory analysis done previously, the earlier impact for the larger gaps is explained by the much greater core radius of the TLV.

It is interesting to notice the very large increase in intensity of the turbulent fluctuations between planes 61% c_a and 95% c_a in case A. The radius of the red zone more than doubles with turbulent fluctuations thus greater than 30%. The fragmentation observed in the Q-criterion (Figure 4.10a) and in the axial vorticity evolution through the passage (Figure 4.19), occurs in-between these two planes and would explain the significant increase in the TKE, generating large losses. In case B, the zone for which turbulent fluctuations are greater than 20% grows importantly between the same two planes but the intensity of the fluctuations is far less significant. In case C, this augmentation is not observed.

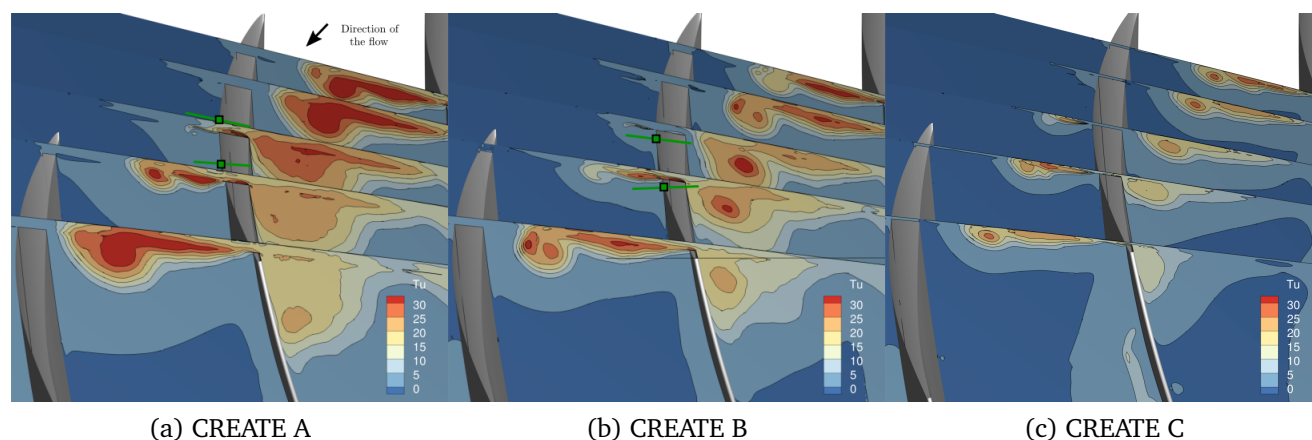


Figure 4.23: Streamwise evolution of the resolved turbulence level contours (in %) in planes perpendicular to the suction side of the blade (10, 21, 40, 61 and 95% axial chord.) The green squares indicate the position of the slope change in the leakage velocity plot.

4.2.6.3 Variations of the leakage velocity

The impact of the adjacent TLV on the pressure side of the blade has a big influence on the dynamics of the TLV detaching from the suction side. As turbulent fluctuations are sucked up

in the clearance, the leakage velocity is perturbed and this in turn strongly influences the TLV development. Figure 4.15 illustrated the leakage velocity evolution chordwise for the three gaps. The slope breaks observed in cases A and B are here very relevant to be commented as they coincide with the position where the adjacent TLV impacts the pressure side of the blade in the TKE visualizations commented above and indicated by the squares in the figure:

- In case A, the leakage velocity abruptly drops from 1 to 0.75 in less than 5% axial chord at 40% c_a . A plateau is observed over 10% chord and the leakage velocity seems to recover the same slope as upstream of the break around 55% axial chord.
- In case B, the same slope break is observed with less intensity at midchord. A plateau can be seen upstream of the leakage velocity drop from 40% c_a but also downstream of the velocity drop, exactly as in case A. Again, the position of the drop in leakage velocity corresponds to the impact of the TLV visualized with the turbulent levels in the tip region.
- Finally, in case C, the adjacent TLV does not impact the current blade and no velocity drop is observed.

A correlation is put in evidence between the impact of the adjacent TLV and the sudden variations of the leakage velocity. Qualitatively, the mechanism can be explained by the mixing of the adjacent TLV with the leakage flow within the clearance. The dynamics of the TLV sucked up in the clearance modifies the dynamics of the leakage flow over a portion of the chord. The leakage flow recovers its slope afterwards when the mixing effects of the vortex in the clearance have decayed. The phenomenon can also be seen on the blade loading at 99% height, previously shown. In figure 4.13, at the same respective positions for cases A and B as for the leakage velocity, a drop preceded by a plateau in the blade loading is observed, before the loading recovers its slope. The loading decrease is also stronger for the larger gap than for case B. This can be explained by the TKE and vorticity levels of the TLV, much larger in case A.

This phenomenon is called *double-leakage tip clearance flow* and was previously observed by Hah [61]. This is further discussed in section 4.2.7.

4.2.6.4 Unsteadiness of the TLV

A major difference has been mentioned between cases A and B: a vortex fragmentation occurs with CREATE A while the vortex remains coherent with CREATE B, as observed in the Q-criterion and the resolved turbulence levels of the TLV. After the impact on the pressure side of the blade by the adjacent TLV, the leakage velocity and the turbulence levels are notably affected. This section is intended to analyze the subsequent unsteadiness of the considered TLV.

The time signals are extracted in three probes of the computational domain located within the TLV core radius as indicated by Figure 4.24 for the three tip gap sizes. It is recalled that the TLV core is characterized by minimal levels of density. For cases A and B, their position has been chosen as follows:

- Probe 1 is situated upstream of the adjacent TLV impact.

- Probe 2 is located downstream of the adjacent TLV impact.
- Probe 3 is farther downstream in the TLV. In case *A*, this position corresponds to a broken vortex, as shown in the *Q* criterion before.

The green squares indicate the positions of the beginning and the end of the slope variation in the leakage velocity. These planes are also indicated in Figure 4.23 to locate the impact relatively to the slope variations in the leakage velocity profile (Figure 4.15).

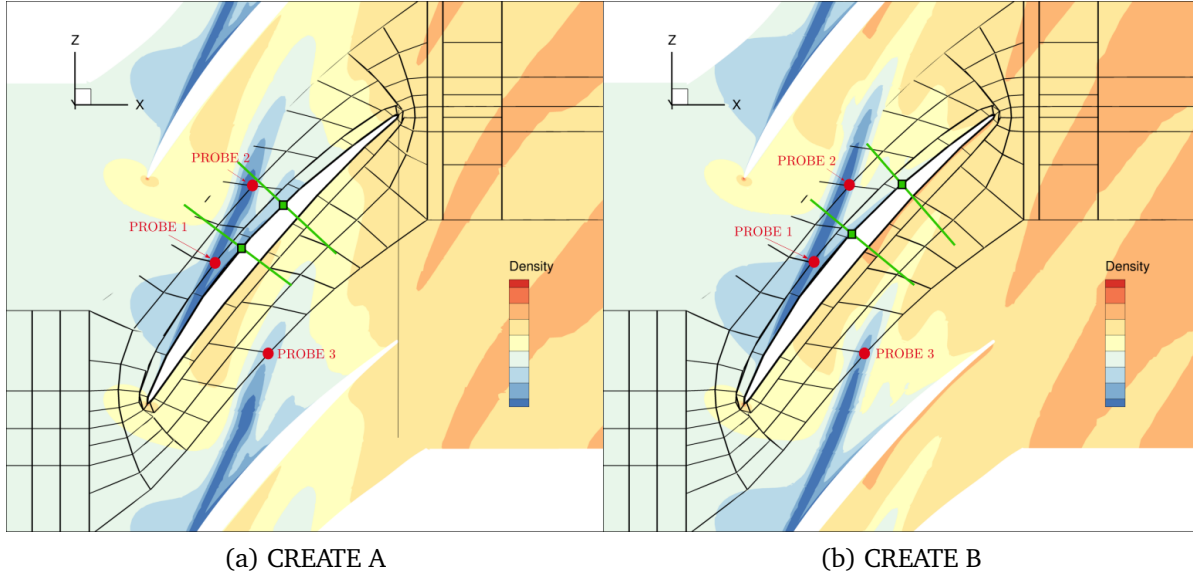


Figure 4.24: Location of the probes where the spectra are extracted in red, following the trajectory of the TLV. The black grid shows the grid of probes where the spectra can be extracted at this height.

Cases A and B Figure 4.25 shows the PSD normalized as a decibel gain, calculated on the axial velocity, as a function of the Strouhal number St_c on CREATE A and B at the three probes. Both cases exhibit a bump around $St_c = 10$ on the second probe, coherent with the bump previously observed at probe 0 for $St_\tau = 0.1$ (Figure 4.22), suggesting again a phenomenon driven by the tip gap length scale. Indeed, the order of magnitude for the ratio τ/c_a is 1%. The Strouhal number St_c is defined by

$$St_c = \frac{f c_a}{r_{tip} \omega}. \quad (4.10)$$

As for the third probe, the overall energy levels are much larger in case *A*: they are 10 *dB* greater than for case *B* over the range of St_c between 1 and 10. The same applies to larger St_c , indicating that the small structures are still very energetic in case *A*. The energy levels augmentation with the axial position is explained by the continuous supply of the TLV by the TSV. The fact that the TLV is then more energetic for case *A* is consistent with the larger turbulent

levels shown before. The TLV/blade interaction being more intense in case *A*, this evolution in the spectrum is coherent.

The most interesting observation concerns the peak observed around $St_c = 0.5$ for CREATE A on the second and third probes, not observed in CREATE B. It is followed by less energetic peaks at $St_c = 1$, $St_c = 2$ in particular. This would indicate a low-frequency energetic phenomenon occurring on the larger gap that does not appear on case *B*, with a fundamental frequency at $St_c = 0.5$ and harmonics. As observed in the Q-criteria shown before, a vortex fragmentation only occurs with the larger gap. The vortex in case *B* remains round over the passage and does not exhibit a track of any collapse. This low-frequency peak at probe 2 coincides with the occurrence of the vortex destructuring in case *A*, that does not occur in case *B*.

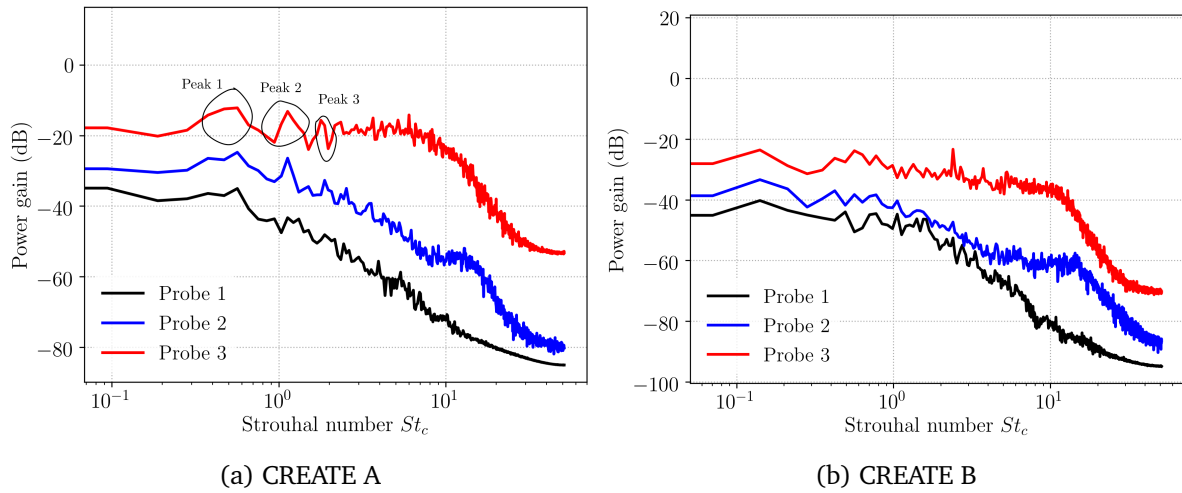


Figure 4.25: Power spectral density of the axial velocity at probes 1, 2 and 3. The reference velocity is $U_{ref} = 1 \text{ m/s}$.

This phenomenon has already been observed in the literature. Boudet *et al.* [11] call *natural unsteadiness* a turbomachine unsteadiness not related to rotor/stator interactions. Rotating instabilities, vortex shedding, or vortex wandering are part of this category. The numerical study of Boudet *et al.* on a fan showed the existence of a wandering motion of the TLV, characterized by low-frequency oscillations of the TLV in the passage. This wandering motion is generally driven by upstream turbulent fluctuations from a boundary layer or another significant source of TKE. The phenomenon has been put in evidence by Bailey and Tavoularis [6] on a wing-tip vortex. Their experiment showed that the amplitude of the wandering increased with increasing free-stream turbulence. In the linear cascade of You *et al.* [154], the authors clearly illustrated the wandering motion of the TLV. A peak was found for a Strouhal number (based on the chord length) about 1 on the pitch component of the velocity. In their case, the source of these oscillations was explained by a shear-layer instability in the clearance jet flow. In our case, the explanation proposed by Boudet *et al.* in their study seems to apply here as well: the wandering motion of the TLV occurs because of the upstream turbulence from the adjacent TLV and the casing boundary layer. In the Fourier analysis, the wandering motion is characterized by several

peaks, associated to the fundamental frequency and its harmonics. Similarly to You *et al.*, the first peak was observed for a Strouhal number of about 1 by Boudet *et al.*

The literature therefore suggests a vortex wandering occurring for the larger gap due to the upstream turbulence from the casing boundary layer and the adjacent TLV. Recall that the TLV fluctuations are mostly resolved, as shown in the numerical analysis in section 4.2.4.1. We suggest that the most important contribution is the adjacent TLV since the casing boundary layer in cases A and B is very similar. In the first case, a wandering motion is observed, not in the two others. With the larger gap, the adjacent TLV impacting the blade present higher levels of turbulence and a bigger core radius. In case B, the adjacent TLV impacts the pressure side but no frequency peak is observed. A vortex wandering may occur on the TLV of case B but with much lower intensity than in case A: the turbulent fluctuations of the adjacent TLV are much stronger for the latter. Following the conclusions of Bailey and Tavoularis, this could explain the stronger vortex wandering occurring in case A, that could then be responsible for the vortex fragmentation observed. On the contrary, with case B, these turbulent fluctuations seem too low to induce TLV low-frequency oscillations causing the vortex structure to divide into smaller ones.

Case C The core radius of the TLV in case C is much lower than for the two other gaps although the mean trajectory is almost the same (confirmed with the positioning of probe 3). As shown in Figure 4.26, probes 1 and 2 have been shifted upstream in case C to ensure an extraction of the spectrum near the TLV core. The evolution of the energy levels with the propagation of the TLV, shown in Figure 4.26, is compared to the two other gaps.

Case C is discussed apart from the two others in this section since no TLV/blade interaction is observed in this case according to the TKE views. In this case, no vortex fragmentation occurs either. Between probes 1 and 2, the order of magnitude of the energy increase is about 1 dB over the whole range of frequencies. Again, the TLF brings turbulent fluctuations in the TLV through the TSV, responsible for this energy increase. The increase between probes 1 and 3 is about 25 dB, for St_c between 1 and 10. This is a major difference from the two larger gaps: the increase at $St_c = 1$ is much lower than at $St_c = 10$ for cases A and B. The TLV enriches with intermediate turbulent structures over the passage while the energy distribution remains more or less the same in case C. The energy levels decrease is only initiated later in frequencies between probes 1 ($St_c \approx 7$) and 3 ($St_c \approx 10$). In cases A and B, the starting point of the decrease is about $St_c = 1$ at probe 1 and is shifted to $St_c = 10$ at probe 3.

4.2.6.5 Summary

In summary, different results can be retained from this investigation on the TLV unsteadiness:

1. The evolution of the energy levels in the three cases confirm the fact that the TLV gets more and more intense over the whole range of frequencies through the passage, due to the continuous feeding with turbulent fluctuations by TLF chordwise. The TSV shown before particularly contribute to the development of the TLV.

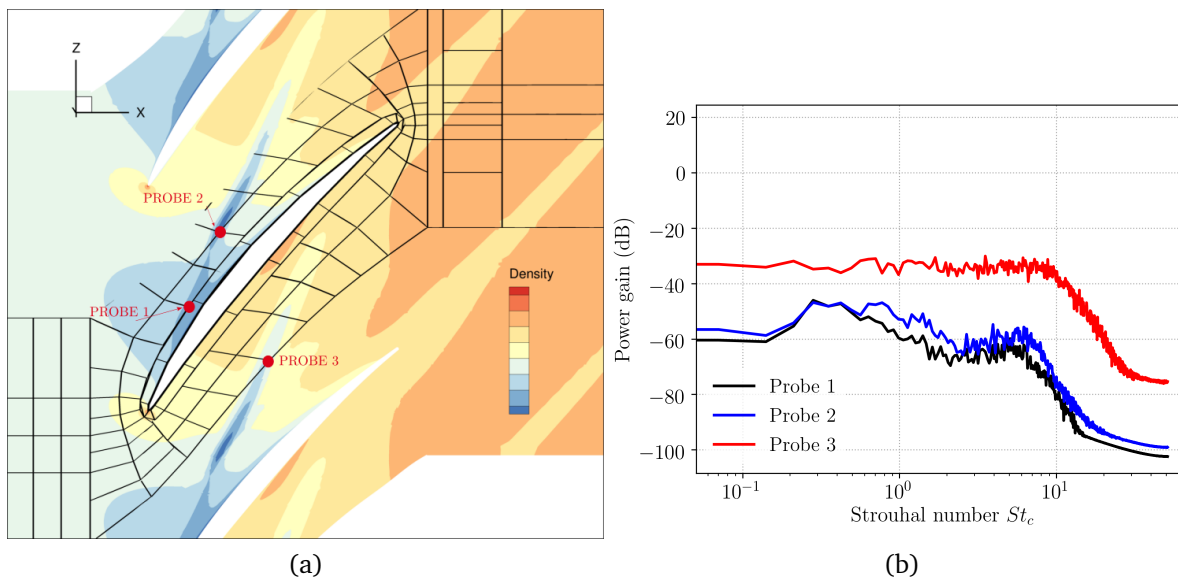


Figure 4.26: (a) Location of the three probes for case C. (b) Power spectral density of the axial velocity at probes 1, 2 and 3. The reference velocity is $U_{ref} = 1 \text{ m/s}$.

2. The energy levels follow the same order as the tip gap sizes: the larger the gap, the more intense.
3. The contribution of smaller structures, corresponding to a chord length Strouhal number $St_c > 1$, more and more significant as the TLV progresses through the passage, is put in evidence for the two larger gaps. The influence of the double-leakage tip clearance flow occurring in these two cases and not in case *C* constitutes a good explanation of the phenomenon.
4. The TLV/blade interaction shown in section 4.2.6.2 for cases *A* and *B* would be responsible for TLV low-frequency oscillations in the former case but not on the other. These oscillations have been identified by a peak frequency on the axial velocity power spectral density around $St_c = 1$. The phenomenon is referred to as *vortex wandering* in the literature. Three different studies on three different configurations put forward a vortex wandering, classically recognized by a frequency peak at $St_c \approx 1$, supporting the hypothesis of TLV oscillations in case *A*, not identified in case *B*.
5. The vortex fragmentation only observed in case *A* through the Q-criterion views could be a consequence of these low-frequency TLV oscillations. These oscillations may exist in case *B* as well but with a much lower intensity and cannot be identified as such in the spectrum. The lower amplitude of these possible oscillations are consistent with the fact that no vortex fragmentation is observed in case *B*.

4.2.7 The vortex wandering

This paragraph is intended to propose an explanation for the fragmentation of the vortex in case A.

The effects induced by a large rotor tip gap (4% of the rotor span) were investigated by Hah [61] on a 1.5 stage axial compressor, based on LES and PIV results for different operating points, compared to the results obtained for a small clearance (0.8% of the rotor span). This revealed the occurrence of a *double-leakage tip clearance flow* at all operating points for the larger gap. This is defined by the impingement of the TLV of the adjacent blade on the pressure side of the current blade, inducing an interaction between this TLV and the clearance flow. This interaction led to the fragmentation of the vortex. No double-leakage tip clearance flow nor any vortex fragmentation were observed with the small gap.

Let us recap on our unsteady analysis:

1. A discontinuity in the slope of the leakage velocity in the clearance exists for the two larger gaps. It is consistent with the slope break observed on the blade loading at the tip at the same axial positions (see Figure 4.15).
2. This discontinuity corresponds to the location where the TLV of the neighbouring passage is sucked up in the clearance. The strong turbulence brought by the adjacent TLV disturbs the leakage flow dynamics, which explains this slope discontinuity (see Figure 4.23).
3. The contours of turbulence levels show the intensity of these fluctuations between the detachment of the TLV and its development through the passage. They are much stronger in case A than in the two other cases (see Figure 4.23).
4. A low frequency resonance of the TLV has been found on CREATE A with a Strouhal number $St_c \approx 0.5$ of the same order of magnitude as that obtained in three studies on the wandering motion of the TLV. The phenomenon is described by low frequency oscillations of the TLV supplied by the upstream turbulence of the endwall boundary layer and the adjacent TLV. In our case, the wandering motion being observed only in case A with a casing boundary layer nearly identical in case B, this suggests that the vortex wandering is mostly a response to the adjacent TLV turbulence (see Figure 4.25).
5. From this wandering could originate the fragmentation of the vortex observed in case A, clearly shown in the Q-criterion, where the TLV loses its round homogeneous structure and divides into multiple small vortices. The wandering motion could cause the burst of the vortex. Nonetheless, drawing a clear line between these two phenomena is complicated: both could simply describe the same phenomenon.
6. The vortex fragmentation is responsible for very large losses and a strong blockage of the passage. The difficulties encountered in the calibration of the simulation with RANS on CREATE A may be explained by the strong unsteadiness and the large blockage induced by the fragmentation.

7. A last remark concerns the time-averaged Q-criterion (Figure 4.10a) and the axial vorticity contours (Figure 4.19a) of CREATE A: although the ZDES is converged statistically, little turbulent structures are still observable in the average of those two values. They should normally be smoothed with the averaging. This would confirm a low-frequency phenomenon (a vortex wandering) that requires more time steps to be averaged smoothly on the Q-criterion and the axial vorticity. This is only observed for the larger gap (CREATE A).

The results obtained with case A and case C are very similar to the results got by Hah for the two tip gap sizes he investigated:

- A vortex fragmentation is observed for the larger gap, due to the double-leakage tip clearance flow, bringing significant turbulent fluctuations to the development of the TLV. A correlation between these fluctuations and the fragmentation of the TLV is conjured up in his study. It seems to be very similar for CREATE A ($\tau/b > 2.5\%$).
- No double-leakage tip clearance flow is observed for the small gap in Hah’s study and neither for CREATE C, and the TLV keeps its round structure through the passage.

CREATE B here constitutes an intermediate case where the double-leakage tip clearance flow is observed but no vortex fragmentation occurs. The spectrum peak characterizing the vortex wandering is detected in case A but not in case B.

Table 4.7 summarizes the influence of the tip gap size on the double leakage phenomenon and its possible influence on the vortex fragmentation, only observed in case A, the largest gap. A possible vortex wandering that would generate such a fragmentation should be investigated further as well as the occurrence of a vortex breakdown.

	CREATE A	CREATE B	CREATE C
Slope breaks	Yes	Yes	/
Double leakage	Yes	Yes	/
Vortex fragmentation	Yes	/	/

Table 4.7: Summary on the sensitivity analysis to the tip gap size on the third rotor of CREATE.

On the question of whether such a fragmentation of the TLV could be a vortex breakdown, further analyses should be done. For example, the criterion established by Furukawa *et al.* [50] considers the existence of a stagnation point where the breakdown begins.

On the discontinuity of the leakage velocity, further investigations should be conducted with RANS and higher resolutions. A possible criterion may be established regarding the position of the slope discontinuity and its magnitude related to the occurrence of a vortex wandering or/and a vortex fragmentation. The unsteady RANS approach may be poor in that regard following the analysis made in section C.2 where the RANS SA showed a rapid diffusion of the TLV. Moreover, such complex turbulence/TLF interaction seems complicated to be modelled correctly

with RANS. Multiple simulations varying the incidence and the tip gap size could be very useful to determine whether a criterion could be established.

The wandering motion of the TLV and the possible TLV breakdown could initiate rotating instabilities or even rotating stall [136] [148]. Indeed, if the mass flow rate is reduced, we saw that the TLV was shifted upstream, closer to the leading edge. The spike inception of rotating stall is related to the alignment of the TLV with the leading edge plane of the rotor. Hence, for more throttled operating points, the mean adjacent TLV impact is closer to the leading edge. If it is close enough and if the amplitude of the TLV oscillation is sufficiently large, the TLV could temporarily spill in front of the leading edge plane and initiate a rotating stall, as described in Chapter 1. Figure 4.27a illustrates such a scenario.

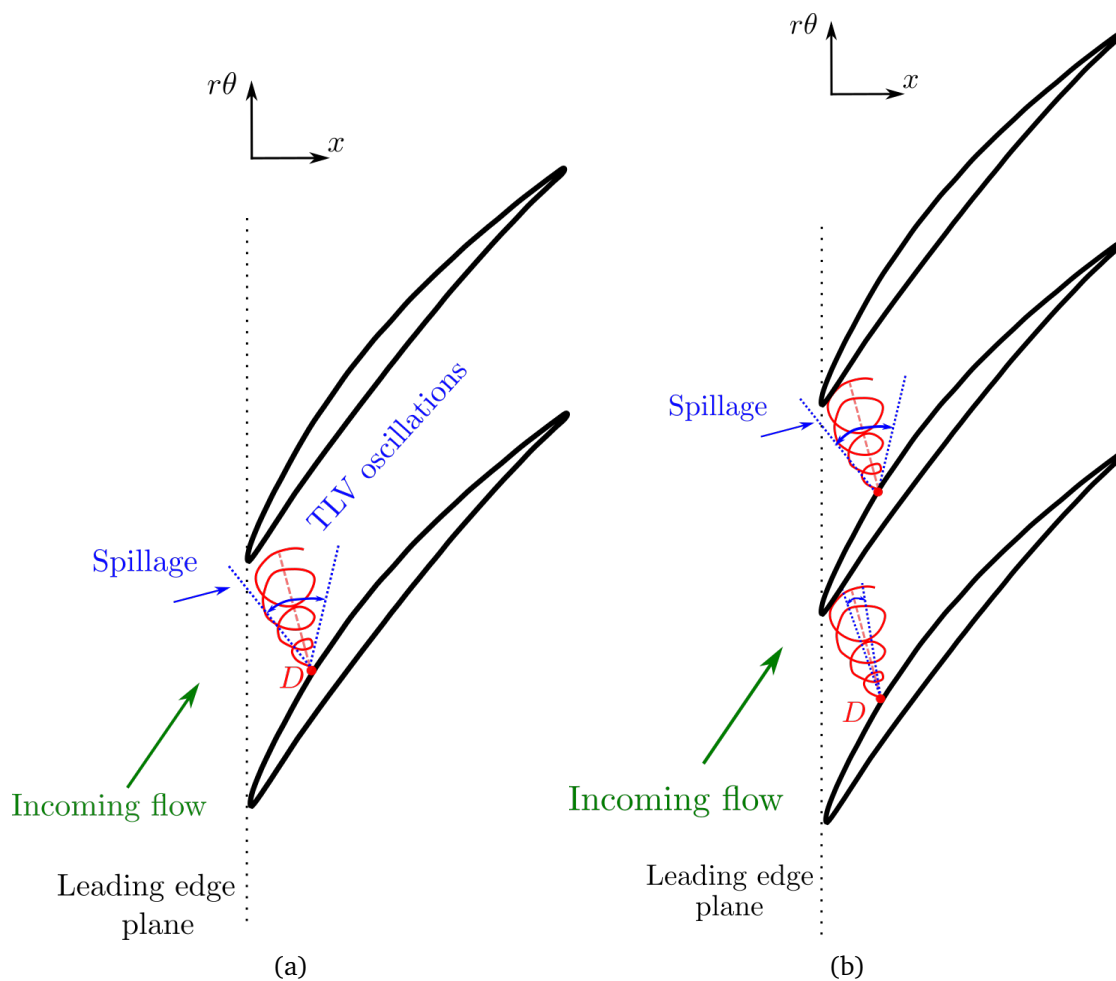


Figure 4.27: (a) Illustration of the wandering motion of the TLV core (in blue) in a rotor passage around mean position over time (in red dashed). In these conditions, the amplitude of the oscillations is such that a spillage occurs in front of the leading edge of the neighbouring blade, likely to trigger a rotating stall due to a spike inception. (b) Illustration of the excitation of the TLV oscillations from one passage to another. D indicates the detachment point of the TLV in both figures.

For that matter, the description of the mechanism is here based on a simulation with a periodicity condition. Throttling the machine towards the minimal mass flow rate makes this assumption less and less reliable. One could imagine that the TLV wandering actually excites the adjacent passage, and then the other with more intensity, and so on (see Figure 4.27b). The wandering motion could gain in intensity from one passage to another and finally trigger the rotating stall for a sufficient amplitude of oscillations, by a TLV spillage in front of the leading edge plane. Simulations with more passages would be very useful to investigate this possible mechanism.

4.3 Conclusions

In this chapter was presented a sensitivity study on the tip gap size and its influence on the tip-leakage flow.

Because the simulation is restrained to a single passage of one rotor, a calibration of the boundary conditions at the inlet and the outlet was required. The injected variables thus calibrated were kept for all the simulations for the parametric study on the tip gap size conducted with the ZDES approach.

The parametric study on the tip gap size presents a real interest to go further into the comprehension of the tip-leakage flow. With the same boundary conditions for the three tip gap sizes tested, the study focused on the impact of the tip gap size variations onto three characteristics of the TLV: its circulation, its detachment point and its trajectory. If the position of the detachment point and the mean trajectory are little affected by the tip gap size, the main influence lies in the circulation: a larger tip gap yields a stronger tip-leakage vortex.

The unsteady analysis brings interesting results on the dynamics of the TLV depending on the tip gap size. The benefits of using ZDES are clearly illustrated in the unsteady behaviour of the TLV. The results indicate a strong modification of the TLF dynamics by the impact of the adjacent TLV on the pressure side of the current blade. The resolved fluctuations of the adjacent TLV interact with the leakage flow in the clearance. This impacts directly the leakage velocity and subsequently the formation of the TLV on the suction side.

The mean analysis along with the unsteady analysis bring interesting results to the comprehension of the onset of instabilities. Regarding spike initiated rotating stall, the spillage of the TLV in the adjacent passage upstream of the leading edge is a well-known criterion identified in the literature. Increasing the gap size increases the TLV core radius and the intensity of the turbulent fluctuations. Although the mean trajectory is the same, the core radius and circulation increases strengthen the double leakage phenomenon and possibly reinforce the amplitude of the TLV low-frequency oscillations. Combined to that, for higher incidences, the mean trajectory of the TLV is shifted upstream. The hypothesis is the following: if the TLV in average impinges the pressure side of the adjacent blade close enough to the leading edge, sufficient oscillations of the TLV could lead to a spillage in front of the leading-edge plane. Other sources of excitations may also contribute to this alignment (*e.g.* wakes, acoustic resonance).

The hybrid RANS/LES approach brings interesting analyses on the influence of the tip gap

size on the tip-leakage flow, thanks to its high resolution. Chapter 5 uses the Vortex Lattice Method (VLM) presented in Chapter 3 to estimate its capabilities regarding the sensitivity of TLF to the tip gap size on a simplified TLF configuration, in steady conditions. This is done on a single blade configuration, on the prediction of the three features of the TLV analyzed through the present chapter, with a particular focus on the circulation. However, the application of the VLM to CREATE is also discussed at the end of the next chapter, as a prospect.

EVALUATION OF THE VORTEX LATTICE METHOD ON A TLF
CONFIGURATION AND MODELLING OF THE TIP-LEAKAGE
VORTEX

Contents

5.1 Presentation of the experiment	151
5.1.1 The experimental rig $S2l$	151
5.1.2 Experimental measurements	151
5.1.3 Numerical results	153
5.2 Evaluation of VLM on $S2l$	154
5.2.1 Conditions of application	154
5.2.2 Distribution of bound circulation	155
5.2.3 Shed circulation	156
5.2.4 Detachment point	161
5.2.5 Trajectory of the TLV	163
5.3 Construction of a viscous model	165
5.3.1 Viscous diffusion of a vortex dipole	165
5.3.2 Estimation of the eddy viscosity	168
5.3.3 Principle of the new model	169
5.3.4 Application to $S2l$	171
5.3.5 Axial evolution of Γ_{TLV}	174
5.3.6 Prediction of the circulation on $S2l$	174
5.4 Viscous model applied to VLM	176

5.4.1	Description of the new model	176
5.4.2	Results on the circulation	178
5.5	Discussions	181
5.5.1	Endwall/TLV interaction	181
5.5.2	Estimation of the eddy viscosity	181
5.5.3	Application to CREATE?	182
5.6	Conclusions	183

Chapter 3 introduced VLM and how it was extended to tip-leakage flow configurations, investigating different parameters on the grid size, the wake and the periodicity. The idea was to establish some criteria to be used to evaluate the method on actual tip-leakage flow configurations, where experimental and better resolved numerical results are available. The purpose of this chapter is to assess the capabilities of the module on a TLF configuration where the tip gap size is varied. The experimental rig is presented with the measurements and the RANS simulations available. The results given by VLM are discussed considering three main characteristics of the TLV (point of detachment, trajectory and axial evolution of circulation). Throughout this chapter, a model predicting the circulation of the TLV is constructed.

5.1 Presentation of the experiment

5.1.1 The experimental rig *S2l*

The effects of the tip gap size have been investigated on the experimental rig *S2l*, located at ONERA in Meudon, in the frame of the PhD thesis of Deveaux [42]. The rig consists of a single blade (NACA0012 airfoil) whose distance from its tip to the endwall can be adjusted. The tip gap size varies between 0.5% and 13% chord length. The range of tip gap sizes goes from sizes representative of actual compressors (up to $\approx 4\%$ c) to larger tip gaps where viscous effects have much less impact. Figure 5.1 shows the experimental rig with the variable tip gap size τ . Table 5.1 summarizes the main parameters of the experiment, to be reproduced in the VLM module *PyLiSuite*.

U_∞	40 m/s
Re	550 000
M_∞	0.1
P_∞	101325 Pa
Tu	0.07%
Chord length c	200 mm
Span b	560 mm
Angle α	10°
τ/c	From 0.5% to 13%

Table 5.1: Main parameters of the experiment.

The angle $\alpha = 10^\circ$ was chosen so that the blade be sufficiently loaded without getting too close to stall. The idea was to be able to observe a strong tip-leakage vortex.

5.1.2 Experimental measurements

Two types of measurements that were carried out on *S2l* are used in the present thesis for the comparisons with VLM:

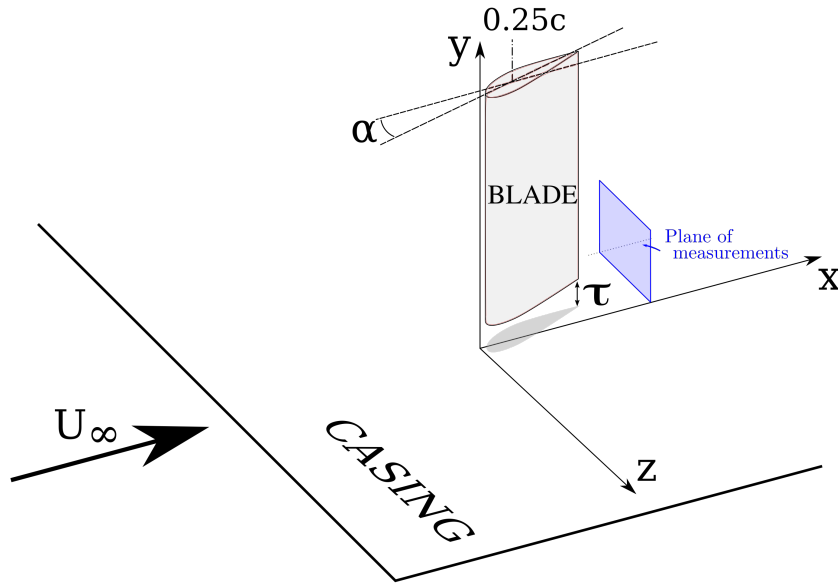


Figure 5.1: Sketch of the tip-leakage flow configuration *S2l* on a single blade.

- Five-hole probe measurements in the plane situated at $x = 1.05c$. They are used to calculate the TLV circulation by integrating the axial vorticity in the tip region. Figure 5.2 shows a map obtained by Deveaux with an incoming boundary layer at casing with a momentum thickness $\theta/c = 0.6\%$. It must be noted that the vorticity of the TLV is isolated from the secondary vorticity (of opposite sign) induced by the interaction between the TLV and the boundary layer. The circulation of the TLV is calculated by integrating only the positive axial vorticity, following

$$\Gamma_{TLV} = \int_{S_{TLV}} \omega_x \, dy \, dz, \quad (5.1)$$

over the surface area S_{TLV} , corresponding to the location of the TLV. In the rest of the chapter, the circulation Γ_{TLV} is therefore counted positive ¹.

- Laser Doppler Anemometry (LDA) measurements at five axial positions, from $x = 0.25c$ to $x = 1.05c$, to follow the trajectory of the TLV core.

The spanwise extension of the measurements is restricted to the tip region. From the first measurements, the total and static pressures can be measured along with the velocity components. The LDA measurements yield the mean velocity components and their RMS fluctuations,

¹In Deveaux's thesis, the circulation of the TLV is negative but for sake of simplicity, the convention has been changed in the present thesis.

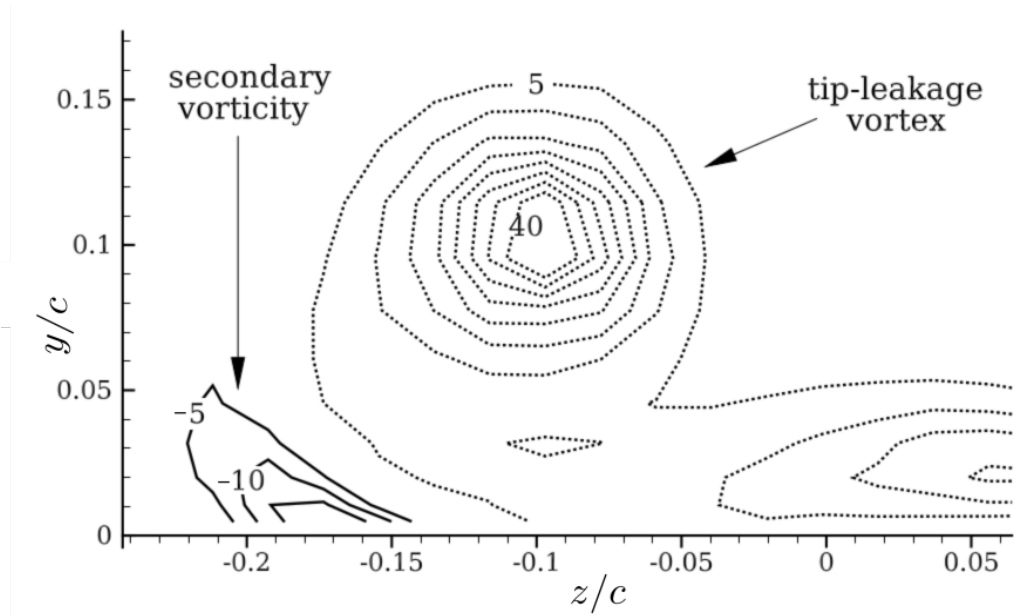


Figure 5.2: Description of the TLV from the 5-hole probe measurements with $\tau/c = 3.5\%$. Dotted lines represent the positive vorticity, solid lines the negative vorticity, adapted from [42].

characterizing the turbulence. Given the low-resolution approach of VLM, the present thesis sticks to the mean values. More details on these measurement techniques can be found in Deveaux's thesis.

5.1.3 Numerical results

RANS results are also available on this configuration. The software *elsA* was again used for the numerical study on *S2l*. In Deveaux's thesis, five turbulence models were investigated in comparison to the experimental results. Among them, four (Spalart-Allmaras, Menter's $k-\omega$ BSL and SST, and Smith's $k-l$) rely on the Boussinesq hypothesis, while the latter (RSM SSG/LRR- ω) is based on seven transport equations. The turbulence model that showed the best agreement with the experimental measurements, in terms of predictions of the flow across the gap and the TLV, is the RSM. The results obtained with this model are retained for the study.

These predictions in particular concern:

1. **Within the gap:** The contraction coefficient σ of the vena contracta in the gap at $\tau/c = 1\%$.
2. **In the TLV:** At the axial position $x/c = 1.05$, the velocity component profiles and the static pressure profile in the TLV, plotted against the five-hole probe measurements spanwise and pitchwise around the position of the TLV core, located by the maximum of axial vorticity.

Two boundary conditions at the casing are compared throughout the chapter to estimate the impact of the boundary layer on the TLV development:

- A non-penetration condition, inviscid wall boundary condition, consisting in imposing a zero normal velocity component. In that case, there is no boundary layer at the casing.

- A no-slip condition, with a developed incoming boundary layer of momentum thickness $\theta/c = 0.6\%$. The corresponding thickness δ is $\delta/c = 4.95\%$, for a boundary layer that therefore immerses the tip gap for 7 out of the 10 sizes tested.

5.2 Evaluation of VLM on *S2l*

5.2.1 Conditions of application

The conditions of application of the VLM to the experimental case are recalled in this section. Referring to Chapter 3, the case considered is represented by a flat plate (camber formulation) of aspect ratio $AR = 2.8$, over which a symmetry condition is used to replicate the presence of a tip gap. The non-penetration condition is applied on the blade of span $2b$, the hub symmetry being guaranteed at $y = b$ with a mirror blade. This corresponds to case 11 introduced in Chapter 3. The results will only be extracted in the region of interest, between $y = 0$ and $y = b$, the actual blade used in the experiment. The idea is to apply the non-penetration condition on the blade by computing the velocity with Biot-Savart's law from the circulation distribution over 20 other blades spaced of 2τ with one another (see section 3.4.3).

Only the camber formulation is used here since criterion (3.41) is not satisfied with the surface formulation, the prescribed wake thickness being too large. The width-to-span ratio indeed writes:

$$w_{wake} = \frac{t_{max}}{b} \quad (5.2)$$

with t_{max} the maximum thickness of NACA0012, which is $t_{max} = 12\%c$. Equation (5.2) then rewrites:

$$w_{wake} = 0.12/AR = 4.3\% > 2\%, \quad (5.3)$$

and the error made on the lift coefficient would exceed 12% according to section 3.3.3. The blade geometry treated with VLM is reduced to a flat plate with the camber formulation, since the NACA0012 airfoil has no camber. The grid is kept constant for all the tip gap sizes treated, summarized in Table 5.2, following criterion (3.44) on the smaller tip gap size. The resulting grid (between $y = 0$ and $y = b$) consists of $m = 37$ elements chordwise, and thus $n = 92$ spanwise. The size of the linear system to be solved is therefore 37×184 for each tip gap.

τ/c (%)	0.5	1	1.5	2.5	3.5	4.5	6	8	13
--------------	-----	---	-----	-----	-----	-----	---	---	----

Table 5.2: Tip gap sizes tested with VLM on *S2l*.

Figure 5.3 shows the discretization used for the flat plate between the tip ($y = 0$) and the equivalent hub ($y = b$). The red lines represent the legs of the horseshoe vortices shed to infinity, with an intensity $\Delta\Gamma_j = \Gamma_j - \Gamma_{j-1}$, for the j^{th} vortex element.

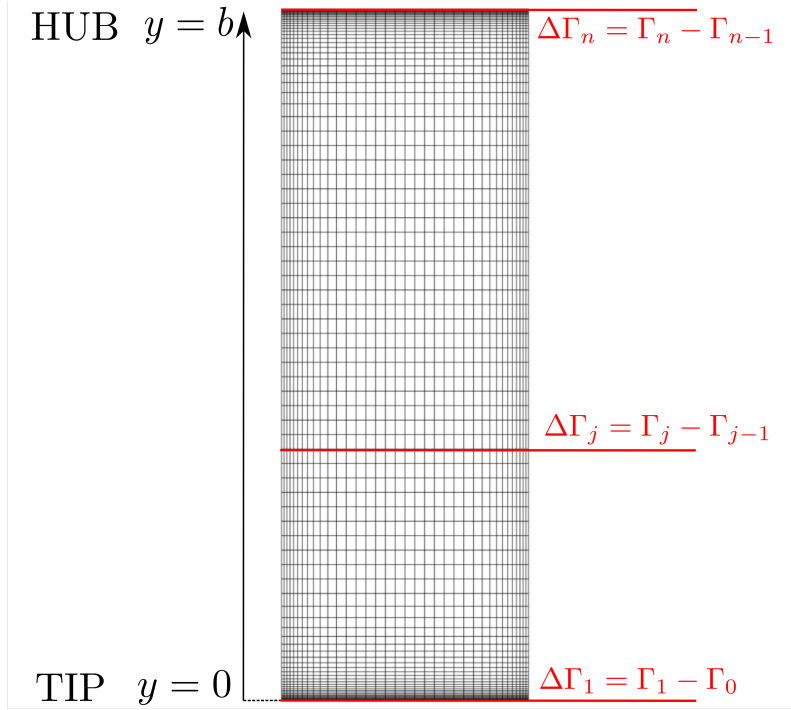


Figure 5.3: Discretization used on the flat plate between the hub ($y = b$) and the tip ($y = 0$). 37 points chordwise and 92 points spanwise. The red lines represent the legs of the shed horseshoe vortices along the span.

5.2.2 Distribution of bound circulation

Let us first analyze the impact of the tip gap size on the bound circulation Γ_b through the lift coefficient evolution C_L . It is recalled that the lift coefficient is related to the bound circulation as:

$$C_L = \frac{2\Gamma_b}{U_\infty c} \quad (5.4)$$

Figure 5.4a shows the evolution of the total lift coefficient as a function of the tip gap size τ . The circulation $\Gamma_b(y)$ is discretely computed at each spanwise position j of the vortex grid on the flat plate with VLM as

$$\Gamma_j = \sum_{i=1}^m \Gamma_{i,j}. \quad (5.5)$$

Two things can be noted in this figure. First, the total lift coefficient decreases with the tip gap size. Second, the slope of the curve flattens with the tip gap size, getting closer and closer to the infinite gap case for which the lift is the lowest. To understand better this evolution, Figure 5.4b exhibits the lift distribution over the span for three different tip gap sizes. The constant lift lines in dashed and dotted lines indicate the two-dimensional c_l for which no vorticity is shed. With VLM, this case was treated in Chapter 3 with a large aspect ratio. With RANS, the simulation was carried out in 2D with one grid element spanwise. The difference between the two values is due to the fact that the linearity assumption on the lift polar is slightly lost at

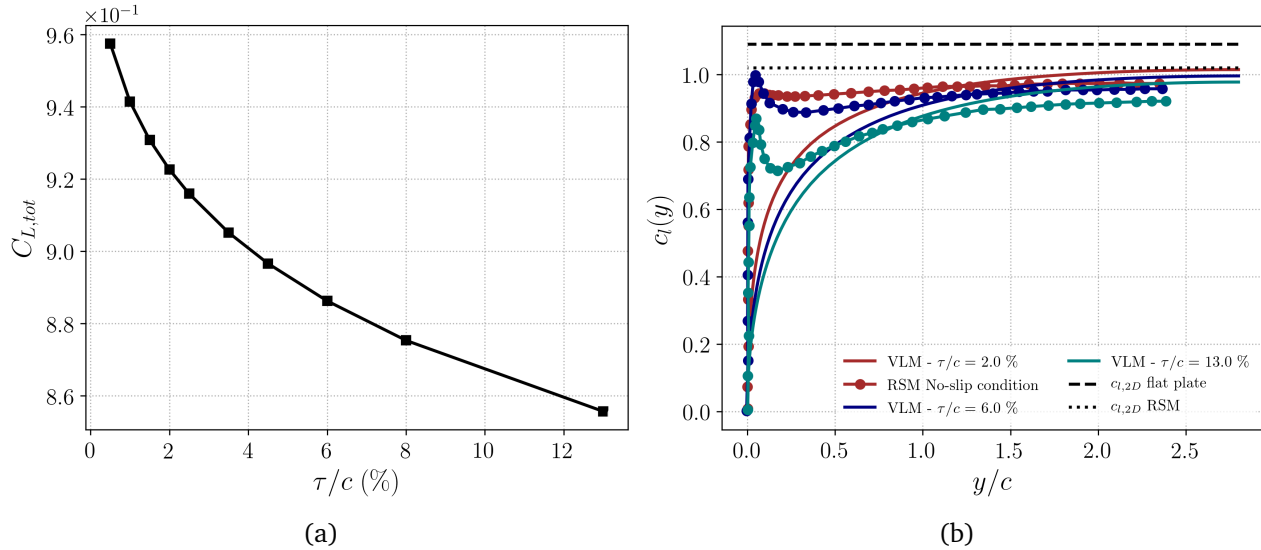


Figure 5.4: (a) Evolution of the lift coefficient C_L with respect to the tip gap size τ obtained with VLM. (b) Spanwise distribution of lift with VLM and from the RSM simulation with a no-slip condition at casing and $\theta/c = 0.6\%$.

$\alpha = 10^\circ$ where viscous effects are more and more important (stall is about $\alpha \approx 15^\circ$ for the NACA0012 airfoil, see for example [116]).

The total circulation (resp. lift) is simply computed by summing the circulations of every panel over the span in VLM. The decrease observed in the lift coefficient is coherent with the fact that the lift is lower over the whole span for the larger gap (13%) than for the two smaller gaps plotted. Regarding the comparison with the 3D RANS simulations, the tendency in terms of lift distribution as a function of the tip gap size is the same: the larger the gap, the farther from the $2D$ lift coefficient. Two major differences can be noted other than the values of the $2D$ lift coefficients. Between hub ($y/c = 2.8$) and midspan ($y/c = 1.4$), VLM overestimates the lift compared to RSM, but getting closer to the tip, the two curves cross over. This crossover occurs closer to the tip with larger gaps and this is particularly remarkable with $\tau/c = 13\%$. This is due to the presence of a peak of high intensity in the tip region captured by the RANS simulations. This peak is larger for the larger gaps and is barely noticeable for $\tau/c = 2\%$. Deveaux explains the presence of this peak, in the lift coefficient, for the large gaps by two combined effects: the closer proximity of the TLV with the blade suction side and its larger circulation.

5.2.3 Shed circulation

One of the most interesting features of the TLV is its circulation since it is a good indicator of how it disturbs the flow. One of the consequences of a larger TLV circulation is the diminution of the deflection that would be obtained if the streamlines followed the deviation of the blade. This has a big impact on compressor rotors as described in Chapter 1.

The lifting line theory gives the way to estimate the TLV circulation by calculating the shed

circulation defined by

$$\Gamma_{shed} = \int_{y=0}^b -\frac{d\Gamma}{dy} dy \quad (5.6)$$

From Figure 5.4b, the variations of circulation (resp. lift) are much larger near the tip than at the hub where the curve is flat, corresponding to $\frac{d\Gamma}{dy} = 0$ and no subsequent shed circulation. As it was observed experimentally and numerically, the vast majority of the circulation is shed at the tip. The integration of $-\frac{d\Gamma}{dy}$ over the whole span as a way to estimate the TLV circulation therefore seems consistent.

Now, the tendency observed in Figure 5.4a with VLM is explained by the fact that the shed circulation is calculated as an alternate sum with the VLM:

- for the first node, $j = 0$, $\Delta\Gamma_1 = \Gamma_1 - \underbrace{\Gamma_0}_{= 0 \text{ due to Helmholtz's theorem}}$ (the node at the tip)
- for the j^{th} node, $\Delta\Gamma_j = \Gamma_j - \Gamma_{j-1}$

For each $\Delta\Gamma_j$ over the span of the blade, a circulation $-\Delta\Gamma_j$ must be shed according to the lifting line theory, following Helmholtz's principle: no vortex line can end in a fluid. As a consequence of this principle, the circulation at the tip is zero and any variation on the spanwise circulation must be shed to infinity to compensate that variation, by conservation of the circulation in potential theory. The shed circulation therefore writes:

$$\Gamma_{shed} = -\sum_{j=1}^n \Delta\Gamma_j = -[(0 - \Gamma_1) + (\Gamma_1 - \Gamma_2) + \dots + (\Gamma_{n-1} - \Gamma_n)] = \Gamma_n \quad (5.7)$$

The shed circulation then corresponds to the bound circulation at the hub. The tendency observed in Figure 5.4b consequently predicts a decrease of the shed circulation when the tip gap size increases.

Figure 5.5 compares the shed circulation predicted by VLM based on equation (5.7) and the circulation of the TLV obtained experimentally. The latter is calculated by integration of the axial vorticity in the tip region based on the 5-hole probe measurements in plane $x/c = 1.05$. As mentioned in section 5.1, only the positive axial vorticity is integrated to avoid counting the influence of the induced vortex.

The first important thing to notice is that the method achieves a very good agreement with the experiment for the two larger gaps ($\tau/c = 8$ and 13%). This is an important result, since it shows that the VLM, originally developed for external aerodynamics, can be applied to TLF. The quality of the results for large gap values is consistent with the hypotheses of the method, since viscous effects are more likely to be negligible in these conditions. In order to improve the results at lower gap values, a viscous model will have to be introduced thereafter.

Looking at the tendency of the evolution with τ of the normalized circulation Γ_{TLV} predicted with VLM, it follows the observations done with the spanwise distribution of circulation: VLM predicts a decrease of the shed circulation when the tip gap size increases. This decrease is however slight since it ranges between 0.48 and 0.52. The tendency is opposite to that from the experiment, where the circulation increases over a wider range with τ/c . Here, the viscosity

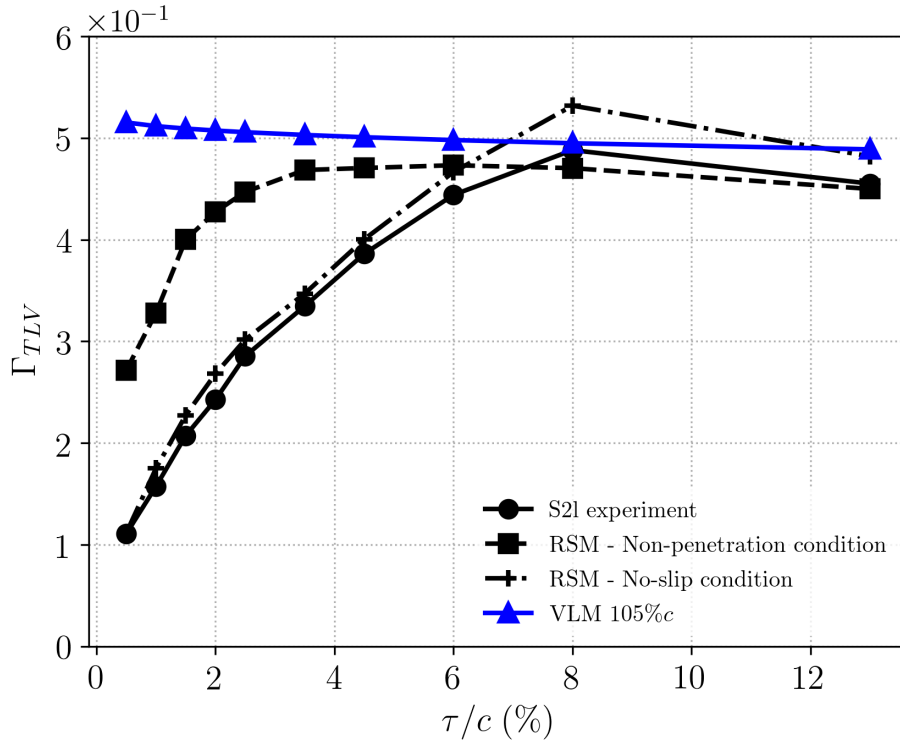


Figure 5.5: Normalized circulation of the TLV at position $x/c = 1.05$, as a function of the tip gap size, from the experiment, from the RSM based on a non-penetration condition at casing, and from the integration of the shed vorticity with VLM. The circulation is normalized by $U_\infty c$.

probably plays a role in explaining why the tendency is not good and in the important difference between the VLM and the experiment for the smaller gaps ($\tau/c < 8\%$).

Let us now comment on the circulation calculated with the RANS simulation with a non-penetration condition at casing. First, the values for the two larger gaps are close to VLM and the experiment. For lower values of the tip gap, the circulation is overestimated with this boundary condition at casing compared to the experiment. The overestimate is about constant (≈ 0.15) between $\tau = 0.5$ and $2.5\% c$ and drops as the tip gap size increases. The fact that the boundary layer is not accounted for by the non-penetration condition with the RANS simulation could explain this behaviour: for larger gaps, the interaction of the TLV with the boundary layer is less and less significant and the non-penetration condition then seems sufficient to predict the experimental value of the TLV circulation correctly. The non-penetration condition applied with RANS nevertheless captures correctly the TLV circulation increase with the gap size, contrary to VLM.

In Figure 5.5, the results from RANS with the non-penetration condition are intermediate between the experiment and the VLM. This is consistent with the level of description of the viscous effects: they are included in the simulation, except for the development of the casing boundary layer, while they are completely neglected in VLM.

Moreover, VLM is in good agreement with the RANS simulation for $\tau > 3.5\% c$, with a slight constant overestimate of the circulation up to $\tau/c = 13\%$. A slight decrease can be seen

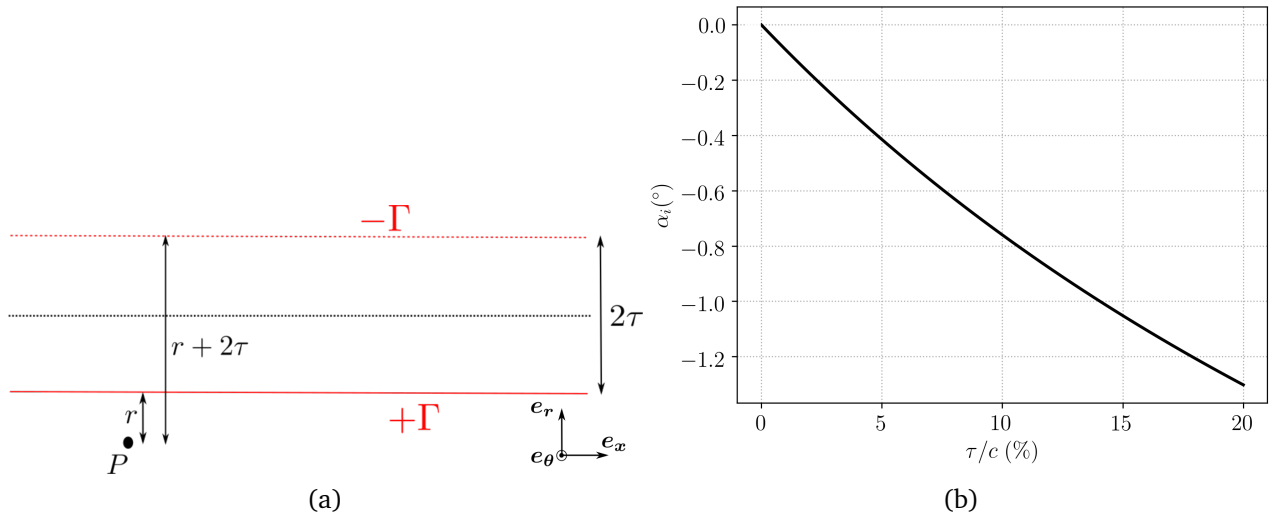


Figure 5.6: (a) Sketch of two infinite vortices of opposite circulation $\Gamma = 0.5 U_\infty c$ (about the value predicted by VLM for the larger gaps, see Figure 5.5) at 2τ from each other. (b) Induced angle at point $P(x, r = c)$ as a function of the normalized tip gap size τ/c .

with the two approaches for increasing tip gap sizes. Finally, as seen in Figure 5.5, including the development of the casing boundary layer in the RANS simulation allows a good agreement with the experiment.

5.2.3.1 Interaction of two infinite potential vortices

How can the decrease of shed circulation with increasing τ be explained with VLM? Let us simplify the potential calculation to the interaction of two infinite potential vortices. This simplification is done with the aim of understanding better the tendency obtained with VLM, knowing that most of the TLV circulation is shed at the tip. Figure 5.6a illustrates the interaction of two mirror infinite vortices of opposite circulations, 2τ away from each other, representing a simplified TLV and its image.

Biot-Savart law enables to calculate the velocity induced by the circulations of the two infinite vortex lines, which expresses as follows, in cylindrical coordinates:

$$\mathbf{V}(P) = \frac{\Gamma}{2\pi} \left[\frac{1}{r} - \frac{1}{r+2\tau} \right] \mathbf{e}_\theta = \frac{\Gamma}{2\pi} \frac{2\tau}{r(r+2\tau)} \mathbf{e}_\theta \quad (5.8)$$

Referring to Appendix B, the induced angle α_i can be expressed as

$$\alpha_i = \text{Arctan} \frac{-V_\theta}{U_\infty} \quad (5.9)$$

As an illustration, Figure 5.6b shows the evolution of the induced angle α_i as a function of the tip gap size at P with $r = c$. The larger is the gap, the larger is the downwash and subsequently the lower is the lift, even far from the vortex pair.

Note that the effect on the vortex pair is a drift in the tangential direction, due to the mutual interaction of one vortex with the other.

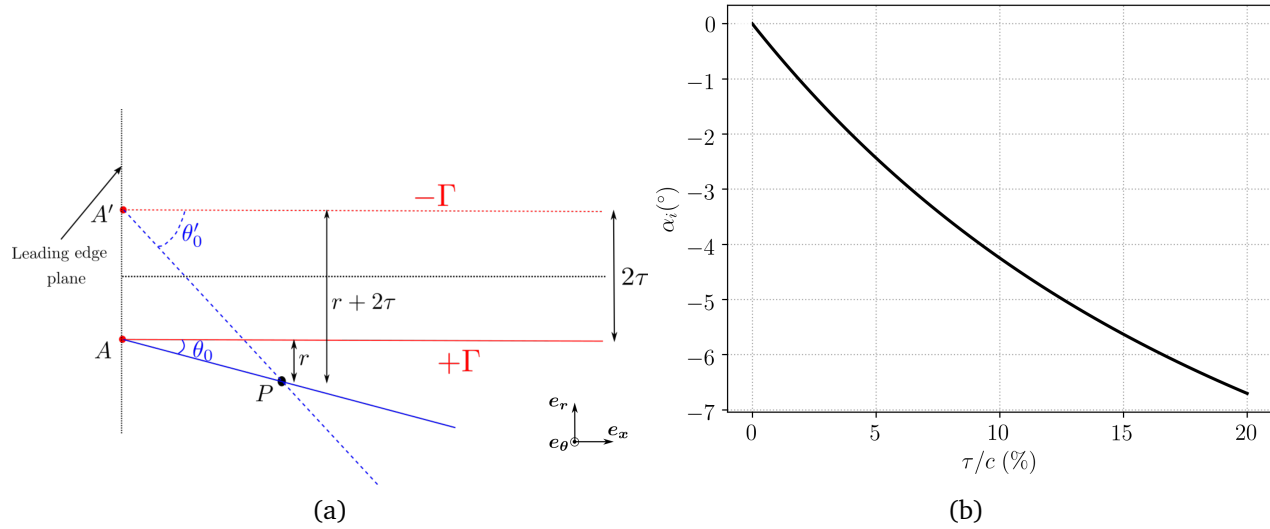


Figure 5.7: (a) Sketch of two semi-infinite vortices of opposite circulation $\Gamma = 0.5 U_\infty c$ at 2τ from each other. (b) Induced angle at point $P(x = 0.5c, r = c)$ as a function of the normalized tip gap size τ/c .

5.2.3.2 Interaction of two semi-infinite potential vortices

To go further than the case of two infinite potential vortices, the case of two semi-infinite vortices with opposite circulations is considered, starting at an equivalent leading edge plane. They better model the TLV at the tip of the blade and its image, 2τ distant from it, as exhibited in Figure 5.7a. The induced velocity at point P is expressed as follows:

$$\mathbf{V}(P) = \frac{\Gamma}{2\pi} \left[\frac{1}{r}(1 + \cos \theta_0) - \frac{1}{r + 2\tau}(1 + \cos \theta_0') \right] \mathbf{e}_\theta \quad (5.10)$$

The evolution of the induced angle with τ , in Figure 5.7b, at $P(x = 0.5c, r = c)^2$, is the same as for two infinite vortices but the levels are more important in that case.

Getting back to the evolution of Γ_{TLV} predicted by VLM (Figure 5.5), an explanation to the decrease with the tip gap size can be brought. The simplification of the problem to two semi-infinite vortices of opposite circulations showed that the larger is the gap, the larger is the induced angle and hence, the lower is the lift. This effect is still significant a chord length away from the vortex pair. Consequently, a decrease of lift at the hub and all over the span when the gap size increases can be expected. The augmentation of τ induces a decrease of the lift over the whole span, equivalent to a decrease of the bound circulation $\Gamma_b(y)$ and $c_l(y)$. As explained before, the shed circulation is calculated with equation (5.7) and the global decrease of the bound circulation with the tip gap size therefore explains the tendency obtained with VLM on Γ_{TLV} . With the potential approach, opening the gap thus has a slight beneficial effect since the circulation of the TLV decreases. Physically, it behaves otherwise and other effects must be considered.

² $\cos \theta_0 = \frac{x}{\sqrt{x^2 + r^2}}$

The retained vorticity coefficient K of Lakshminarayana and Horlock (see Chapter 1) in their lifting line model was introduced for the same reason. The shed circulation as a function of the tip gap τ depends on this coefficient K and is worth $(1 - K)\Gamma$, with $1 - K$ an increasing affine function of the tip gap size. The idea is that for a larger gap, K quantifies the retained vorticity, less and less important as the tip gap value grows.

5.2.3.3 Axial evolution of Γ_{TLV}

With the help of VLM, it is possible to get the axial evolution of $\Gamma_{TLV}(x)$. It is compared to what is obtained with the RANS RSM simulation, with the non-penetration condition. The advantage of using VLM compared to the lifting line theory when applied to TLF is the discretization of the chord. The increase of the circulation along the chord replicates better the physics described in Chapter 4, where the TSV feed the total circulation of the TLV developing. Indeed, several vortices are shed through the legs of the HSV discretizing the blade and increase the total shed circulation along the chord (see Figure 3.8 as an illustration). In our case, $\Gamma_{TLV}(x)$ increases at every x_i where a HSV is located and writes:

$$\Gamma_{TLV}(x) = \sum_{i=0}^{i_x} \Gamma_i^{shed} \quad (5.11)$$

where i_x is such that $x_{i_x} < x < x_{i_x+1}$. The circulation Γ_i^{shed} is the result of the integration of $-\frac{d\Gamma}{dy}$ between $y = 0$ and $y = b$ at the axial position x_i . For $x > c$, the total circulation shed Γ_{TLV} from (5.7) is retrieved and is no longer dependent of x .

Figure 5.8 shows the development of the circulation along the chord for three tip gap sizes, with VLM and with RANS RSM with a non-penetration boundary condition at casing. The increase of circulation with VLM is less and less significant close to the trailing edge. Most of the circulation is indeed shed at the leading edge. The rate of increase is similar to RANS, although nearly no difference can be seen between the three tip gap sizes. Consistently with the evolution of Γ_{TLV} with the tip gap size, which indicated a very slight decrease of the circulation, the total circulation shed at the trailing edge for the larger gap is slightly lower than that of the lower gap with VLM. Since the circulation is conserved in potential theory, it remains constant downstream of the trailing edge with VLM. This is another difference with RANS: in RANS, the circulation starts decreasing downstream the trailing edge and more importantly with the smaller gap, reaching half of the maximum circulation value after $80\%c$. In comparison, for $\tau/c = 6\%$, half of the maximum circulation is obtained more than one chord downstream of the trailing edge.

5.2.4 Detachment point

The position where the TLV detaches is important to correctly predict the development of the TLV in the passage. In Chapter 4, it was shown that the position of the detachment point is situated at the maximum transverse velocity, which also corresponds to the maximum blade

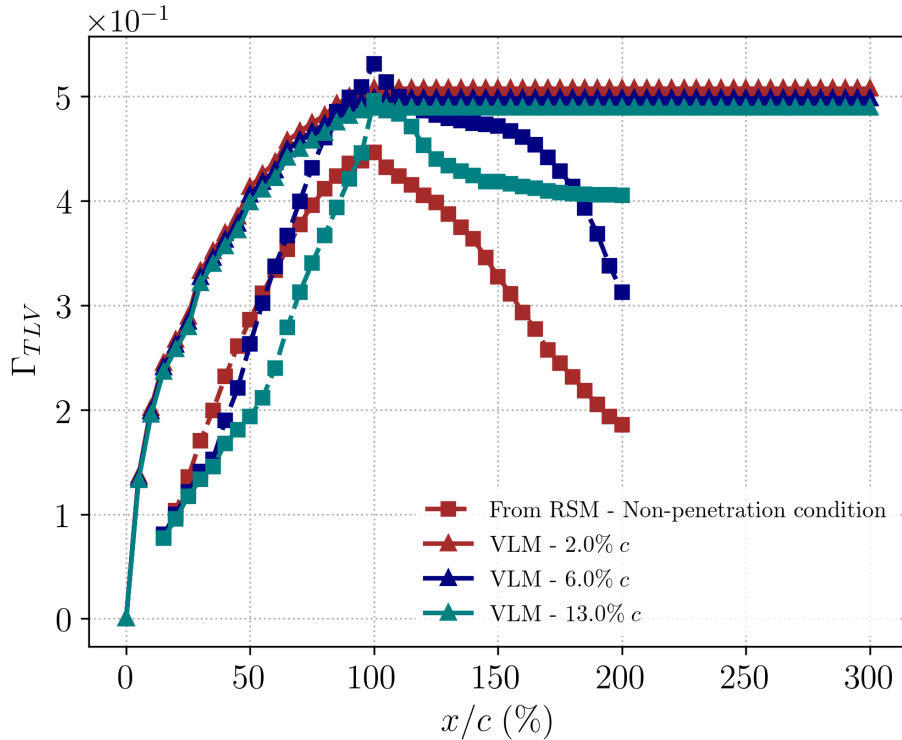


Figure 5.8: Axial evolution of Γ_{TLV} predicted with VLM and RSM with a non-penetration condition at casing.

loading along the chord $\Delta c_{p,max}$ at the tip. As described in Chapter 3, the blade loading can be calculated from the circulation distribution over the blade.

Figure 5.9 shows the blade loading at midspan and at the tip through the axial evolution of the pressure difference coefficient Δc_p . Both boundary conditions at casing for RSM are plotted in the figure, superimposing perfectly. The figure compares the values extracted with VLM and with RSM for four tip gap sizes ($\tau/c = 3.5, 6, 8$ and $13\% c$). At midspan, both with VLM and RSM, the loading is unaffected by the tip gap size. Sufficiently far from the tip given the dimensions of the blade, such a result is coherent with the fact that the tip-leakage effects are limited to the tip region of the blade. Regarding the differences between VLM and RSM, VLM predicts a loading slightly underestimated between the leading edge and midchord and, on the contrary, overestimated down to the trailing edge. Nevertheless, coherently with the lift distribution of Figure 5.4, the difference between VLM and RSM is not large at midspan.

At the tip, the two approaches compare differently and VLM underestimates the blade loading. Again, this can be observed through the lift distribution: close to the tip, c_l drops continuously. More interestingly, the chord loading distribution with VLM slightly decreases with the tip gap increase, tendency also got with RSM in the first 40% chord length. But contrary to VLM, RSM presents a bump on the loading shifted towards the trailing edge when increasing the gap and more visible for $\tau/c > 6\%$. This bump corresponds to the position where the TLV actually detaches from the suction side of the blade. The positions of the local maximum observed on the blade loading at the tip are summarized in Table 5.3. One can notice the shift towards the

trailing edge when the gap is increased, getting very close to the trailing edge for the larger gap.

The VLM is therefore insufficient to correctly predict the position of the detachment point as a function of the tip gap size.

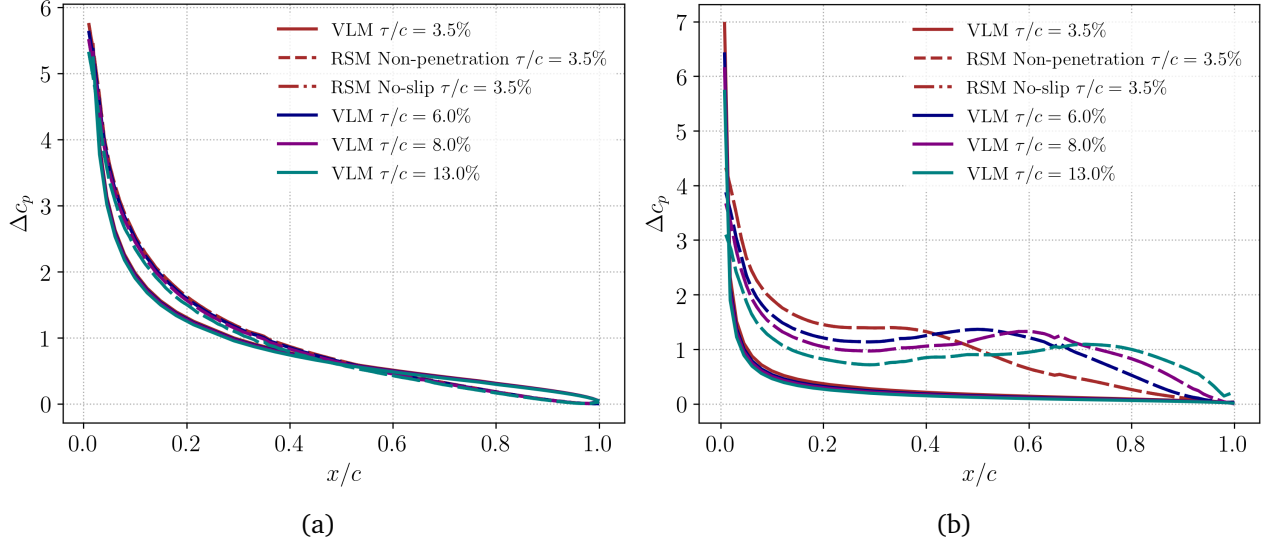


Figure 5.9: Axial evolution of the pressure difference coefficient Δc_p for three tip gap sizes, (a) at midspan, and (b) at the tip ($y = 2\% b$, the tip being at $y = 0$).

τ/c (%)	3.5	6	8	13
x/c	0.39	0.51	0.6	0.77

Table 5.3: Position of the local maximum of Δc_p at the tip, for the different tip gap sizes plotted in Figure 5.9, predicted by RSM.

5.2.5 Trajectory of the TLV

The trajectory of the TLV determined with Chen's correlation introduced in the literature review is compared with LDA measurements and RSM simulations for different values of the tip gap size. First, a quick explanation on how the vortex core position is determined in Deveaux's thesis is necessary. The vortex core position (y_c, z_c) is calculated as the centroid of axial vorticity in the tip-leakage vortex delimited by the region of surface area S_{TLV} [43]:

$$(y_c, z_c) = \frac{\int_{S_{TLV}} (y, z) \omega_x \, dydz}{\int_{S_{TLV}} \omega_x \, dydz} \quad (5.12)$$

Let us first comment on the trajectory of the TLV obtained with LDA for the three tip gap sizes exhibited in Figure 5.10a. The tip gap size here has a big impact on the TLV trajectory. The TLV is indeed closer and closer to the blade suction side for increasing gaps. That is because the

detachment point (DP) is located closer and closer to the trailing edge of the blade. The RSM simulations fit quite well to the LDA measurements for the three gaps showed.

The slope of the TLV trajectory predicted by Chen's correlation is plotted in Figure 5.10a against the other trajectories. There is no influence of the tip gap size, since the loading at midspan is unaffected. The starting point of the curve is situated at the leading edge since the VLM does not capture the bump observed in the loading at the tip, indicator of the TLV detachment. The positions of the detachment points associated to each gap is indicated by the black crosses for the RSM simulations.

Downstream of the detachment point, the slope predicted with Chen's correlation is relevant compared to the TLV trajectories obtained with RSM for the three different gaps. This is remarkable for the two larger tip gap sizes, 6% c and 13% c . For the smaller gap, the tendency is good from the point of detachment to 70% c where the trajectory is curved and deviated towards the suction side. This could be due to the interaction of the TLV with the casing boundary layer and the viscous effects, which tend to reduce the drifting velocity of the TLV.

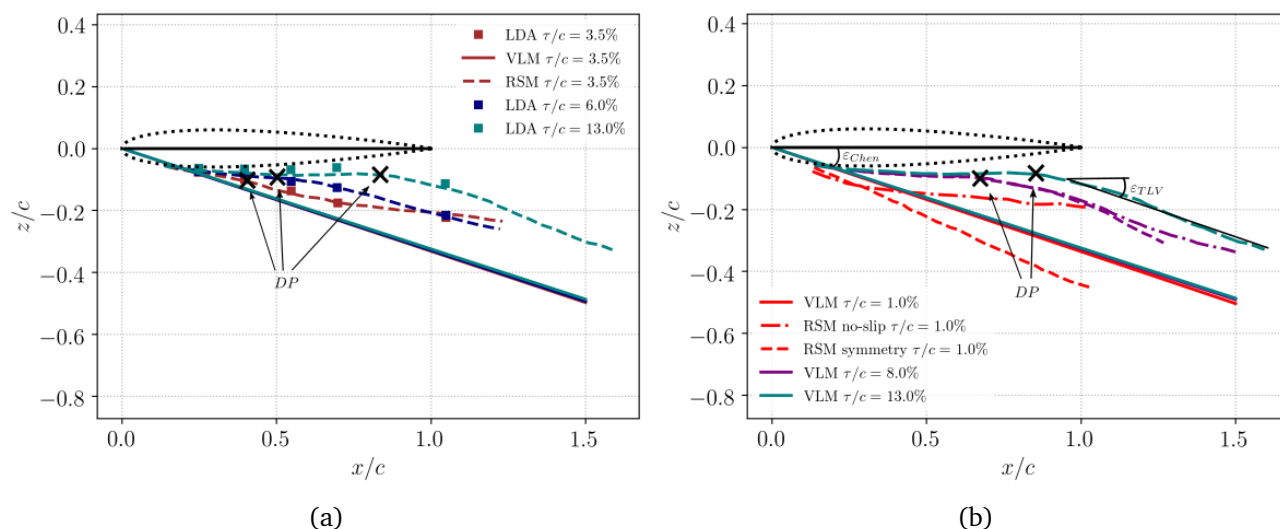


Figure 5.10: Lateral trajectory of the TLV, comparing VLM with Chen's correlation to numerical and experimental results (a) VLM, LDA measurements and RSM with a no-slip condition at casing. (b) VLM and RSM with non-penetration and no-slip conditions. The black crosses indicate the approximate position of the detachment point of the TLV (DP).

This effect is emphasized in Figure 5.10b, where the no-slip and the non-penetration conditions at casing are compared with RSM. For the smaller gap ($\tau/c = 1\%$), the trajectory is rapidly deviated with the no-slip condition compared to the straight line predicted with the non-penetration condition. From about 30% chord length, the TLV is deviated towards the suction side and the slope of the trajectory largely decreases. Compared to $\tau/c = 3.5\%$, the deviation occurs more upstream and reduces the slope more intensely with this gap, the second smallest in the range of sizes treated. The proximity of the tip to the casing favours this phenomenon by intensifying the interaction of the TLV with the casing boundary layer. In comparison, for the two larger gaps of the study ($\tau/c = 8\%$ and 13%), the trajectories predicted with the no-slip and

the non-penetration conditions at the casing are the same and follow a straight line. Moreover, the slope of this straight line is the same in the three cases with the non-penetration condition. A slight deviation only occurs downstream of the trailing edge for $\tau/c = 8\%$.

Finally, the slope predicted by Chen's correlation and VLM is in acceptable agreement with the slope obtained with RSM and the non-penetration condition at casing for the three gap sizes. The RSM slope is measured by an angle, denoted ε_{TLV} and indicated in the figure as an example for $\tau/c = 13\%$. It is calculated from the detachment point, whose position is marked by a cross. For $\tau/c = 1\%$, the trajectory obtained with the non-penetration condition is a straight line from its starting point and the slope is then calculated between the two ending points of the curve.

However, the angle predicted with the correlation overestimates the angle obtained with the no-slip condition, that is closer to the LDA measurements because the casing boundary layer effects are taken into account. Let us recall that Chen's correlation was calibrated on a compressor configuration [65]. One effect is the moving endwall, that moves the TLV farther away from the suction side. With the present configuration, the casing is not in motion in the frame of reference of the blade, and the TLV is actually closer to the suction side than it would be with a moving endwall. By using the coefficient of Chen's correlation $K_{Chen} = 0.46$, the trajectory slope for the single blade here is therefore overestimated. This was observed by Kang and Hirsch [71] on their linear cascade, which led them to set the coefficient K_{Chen} to 0.19 for a good fit for the TLV trajectory.

5.3 Construction of a viscous model

The previous section showed the results of the Vortex Lattice Method applied to TLF. It clearly indicates that the potential approach is not sufficient to model the TLV since the increase of the TLV circulation with τ is not captured. This feature is essential to correctly model TLF and very important since the amount of circulation directly relates to the overall deviation in the tip region (see section 1.4.4): a stronger TLV is responsible for a stronger perturbation of deviation and for subsequent additional losses. One of the major effects not considered with the VLM is the viscosity. This section is intended to go through this effect and see how it changes the results from VLM.

5.3.1 Viscous diffusion of a vortex dipole

As explained in the previous section, the interaction of two semi-infinite potential vortices with an opposite circulation cannot explain the evolution of the TLV circulation with the tip gap size. Adding the viscosity to the problem is envisaged through this section. First, the interaction of two contra-rotating vortices diffusing with time due to viscosity is investigated through a literature review.

Van Geffen and Van Heijst performed numerical simulations on the viscous diffusion of a two-dimensional Lamb dipole [140], represented in Figure 5.11. Their analysis was done following experiments on vortex dipoles whose characteristics are well described by the Lamb dipole [82].

Their study shows that the Lamb dipole moves along a straight line with a decreasing velocity $U(t)$ and an increasing radius $a(t)$, compared to an inviscid vortex pair that also moves along a straight line but with a constant drift velocity U_{drift} and a constant radius. The particular case introduced in Figure 5.7 is irrotational and the core radius is therefore $a = 0$ and remains constant. Viscosity would affect these characteristics.

The most interesting result of their study concerns the evolution with time of the vortical dipole. The dipole evolution with time can be divided into two phases, starting from a situation comparable to Figure 5.7 in two dimensions (*i.e.* two singular vortices of opposite circulation):

- The radius of the two vortices grow until they reach $a(t) = \tau$.
- The two vortices collide and non-linear effects come up.

The first phase is well described with the radius growth only and the circulation of the area with a positive (resp. negative) vorticity remains constant. The core radius diffusion with time can be calculated as:

$$a^2(t) = a_0^2 + 4\nu t, \quad (5.13)$$

with a_0 the initial radius, following Lamb's vortex equation (see Appendix B).

In the second phase, the circulation magnitude of the positive (resp. negative) part starts decreasing, leaving trails of vorticity behind, due to the interaction of the two vortical structures. However, the Lamb dipole maintains its structure over time, as represented by Figure 5.11, with two slightly elliptically-deformed vortices. A line can clearly be drawn between positive and negative vorticities. The authors also tested other initial conditions for the development of a vortex pair: their results show that all the vortex pairs they considered evolve towards a dipolar structure with Lamb-like characteristics.

The Direct Numerical Simulation (DNS) from Delbende and Rossi [39] was initiated with a system of two slightly elliptical Lamb-Oseen vortices, with opposite circulations $\pm\Gamma_0$, separated by a distance b_0 from each other, with an initial radius $a_0 = 0.1b_0$. Figure 5.12 shows the time evolution of the dipole up to the dimensionless time $t = 1000$, based on the time scale $T_0 = b_0^2/\Gamma_0$. Up to $t = 40$, the distance between the vortices remains constant and their radii grow. After that, the distance between the vortices increases, the core of the vortices keep growing and a trail of vorticity appears. This trail is a result of both the vorticity diffusion outside the dipole head and its convection downstream. The authors investigate the use of an analytical solution for the trail structure, modelling the thickness and the maximal vorticity evolution, accounting for the formation of the trail at the collision of the two vortices and its convection. Their DNS enables to identify three main phases of development of the vortices: the first one is similar to the first phase found by Van Geffen and Van Heijst until $t = 40$. The second phase can be further divided into a transient evolution (until $t = 450$) and a steady one after that, where the dipole characteristics can be described with a self-similar hypothesis. During the transient phase, the two vortices seem to get elongated in one direction, increasing the ellipticity of the structures, which are then no longer circular.

The circulation magnitude of the positive (resp. negative) vortex is also found to decrease with time due to the shedding of the vorticity trail.

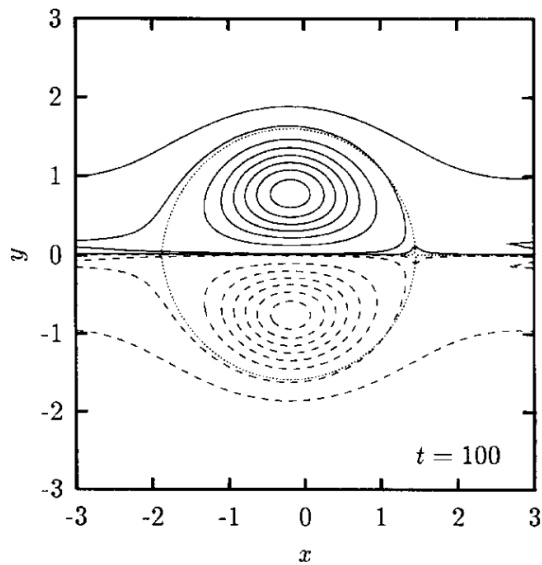


Figure 5.11: Contours of vorticity of the evolved Lamb dipole, from [140]. Solid lines represent the positive vorticity, dashed lines the negative one.

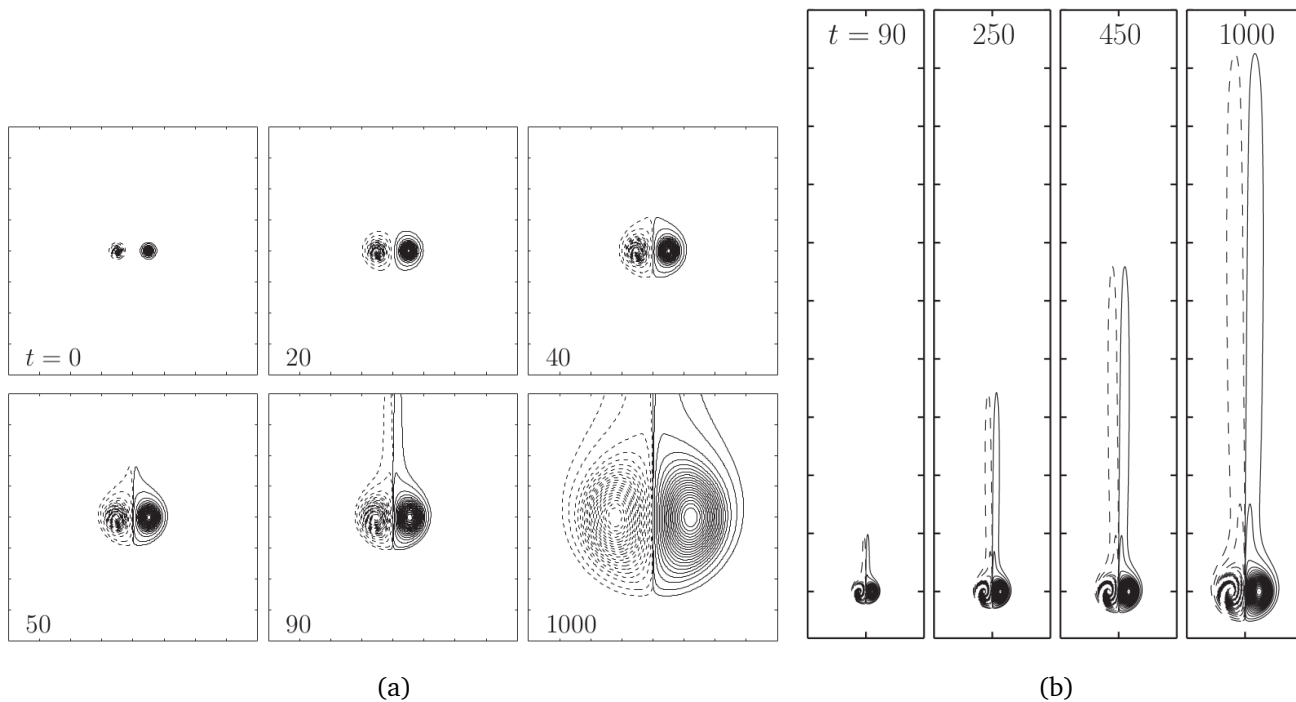


Figure 5.12: Evolution with time of the Lamb dipole, from [39]. Solid lines represent the positive vorticity contours, dashed lines the negative one.

5.3.2 Estimation of the eddy viscosity

Trailing vortices downstream of an airplane wing are persistent structures that decay due to the action of viscosity and turbulent stresses. The action of a molecular viscosity ν to predict the decay of such structures is insufficient since it leads to time scales of decay much larger than the observed physical time. In order to account for the turbulence, Squire [133] assumed that the decay of a turbulent vortex could be calculated from a constant eddy viscosity ν_t . The diffusion of the vortex is then modelled by the diffusion of a laminar vortex with an apparent viscosity $\nu + \nu_t$, acting faster on the rate of diffusion and then dissipation, in better agreement with the experimental observations. With Squire's model, the eddy viscosity is uniform over the entire flow field and is proportional to the circulation of the trailing vortex Γ :

$$\nu_t = \alpha\Gamma \quad (5.14)$$

The decay is studied through the time evolution of the maximum tangential velocity in the vortex (see Appendix B for more details on the analytical vortex models). It showed good agreement regarding the decrease tendency of the velocity, varying like $t^{1/2}$, and the rate of dissolution depending on the circulation Γ .

Owen's model [102] goes further than Squire by making the coefficient α in equation (5.14) dependent of the circulation as well. The decay is also envisaged by representing the trailing vortex as an analytical vortex similar to Lamb's with three main zones:

1. The core similar to a solid body in rotation, free from any rate of strain and containing most of the vorticity ($V_\theta \propto r$).
2. An annular disk around the core where the turbulent stresses act (V_θ is a constant).
3. The outer irrotational flow with a circulation equal to Γ ($V_\theta \propto 1/r$).

Figure 5.13 shows the evolution of the pitch component of the velocity with the radius. Lamb's analytical vortex is in fact very similar to Rankine vortex with the same zones 1 and 3 but with a transition zone in-between that would fairly correspond to zone 2 described by Owen, approximated as uniform in his model.

The radius of the vortex core is found to be growing as Lamb's vortex with an apparent viscosity $\nu + \nu_t$ following:

$$R_c = \sqrt{4(\nu + \nu_t)t} \quad (5.15)$$

The eddy viscosity ν_t is estimated by Owen with equation (5.14) but α is not a constant and is calculated as:

$$\alpha = \Lambda^2 \left(\frac{\Gamma}{\nu} \right)^{-1/2} \quad (5.16)$$

In fact, the eddy-to-molecular ratio can be written as

$$\nu_t/\nu = \frac{1}{\sigma^2} \quad (5.17)$$

with σ defined by

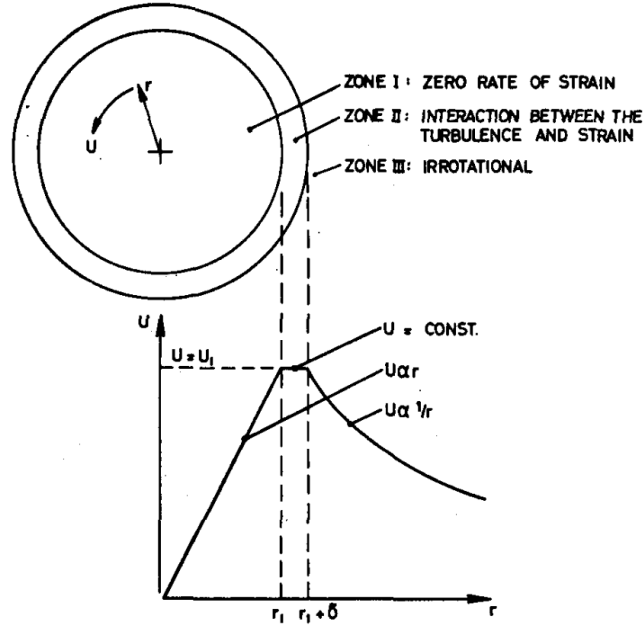


Figure 5.13: Turbulent analytical line-vortex model from Owen [102], represented by the evolution of the circumferential velocity V_θ , denoted U in the figure, with the radius r .

$$\sigma^2 = \delta_{Owen}/R_c, \quad (5.18)$$

and prescribed to a constant value. δ_{Owen} represents the thickness of the plateau in Owen's vortex model where turbulence is acting (Zone 2), driven by different coefficients introduced in the article, defining the global coefficient Λ . From equation (5.17), it can be seen that when δ_{Owen} is decreased compared to R_c , the eddy-to-molecular ratio will increase. With time, the core radius precisely increases but the eddy viscosity is assumed constant in the model, which means that the modelled δ_{Owen} also increases with time, at the same pace as the core radius, thus maintaining a constant ratio. The vorticity spreads over a larger area due to diffusion and the turbulence stresses act on a larger area as well on the diffused vortex. As a consequence, the turbulence also appears to be spread out over a larger area in this model.

The characteristics of Owen's vortex model are similar to Lamb's. The advantage of using Lamb's analytical vortex lies in the relative simplicity of the expression of the circumferential velocity and the associated axial vorticity. Applying the viscous diffusion with the apparent viscosity $\nu + \nu_t$ is indeed straightforward with Lamb's vortex model. Besides, the model has the advantage of presenting a continuous slope in-between the rotational region (zone 1) and the irrotational region (zone 3).

5.3.3 Principle of the new model

In order to account for the viscosity, let us consider the same two vortices with circulations $\pm\Gamma$ introduced in Figure 5.7. As shown in Figure 5.14, a core radius R_c containing most of the

vorticity can be defined, following Lamb's analytical vortex expression:

$$\omega_x(r, t) = \frac{\Gamma}{2\pi R_c^2} e^{-r^2/R_c^2} \quad (5.19)$$

The core radius R_c varies with the convective time t as

$$R_c = \sqrt{4(\nu + \nu_t)t} \text{ with } t(x) = \frac{x - x_{DP}}{U_\infty}. \quad (5.20)$$

x_{DP} is the axial position of the TLV detachment point, set at the leading edge with the model. The circulation of the TLV is entirely shed at x_{DP} . The temporal evolution of the viscous diffusion is directly turned into a spatial evolution through the convective relation of equation (5.20).

The eddy viscosity ν_t is estimated thanks to Owen's correlation which depends on the circulation Γ and the molecular viscosity ν :

$$\nu_t = \nu \Lambda^2 \sqrt{\frac{\Gamma}{\nu}} \quad (5.21)$$

The integration of a single vortex of vorticity $\omega_x(r, t)$ over a plane perpendicular to the axis x along which the vortex diffuses, at any time position t always yields

$$\int_{\theta=0}^{2\pi} \int_{r=-\infty}^{+\infty} \omega_x(r, t(x)) r \, dr \, d\theta = \Gamma \quad (5.22)$$

We saw in the last section that the tip gap size has nearly no influence on the circulation shed. The shed vorticity captured with VLM can be summarized by two extreme cases:

- $\tau/c = 0$ with no vorticity shed. This case is equivalent to a flat plate with an infinite aspect ratio because of the symmetry condition, meaning that the circulation does not vary spanwise, explaining the zero shed vorticity.
- $\tau/c = \infty$ for which the vorticity shed corresponds to the bound circulation at the hub.

In-between, the circulation decreases but very slightly, because the circulation at hub decreases. In fact, the potential approach nearly comes down to an open/closed tip regarding the TLV circulation. Opening the gap with VLM has a slight beneficial effect on the TLV circulation through the evolution of the shed vorticity, but the tip gap size influence remains small.

The idea of the new model is presented in Figure 5.14. The viscous effects are considered through the diffusion of the two contra-rotative Lamb vortices, of circulation magnitude Γ , showed for two tip gap sizes in the figure. The circulation of the TLV, Γ_{TLV} , is the result of the integration on the added vorticities (of opposite sign), from the two vortices, in the tip region (between the dotted line and down the solid line). The initial circulation magnitude is the output of the VLM, yielding the total shed circulation, nearly constant with the tip gap size τ .

For the smaller tip gap size on the left-hand side, the two vortices mix out more rapidly. Their earlier mixing yields an earlier decrease of the total circulation of each vortex. On the contrary, with the larger gap, the two vortices diffuse longer with a core radius $R_c < \tau$ and do not mix.

The idea of the model is discussed through different values for the tip gap size τ , defining different ranges of gaps:

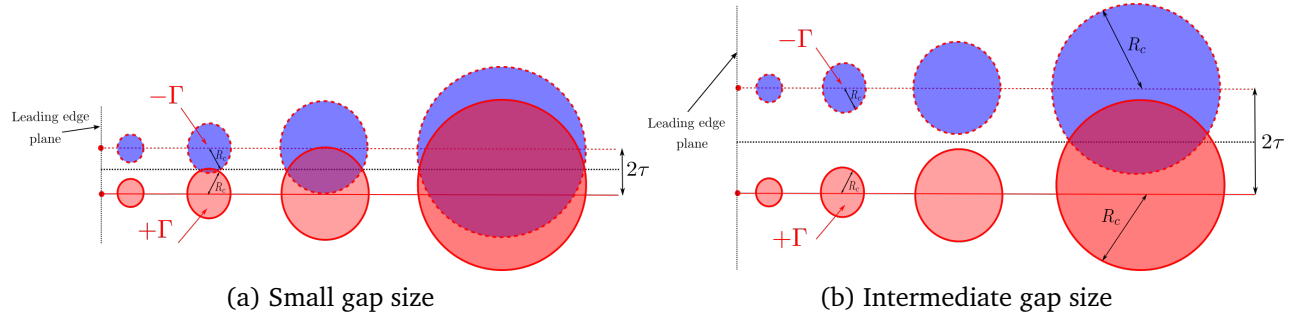


Figure 5.14: Sketch of the modelled interaction of two contra-rotating Lamb-Oseen vortices diffusing with time.

- For $\tau/c = 0$, the two Lamb vortices are completely merged. Since their evolution with time is the same, the circulation in the tip region is zero for any axial position.
- For a small τ/c , the two vortices quickly mix out and the circulation drops.
- For an intermediate gap, the core radius R_c becomes greater than τ farther downstream.
- For a large gap, the core radius remains lower than τ all over the chord: the circulation in the tip region is the same at the trailing edge as at the leading edge. The circulation will only decrease farther downstream.
- Finally, for an infinite gap, the two vortices will never mix out and the circulation will never decrease in the model. Physically, this would correspond to the trailing vortices shed downstream of an aircraft wing that are persistent and energetic. The time scale for their decay is indeed much greater than the advective time $T_{adv} = c/U_\infty$.

5.3.4 Application to *S2l*

Let us now apply this model to the *S2l* configuration. The absolute value of the initial circulation of the two vortices is chosen as the value obtained for the larger gap $\tau/c = 13\%$ with VLM, which fits well the experimental value ($\Gamma = 0.5U_\infty c$).

The model is applied to *S2l* for the range of gaps of Table 5.2. The axial vorticity is integrated at the four stations indicated in Figure 5.15, yielding the modelled circulation of the TLV:

$$\Gamma_{TLV} = \int_{\theta=0}^{2\pi} \int_{r=0}^{r_{tip}+\tau} \omega_x(r, t(x)) |r - r_{tip}| dr d\theta \quad (5.23)$$

with

$$\omega_x(r, t(x)) = \omega_x^+(r, t(x)) + \omega_x^-(r, t(x)). \quad (5.24)$$

The exponent sign in the notation corresponds to the sign of the circulation Γ of each vortex. The axial vorticity will be normalized by the advection time T_{adv} in the rest of the thesis, except if mentioned otherwise, as

$$\tilde{\omega}_x(r, t) = \omega_x(r, t) T_{adv}. \quad (5.25)$$

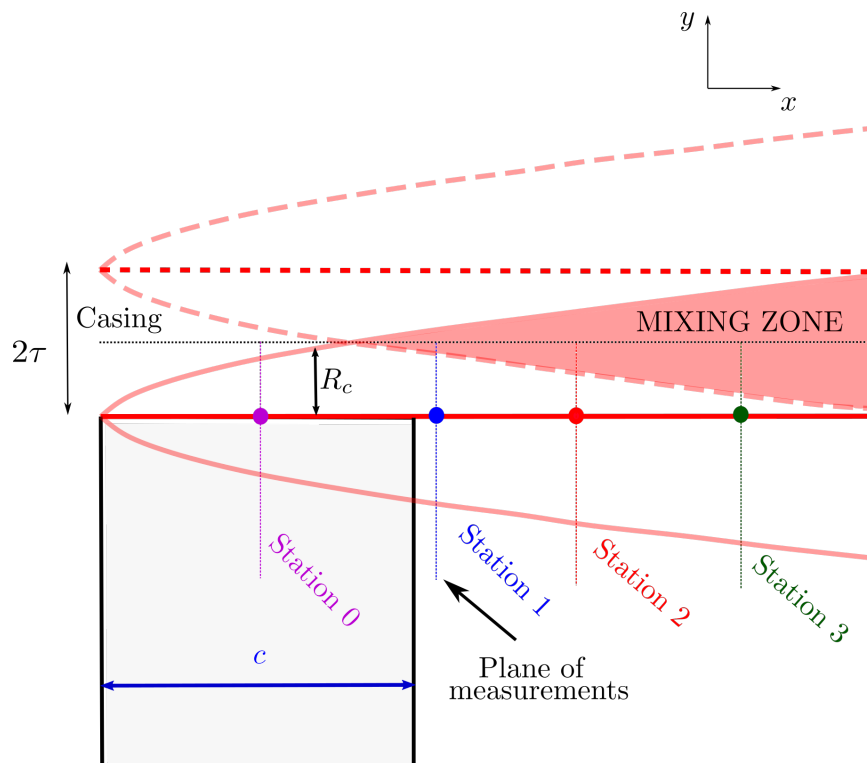


Figure 5.15: TLV core radius growth predicted by the model from the leading edge. The axial vorticity resulting from the mixing of the two vortices is integrated at the four different stations in the figure. Station 1 in particular corresponds to the plane of the experimental measurements.

However, for clarity, the notation is lightened to $\omega_x(r, t)$ for the normalized axial vorticity.

Figure 5.16 shows the normalized axial vorticities of each vortex as a function of the radius in the tip region, from the leading edge ($\omega_x = 0$ everywhere except at r_{tip} and $r_{tip} + 2\tau$ where $\omega_x = \pm\Gamma$) to one chord length downstream of the trailing edge, for two tip gap sizes. The development of the vortices is always the same and the figure illustrates how the vorticity spreads out over a larger and larger radius. It follows equations (5.19)-(5.21) with the coefficient Λ here set to 0.58³. In particular, the maximum vorticity decreases at the same time as the core radius increases, comparing the purple and green curves for example.

What changes is the tip gap size τ and as already described by the sketches before, the two vortices start mixing out earlier for the small gap than for the large gap. In particular, for the small gap at station 0 (midchord), negative vorticity already invaded the tip region, which consequently reduces the positive circulation in that region. When convected, the diffusion of the negative vortex further decreases the total circulation up to $r_{tip} + \tau$, position of the fictive equivalent casing in the model.

When the two vortices are added together in Figure 5.17, the influence of the tip gap size on the TLV circulation is observable through the maximum of vorticity. At station 0, the peak is slightly diminished for $\tau/c = 2.5\%$ at $r = r_{tip}$, compared to $\tau/c = 8\%$. At station 1, the peak is clearly lower for the small gap ($\omega_{max} \approx 40$) than for the large gap ($\omega_{max} \approx 50$). Farther

³This choice is justified in section 5.3.6

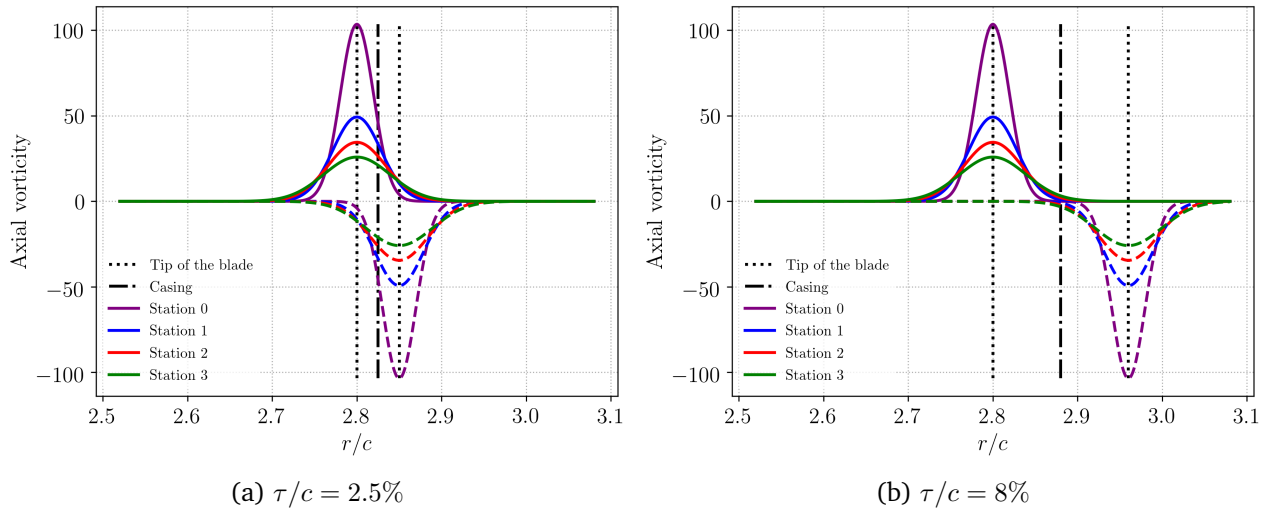


Figure 5.16: Normalized axial vorticity against the radius in the tip region. The distributions of ω_x are plotted independently for the two vortices. The solid lines represent the evolution of $\omega_x^+(r, t)$, the dashed lines that of $\omega_x^-(r, t)$.

downstream, the same applies with even more difference since the negative vortex is present in a larger part of the tip region. Let us now see how this affects Γ_{TLV} as a function of the tip gap size.

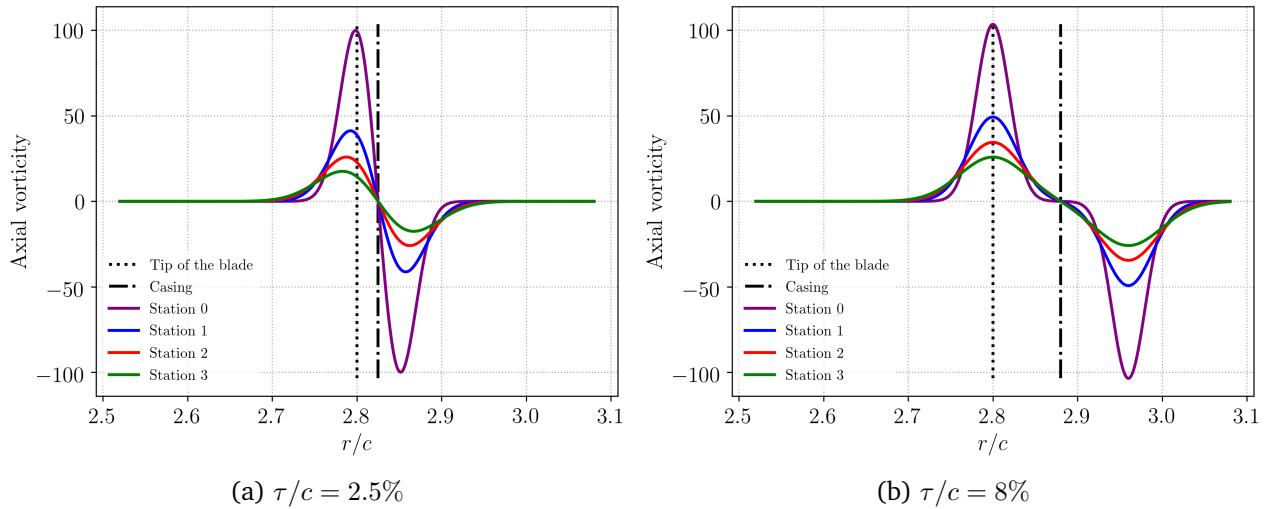


Figure 5.17: Normalized axial vorticity resulting from the sum of the two vorticities, against the radius in the tip region.

5.3.5 Axial evolution of Γ_{TLV}

This subsection is intended to compare the circulation decrease obtained with the model to what occurs in reality, before applying it to the $S2l$ configuration. Figure 5.18a compares the evolution with the dimensionless time \tilde{t} of the positive circulation, got from the DNS of Delbende and Rossi [39], to our TLV circulation Γ_{TLV} calculated with the model. The time scale used is $T_0 = \frac{4\tau^2}{\Gamma}$. This is done with different values of Λ . Two of them are particularly important to mention:

- $\Lambda = 0.32$ yields an evolution that fits very well the DNS curve up to $\tilde{t} = 600$. This corresponds to a large physical time as it can be seen in Figure 5.18b where the physical duration time $\Delta t_{phys} = \tilde{t} \times T_0$ normalized by the advection time is plotted against the gap size. For gaps greater than $1.5\%c$, the physical time exceeds one advection time, encouraging the use of the model to calculate the TLV circulation in plane $x/c = 1.05$. For gaps lower than this value, the mixing is quicker and occurs within the chord length, starting at the leading edge in the model. As seen in Figure a, the slope after $\tilde{t} = 600$ seems to diverge from that obtained with the model in terms of circulation decrease. After $\tilde{t} = 1000$, the validity of the model for these gap values cannot be ensured although the variations obtained on Γ are assumed to be in acceptable agreement with the actual physics of the dipole.
- $\Lambda = 0.42$ corresponds to $Re_\Gamma = \frac{\Gamma}{\nu + \nu_t} = 2500$, Reynolds number based on the circulation used in the DNS.

Although quite simple in its principle, the model gives very satisfying results compared to the DNS, capturing the good decrease tendency. Applied with the same Re_Γ , the model overestimates the decrease compared to the DNS as illustrated by the red curve compared to the dashed black curve in Figure 5.18a. Nevertheless, the slope of the decrease is good. Adapting the value of Λ to 0.32 allows a good fit for gaps greater than $2\%c$ and an acceptable fit for gaps lower than $1\%c$. Figure 5.18b indeed shows the normalized time $\Delta \tilde{t}_{phys}$ (in terms of one advective time period T_{adv}) over which the circulation decrease fits well with the DNS, for $\Lambda = 0.32$.

In the model, the coefficient Λ controls how fast the two vortices will mix out. Physically, this coefficient contains different effects that seem to be correctly modelled by controlling this single coefficient. These effects concern the viscous interaction of the TLV with the endwall but also the turbulence fluctuations induced by the presence of the TLV and modelled by an eddy viscosity ν_t . The RSM results suggest that the interaction of the endwall with the TLV increases the diffusion by intensifying the turbulence stresses in the TLV. In the model, this is substantiated by a higher ν_t/ν value, as a classic RANS turbulence model would do.

5.3.6 Prediction of the circulation on $S2l$

Evolution of Γ_{TLV} with the tip gap size

Figure 5.19 compares the different approaches regarding the TLV circulation. Experimental measurements and RANS RSM with the two boundary conditions at casing are plotted in the figure.

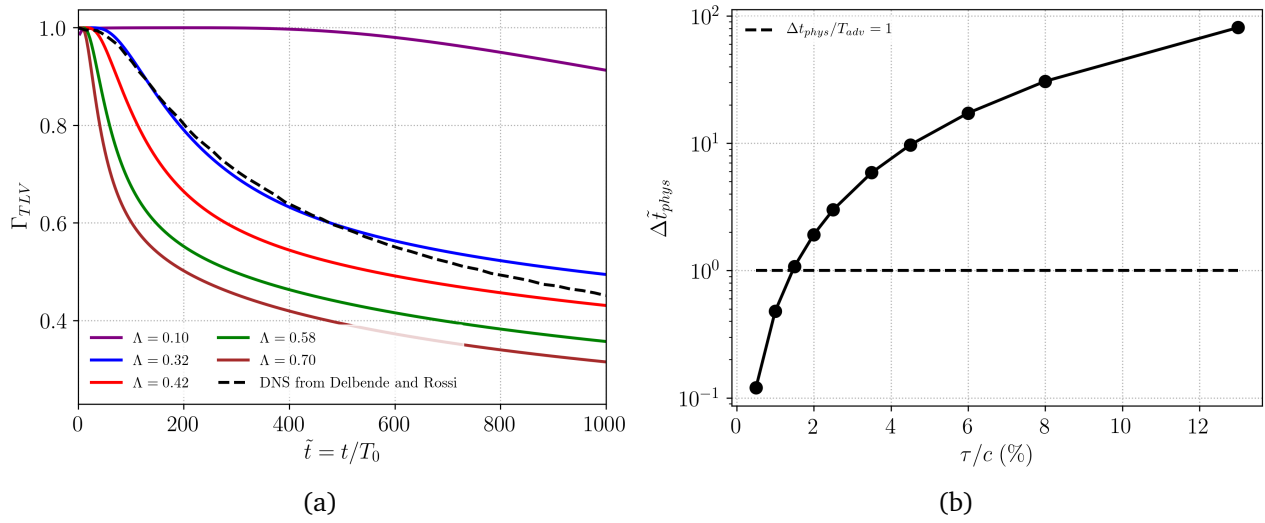


Figure 5.18: (a) Normalized circulation of the TLV as a function of the dimensionless time $\tilde{t} = t/T_0$ introduced by Delbende and Rossi [39] with $T_0 = \frac{\Gamma}{4\tau^2}$. (b) Evolution of $\Delta t_{phys}/T_{adv}$ with respect to the tip gap size, duration time over which the circulation decrease fits well with the DNS, for $\Lambda = 0.32$.

For the VLM with the viscous model, two values of Λ are tested. The evolution from station 0 (in purple) to station 3 (in green) is shown. This parameter controls the level of turbulence mixing through the calculation of ν_t/ν : with a larger Λ , the eddy-to-molecular viscosity ratio increases and the core radius growth is accelerated, according to equation (5.20). What these figures first show is that the increase of the TLV circulation with the tip gap size is well captured by the model, for these values of Λ . Only very small values of Λ would lead to a constant value of the circulation predicted with respect to τ/c . In that case, it means that the diffusion is very slow: the time scale associated to the core radius growth is much larger than the advection time T_{adv} .

The time t_c at which $R_c = \tau$ gives a good order of magnitude of when the two vortices first collide and can be calculated as:

$$t_c = \frac{\tau^2}{4(\nu + \nu_t)} \quad (5.26)$$

Whenever $t_c < T_{adv}$, the circulation Γ_{TLV} in the tip region will have decreased from its initial value Γ , after one chord length. When Λ increases, ν_t is also increased, which tends to reduce t_c . This explains the following remarks on the circulation evolution depending on the value of Λ . The good prediction of the TLV circulation increase with the tip gap size strongly depends on Λ with the model. The blue curve, from the model at station 1 (105% c), is compared to the solid black line with circles, corresponding to the experiment, at the same position:

- For $\Lambda = 0.32$, the mixing is insufficient and the TLV circulation remains greater than the experimental one for the whole range of gaps, even far downstream the trailing edge at $x/c = 200\%$. However, the slope at this latter position is close to the experimental augmentation with the tip gap size (Figure 5.19a).

- For $\Lambda = 0.58$, the fit is nearly perfect with the experiment, for tip gaps between $0.5\%c$ and $8\%c$. Only the larger gap shows a larger difference with the experiment. The model indeed does not capture the decrease of Γ_{TLV} between $\tau/c = 8\%$ and $\tau/c = 13\%$ and therefore overestimates the TLV circulation for the latter value (Figure 5.19b).

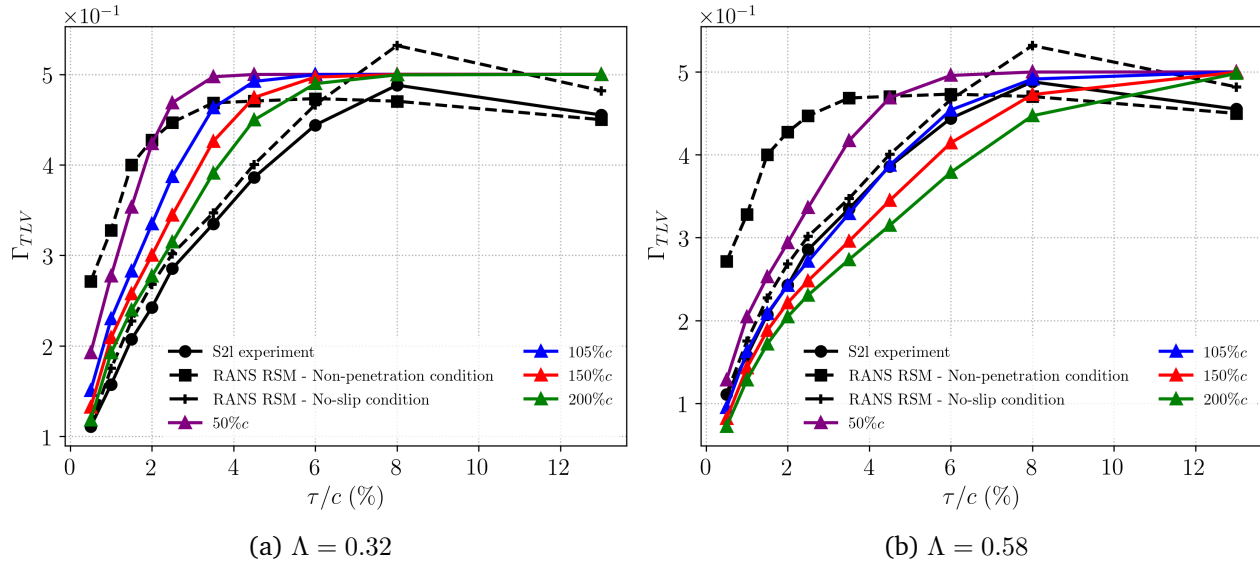


Figure 5.19: Normalized circulation of the TLV as a function of the tip gap size at four different axial stations from the model (triangles), compared with Γ_{TLV} obtained with the experiment (round), the RANS RSM with a no-slip condition at casing (crosses) and the RANS RSM with a symmetry condition at casing (squares). Two values of Λ are tested. (a) The equivalent of Λ is $\nu_t/\nu = 46$. (b) The equivalent of Λ is $\nu_t/\nu = 150$.

The evolution of Γ_{TLV} as a function of the convective time t (Figure 5.18) captured by the two-vortex model does however not correspond exactly to the physics of TLF. Along the chord, the circulation of the TLV is supposed to increase. Downstream of the trailing edge, the circulation starts decreasing by mechanisms of diffusion and dissipation until the TLV eventually decays. The model is based on the total shed circulation calculated from the spanwise distribution of circulation obtained with VLM. The benefits of VLM precisely lies in the discretization of the chord and the possibility to get the shed circulation distribution along the chord. The next section deals with an extension of the present model to take advantage of this benefit.

5.4 Viscous model applied to VLM

5.4.1 Description of the new model

The model presented in the previous section uses two vortices with an opposite circulation, that are shed at the leading edge. The circulation used in Lamb's analytical vortex model is the total shed circulation predicted by the VLM, for example for the larger gap.

It is possible to extend the two-vortex model to a VLM model, by using the chordwise distribution of shed circulation. Instead of applying the viscous model to a single pair of vortices $\pm\Gamma$, the VLM model considers a system of vortex pairs, whose respective circulation $\pm\Gamma_i$, is extracted from the VLM.

The diffusion of each elementary dipole is phase-lagged with the next one and even more with the one after. Thus the vortex pair shed at the leading edge has more time to be diffused than those farther downstream. The resulting $\Gamma_{TLV}(x)$ consists of the contribution of each vortex dipole coming from upstream. This description is closer to the physics of TLF: with the single dipole that starts being diffused at the leading edge, the modelled TLV is dissipated along the chord and loses in intensity all along. Physically, the TLV is in fact supplied by TSV all along the chord and its circulation therefore actually increases. The VLM model described as such could help to recover the circulation increase along the chord.

Figure 5.20 shows the shed circulation between the leading edge and the trailing edge obtained with VLM, for three different tip gaps. Note that for a given tip gap size, the sum of the circulations along the chord, yields the total shed circulation plotted in Figure 5.5. Coherently with the results of Figure 5.5, the tip gap size nearly has no influence on the distribution of shed circulation. A very large contribution to the TLV circulation is situated near the leading edge. This result confirms what was described with Khalid's model in the literature review [75], indicating that the most energetic structures due to TLF were found near the leading edge.

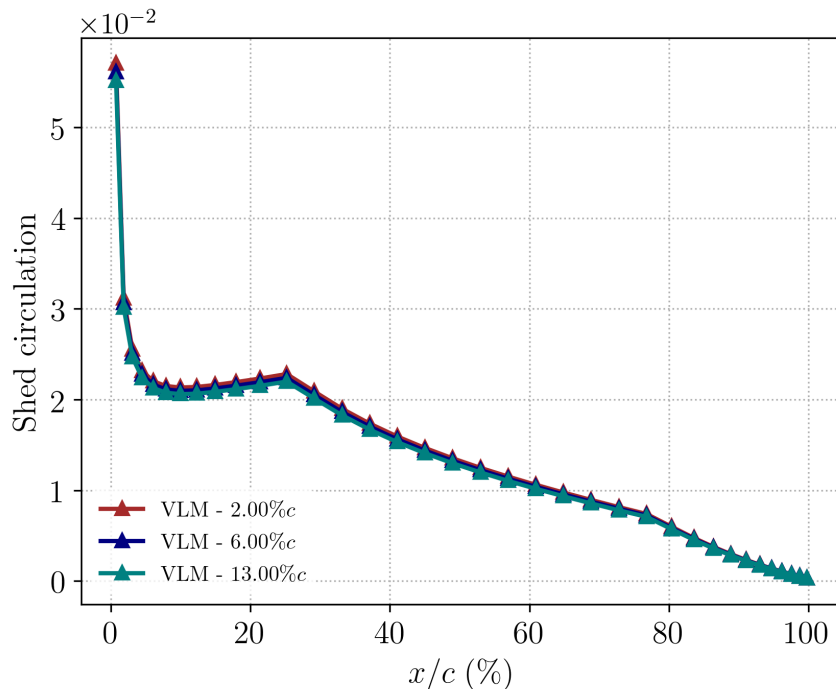


Figure 5.20: Normalized circulation shed at the blade tip as a function of x/c , as predicted by the VLM.

The viscous model is now applied to this circulation distribution. Each shed circulation of the chordwise distribution is denoted Γ_i^{shed} for i between 1 and m , leaving from position x_i , displayed

by the abscissa of the triangles in Figure 5.20. To each circulation Γ_i^{shed} , the two-vortex model is applied from the position x_i :

1. The eddy viscosity $\nu_{t,i}$ is computed with Owen's correlation

$$\nu_{t,i} = \nu \Lambda^2 \sqrt{\frac{\Gamma_i^{shed}}{\nu}}. \quad (5.27)$$

2. The core radius $R_{c,i}$ is obtained from the calculated $\nu_{t,i}$ with (5.20).
3. The axial vorticity of each vortex of the dipole $\omega_{x,i}$ is calculated with (5.19).
4. The integration of the axial vorticity downstream of x_i yields the modelled viscous evolution of the circulation Γ_i^{dipole} of the i^{th} dipole, based on equation (5.23).
5. The total circulation of the TLV, as a function of the axial position x , consists of the sum of all the circulations:

$$\Gamma_{TLV}(x) = \sum_{i=1}^{i_x} \Gamma_i^{dipole}(x), \quad (5.28)$$

where i_x is the index introduced in equation (5.11). Note that the circulation $\Gamma_{TLV}(x)$ can this time vary for $x > c$, with the VLM viscous model. Figure 5.21 offers an illustration of the viscous correction integrated to VLM.

Note that the development of each dipole is independent from one another in the model, which means that they do not interact with one another. Also note that the coefficient Λ is chosen equal for all the elementary vortices. Consequently, the eddy viscosity related to the vortices near the leading edge is greater than downstream, following the chordwise distribution of shed circulation shown in Figure 5.20. This is consistent with the fact that the contribution to the losses of the TLV is mostly due to the structures near the leading edge.

5.4.2 Results on the circulation

5.4.2.1 Evolution of Γ_{TLV} with the tip gap size

Let us see the results obtained on the TLV circulation at the plane of interest of station 1. Figure 5.22 compares the evolution of Γ_{TLV} with the first two-vortex model and with the VLM model, against the experimental and RANS results, for two values of Λ . With the value used for the two-vortex model ($\Lambda = 0.58$), the VLM model overestimates the TLV circulation obtained with the experiment, but seems to replicate quite well the evolution predicted by RSM with the non-penetration condition, *i.e.* when the boundary layer at casing is not accounted for. Increasing Λ to 1.5 reduces the resulting TLV circulation for the small gaps and realizes a nearly perfect fit on the experimental measurements, except for the larger gap. On the other hand, this coefficient is too large for the two-vortex model, which underestimates the TLV circulation at station 1 for all the gaps, by overestimating the diffusion along the chord.

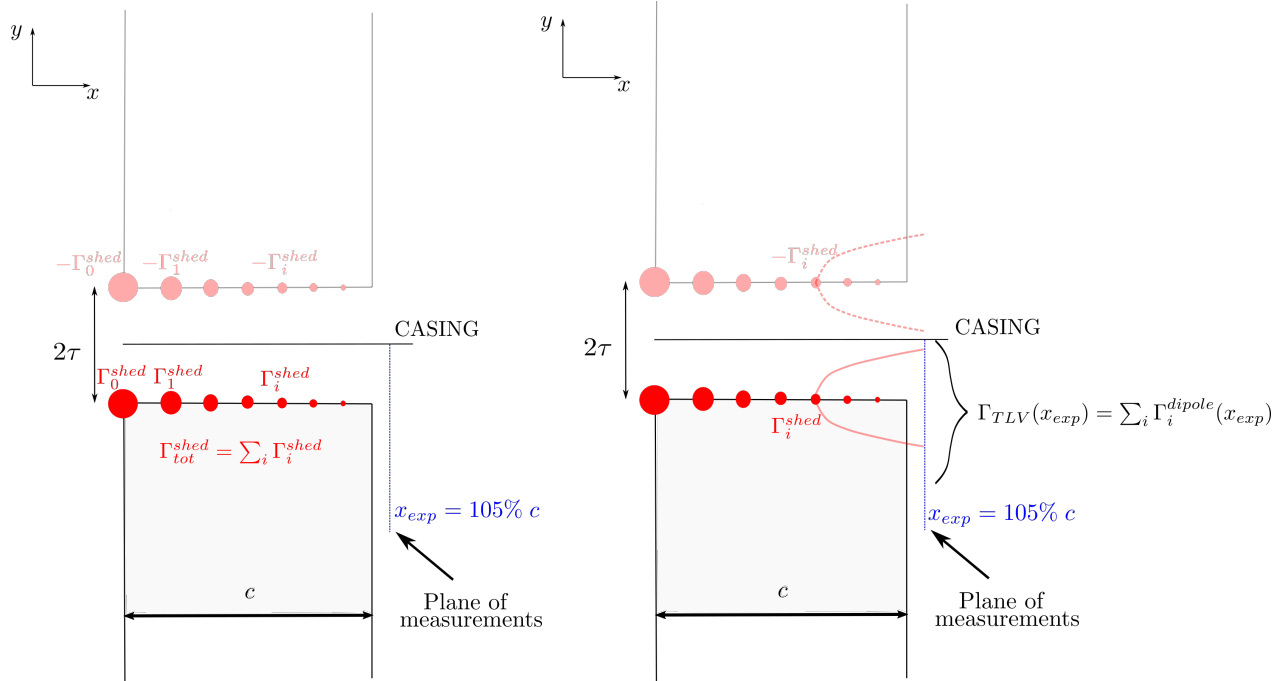


Figure 5.21: Illustration of the viscous correction integrated to the chordwise distribution of shed circulation predicted by VLM. (a) Chordwise distribution of mirror shed circulations. (b) Application of the viscous model to the i^{th} vortex pair.

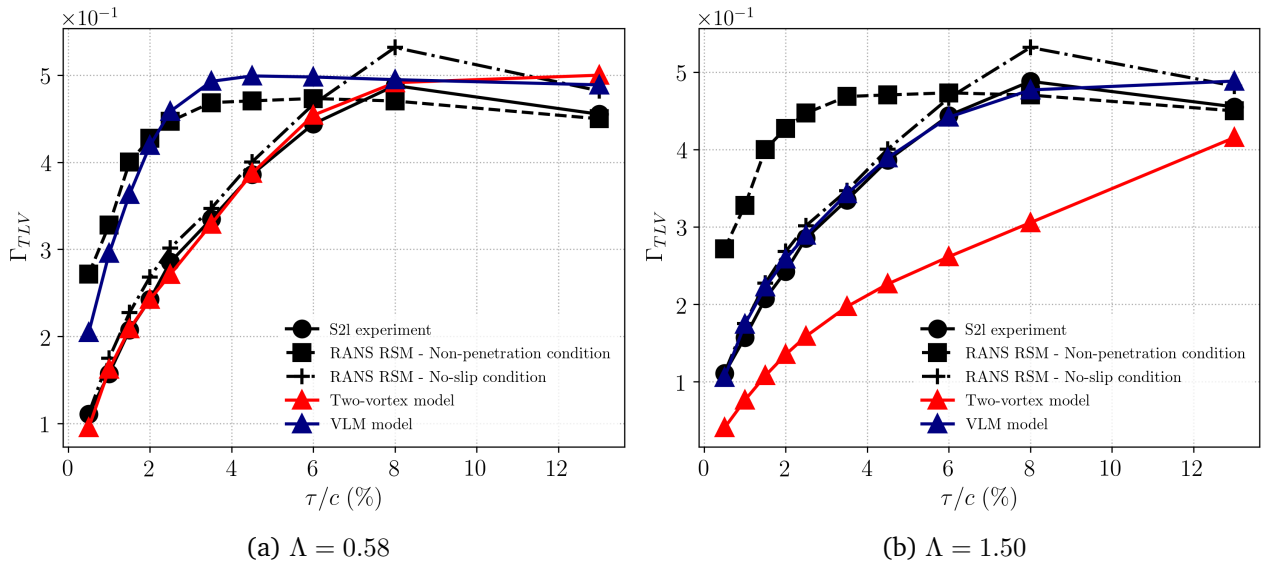


Figure 5.22: Normalized circulation of the TLV with respect to the normalized tip gap size, predicted by the two-vortex model and the model based on VLM, compared to the experiment and the RANS.

5.4.2.2 Axial evolution of Γ_{TLV}

The application of the viscous model to each elementary vortex enables a more physical description of the circulation evolution chordwise as it can be seen in Figure 5.23. Figure 5.23a displays the evolution obtained with $\Lambda = 0.58$, compared to that from the RSM simulation with the non-penetration condition, in coherence with the fit observed in Figure 5.22a. The slope of the increase is well captured but the decrease downstream the trailing edge is largely underestimated by the VLM model.

With $\Lambda = 1.5$, the fit of the VLM model is good with the RSM no-slip condition. Figure 5.23b compares the axial evolution of the TLV circulation for this coefficient value with the RSM results obtained with the no-slip condition. Although the peak on Γ_{TLV} is underestimated by the model, the tendency is quite good and predicts an increase over the chord and a decrease of the circulation from the trailing edge.

Contrary to the two-vortex model, the increase of the circulation is well depicted by the VLM model all along the chord. For the three tip gap sizes here evaluated, the increase is less and less important with the decrease of the gap, but it is also coherent with the fact that the vortex structure for the smaller gaps is much less intense. Downstream of the trailing edge ($x/c > 1$), the circulation decrease is also captured. The decrease is slow and there is no clear tendency between the gap size and the slope of the decrease. Note that this decrease is slower than that obtained with RANS. Other experimental measurements would have been interesting at downstream positions to assess whether the RANS diffusion and dissipation capture correctly the physics of the TLV decay.

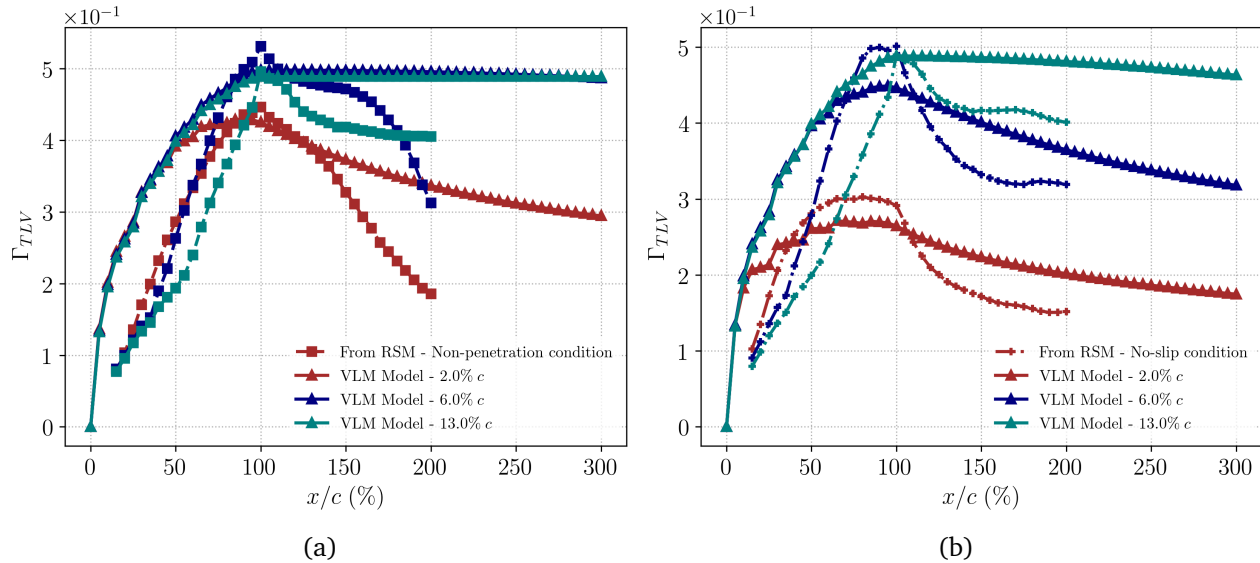


Figure 5.23: Axial evolution of the normalized circulation Γ_{TLV} for three tip gap sizes, captured by the model and compared to the RANS. (a) RSM with a non-penetration condition at casing, $\Lambda = 0.58$ for the VLM model. (b) RSM with a no-slip condition at casing, $\Lambda = 1.5$ for the VLM model.

5.5 Discussions

5.5.1 Endwall/TLV interaction

The circulation increase with the gap size is modelled by a system of two mirror vortices that collide and cancel each other out, resulting in a reduction of the total circulation for small gaps. The endwall is not directly represented in the model and one must question the consistence of the model to represent this interaction. Let us recall the differences between the interaction of two vortices and the interaction of a vortex with an endwall.

In Deveaux's thesis, two main effects are found between the use of a symmetry condition and a no-slip condition at casing. The first concerns the drift velocity that decreases with the no-slip condition, due to the interaction of the TLV with the boundary layer. The viscosity smoothens the drift of the TLV and it is clearly visible for the smaller gaps.

The rebound of the TLV with the boundary layer is the second effect. Well described by Brion [13], the interaction of the TLV with the boundary layer first generates the induced vortex with a circulation $\Gamma_{induced}$ of opposite sign to the circulation Γ_{TLV} . The third effect is due to the interaction of the vortex pair which gets the system farther from the endwall. As a consequence, the resulting vertical position of the TLV is farther from the casing than it would be without a boundary layer.

The latter effect is not taken into account with the model since the position of the TLV center remains constantly at the tip of the blade. However, the influence of the casing boundary layer is modelled by the increase in the eddy viscosity in the model. From Figure 5.22, the evolution of the TLV circulation with the two boundary conditions can be replicated by varying ν_t/ν : increasing it probably combines both the effects of the TLV and the boundary layer on the turbulent mixing.

5.5.2 Estimation of the eddy viscosity

The use of a system of mirror Lamb vortices enables to calibrate the model to the experimental results through a single coefficient Λ , quantifying the turbulent development and mixing of the initial potential vortices shed along the chord. The corresponding values of ν_t/ν based on the calibrated Λ are physical and coherent with the order of magnitude of an eddy viscosity in a TLV mixing with a boundary layer (see the RANS simulation in Chapter 4 for example). However, such a model would possibly be useful for rotor blade predesigns.

If preliminary designs are sought regarding tip-leakage flow and the estimation of the circulation, the module *PyLiSuite* along with the viscous model could be used as follows:

1. Apply the VLM on the blade design to be tested, based on a camber formulation, and get the shed circulation distribution. The results from the VLM serve as an input to the viscous model.
2. Set $\nu_t/\nu = 100$ at the leading edge, which is a good order of magnitude for the eddy-to-molecular viscosity ratio. The corresponding Λ from Owen's correlation can then be used

to calculate ν_t/ν over the chord, associated to each independent pair of vortices in the VLM model.

Representing the TLV as a stable and persistent structure through the diffusion of a Lamb vortex seems to be coherent. When specifically applied to turbomachinery, including other effects with this viscous model can be discussed: the periodicity has been validated in Chapter 3 on a linear cascade and applying the viscous model on such configurations could be done. As explained in the literature review, the relative motion between the blade and the casing wall induces the generation of a scraping vortex: the presence of this vortex could possibly be modelled by a modification of ν_t . The capabilities of the viscous VLM model are discussed in the next section on its application to the compressor CREATE.

5.5.3 Application to CREATE?

The VLM has been applied to a single blade TLF configuration but what about its use on an actual compressor configuration? Let us discuss on the application of VLM to the third rotor of CREATE, analyzed in Chapter 4 with the ZDES.

The application to such a configuration is not straightforward with the VLM. If the third rotor is treated with VLM by discretizing the camber of the blade with HSV, different difficulties are to be mentioned:

- The code *PyLiSuite* has only been developed for linear geometries, in cartesian coordinates, which needs to be extended to annular geometries in order to correctly apply the symmetry and the periodicity conditions for CREATE. In Chapter 3, we saw that it is also possible to directly discretize the casing wall, instead of applying a symmetry condition. This would probably help to process annular configurations.
- *PyLiSuite* is formulated in the absolute frame of reference. Developments are necessary to represent rotating bodies.
- The flow conditions with the VLM are given by the magnitude and the orientation of U_∞ . The mainstream velocity field to be applied with the non-penetration condition on the blade must be a solution of the potential equation (3.5). Hence, constructing a potential solution close to the radial profiles of plane 280 should be investigated further. An expedient is to prescribe a constant value over the whole span for the velocity magnitude and the angle of attack. The problem with that solution is that the third rotor of CREATE is particularly three-dimensional, and if the incidence angle and the velocity are well-adapted to a certain radial position (at the tip for example), it is not at other radii (at the root for example).
- The Mach number is about 0.7 at the tip in plane 280 of CREATE: the Prandtl-Glauert correction may not be valid anymore (valid up to $M_\infty \approx 0.6$).
- The choice of the HSV angle θ_{HSV} is prescribed to a single value in the current code. It would be interesting to test variations of this angle spanwise, adapting to the stagger angle

of the blade, varying with the radius. Indeed, the stagger angle γ_{root} for CREATE is more than 10° lower than at the tip. In order to minimize the thickness of the wake at the trailing edge ($t_w = \eta_{c,max}$) for a given radial position, a good value for θ_{HSV} is $\gamma(r)$.

The VLM code, *PyLiSuite*, can still be improved to go towards compressor configurations, in order to predict the TLF, with the aim of being as close as possible to the ZDES simulations, our reference.

5.6 Conclusions

An attempt at modelling three characteristics of the TLV has been done on a single blade TLF configuration throughout this chapter: the detachment point, the trajectory and the circulation of the TLV. The modelling can be summarized by Figure 5.24, showing a cambered blade with a camber line coloured in red over which the vortices are distributed on, the point of detachment DP , the mean trajectory line that the TLV core follows as its circulation varies.

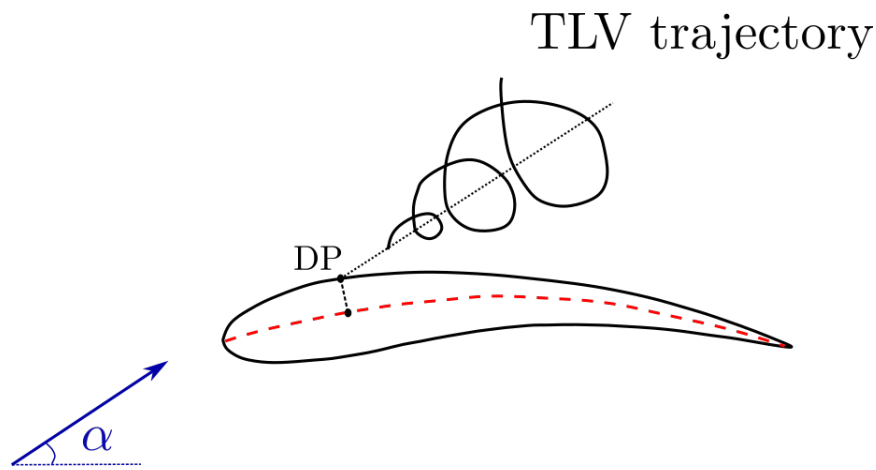


Figure 5.24: Sketch of a cambered blade from which the TLV detaches at DP . The camber line over which the HSV are distributed is indicated by the dashed red line.

Let us summarize the possibilities given by VLM and the introduction of viscosity to model the TLV circulation:

1. **Detachment point:** At the tip, the potential approach is not adapted to get the loading distribution with the camber formulation, and the local maxima captured with RANS on the loading are not by VLM. The detachment point cannot be positioned according to this criterion and is placed at the leading edge in the model. In the tip region, using vortex singularities yields a very low blade loading, due to Helmholtz's principle, imposing a zero circulation at the tip. Modelling blockage by adding sources on the blade camber could help in that regard.
2. **Trajectory:** The prescribed wake formulation does not allow changing the angle of the HSV legs with respect to the chord line of the blade and the trajectory of the resulting

shed vortex is not directly captured by the method. Instead, one must resort to a correlation based on the midchord loading to estimate the mean TLV trajectory, validated by Chen on compressor configurations. On the single blade configuration *S2l*, differences are noted between the trajectory predicted by Chen's correlation and the experiment, precisely because the correlation is based on compressor configurations. The trajectory obtained with the experiment and the RSM simulations from the detachment point is affected by the endwall boundary layer for the small gaps. It is visible by comparing the results between the non-penetration condition and the no-slip condition at casing.

- 3. Circulation:** The direct application of VLM yields the circulation distribution over the blade, from which the total shed circulation can be calculated. A first good achievement of VLM is its capability to accurately predict the shed circulation for large tip gaps. However, the VLM alone is not capable of predicting the right increase of Γ_{TLV} with the tip gap size. For a proper prediction at low gap values, a viscous model has to be introduced. The idea of the new model tested in the present thesis is to consider a pair of contra-rotating analytical vortices, whose core radius grows with time by a viscous diffusion process. These vortices are shed at the equivalent leading edge plane with a circulation $\pm\Gamma$, calculated with the VLM. Turbulence is considered in the model by adding an eddy viscosity to the molecular viscosity, accelerating the growth of the two mirror vortices. The tip gap size here affects how fast the two vortices will mix out together. For a small gap, the circulation of the system in the equivalent tip gap region drops quickly whereas for a large gap, the two structures conserve their circulation far downstream. The physical process occurring in a Lamb dipole is simplified with the model, but the slope of the circulation decrease fits surprisingly well over a long time with a reference DNS, on the dynamics of a vortex dipole. The value of ν_t/ν used in the model controls how fast the circulation drops. With this model, the experimental increase of the TLV circulation with the gap size can be recovered. This two-vortex model can then be extended to a VLM model, benefiting from the chordwise discretization of the shed circulation. This enables to recover the TLV circulation increase, physically observed, along the chord.

The use of the Vortex Lattice Method developed and described in Chapter 3 is not sufficient to correctly model the TLV as a function of the tip gap size. However, additional models have been developed, on the trajectory and the diffusion of the TLV, and appear to be capable of reproducing part of the physics of TLF.

CONCLUSIONS

The present thesis is an investigation on the tip-leakage flow, which involves very complex phenomena responsible for massive losses at the rotor blade tips. The first part of the thesis allowed understanding the topology at stake in the tip region and the main parameters driving TLF. The literature review put forward the main characteristics of the tip-leakage vortex (TLV) forming at the blade tip and its impact on the performance of the rotor. Depending on the tip gap size, it can be particularly affected and completely change the flow dynamics in the tip region. The objective of this thesis was precisely to relate these characteristics to the tip gap size through the use of two methods:

- One focusing on the unsteady flow analysis by the use of ZDES simulations on a compressor rotor for three different tip gap sizes.
- Another aiming at developing a low-resolution model of the TLV characteristics with the use of the Vortex Lattice Method (VLM) on a simplified TLF configuration.

On the one hand, the use of the ZDES has confirmed results from the literature on the influence of τ on the topology of TLF. Concerning the three TLV characteristics, the increase of the tip gap size shifts the detachment point of the TLV towards the trailing edge but has no influence on the TLV trajectory. The angle between the TLV core and the chord line at the tip does not vary for the three tip gap sizes tested, confirming the results of Chen's correlation presented in part I. Regarding the intensity of the TLV, the simulations showed that the circulation increases with the tip gap size: both the vortex core radius and the vorticity levels within the core are increased.

The combination of these effects is particularly interesting regarding the influence on the double leakage phenomenon. Indeed, with the same trajectory, a stronger and larger TLV, the impingement of the neighbouring TLV occurs closer to the leading edge of the blade and with more intensity.

The benefits of using ZDES can be appreciated here through the resolution of the largest turbulent eddies. With the largest tip gap size, the interaction between TLF and the neighbouring

TLV is emphasized, which directly affects the axial evolution of the leakage velocity. A large drop in the magnitude of the leakage velocity is observed for that case, which is clearly related to the position where the neighbouring TLV starts impinging the pressure side of the blade.

The impact of the tip gap size τ on the double leakage phenomenon brings new elements to the analysis of TLF and its comprehension. The high-fidelity investigation has showed how increasing the tip gap size particularly emphasizes the double leakage phenomenon, consequently affecting the TLV coherence and even stability.

On the other hand, the module *PyLiSuite* developed throughout the present work, based on the Vortex Lattice Method (VLM), proved to be accurate for large tip gaps. The VLM developed is originally based on external aerodynamics and was extended to TLF configurations in Chapter 3. The advantage of such a method is the limited number of assumptions on which it relies and the limited amount of time it needs to run (~ 30 s). The latter point is crucial for designers and is particularly pointed out in the frame of this thesis: compared to RANS, this kind of methods can be used more efficiently for pre-designs. Optimization processes are thus made possible through the capability of massively testing blade designs.

It is also crucial for the method to be sufficiently accurate. From the good agreement between the experiment and VLM for the large gaps, the present thesis showed that the influence of the tip gap size on the TLV circulation can be modelled accurately by adding a viscous correction to the VLM. The evolution of the circulation as a function of the tip gap size with the VLM model on the simplified configuration *S2l* put forward two main observations:

1. The VLM method is accurate for large tip gaps ($\tau/c > 8\%$) without the viscous correction.
2. This result serves as basis to the newly developed viscous correction added to VLM that enables to fit perfectly to the experiment over the whole range of gaps considered, without modifying the results for the large tip gaps. The viscous correction basically considers the viscous diffusion of two contra-rotating vortices, whose cores are distant by 2τ , and their mixing. The diffusion is controlled by the initial circulation Γ_0 obtained from the VLM with the largest gap and a coefficient Λ quantifying the turbulent diffusion of the vortices.

This gives another interpretation of the TLV circulation dependence to the tip gap size that may be tested on more representative TLF configurations.

The combination of the short computational time requirements of the VLM, the features developed in the present work regarding TLF configurations, and the excellent prediction of the TLV circulation brought by the development of the new viscous model added to VLM already makes *PyLiSuite* a very interesting tool for analyzing and modelling TLF.

Further work

If the present work has enabled achievements in the comprehension and the modelling of the influence of the tip gap size on the tip-leakage flow, by analyzing the formation of the tip-leakage vortex, it also opens interesting possibilities for future work.

First, regarding the influence of the tip gap size, there are several main tracks that could be followed:

-
1. Other tip gap sizes with the same hybrid RANS/LES approach may be simulated to enrich the database. The existence of an intermediate case pushes to go further in the comprehension of how the double leakage phenomenon plays a role on the vortex disintegration and a possible vortex wandering/breakdown.
 2. If a criterion is sought on the leakage velocity extracted in the clearance, about the possible occurrence of a vortex fragmentation or vortex wandering, such high-resolved simulations would be very helpful. Unsteady RANS simulations may be poorly adapted because the sudden velocity drop seems to be dependent on the resolved turbulent fluctuations, given by a LES resolution of the TLV in our case. It would however be worth analyzing how the double leakage is simulated with URANS and how the turbulence modelling impacts the TLV/blade interaction in that case.
 3. The unsteadiness can be analyzed further with the use of the Γ_1 and Γ_2 functions, which enable to capture the position of the TLV core accurately over time and the extension of its core radius [10] [57].
 4. In order to go beyond the simplified TLF configuration with the VLM in terms of prediction of the TLV circulation, extensions to annular cascades must be considered.
 5. The VLM model captures very accurately the circulation as a function of the tip gap size on the simplified TLF configuration but the detachment point and the trajectory of the TLV still require a better prediction. Two main ideas can be brought up to improve their prediction:
 - Distributing discrete sources over the camber to account for the thickness of the blade could be interesting. First, it is hoped that it would help improve the prediction of the loading at the tip, constrained by Helmholtz’s principle. Capturing the local maximum of Δc_p in order to locate the detachment point is aimed for. Second, using sources enables to introduce attached boundary layer effects by means of an integral method. This can be done through the use of viscous-inviscid coupling by calculating the surface velocity and pressure distribution from the potential approach. From this, the integral quantities of the boundary layer (δ^* , H) can be estimated along with the skin-friction coefficient. Each cell of the body surface is displaced according to the displacement thickness and the potential method is applied on this modified geometry. The process is repeated until convergence on the boundary layer quantities.
 - Changing the wake formulation and applying a free-wake formulation to go beyond the limitations induced by the prescribed wake used in the present thesis. This latter formulation is indeed limited to a flat wake with vortices that must be shed at the trailing edge to satisfy a correct Kutta condition. By using a free wake formulation, it is hoped to capture the TLV trajectory directly without resorting to a correlation. Moreover, it would give an additional degree of freedom to the method. The vortex ring model as presented in Katz and Plotkin [72] could be for example tested. Another intermediate choice to alleviate the problems of lift predictions due to Kutta’s
-

condition could be to only use horseshoe vortices to discretize the cells corresponding to the trailing edge and discretize the rest of the blade with ring vortices.

Beyond the influence of the tip gap on TLF, the author believes that the analysis and the modelling of TLF could be enriched following several possible directions:

1. The experiment of Bailey and Tavoularis showed that turbulent fluctuations were involved in triggering the oscillations of their wing-tip vortex. In our simulations, the only resolved turbulent fluctuations impinging the blade are due to the TLV formation in a casing boundary layer treated with RANS upstream of the row. A wall-modelled LES would probably bring new results on (i) the interaction of the TLV with the casing boundary layer and (ii) the resulting interaction of the TLV with the clearance flow. The third mode of ZDES can be envisaged in that regard with the injection of turbulent fluctuations at the inflow.
2. The phenomena induced by the vortex fragmentation (possible vortex wandering) are likely to break the periodicity assumption over the passages, in particular with more throttled operating points. With the same ZDES resolution, simulations over the whole circumference or over an extended sector could bring interesting results despite their cost. Increasing the incidence on the third rotor by working at more throttled operating points and leading the same mean and unsteady analyses may be interesting regarding the double leakage analysis and the onset of instabilities.
3. The VLM model constructed and tested in the present thesis can be applied to low-compressible flows and uniform inflow conditions. Improvements regarding the extension to transonic/supersonic flows is crucial if the module aims at being applied to representative compressor rotor designs. Likewise, being able to use generalized inflow profiles, solutions of the potential flow problem and close to real inflow profiles for a rotor, would represent a major improvement.

All these suggestions for further work are part of the same objective in the frame of the present work: being able to accurately predict the three mean characteristics of the TLV with the VLM on CREATE, by using the ZDES simulations as a reference. Such an achievement with the VLM would open very large prospectives in terms of predesign of compressor rotors over a much wider scope, and with the possibility of varying massively the parameters of designs. Recall that the TLF is problematic on compressors (and turbines) of current jet engines and the next generation of engines to come will very likely be affected by this very limiting phenomenon. Representing and modelling correctly TLF has been and remains a big challenge for the years to come and we hope that this work has contributed to go towards a better representation of TLF.

APPENDICES

APPENDIX A

DETAILS ON THE MODELS

Contents

A.1 Storer and Cumpsty's model	192
A.1.1 Derivation of the equations	192
A.1.2 Application to a simple case	194

A.1 Storer and Cumpsty's model

A.1.1 Derivation of the equations

Mass conservation

Considering the problem as incompressible, one can write the conservation of the mass in the axial direction as follows

$$\rho V_{\text{exit}} A = \rho V A + \rho V a \sin\zeta \quad (\text{A.1})$$

The left-hand side represents the mass flow rate at the exit, the right-hand side the two contributions of the mainstream and the leakage flow to the total mass flow.

Momentum conservation

Applying the conservation of axial momentum before the mixing and after the mixing yields the following expression:

$$\rho V A \cdot V + \rho V a \sin\zeta \cdot V \cos\zeta = \rho A V_{\text{exit}} \cdot V_{\text{exit}} + (p_{\text{exit}} - p) A \quad (\text{A.2})$$

Equation (A.1) gives an expression for the ratio V/V_{exit} as a function of $\chi = a/A$ and ζ :

$$V/V_{\text{exit}} = \frac{1}{1 + a/A \sin\zeta} \quad (\text{A.3})$$

Substituting this expression into equation (A.2) allows obtaining the stagnation pressure loss and the loss coefficient

$$\frac{\Delta P_0}{\frac{1}{2}\rho V_E^2} = \chi \sin\zeta \left(\frac{2 + \chi \sin\zeta - 2\cos\zeta}{(1 + \chi \sin\zeta)^2} \right), \quad (\text{A.4})$$

where $\chi = \frac{a}{A}$ is the ratio of the flow areas, respectively denoted a and A in figure 1.32, and ζ designates the angle between the jet and the main flow. The ratio of the flow areas is given by

$$\chi = C_D \frac{\sigma \tau / c}{h / c \cos\gamma}, \quad (\text{A.5})$$

with τ the clearance gap, c the chord length, σ the solidity, γ the stagger angle and $C_D = 0.8$ a discharge coefficient applied to fit better with the results. The latter can for example be calculated as the ratio between the actual mass flow rate passing in the clearance and the theoretical one obtained from the c_p distribution with Rains' theory, if no separation was taking place within the clearance. The analytical relation derived by Moore and Tilton [97] links the contraction coefficient σ , ratio between the effective section area in the presence of the vena contracta and the section area unaffected by it as follows

$$C_D = \frac{\sigma}{\sqrt{1 - 2(\sigma - \sigma^2)}} \quad (\text{A.6})$$

Theoretically, $\sigma = \frac{\pi}{\pi+2}$ can be estimated from a potential flow theory analysis ¹ [92]. The results of the experiments carried out by Moore and Tilton in a linear cascade of turbine confirm the value for σ .

Denoting V_S the streamwise component of the jet velocity and V_L the normal component, the angle ζ is given by

$$\tan\zeta = V_L/V_S. \quad (\text{A.7})$$

Now, the definition of ζ is local, since it is based on the local velocity components of the leakage flow. Yet, the clearance flow angle varies all along the chord and across the gap. To get a reliable value of ζ to be applied in equation (A.4), one would need the values of V_L and V_S for a reasonable number of positions along the chord. This is generally difficult to obtain and an approximation is used to estimate $\bar{\zeta}$, the mean angle along the chord:

$$\tan\bar{\zeta} = \frac{\int_0^c V_L dl}{\int_0^c V_S dl} \quad (\text{A.8})$$

This approximation simply considers the average leakage velocity divided by the average streamwise velocity to calculate the mean leakage angle. The average streamwise velocity V_S on the pressure side can reasonably be approximated by the outlet velocity V_2 . The leakage flow velocity is determined by the difference in pressure between the pressure side of the blade well away from the tip and the suction side of the blade very near the tip as shown in a previous publication from Storer and Cumpsty's experiment [135]. Considering the tangential blade force, the average pressure difference can be estimated, leading to an estimation of the leakage angle

$$\tan\bar{\zeta} = \cos\alpha_2 \sqrt{2 \frac{\tan\alpha_1 - \tan\alpha_2}{\sigma \cos\gamma}}, \quad (\text{A.9})$$

where γ is the stagger angle of the blade considered and $\sigma = c/s$ is the solidity of the blade (chord-to-pitch ratio). α_1 and α_2 respectively stand for the inlet and the outlet flow angles. This expression applies for small camber blades with low profile loss.

Equations (A.4) and (A.10) provide a simple way of estimating the tip clearance losses. The assumptions made limit the range of validity but give a good way of investigating the sensitivity of tip clearance losses to classic design parameters of compressors.

Indeed, equation (A.10) can be rewritten as

$$\tan\bar{\zeta} = \cos\alpha_2 \sqrt{2 \frac{\psi/\phi}{\sigma \cos\gamma}}, \quad (\text{A.10})$$

with $\psi = \Delta h_0/U^2$ is the loading coefficient and $\phi = V_x/U$ is the flow coefficient. This expression has to be applied in the frame relative to the blade, meaning β must be used for rotors instead of α .

¹See the section *Flow through an aperture* in Milne-Thomson's book.

A.1.2 Application to a simple case

Their model can be applied on a repeating stage of a compressor with equal axial velocity and flow direction at inlet and outlet. A clearance is assumed at the rotor tip and at the stator hub. The geometry of the blades is arc circular, the incidence upstream of the rotor as well as the stator is zero. Also, the hub-to-casing ratio is assumed close to 1 enough to take ϕ and ψ equal at casing and hub. Finally, the degree of reaction R is taken equal to 0.5.

The loss in efficiency is compared with that obtained by Storer and Cumpsty in their article using their model. It is defined by:

$$1 - \eta = \frac{\phi^2}{2\psi} \left[\frac{\omega_R}{\cos^2\beta_1} + \frac{\omega_S}{\cos^2\alpha_2} \right], \quad (\text{A.11})$$

with η the stage efficiency, ω_R and ω_S the loss coefficients for the rotor and the stator calculated with equation (A.4), and β_1 and α_2 the inlet flow angles for the rotor and the stator, in their respective frame of reference.

A parameter study is made on ϕ and ψ considering this stage. To understand how the model works, let us calculate ω_R the loss in stagnation pressure which is calculated by equation (A.4). To do so, the following steps are to be followed:

1. ϕ , ψ and R are fixed. The relative flow angles β_1 and β_2 can be calculated using

$$\psi/\phi = \tan\beta_1 - \tan\beta_2 \quad (\text{A.12})$$

$$R = \phi/2(\tan\beta_1 + \tan\beta_2) \quad (\text{A.13})$$

Hence, the absolute flow angles α_1 and α_2 responding to the same equation

$$\tan\alpha_i = 1/\phi - \tan\beta_i, \quad i = 1, 2 \quad (\text{A.14})$$

2. Knowing the flow angles, the geometric angles β'_i must be calculated to get γ the stagger angle. In that particular case of a circular arc camber line, $\gamma = 1/2 (\beta'_1 + \beta'_2)$. The inlet geometric angle is equal to β_1 since the incidence is assumed to be zero. The outlet one is calculated using Carter's rule, an empirical relationship between the nominal deviation and the incidence

$$\delta = \beta_2 - \beta'_2 = m\theta(s/c)^{0.5} \quad (\text{A.15})$$

$$\text{with } \theta = \beta'_1 - \beta'_2 \text{ the camber angle} \quad (\text{A.16})$$

$$\text{and } m \text{ is given by } m = 0.23(2a/c)^2 + \beta_2/500 \quad (\text{A.17})$$

The maximum camber of the blade is at distance a from the leading edge of the blade and all the angles in equation (A.17) are in degrees. For a circular arc blade, $a = 0.5$ and β'_2 can be calculated.

3. The stagger angle calculated, equation (A.10) can be used to get the leakage angle and finally the stagnation pressure loss. Assuming that inlet and outlet axial velocities are the equal, $V_1 \cos \beta_1 = V_E \cos \beta_2$. Hence, equation (A.4) may be rewritten

$$\omega_R = \frac{\Delta P_0}{\frac{1}{2} \rho V_1^2} = \chi \sin \zeta \left(\frac{2 + \chi \sin \zeta - 2 \cos \zeta}{(1 + \chi \sin \zeta)^2} \right) \frac{\cos^2 \beta_1}{\cos^2 \beta_2} \quad (\text{A.18})$$

Likewise with the stator: assuming a repeating stage, the inlet flow angle is α_2 and the outlet flow angle is α_1 . The incidence is again assumed to be zero and the exact same process can be applied to compute the losses for the stator.

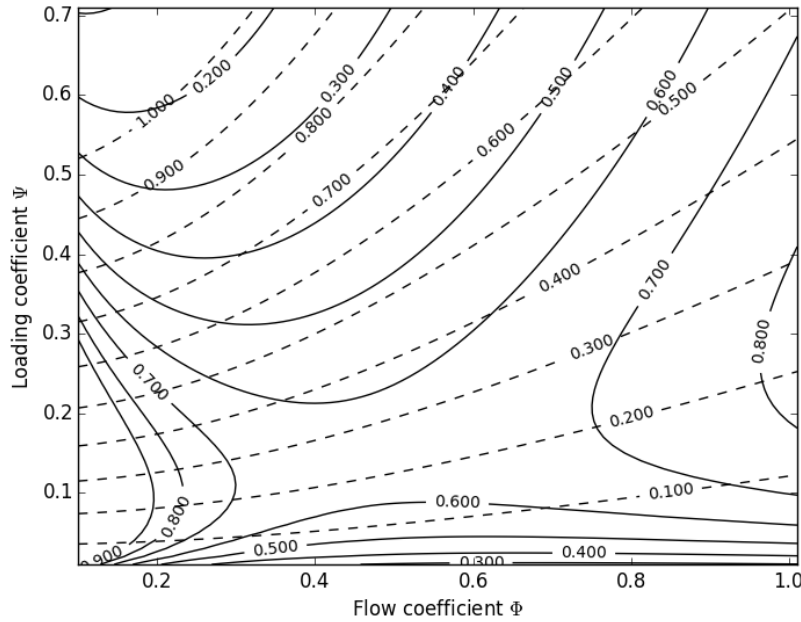


Figure A.1: Loss in efficiency due to tip clearance flow for a repeating stage of compressor for 50% degree of reaction, from model's application.

Varying the blade loading and the load coefficient, a map of the losses is obtained. Figure A.1 show contours of normalized efficiency with clearance gap-to-span ratio τ/h . The solid lines denote the normalized losses in efficiency from equation (A.11), the dashed ones denote the Lieblein coefficient for the rotor defined in section 1.1, and rewritten as follows

$$DF = (1 - \cos \beta_1 / \cos \beta_2) + s/c \cos \beta_1 / 2 (\tan \beta_1 - \tan \beta_2) \quad (\text{A.19})$$

since the flow is assumed incompressible here.

This kind of map is particularly interesting for a first design of the blades. Usually, the nominal value taken for the diffusion factor DF is 0.45 for a reasonable number of stages and a reasonable diffusion to remain away from instabilities. Hence, following this value for the diffusion factor, a first design would take the couple of values (ϕ, ψ) minimizing the losses in efficiency, in our case around $(0.43, 0.29)$.

COMPLEMENTS ON POTENTIAL FLOW METHODS

Contents

B.1 Prandtl's lifting line theory	198
B.1.1 The lifting line equation	198
B.1.2 Glauert's method	199
B.2 Three types of singularities	200
B.2.1 The source	200
B.2.2 The doublet	200
B.2.3 The vortex	201
B.3 Analytical vortices	202

B.1 Prandtl's lifting line theory

B.1.1 The lifting line equation

The lifting line theory relies on two main assumptions on the dimensions of the body:

- The maximum thickness is much lower than the chord length
- The aspect ratio of the object is much greater than 1, *i.e.* the body is slender and replicating its presence by a line of vorticity can therefore be justified.

The derivation of the integrodifferential equation on the circulation is done in details by Katz and Plotkin ¹ [72] by making sure the sum of the normal components of the velocity induced by the wing w_b , the trailing vortices w_i and the normal velocity component (towards z) is zero:

$$w_b + w_i + U_\infty \sin \alpha = 0 \quad (\text{B.1})$$

Applying Biot-Savart's law, relating the velocity perturbation $\Delta \mathbf{u}(P)$ due to a vortex line element $d\mathbf{l}$ of circulation $\Delta\Gamma$, at a distance $r = ||PM||$ from the vortex line at point M , can be written,

$$\Delta \mathbf{u} = -\frac{1}{4\pi} \frac{\Delta\Gamma \times d\mathbf{l}}{r^3} \quad (\text{B.2})$$

This allows deriving the Prandtl's lifting line equation over the lifting line spanning between $y = -b/2$ and $y = b/2$, where the circulation $\Gamma(y)$ is the unknown of the problem:

$$-\frac{\Gamma(y)}{\pi c(y)U_\infty} - \underbrace{\frac{1}{4\pi U_\infty} \int_{y'=-b/2}^{b/2} \frac{\frac{d\Gamma}{dy'} dy'}{y-y'}}_{w_i/U_\infty} + \sin \alpha = 0 \quad (\text{B.3})$$

As already explained in the rest of the thesis, the shed vorticity corresponds to $-\frac{d\Gamma}{dy}$, a positive variation of the circulation over the line being compensated by the circulation of the wake vortices, which is then opposite due to Kelvin's conservation of the circulation. This equation can simply be interpreted in terms of angles as shown in Figure B.1 and written in the following equation with $\alpha \ll 1$:

$$-\alpha_e - \alpha_i + \alpha = 0 \quad (\text{B.4})$$

The downwash induced by the trailing vortices modifies the geometric angle of attack α and reduces the effective angle of attack seen by the body. This actually corresponds to less lift generated, indicated in Figure B.1 by the passage from l to l_e . In effect, this also corresponds to the generation of induced drag due to the downwash w_i which can be expressed as

$$d_i(y) = -\rho U_\infty \tan \alpha_i \Gamma(y) \quad (\text{B.5})$$

The total lift and drag can be calculated by integrating the lift and drag per unit span over the span.

¹Section 8.1

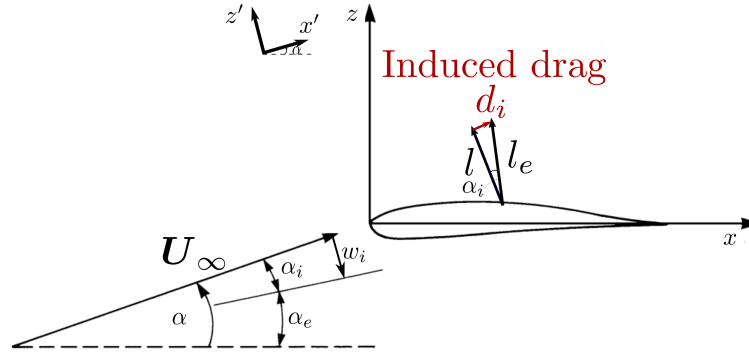


Figure B.1: Decomposition of the angle of attack α as a function of the effective angle α_e and the induced angle α_i from equation (B.4).

B.1.2 Glauert's method

Equation (B.3) does generally not admit analytical solutions and numerical strategies must be used to find numerical solutions to the lifting line equation. Glauert's method is probably the most famous and simple way of solving it numerically. The idea is to decompose the circulation into a Fourier series, proceeding to a variable change, setting

$$y = -b/2 \cos \theta \quad (\text{B.6})$$

and writing

$$\Gamma(\theta) = 4bU_\infty \sum_{k=1}^{\infty} A_k \sin(k\theta). \quad (\text{B.7})$$

ensuring the circulation is zero at the tips ($\theta = 0$ and π).

The induced velocity w_i can be reexpressed by using the Glauert's integral

$$\frac{1}{\pi} \int_0^\pi \frac{\cos(k\phi)}{\cos \theta - \cos \phi} d\phi = \frac{\sin(k\theta)}{\sin \theta} \quad (\text{B.8})$$

yielding

$$w_i = U_\infty \sum_{k=1}^{\infty} \frac{kA_k \sin(k\theta)}{\sin \theta} \quad (\text{B.9})$$

Finally, equation (B.3) can be rewritten

$$\sum_{k=1}^{\infty} A_k \sin(k\theta) \left(4b + \frac{kC_{l_\alpha} c(\theta)}{\sin \theta} \right) = C_{l_\alpha} c(\theta) \alpha \quad (\text{B.10})$$

This equation can be rewritten as a linear matrix system and simply resolved over the span, ranging from $\theta = 0$ to π , for a finite number of Fourier coefficients A_k . The resulting circulation is obtained afterwards. This has for example been applied to the elliptic wing presented in the thesis, classical example of use of the method.

B.2 Three types of singularities

It can be shown that the potential solution is a combination of two elementary solutions of the Laplace equation:

1. The source σ
2. The doublet μ

Other types of singularities can be constructed out of these elementary solutions, as the vortex singularity used in the thesis with VLM. The three singularities are described further in the following sections.

B.2.1 The source

The potential of a source element placed at the origin of a spherical frame of strength σ , can be written

$$\Phi = -\frac{\sigma}{4\pi r} \quad (\text{B.11})$$

from which the velocity can be computed by applying the gradient operator on the potential. In spherical coordinates, the velocity is directed towards r only and writes

$$\mathbf{u} = \frac{\sigma}{4\pi r^2} \mathbf{e}_r \quad (\text{B.12})$$

The velocity obtained presents a singularity for $r = 0$, where the source element is placed, and decays as $1/r^2$.

B.2.2 The doublet

The doublet can be seen as the interaction of a source and a sink (source with $\sigma < 0$), with an infinite strength σ but infinitely close to each other, the distance l between the two tending towards 0. The product $\sigma \times l$ yields the doublet strength μ , which is finite.

The potential due to a doublet vector $\boldsymbol{\mu}$, directed from the sink (at $r = 0$) to the source with an intensity μ , can be written

$$\Phi = \frac{\boldsymbol{\mu} \cdot \mathbf{r}}{4\pi r^3} \quad (\text{B.13})$$

As an example, one can consider the doublet vector oriented towards x in cartesian coordinates: $\boldsymbol{\mu} = \mu \mathbf{e}_x$. The potential at a point $P(r, \theta, \phi)$ is then

$$\Phi(P) = \frac{-\mu \cos \theta}{4\pi r^2} \quad (\text{B.14})$$

The streamlines due to this doublet are shown in Figure B.2.

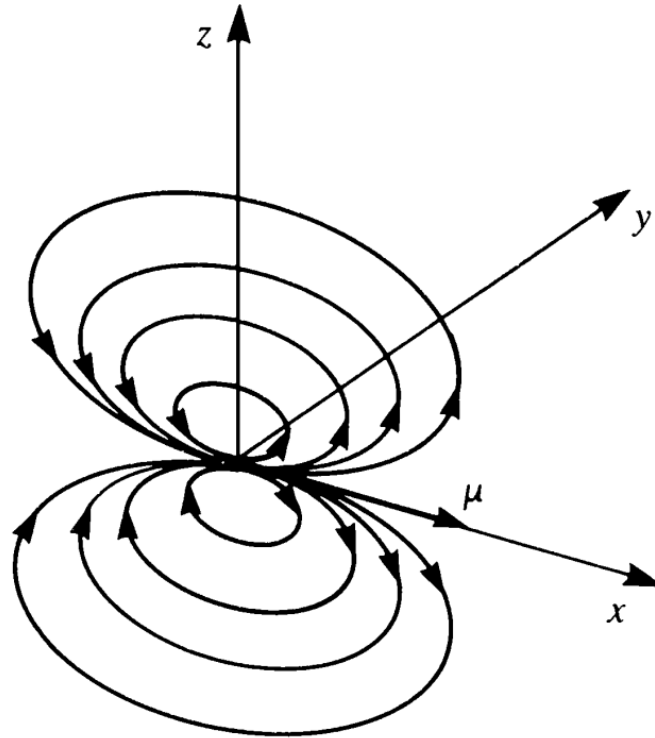


Figure B.2: Streamlines due to the doublet vector μ oriented in the axis direction x .

B.2.3 The vortex

The source provides an elementary solution for which the velocity only has a radial component. Another type of solution can be constructed with a component towards θ only in cylindrical coordinates. The velocity due to the presence of a vortex of circulation Γ , oriented towards the axial direction, can be written

$$\mathbf{u} = -\frac{\Gamma}{2\pi r} \mathbf{e}_\theta \quad (\text{B.15})$$

And the corresponding potential is therefore by integration:

$$\Phi = -\frac{\Gamma}{2\pi} \theta + K, \quad (\text{B.16})$$

with K a constant of integration, that can be set to zero.

It must be mentioned that the flow is irrotational with this type of solution in any case. Indeed, the vortex elements are discrete singularities concentrated on a point, *i.e.* over a zero surface area. The integration of them results in no vorticity generated since the vortex element has, in effect, no core. These singular vortices are usually called *irrotational vortices* for this reason. The Rankine vortex is a perfect illustration of how vorticity can be added to the vortex representation. As introduced in the literature review, the tangential velocity V_θ increases linearly over the core radius R and decreases as $1/r$, exactly as the singular vortex element. This core radius is responsible for a generation of vorticity.

B.3 Analytical vortices

The Vortex Lattice Method (VLM) is based on potential vortices, also referred to as *irrotational* vortices. The circulation Γ of such vortices is concentrated on a vortex line. If the induced velocity due to this vortex is calculated, the result diverges when getting too close to the vortex line. Indeed, the induced velocity at a distance r from a line of circulation Γ oriented towards x writes

$$\mathbf{V}(r) = \frac{\Gamma}{2\pi r} \mathbf{e}_\theta \quad (\text{B.17})$$

in cylindrical coordinates.

The resulting axial vorticity, calculated as

$$\omega_x(r) = \frac{1}{r} \left(\frac{\partial(rV_\theta)}{\partial r} - \frac{\partial V_r}{\partial \theta} \right) \quad (\text{B.18})$$

is therefore null everywhere in the field, except over the vortex line, where the axial vorticity is infinite. Hence the name of the potential vortex, irrotational.

It is possible to add vorticity by giving the vortex line a radius, where the vorticity is concentrated. This is the Rankine vortex. The tangential velocity of this vortex, of circulation Γ , writes:

$$V_\theta(r) = \begin{cases} \frac{\Gamma r}{2\pi R_c^2} & \text{if } r \leq R_c \\ \frac{\Gamma}{2\pi r} & \text{if } r > R_c \end{cases} \quad (\text{B.19})$$

For $r \leq R_c$, the tangential velocity increases linearly with the distance from the core, up to the edge at the position $r = R_c$. The vortex consists of two regions: the central core for $r \leq R_c$, comprising the vorticity and an outer region where the vortex is irrotational (for $r > R_c$).

Finally, Lamb's vortex is interesting since its behaviour is the same as Rankine's for r close to 0 and far from the core center. The advantage is that, in the middle, the axial vorticity is continuous. Indeed, the tangential velocity writes for a Lamb vortex:

$$V_\theta(r) = \frac{\Gamma}{2\pi r} (1 - e^{-r^2/R_c^2}) \quad (\text{B.20})$$

and the axial vorticity is:

$$\omega_x(r) = \frac{\Gamma}{\pi R_c} e^{-r^2/R_c^2} \quad (\text{B.21})$$

Figure B.3 shows the tangential velocity and the axial vorticity of these three line vortex representations.

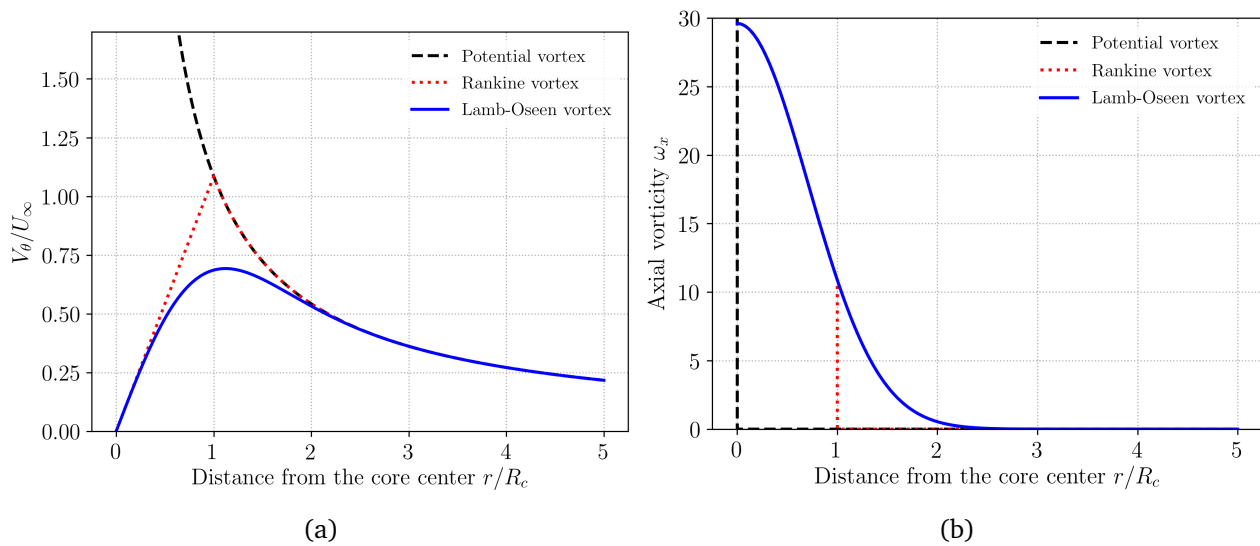


Figure B.3: (a) Normalized tangential velocity as a function of the distance to the core for three analytical vortices. (b) Resulting axial velocity $\omega_x(r)$.

PRELIMINARY STUDY TO THE ZDES APPROACH

Contents

C.1 Calibration of the boundary conditions	206
C.1.1 Three-stage simulation	206
C.1.2 Calibration of the ZDES simulation	208
C.2 Comparisons of RANS/ZDES results	213
C.2.1 Performance	214
C.2.2 Radial profiles	214
C.2.3 Tip flow analysis	217

C.1 Calibration of the boundary conditions

C.1.1 Three-stage simulation

With the resolution of the hybrid approach, only one passage of the rotor can be simulated with a reasonable number of elements, here about 100 million as explained in section 4.1.3. The difficulty then lies in the boundary conditions at the inlet and the outlet to reproduce as well as possible the flow conditions upstream and downstream the third rotor. Directly using the experimental profiles would be possible but no measurements are available in the endwall boundary layers near the walls since the pneumatic probes are located between 5 and 95 % height. An extrapolation up to casing and down to hub from these positions induces a non-physical boundary layer at the inlet that forces the solver to compensate and recover a physical boundary layer. This extrapolation particularly impacts the inlet direction of the flow: the incidence angle is mispredicted and the stability of the simulation strongly affected. Besides, this compensation requires an adaptation length that can be greater than 30 times the thickness of the initial boundary layer. In our case, this represents a duct more than 10 chords long, increasing the number of elements significantly for the ZDES resolution.

Another solution is to find the equivalent design operating point with the RANS approach by simulating the whole compressor with the model of Spalart-Allmaras (SA), to remain consistent with the ZDES formulation used. This wide-domain RANS simulation can then be used to define the ZDES boundary conditions on the rotor alone. Nevertheless, because of the assumptions lying behind RANS turbulence modelling but also due to the difficulty of reproducing boundary conditions, the RANS and experimental flow structures and fields generally present differences. The compressor map described by both approaches, for one fixed revolution speed, is therefore also different and picking the right operating point corresponding to the experimental one can be challenging.

C.1.1.1 Criterion for the operating point calibration

A well-accepted and common criterion to find the operating point with the 3-stage simulation is based on the equality of the Π/\dot{m}_{std} ratio, with

$$\dot{m}_{std} = \frac{\dot{m}\sqrt{T_{t1}}}{P_{t1}} \quad (\text{C.1})$$

The indices 1 and 3 are defined in Figure 1.3 in Chapter 1 across a compressor stage, designating the flow conditions upstream of the rotor and downstream of the stator. This classical criterion is used to calibrate RANS simulations with the experimental compressor map. This choice is explained in Rochuon's thesis [115]: at the outlet of one stage, the flow conditions between the experiment and the simulation can be considered as equivalent if the Mach number and the absolute fluid angle are the same. The equality of M_3 and α_3 ensures that the stage outlet conditions are the same for a fixed revolution speed. Writing the expression of the mass flow rate downstream the stator for a passage section S_3 :

$$\dot{m} = \rho_3 V_3 \cos\alpha_3 S_3 \quad (\text{C.2})$$

Number of elements	13×10^6
RANS turbulence model	Spalart-Allmaras
Spatial scheme	Jameson
Inter-row condition	Mixing planes
Inlet	Map from Riéra [113]
Outlet	Radial equilibrium
Walls	Adiabatic no-slip

Table C.1: Recap of the main numerical parameters of the 3-stage simulation.

Re-expressing (C.2) as a function of the Mach number in terms of standard mass flow rate:

$$\dot{m}_{std} = \underbrace{P_{s3}/P_{t1}}_{\Pi_{3,s-t}} \sqrt{\frac{\gamma T_{t1}}{R_{gas} T_{s3}}} M_3 \cos \alpha_3 S_3 \quad (C.3)$$

Assuming the inlet total temperature T_{t1} , γ and R_{gas} are constant, the quantity

$$\frac{\dot{m}_{std}}{\Pi_{3,s-t}} \quad (C.4)$$

should be the same in the experiment and the simulation.

The criterion can also be used for total-to-total compression ratios since

$$\frac{P_{s3}}{P_{t1}} = \frac{P_{s3}}{P_{t3}} \times \frac{P_{t3}}{P_{t1}} = \left(1 + \frac{\gamma - 1}{2} M_3^2\right)^{\frac{\gamma}{\gamma-1}} \Pi_{3,t-t} \quad (C.5)$$

C.1.1.2 Calibration of the 3-stage RANS simulation

Figure C.1 shows the computational domain used for the 3-stage steady RANS simulation and Table C.1 summarizes the main characteristics of the 3-stage simulation. The third rotor is indicated in green in the domain. The inlet block upstream of rotor 1 is displayed in blue and the outflow block is colored in red.

Each row of the compressor is simulated over one single passage. Because of the relative motion of the rotor frame with respect to the stator frame, the flow conditions at the inter-row must be averaged pitchwise before being transferred to the next row. This is referred to as a mixing plane condition for every inter-row plane.

The inlet map is extracted from Riéra's work and corresponds to the flow conditions between the IGV and the first rotor. This is imposed as the inlet condition of the block in blue in the figure, corresponding to the plane 25A shown in the meridian view of CREATE in Figure 4.2. Several simulations have been performed for different pivot pressures at the outlet, starting from a point near choke and climbing the characteristic map to the left up to the peak efficiency, that is of interest in the thesis, based on the criterion derived above.

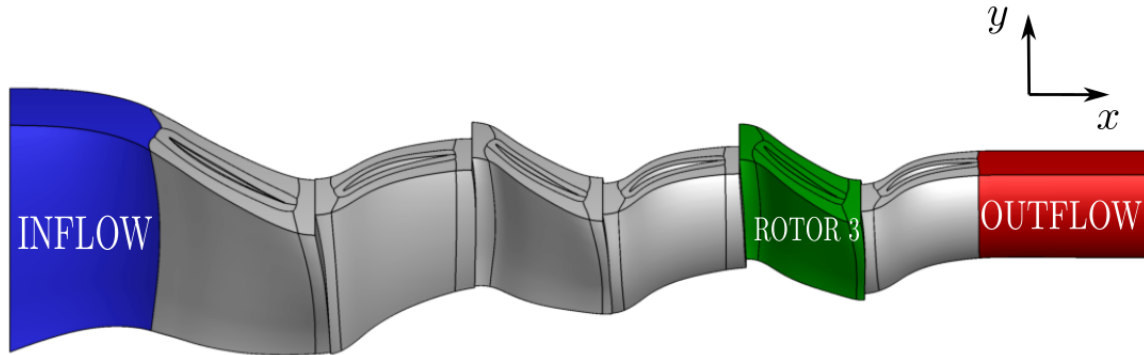


Figure C.1: Illustration of the computational domain used for the 3-stage RANS simulation of the preliminary study. The blades shown are deformed on purpose in the picture.

Figure C.2a shows the compressor map of CREATE and the line corresponding to a constant Π/\dot{m}_{std} ratio. The compressor map is here partly reconstructed up to the operating point indicated by the blue square in the figure, close to the constant Π/\dot{m}_{std} ratio line. This was done by starting with the first operating point at choke ($\dot{m}_{std} = 1.13$) and progressively increasing the static pressure at the outlet to progress through the compressor map. It can be noted that the numerical compressor map is shifted to the right compared to the experimental one. The mass flow rate predicted by the RANS simulations is overestimated for a fixed compression ratio: the difference is nearly constant and is about 0.05 in terms of normalized standard mass flow rate.

The operating point indicated by the blue square in the figure is located at ($\dot{m}_{std} = 1.034$, $\Pi = 0.987$), normalized by the values of the experimental operating point. The simulation is particularly sensitive when reducing the mass flow rate further. Closer to the surge limit, the convergence is very complicated to obtain with the steady RANS.

The numerical operating point indicated in the figure is chosen for extracting the flow conditions upstream and downstream rotor 3, in planes 280 and 28A. It corresponds to the peak efficiency of the compressor with this turbulent model as indicated in Figure C.2b by the blue square. The profiles extracted in planes 280 and 28A are now used for the calibration of the single-stage ZDES simulations across the third rotor.

Note that the Spalart-Allmaras turbulence model has been chosen for the calibration to be consistent with the ZDES formulation used, based on the Spalart-Allmaras transport equation on the turbulent variable $\tilde{\nu}$.

C.1.2 Calibration of the ZDES simulation

Inlet boundary condition In order to compare reasonably to the experimental results, the simulation needs to be calibrated to the profiles obtained with the 3-stage RANS simulation presented in section C.1.1 for the operating point chosen. The calibration is carried out with RANS-SA on the isolated row before applying the calibrated boundary conditions to the ZDES

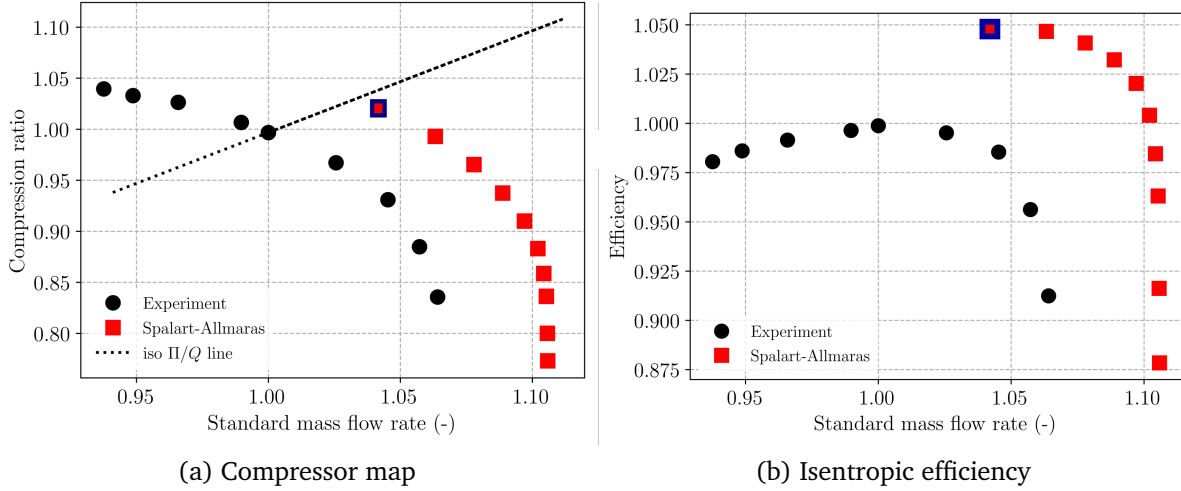


Figure C.2: Characteristic compressor map and isentropic efficiency of CREATE from the experimental measurements and obtained with the 3-stage RANS-SA approach. The operating point picked for the simulation is indicated with the blue square. The quantities are normalized by the experimental values obtained at the experimental nominal point.

simulations, on the same computational domain.

As explained before, the inlet and outlet boundary conditions are placed sufficiently far from the row to make sure they do not interfere with the simulation. Boundary conditions imposed too close to the region of interest may force the behaviour of the resulting solution. The plane 280 is too close from the leading edge plane of the third rotor (less than $0.25c_a$ in the axial direction) and the injection cannot be performed at this position. That is why the computational domain has been extended upstream of the row (cf. Figure 4.3) and the inlet boundary condition imposed $1.5c_a$ upstream of plane 280.

When imposing the conditions extracted in plane 280 from the 3-stage simulation at the inlet for the isolated row, the influence of the other rows is not accounted for in the simulation because only the third rotor is considered. The profile obtained is therefore largely modified through the channel between the inlet plane and plane 280, where the condition is sought to be the same as in the 3-stage simulation. The conditions supplying the rotor are not the same and the resulting gradients on the profiles obtained in plane 280 are significantly different.

Figure C.3 shows the profiles of P_t , T_t and α :

- Extracted from the 3-stage RANS simulation at plane 280 (dashed lines), which therefore represent the target profiles.
- Extracted in the isolated-row RANS-SA simulation at plane 280 (solid lines) after injecting the target profiles in the inlet plane.

Between the injection plane and plane 280, the three profiles have clearly been deformed. This is particularly visible on the absolute fluid angle α : the incidence angle on the third rotor is significantly affected and must be recalibrated, to get closer to the nominal flow conditions.

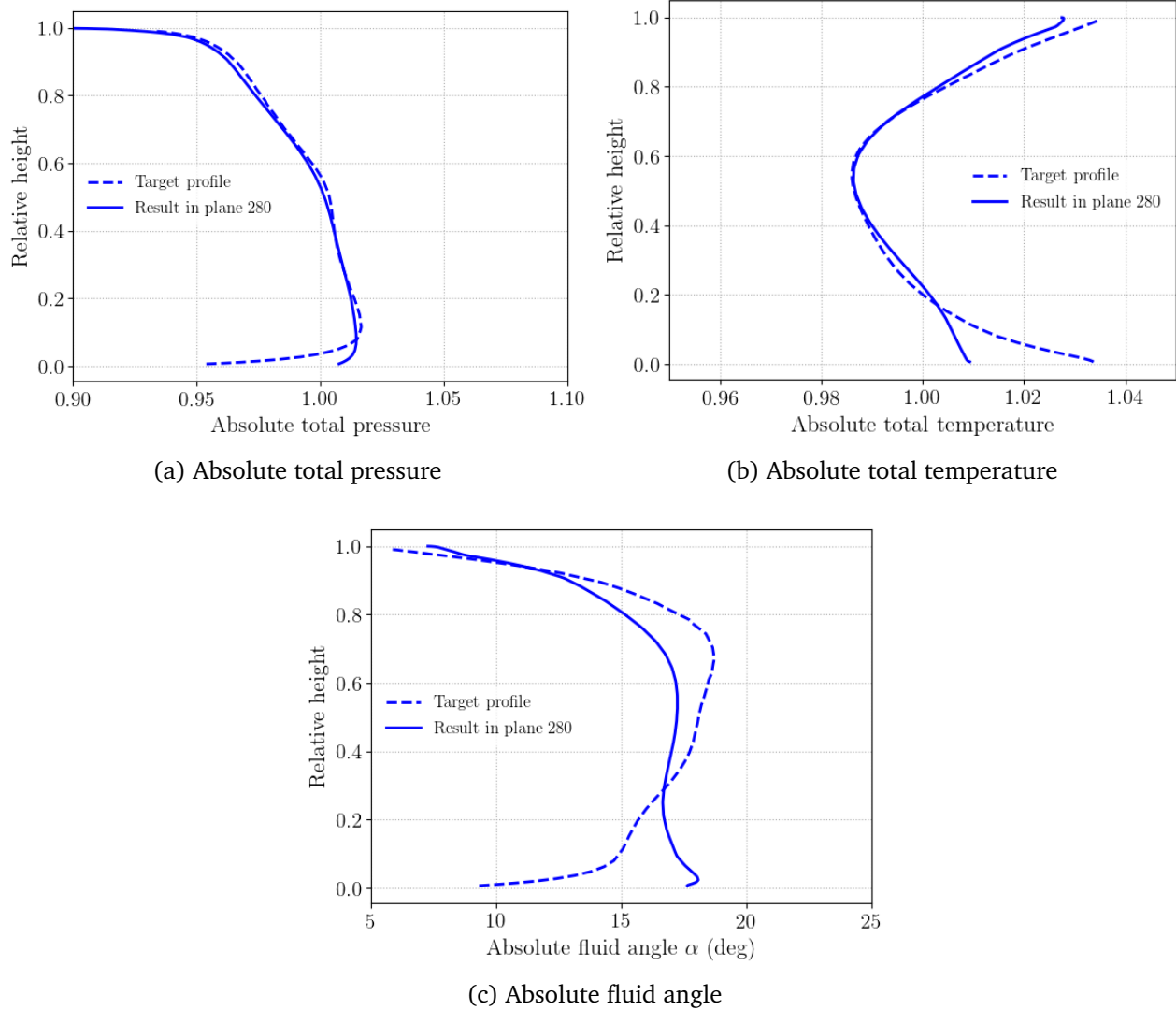


Figure C.3: Comparison between the target profiles from the 3-stage simulation and the resulting profiles in plane 280 with the isolated row.

This is due to the fact that the influence of the five other rows in the three-stage simulation is here not considered. In particular, the rotor/stator interactions (wakes and potential effects) are not accounted for on the single row and a calibration based on a simulation where these effects are treated is necessary.

The calibration is carried out iteratively on the five values injected at the inlet (cf. section 4.1.4). For each value, three profiles are used:

- The target, from the 3-stage simulation, in plane 280.
- The profile injected at the inlet.
- The profile obtained in plane 280 in the isolated rotor simulation.

For each calibration injection, the new boundary conditions injected depend on these three profiles and are calculated using the following expression, here applied on the absolute fluid angle α :

$$\underbrace{\alpha^{new}}_{\text{Black}} = \underbrace{\alpha^{target}}_{\text{Dashed blue}} - \underbrace{\alpha^{280}}_{\text{Solid blue}} + \underbrace{\alpha^{injected}}_{\text{Red}} \quad (\text{C.6})$$

Figure C.4 shows an illustration of the calibration process on α . The same process is applied to P_t , T_t , φ and $\tilde{\nu}$. The red profile is the profile injected at the inlet at the current iteration of calibration. The blue one is the result obtained in plane 280, which is compared to the target profile (dashed blue line). The black profile results from the application of equation (C.6). This profile then becomes the new red profile for the next iteration of calibration and the same process applies. The process is repeated until a convergence on the black profile is obtained. The convergence is estimated qualitatively: as soon as the solid blue line for all the values injected superimposes well with the dashed blue line, and if the next iteration of calibration yields the same solid blue line, the calibration is considered good enough.

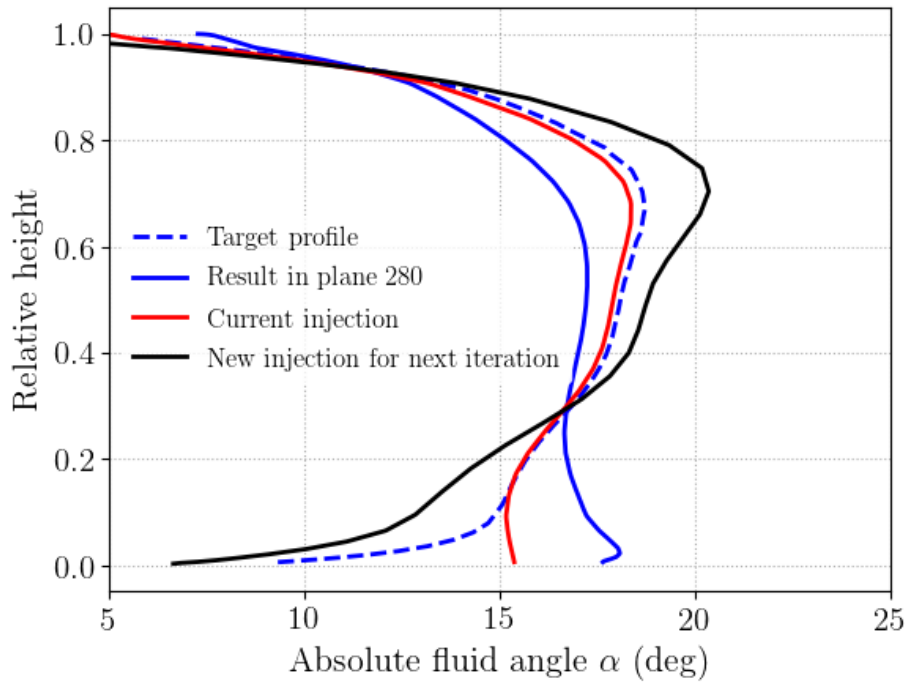


Figure C.4: Illustration of the calibration process after the first iteration.

Figure C.5 shows the results of the calibration on the total pressure P_t , the total temperature T_t and the absolute fluid angle α , after thirteen iterations. The solid blue line resulting from the injection of the solid red line fits well the target profile for each value calibrated, especially in the last 20% near casing, our zone of interest for the investigation on the tip-leakage flow. The red profiles are then kept for the ZDES simulation.

Outlet boundary condition Now that the absolute variables injected are calibrated, it still remains to calibrate the flow incidence by adapting the relative fluid angle β_1 on the rotor.

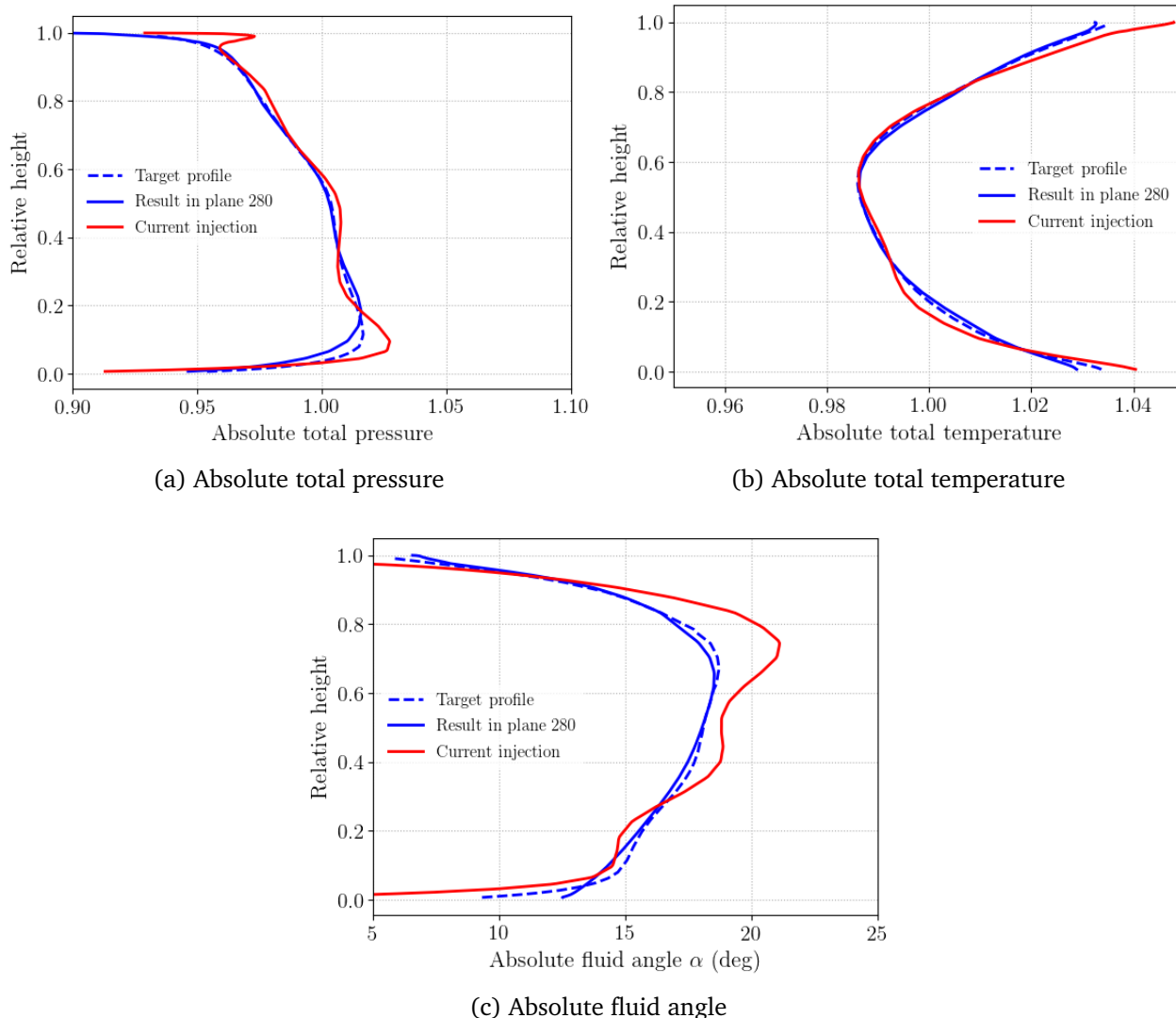


Figure C.5: Calibrated inlet profiles after thirteen iterations. The red profiles are those kept for the simulations.

In order to do that, the outlet static pressure must be modified to ensure a good fit between the static pressure in plane 28A with the isolated rotor and that extracted from the three-stage simulation.

The outlet boundary condition is placed 1.5 axial chord lengths downstream of the row to limit the perturbation of the flow. The grid is also stretched downstream of plane 28A to limit wave reflections. The static pressure extracted from the three-stage simulation in plane 28A is used as the outlet boundary condition in the isolated row configuration (target profile). Figure C.6 exhibits the target profile (dashed line) and the resulting profile in 28A with the isolated row (solid line). As between the inlet and plane 280 on the injected inlet values, the same issue is encountered between plane 28A and the outlet on the static pressure radial profile. A radial equilibrium is imposed at the outlet but the profile is deformed in-between and the resulting

profile in 28A is not preserved.

A solution could be to apply the same procedure described for the inlet conditions to the outlet condition with the static pressure. This nonetheless also modifies the propagation of the inlet boundary condition between the inlet plane and plane 280 and a coupling process of calibration, alternately between the inlet and the outlet is therefore required. Another solution could be to modify locally the geometry of the duct between plane 28A and the outlet.

In the present thesis, the simulations use this uncorrected outlet condition. The objective is mainly to numerically understand the influence of the tip gap size on TLF with the help of a hybrid resolution. As it is shown in the next section, the comparison of RANS/ZDES with the experiments is acceptable enough to keep this formulation.

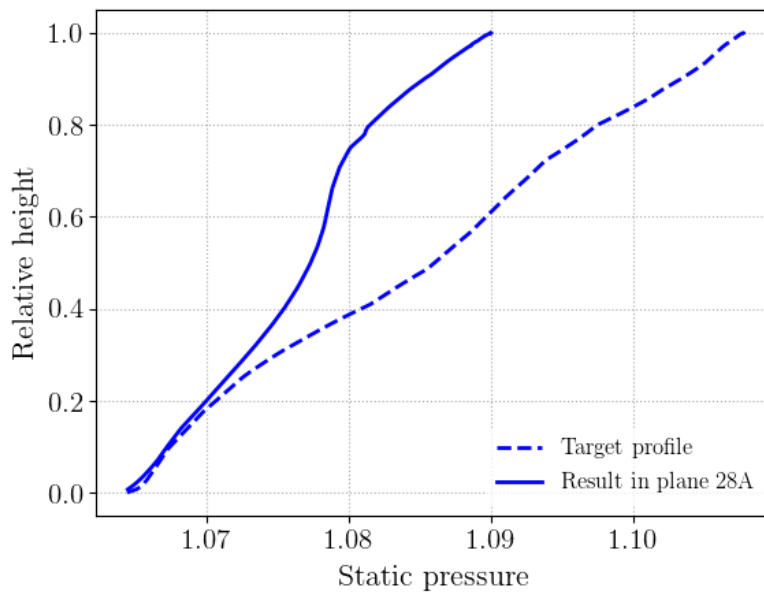


Figure C.6: Comparison of the static pressure profiles from the 3-stage RANS simulation and for the isolated rotor (RANS-SA and ZDES) in plane 28A.

C.2 Comparisons of RANS/ZDES results

Before comparing the results for the three different gap sizes, this section analyzes the results obtained with the ZDES approach in comparison to what is obtained with a RANS SA approach. It gives a first overview of the results and shows the benefits of the hybrid approach to treat this kind of flow. If not otherwise mentioned, all the ZDES results are time-averaged over one-quarter of a revolution, which represents $20 T_{bp}$, where T_{bp} is the blade passing period, and about 20 times the advection time T_{adv} based on the axial chord length and the velocity at the tip of the blade.

$$T_{bp} = \frac{2\pi}{N_{blades} \omega} \quad (C.7)$$

$$T_{adv} = \frac{c_a}{r_{tip} \omega} \quad (\text{C.8})$$

C.2.1 Performance

The overall performance of the row can be summarized by Table C.2 for the operating point corresponding to the inlet and outlet boundary conditions defined in the previous section. The mass flow is overestimated numerically with the two approaches compared to the experiment. Logically, the compression ratio is underestimated, a bit more for ZDES than for RANS. The reason lies in the calibration choices made with the different assumptions mentioned and also in the uncertainties from the experiment. Also, the calibration was done on a coarser mesh on the same computational domain to reduce its cost: it would have been too long and too costly with the ZDES grid. As for the efficiency, it is higher in the numerical simulations because of the modelling assumptions, for example the rotor/stator interactions are not accounted for with the single rotor approach. Regarding the RANS/ZDES comparison, the hybrid approach yields a higher efficiency.

	Mass flow rate	Compression ratio	Efficiency
Experimental design point	1	1	1
Rotor 3 - From 3-stage SA simulation	1.034	0.987	1.037
Rotor 3 Spalart-Allmaras	1.094	0.985	1.023
Rotor 3 ZDES	1.100	0.978	1.067

Table C.2: Performance of the third rotor. Quantities normalized so as to be equal to 1 for the experimental design point.

C.2.2 Radial profiles

The performance table gives a first overview of how the numerical approaches compare to the experiment. Looking at the radial distributions gives more details about the flow characteristics upstream and downstream of the row. The compression and temperature ratios are first good indicators of the quality of the comparison between numerical and experimental results. It is recalled that the measurements from the pneumatic probes are used for the total pressure and temperature. The experimental axial velocity and the relative fluid angle are given by the time and pitch-averaged laser measurements, described in section 2.3.

Different explanations can be put forward to explain the differences between the Rotor 3 Spalart-Allmaras simulation and the experiments in terms of overall performance. First, the rotor-stator interactions, unsteady phenomena, are not taken into account with the isolated approach. Despite the calibration of the boundary conditions, the influence is certainly not completely captured in steady boundary conditions. Second, the cavities upstream and downstream the rotor are not considered in the simulations. The respective suction and the injection from

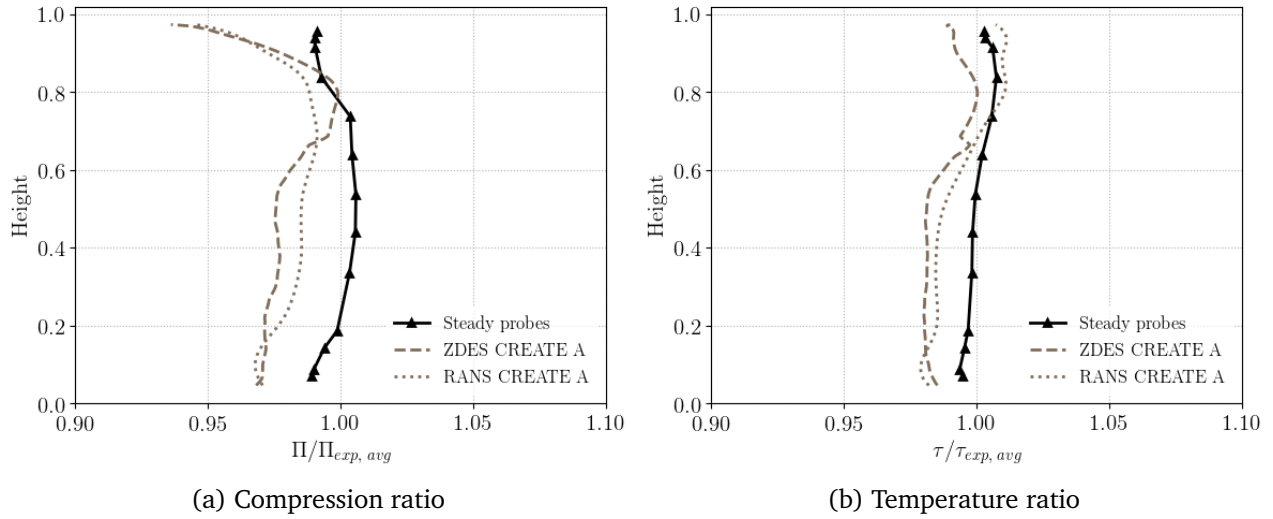


Figure C.7: Compression and temperature ratio distributions between planes 28A and 280.

the cavities of stators 2 and 3 indeed play a role in the flow conditions [88]. The uncertainties of the measurements can also explain the differences. Also, the compression ratio obtained experimentally is based on an average between 5% and 95% of span height. This probably has an impact since the average is weighed by the mass flow rate. From the definition of equation (4.1), the integral is reduced with the decay of the axial momentum ρV_x near the walls if the 5% near the walls are accounted. This is consistent with the observed underestimate obtained numerically compared to the experiment.

Total pressure and temperature ratio distributions Figure C.7 shows the compression and temperature ratios across the third rotor of CREATE for the two numerical approaches and the steady probes. Consistently with Table C.2, the compression ratio for ZDES and RANS is below the experimental one, by less than 5%. The hybrid approach yields more compression ratio in the 20% height near casing when the RANS approach predicts more work done from the root of the blade to midspan. Regarding the temperature ratio, the results fit well with the experiment, the relative difference remaining lower than 2%. Overall, the ZDES yields lower values than RANS over the whole span for the temperature ratio, which explains the higher efficiency obtained compared to RANS. Another important observation concerns the gradient near casing. Around 70% height, the temperature ratio is nearly the same for the two numerical approaches. Up to casing, τ_{RANS} becomes greater than τ_{exp} while the τ_{ZDES} follows the experimental gradients.

A slope discontinuity can be observed in the ZDES approach around 70% height: this would correspond to the RANS/LES interface, where the flow resolution switches from one to the other. It is recalled that the second mode of ZDES treats the boundary layer with RANS. The boundary layer at casing in the rear part of CREATE, upstream of rotor 3, is indeed very thick. It is analyzed in section C.2.3.

Axial velocity and angle distributions Let us compare the incidence and axial velocity profiles ¹. Figure C.8 shows the two profiles in plane 280. The mean levels for the axial velocity are in reasonable agreement with the experiment but the gradients are better captured by the hybrid approach than by RANS. In particular, the minimum at 30% height is well captured by the ZDES, but not by RANS. The axial velocity distribution shows a higher blockage from midspan to casing with RANS results, different by a little more than 5% with the experiment. In comparison, the hybrid approach yields a maximum relative difference of 2%. Coherently, the corresponding relative fluid angle giving the incidence of the flow to the blade compares very well in the tip region with the ZDES, with a maximal relative difference of less than 1° in the last 30% height, while RANS predicts an overincidence of nearly 3°.

The stronger differences at the root of the blade, between both numerical approaches and the experiment, may be attributed to the corner separation, displayed in Figure C.19 for the two approaches.

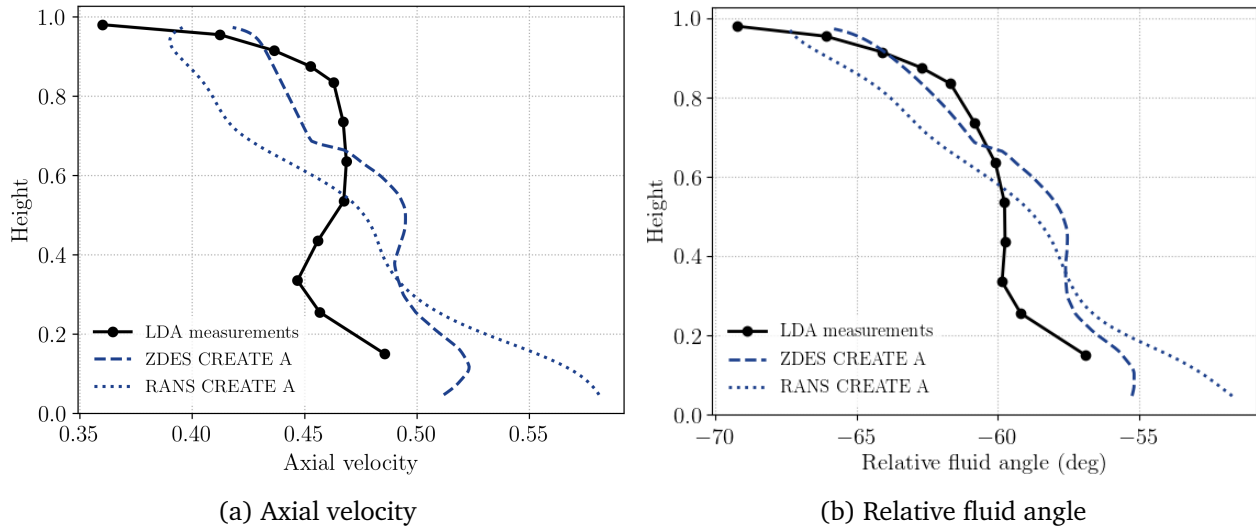


Figure C.8: Radial distributions of normalized axial velocity and relative fluid angle β in plane 280.

In Figure C.9, the same profiles are shown in plane 28A. The ZDES benefits are substantial in the tip region as it can be seen in the velocity and angle profiles compared to RANS. In the upper 20% height, the levels and gradients are in very good agreement with the LDA measurements whereas the RANS predicts a thicker boundary layer at casing, illustrating an important blockage. The strong blockage results from the important diffusion of the TLV with RANS. The tip flow analysis provides good explanations to this result and is dealt with in section C.2.3. This blockage directly impacts the velocity distribution from midspan to hub with an overestimated axial velocity for RANS, effect also seen with ZDES, but to a lesser extent. Regarding the deviation angle, a good prediction is achieved by ZDES over the whole span, while it is overestimated

¹The relative flow angle β_1 is also referred to as *incidence angle* in the thesis since the incidence angle, $i = \beta_1 - \beta'_1$, is simply defined by the difference between the flow angle and the metal angle at the leading edge.

by RANS below 80% and underestimated near the casing. The deflection, calculated as the difference of relative fluid angles between planes 28A and 280, is therefore well predicted in the tip region with the ZDES approach. This ensures that the work done by the rotor is also well predicted according to Euler’s equation.

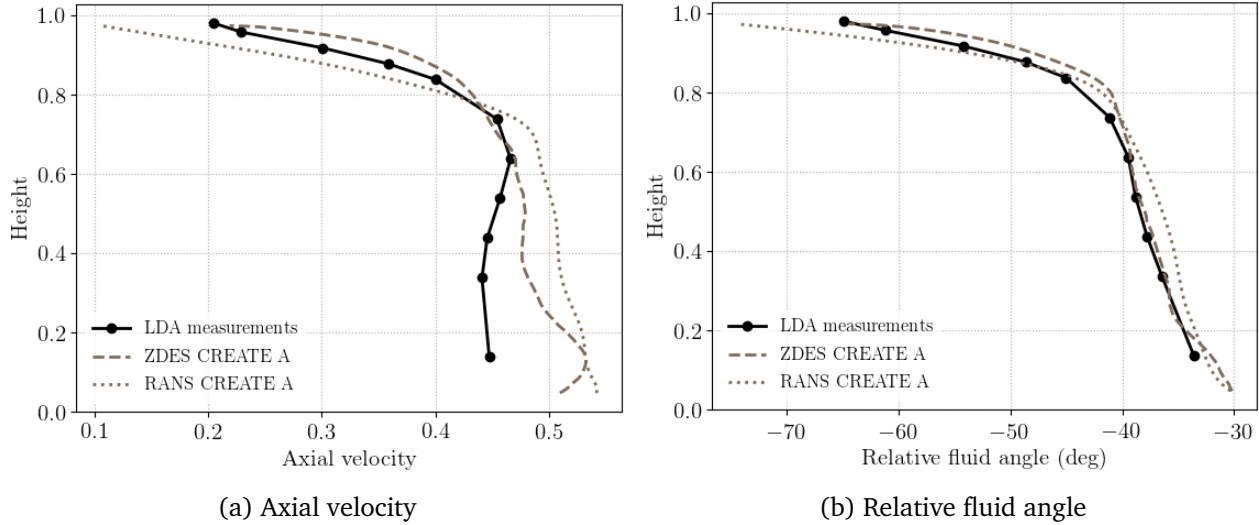


Figure C.9: Radial distributions of normalized axial velocity and relative fluid angle (or deviation angle) β in plane 28A downstream rotor 3.

C.2.3 Tip flow analysis

The flow field in the tip region near casing is analyzed in this section. The topology of the TLF is analyzed and the differences between RANS and ZDES are highlighted. The losses generated by the TLV in the blade passage are also treated.

C.2.3.1 Numerical resolution

As explained in section 2.1, ZDES represents a very good compromise between resolution and computing time by switching between RANS and LES to resolve turbulence within the regions of interest, such as secondary or separated flows, generally mispredicted by RANS. The approach clearly shows benefits regarding the aerodynamic performance obtained, which is in better agreement with the experiment. With the second mode of ZDES used here, the boundary layers are simulated with RANS and the switch to LES occurs around the edge of that one.

A view in plane 280 is displayed in Figure C.10 from the RANS and the ZDES simulations. For both resolutions, this shows the μ_t/μ distribution in the plane. In the case of ZDES, the f_d isolines are also indicated in the figure. The values of the protection function allow identifying the zones treated by RANS and LES: the dashed lines correspond to a nearly fully resolved LES ($f_d = 0.99$) while the solid lines bound a RANS region ($f_d = 0$). In-between, the grey

zone corresponds to the region where the eddy viscosity is destroyed towards a complete LES resolution.

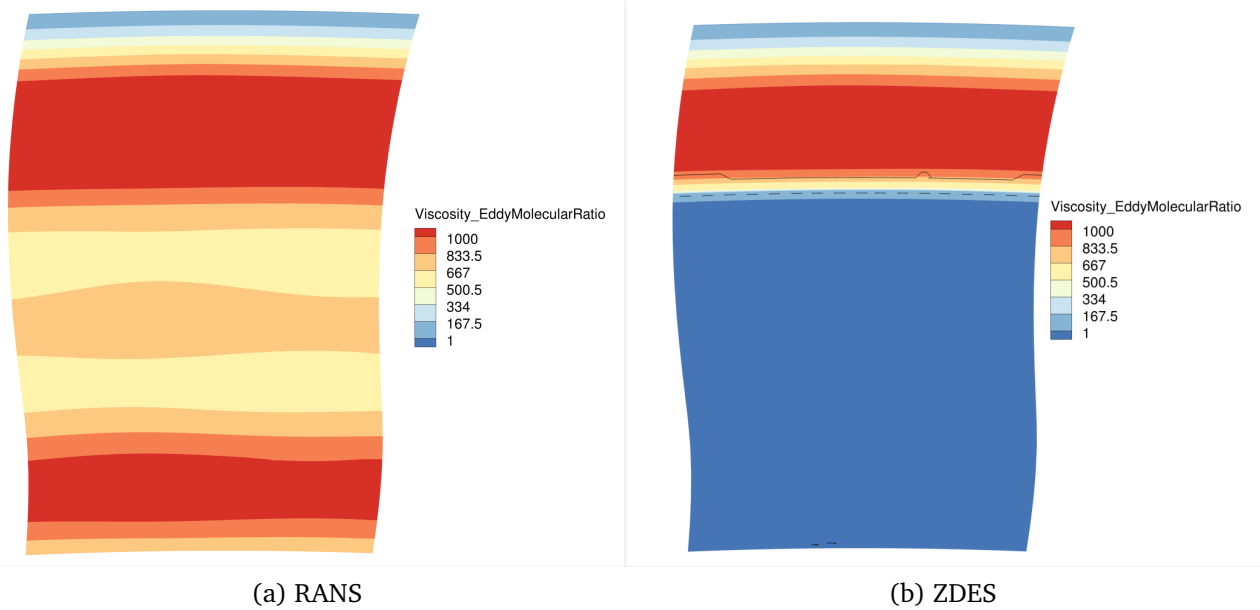


Figure C.10: Contours of μ_t/μ in plane 280 with RANS and ZDES. The isolines of the protection function f_d are also shown for the ZDES. The dashed lines indicate $f_d = 0.99$ (LES zones), the solid lines $f_d = 0$ (RANS zones).

Figure C.10b enables to identify the casing boundary layer region, treated by RANS in the ZDES simulation, from casing over about 30% height. Such a boundary layer completely immerses the tip gap. Below the position of the solid line, the grey zone spans down to the dashed line from where the flow is resolved with LES. The μ_t/μ magnitudes are consistent with the switch: in the RANS region, they are about 1000, decrease throughout the grey zone to reach values lower than 1 in the LES region, order of magnitude typically observed for subgrid scales. The levels are in very good agreement with the RANS simulation of Figure C.10a, in the boundary layer. Below the position of the dashed line, marking the LES frontier, the levels of μ_t/μ suddenly drop with the ZDES while they decrease slowly with RANS. Near the hub wall, the ZDES treats the region with LES, probably because a wall slip condition is applied to the hub wall. This drives differently the destruction of the $\tilde{\nu}$ injected at the inlet compared to casing: the simulation switches to LES in that region and the protection of the boundary layer is not sustained. The focus however remains on the tip region in the present thesis.

In Figure C.11, the contours of the total pressure in plane 280 show that the inflow, right upstream of the row, is the same with the two resolutions. The differences in the levels of μ_t/μ do not affect the inflow condition. A slight difference can be noted within the grey zone, in the shape of the contour isolines, probably due to the switch from RANS to LES.

Figures C.12 and C.13 display the μ_t/μ and total pressure distributions from the RANS and the ZDES simulations, in plane 28A.

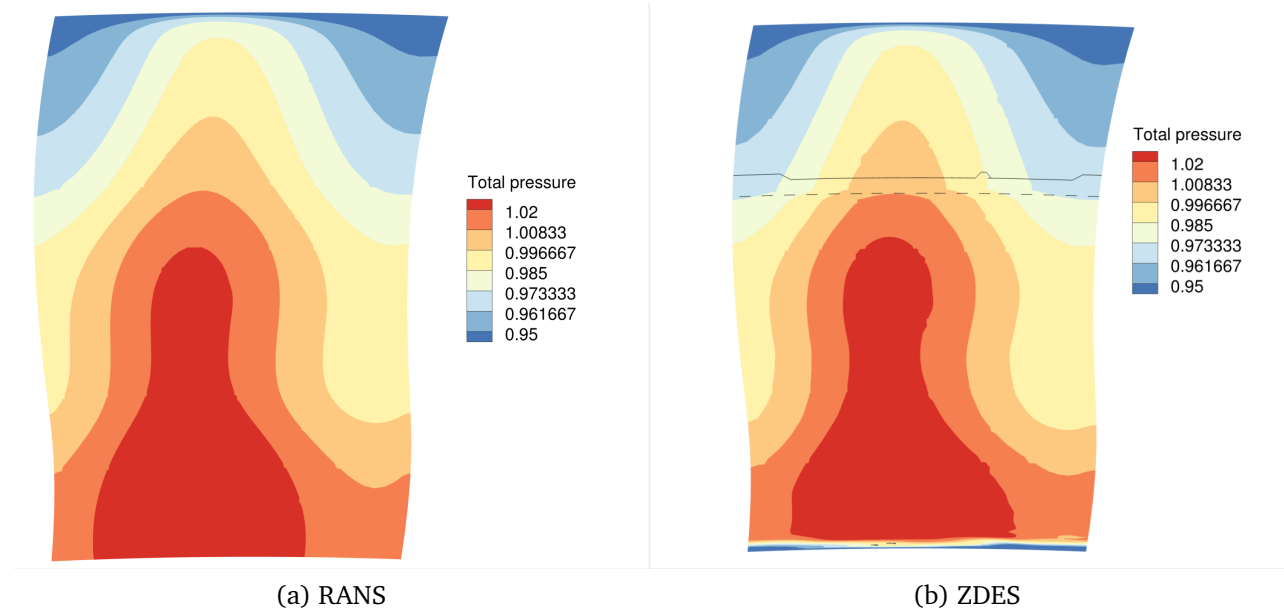


Figure C.11: Contours of total pressure in plane 280 with RANS and ZDES. The isolines of the protection function f_d are also shown for the ZDES. The dashed lines indicate $f_d = 0.99$ (LES zones), the solid lines $f_d = 0$ (RANS zones).

Figure C.12 shows the μ_t/μ contours in plane 28A along with f_d isolines with the same scale as in plane 280, from the RANS and ZDES simulations. Again, the contours of μ_t/μ in Figure C.12b are coherent with the values of f_d , with much higher values within the zones treated by RANS and SGS values in the LES zones. Between planes 280 and 28A, the boundary layer at casing has been sheared by the rotor: in middle pitch positions in the tip region, the flow is now treated with LES, corresponding to the wake and the TLV, as explained afterwards. When looking at the RANS distribution of μ_t/μ in Figure C.12a, the levels are larger than with ZDES everywhere in the plane, even in the zones where the flow is treated by RANS with ZDES.

The difference in numerical resolutions between planes 280 and 28A in the 30 % height near casing can explain the discontinuity in the slopes of total pressure and temperature ratios of the ZDES radial profiles: in plane 280, this region is completely predicted by RANS but in plane 28A, a good part is resolved with LES. As shown before, through the relative fluid angle profiles, the LES treatment is beneficial. The track of the wake is more clearly seen in Figure C.13b, around the middle pitch positions where the total pressure is the lowest. With RANS (Figure C.13a), the levels of total pressure are quite larger at the same middle pitch positions, in the wake.

Figure C.14 allows to observe the evolution of the eddy-to-molecular viscosity ratio with both approaches, through the passage, in-between the two planes 280 and 28A. In RANS, regions with a strong turbulence level can be identified from this ratio. It is preferred to the turbulent kinetic energy, which is not directly modelled with the RANS-SA model (see Chapter 2). It is interesting to note that the values of μ_t/μ are actually smaller through the TLV path than elsewhere over the span with the RANS approach.

In the ZDES, the TLV path is identified within the dashed lines from the point where it

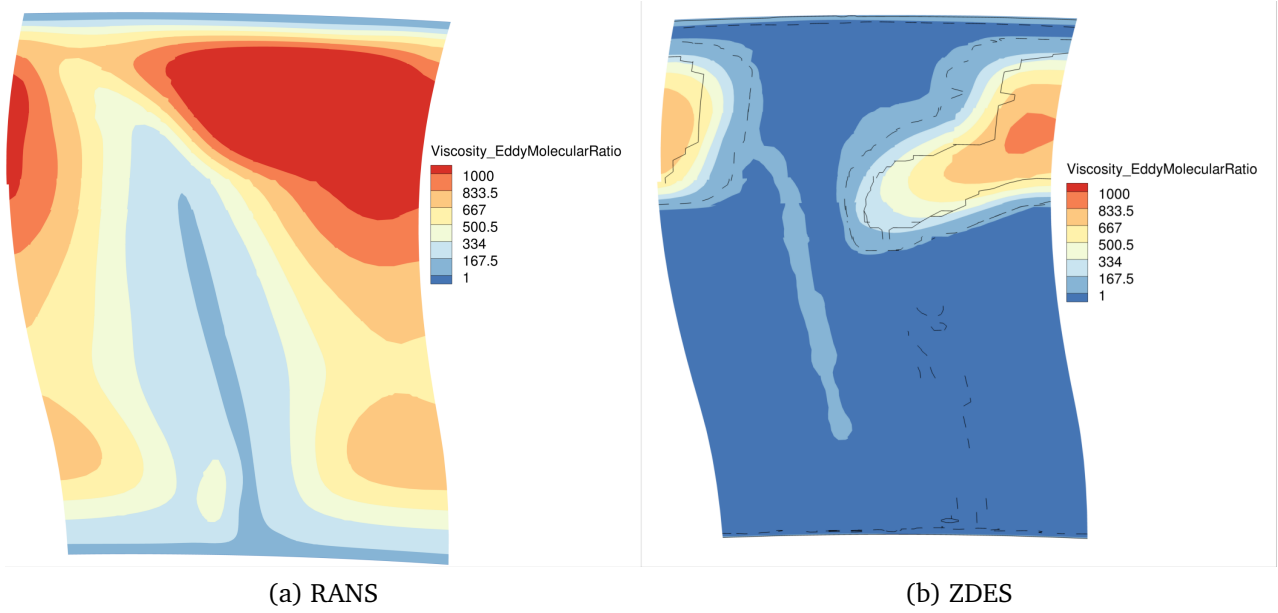


Figure C.12: Contours of μ_t/μ in plane 28A with RANS and ZDES. The isolines of the protection function f_d are also shown for the ZDES. The dashed lines indicate $f_d = 0.99$ (LES zones), the solid lines $f_d = 0$ (RANS zones).

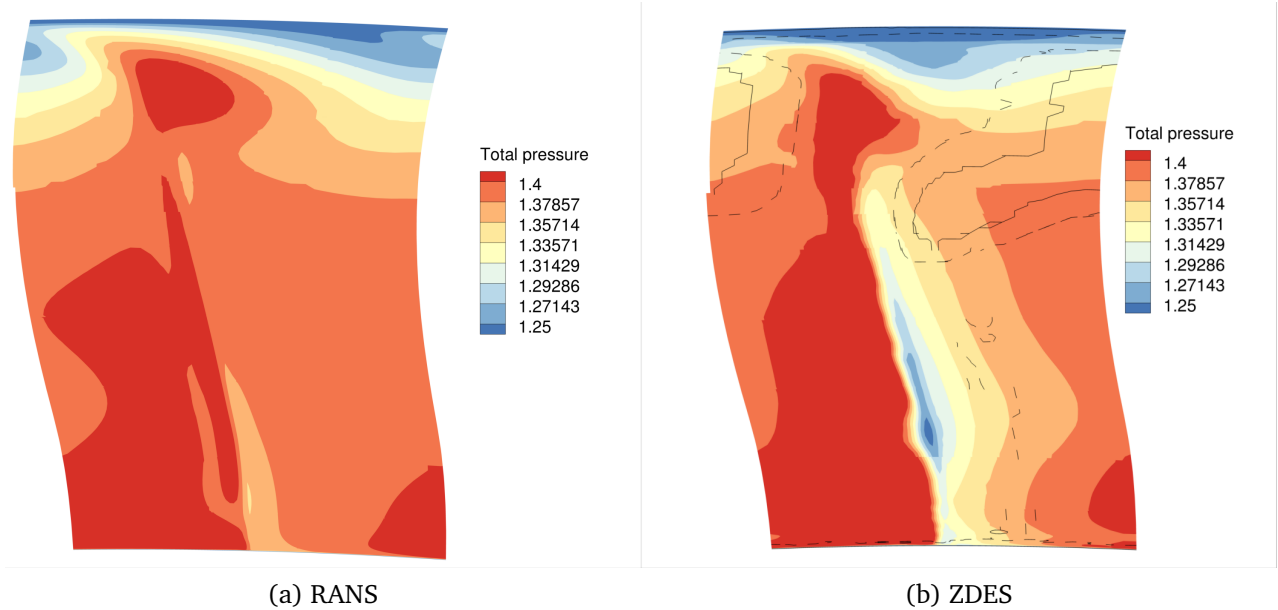


Figure C.13: Contours of total pressure in plane 28A with RANS and ZDES. The isolines of the protection function f_d are also shown for the ZDES. The dashed lines indicate $f_d = 0.99$ (LES zones), the solid lines $f_d = 0$ (RANS zones).

detaches around 20% c_a , corresponding to a full LES resolution. Upstream the row at casing, the boundary layer is completely treated with RANS. Downstream, the TLV path modifies the

treatment, initiates the switch to LES and the rest of the boundary layer, about 30% height thick, is treated with RANS. The main difference between RANS and ZDES between planes 280 and 28A therefore lies in the treatment of the TLV, completely resolved with LES in the hybrid RANS/LES approach.

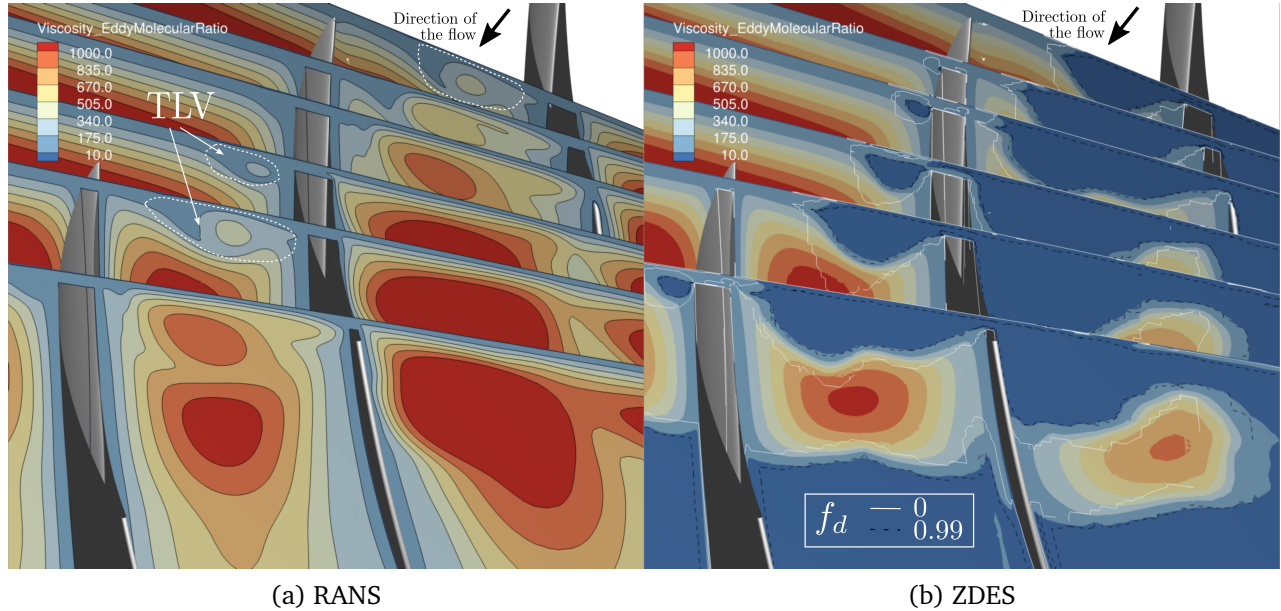


Figure C.14: Eddy-to-molecular viscosity ratio contours for RANS and ZDES cases. In the right-hand figure, isolines represent the two values of the sensor f_d indicated in the legend. A LES resolution corresponds to $f_d = 1$ and a RANS resolution to $f_d = 0$. Planes perpendicular to the suction side of the blade at 0, 10, 21, 40, 61, 95% c_a .

C.2.3.2 Topology of the flow

The topology of the TLF near the suction side can be seen in Figure C.15 for RANS and ZDES with a Q-criterion plotted, identifying the regions with vortices. The Q-criterion is plotted on the time-averaged conditions obtained over $20 T_{bp}$. The helicity here indicates the sense of rotation of the vortical structures. The structures described in the literature review are retrieved here. A vortex sheet is formed and the TLV rapidly detaches downstream the leading edge of the blade. Its interaction with the casing boundary layer generates the induced vortex, slightly visible here due to the RANS resolution near the leading edge with the ZDES. This is similar to the observations of Riéra [113] on the first rotor of CREATE: the little structures in the TLV are not visible with RANS and the induced vortex is hardly observable.

Tip-separation vortices (TSV) keep feeding the TLV formation farther downstream along the chord through a vortex sheet: it is well visible with the ZDES approach from about 30% c_a , where the vortex sheet consists of little vortical structures. These little vortices further energize the TLV. With RANS, the supply after 50% c_a is no longer visible and the structures are probably

quickly dissipated at this position where the LES resolution is a clear benefit. The topology observed with the Q-criterion is the same as that described by Boudet *et al.* in section 1.2.2.

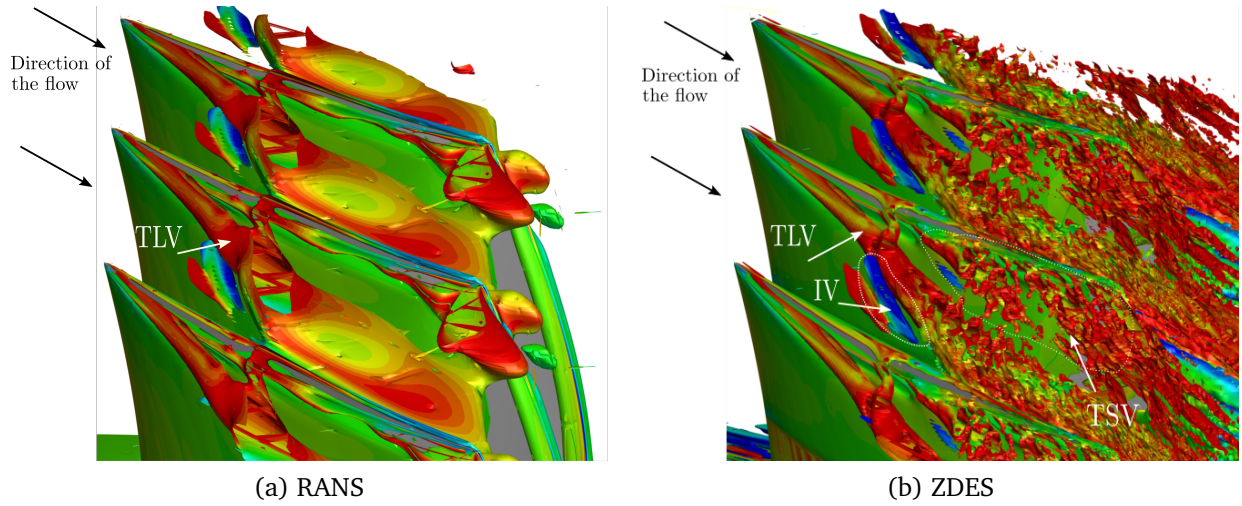


Figure C.15: Q-criterion colored by normalized helicity from -1 (blue) to $+1$ (red). The value for the Q-criterion is the same in both figures. This Q-criterion is computed on the time-averaged flow conditions.

Figure C.16a shows the experimental map of relative tangential velocity W_θ in the rotating frame of reference at 75% axial chord, obtained in the clearance region with the LDA measurements. The numerical solutions are compared with the experimental map in Figure C.16b and c. What was already observed through the vorticity evolution can also be seen here: the vortex region in the RANS approach shows more extension than the ZDES approach near the pressure side of the blade. One can indeed observe a large region of relative tangential velocity deficit near the pressure side of the blade with RANS, caused by the presence of the neighbouring blade TLV. The benefits of the hybrid approach can be appreciated in terms of flow topology: the flow topology obtained with ZDES is clearly more comparable with the experimental measurements than that obtained with RANS. The overestimate of the diffusion obtained with RANS can explain the larger region of W_θ deficit. The larger diffusion of the TLV occurring with RANS was already observed by Riéra [113] on the first rotor of CREATE, compared to the ZDES.

C.2.3.3 Loss analysis

As pointed out by Denton [40], the entropy is a good indicator of losses in turbomachinery. Indeed, for most machines, the flow is closely adiabatic and the entropy increase therefore corresponds to irreversibilities. The entropy variation is computed from the stagnation pressure and temperature, P_t and T_t , as follows

$$\Delta s = c_p \ln \frac{T_t}{T_{ref}} - R \ln \frac{P_t}{P_{ref}}, \quad (\text{C.9})$$

with P_{ref} and T_{ref} the averaged total pressure and temperature in plane 280.

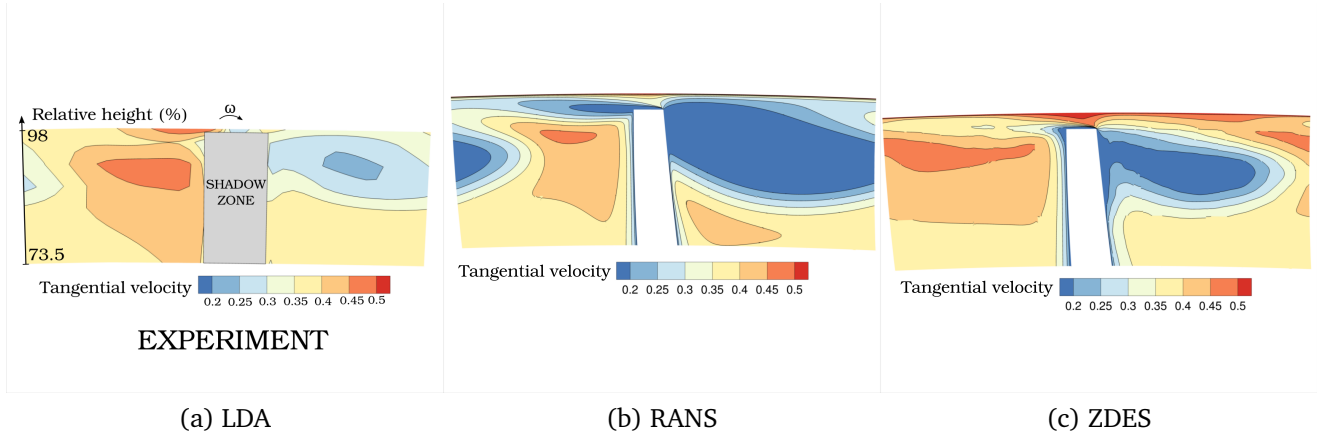


Figure C.16: Map of the opposite of the relative tangential velocity in the tip region, time-averaged in the rotor frame of reference, at 75% axial chord, between 73.5 and 98% height over one passage. The shadow zone approximates the position of the blade.

Representing the entropy in the tip region enables to locate the TLV and its extension in the passage. Figures C.17 and C.18 respectively show a blade-to-blade cut at 94% and 97% height coloured with entropy. The red values correspond to the higher values of entropy, that is, the locations where the losses are most significant. The TLV track is clearly visible at 94% height through these regions of high entropy, due to the significant axial vorticity magnitudes. This seems limited to the very core of the vortex with ZDES, which is smaller than that obtained with RANS. This can be explained by the higher diffusion yielded by the RANS approach: the vortex rapidly grows in size and eventually dissipates, inducing large losses all along its path. At 97%, the losses are spread over the whole passage in RANS while they remain less intense and less extended with ZDES.

The losses can also be illustrated by the vorticity evolution through the passage. The vorticity contours are plotted in Figure C.19 along the chord in planes perpendicular to the suction side of the blade. The influence of the TLV can be seen through the evolution of the axial vorticity in the current passage and its neighbour, given the periodicity in the simulation. For instance, the 61% c_a cut allows observing the vortex characteristics at this position and downstream of the trailing edge of the right-hand neighbouring blade. From this, it is interesting to notice the axial extension of the TLV, which is rapidly dissipated by RANS as it could already be inferred from the entropy analysis. The vorticity has almost completely decayed at this position with RANS while it is still persistent with ZDES. The evolution of the TLV through the passage is quite different depending on the numerical approach:

- With RANS, the vortex rapidly grows in size with a vorticity spread on a large diameter.
- With ZDES, the LES resolution following the vortex detachment allows resolving the most energetic vortical structures, which can clearly be seen from 95% axial chord, distributed around the vortex core. The TLV expansion continues downstream, where the structures divide into smaller and smaller structures.

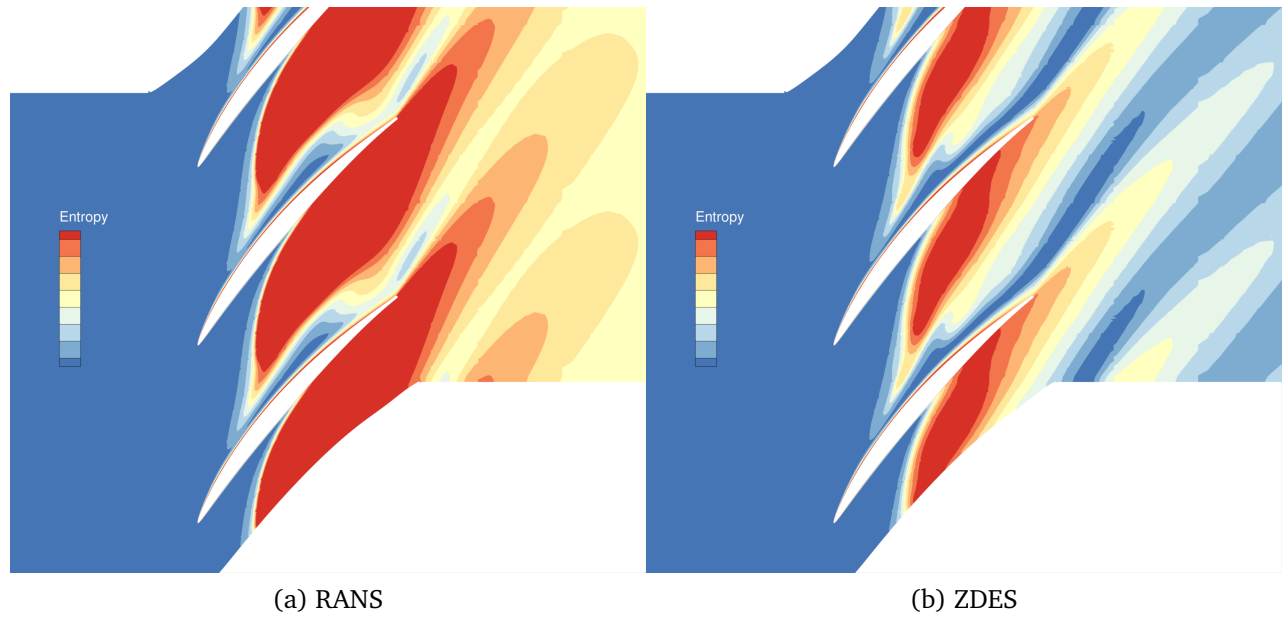


Figure C.17: Entropy contours at 94% height for RANS and ZDES approaches, with the same scale.

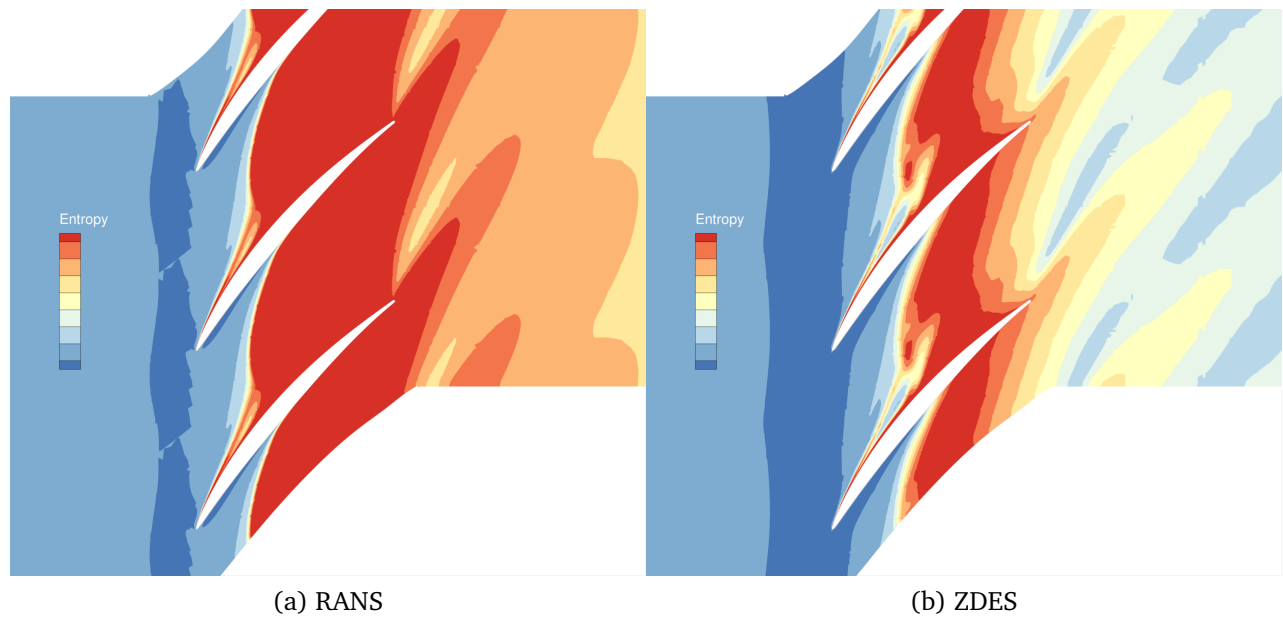


Figure C.18: Entropy contours at 97% height for RANS and ZDES approaches, with the same scale.

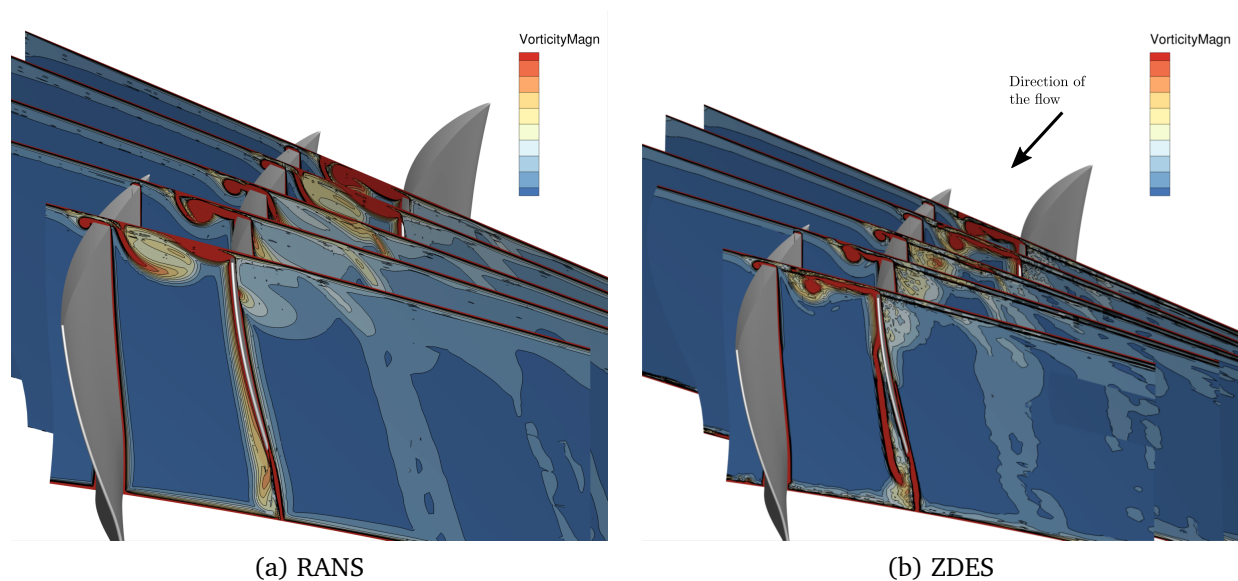


Figure C.19: Vorticity contours on planes perpendicular to the suction side at 10%, 21%, 40%, 61% and 95% c_a , for the steady RANS approach and the ZDES approach.

APPENDIX D

COMPLEMENTS ON CHAPTER 4

Contents

D.1 Derivation of the circulation around a rotor blade	228
--	-----

D.1 Derivation of the circulation around a rotor blade

Part of the study presented at the ASME TurboExpo 2020 [95] has been adapted to this appendix. This was a preliminary study on the Vortex Lattice Method. The idea was to better understand the interest of predicting the circulation at the tip, in particular that of the TLV.

The circulation is defined as the integration of the velocity over a contour C , writing:

$$\Gamma = \int_C \mathbf{V} \cdot d\mathbf{l}, \quad (\text{D.1})$$

where $d\mathbf{l}$ is an elementary vector, everywhere tangent to the contour C .

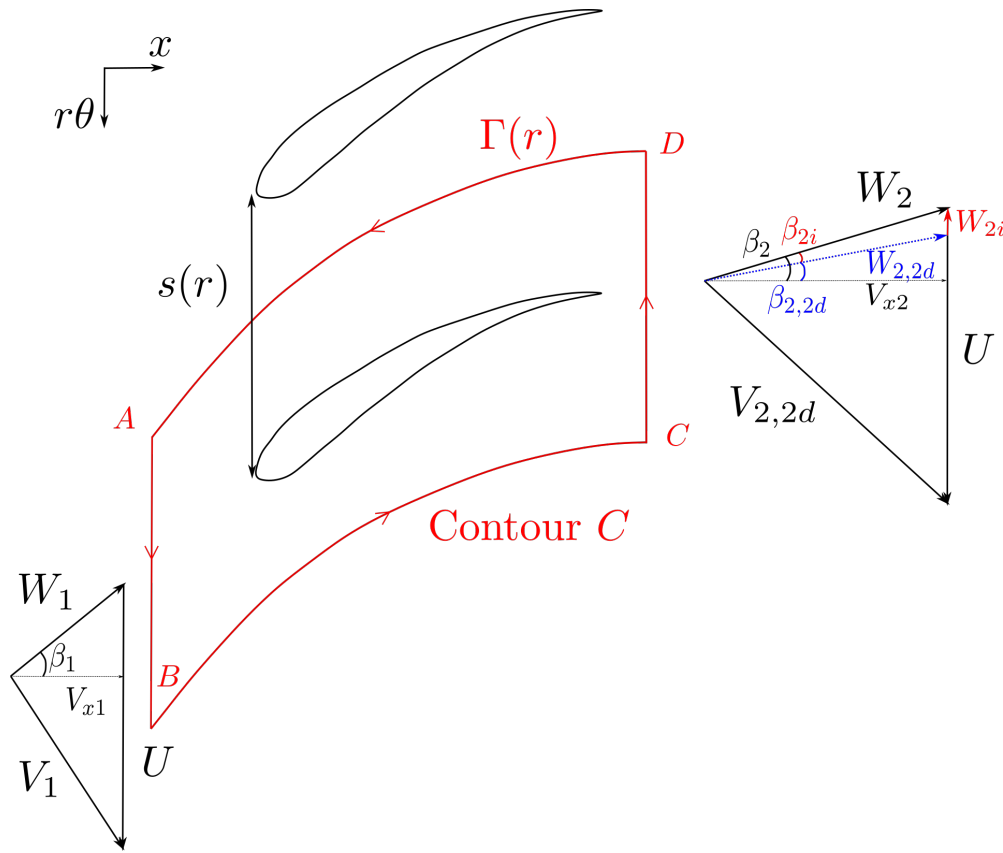


Figure D.1: Velocity triangles illustrating the modification of the deviation $\beta_{2,2d}$, here an underturn, due to the presence of the TLV, inducing the angle β_{2i} .

Let us express the circulation at the radius r , around a blade of a compressor row of pitch $s(r) = \frac{2\pi r}{N_{blades}}$ and consisting of N_{blades} blades. Figure D.1 indicates in red the contour C chosen around the blade. The curved line BC is a translation of the line AD of length $s(r)$ in the $r\theta$ direction. The two segments AB and CD are therefore of length $s(r)$.

Equation (D.1) can be decomposed in four terms, each on one segment of the contour:

$$\Gamma = \Gamma_{AB} + \Gamma_{BC} + \Gamma_{CD} + \Gamma_{DA} \quad (\text{D.2})$$

By periodicity, the two terms Γ_{BC} and Γ_{DA} cancel each other out since $\Gamma_{BC} = -\Gamma_{DA}$. The first term Γ_{AB} can be written:

$$\Gamma_{AB} = s(r)V_{\theta 1} \quad (D.3)$$

Similarly, we have:

$$\Gamma_{CD} = -s(r)V_{\theta 2}, \quad (D.4)$$

and therefore the circulation is a direct function of the deflection ΔV_{θ} :

$$\Gamma(r) = -s(r)\Delta V_{\theta}. \quad (D.5)$$

From Euler's equation, the blade loading is

$$\Delta h_0 = U\Delta V_{\theta}. \quad (D.6)$$

This shows that the circulation $\Gamma(r)$ at the radius r is proportional to the blade loading:

$$\Gamma(r) = -s(r)\frac{\Delta h_0(r)}{r\omega} = \frac{2\pi}{N_{blades}\omega}\Delta h_0(r) \quad (D.7)$$

where $U = r\omega$ and ω is the revolution speed of the row.

Relation (D.7) is verified as long as the flow is periodic over the different passages of the row. This is generally true for nominal incidence angles but getting closer to the surge margin limit may contradict this assumption. In our study, the focus is on the nominal operating points and this relation can reasonably be used.

Now, the blade circulation can be reexpressed as a function of the angles β_1 and β_2 :

$$\Gamma = -s\Delta V_{\theta} = -s\Delta W_{\theta} = -s(V_{x_2}\tan\beta_2 - V_{x_1}\tan\beta_1). \quad (D.8)$$

The idea is to see how the circulation of the TLV at the tip of the blade perturbs the deflection normally obtained if the flow follows the curvature of the blade, from the 2D design. The circulation $\Gamma(r)$ can be decomposed into a 2D component, constant, hence shedding no vorticity, minus the shed vorticity circulation Γ_i contributing to the TLV.

$$\Gamma(r) = \Gamma_{2d} - \Gamma_i \quad (D.9)$$

$\Gamma(r)$ and Γ_i can be calculated from which Γ_{2d} can be determined. This circulation is a constant from Helmholtz's theorems and therefore presents no variation spanwise, which corresponds to no shed vorticity. Finally, using (D.8) and (D.9), and neglecting the influence of shed vorticity on β_1 and V_x , we can define a 2D outflow angle $\beta_{2,2d}$ and an induced contribution β_i with

$$\Gamma_{2d} = -s(V_{x_2}\tan\beta_{2,2d} - V_{x_1}\tan\beta_1) \quad (D.10)$$

$$\Gamma_i = -sV_{x_2}[\tan\beta_{2,2d} - \tan(\beta_{2,2d} - \beta_i)] \quad (D.11)$$

Given the distribution of circulation, it is therefore possible to retrieve the velocity triangles due to that circulation, here assuming a constant flow coefficient V_{x2}/U in the schematic. In reality, as well as the blade loading, the flow coefficient varies due to the presence of the induced circulation: their variation can be computed with Biot-Savart's law, yielding the velocity components.

From the design point of view, if one is only interested in reducing tip-leakage flows, a definition of the ideal case is a constant work design. In that specific case, the circulation Γ does not depend on the radius of the blade since the loading is kept constant spanwise. Without any variation spanwise, no vorticity is shed downstream and the 3D effects do not impact the 2D design of the blade. A criterion to estimate the efficiency of the design regarding tip-leakage flows could be defined as the mean deviation between an equivalent constant work design with the mean circulation Γ_{ref} and the actual design, *i.e.*

$$D_{design} = \frac{1}{r_{tip} - r_{hub}} \int_{r_{hub}}^{r_{tip}} \left| \frac{\Gamma_{blade} - \Gamma_{ref}}{\Gamma_{ref}} \right| dr \quad (D.12)$$

with

$$\Gamma_{ref} = \frac{1}{r_{tip} - r_{hub}} \int_{r_{hub}}^{r_{tip}} \Gamma_{blade}(r) dr \quad (D.13)$$

Defining a coherent and relevant measure of loss is challenging. The present method is inviscid and incompressible so there is no generation of entropy. Losses arise through induced drag and can be evaluated from shed vorticity.

BIBLIOGRAPHY

- [1] LEAP engine from Safran. URL https://www.safran-group.com/media/20150615_leap-engine-continues-deliver.
- [2] K. Aainsqatsi. Turbofan operation, 2008. URL [https://commons.wikimedia.org/wiki/File:Turbofan_operation_\(lbp\).png](https://commons.wikimedia.org/wiki/File:Turbofan_operation_(lbp).png).
- [3] H. W. Allen and M. G. Kofskey. Visualization Study of Secondary Flows in Turbine Rotor Tip Regions. 1955.
- [4] S. R. Allmaras and F. T. Johnson. Modifications and clarifications for the implementation of the Spalart-Allmaras turbulence model. In *Seventh international conference on computational fluid dynamics (ICCFD7)*, pages 1–11, 2012.
- [5] R. H. Aungier. *Axial-flow compressors: a Strategy for Aerodynamic Design and Analysis*. ASME Press. Jan. 2013.
- [6] S. C. C. Bailey and S. Tavoularis. Measurements of the velocity field of a wing-tip vortex, wandering in grid turbulence. *Journal of Fluid Mechanics*, 601:281, 2008. Publisher: Cambridge University Press.
- [7] S. J. Barker and S. C. Crow. The motion of two-dimensional vortex pairs in a ground effect. *Journal of Fluid Mechanics*, 82(4):659–671, 1977. Publisher: Cambridge University Press.
- [8] R. A. Berdanier and N. L. Key. Experimental Investigation of Factors Influencing Operating Rotor Tip Clearance in Multistage Compressors. *International Journal of Rotating Machinery*, 2015, 2015.
- [9] J. L. Bettner and C. Elrod. The Influence of Tip Clearance, Stage Loading, and Wall Roughness on Compressor Casing Boundary Layer Development. In *ASME 1982 International Gas Turbine Conference and Exhibit*, pages V001T01A060–V001T01A060. American Society of Mechanical Engineers, 1982.

-
- [10] J. Boudet. Numerical investigation of the unsteadiness of a fan tip-leakage vortex. Aug. 2017. URL <https://hal.archives-ouvertes.fr/hal-01576613>.
- [11] J. Boudet, A. Cahuzac, P. Kausche, and M. C. Jacob. Zonal large-eddy simulation of a fan tip-clearance flow, with evidence of vortex wandering. *Journal of Turbomachinery*, 137(6), 2015. Publisher: American Society of Mechanical Engineers Digital Collection.
- [12] H. Brandt, L. Fottner, H. Saathoff, and U. Stark. Effects of the Inlet Flow Conditions on the Tip Clearance Flow of an Isolated Compressor Rotor. In *Volume 5: Turbo Expo 2002, Parts A and B*, pages 1123–1132, Amsterdam, The Netherlands, Jan. 2002. ASMEDC. ISBN 978-0-7918-3610-1. doi: 10.1115/GT2002-30639. URL <https://asmedigitalcollection.asme.org/GT/proceedings/GT2002/3610X/1123/292203>.
- [13] V. Brion. *Stabilité des paires de tourbillons contra-rotatifs: application au tourbillon de jeu dans les turbomachines*. PhD Thesis, 2009.
- [14] J. M. Brookfield. *Vortical flows in an adverse pressure gradient*. PhD Thesis, Massachusetts Institute of Technology, 1993.
- [15] R. O. J. Bullock. Aerodynamic Design of Axial Flow Compressors. Technical report, Jan. 1965. URL <https://ntrs.nasa.gov/search.jsp?R=19650013744>.
- [16] L. Cambier, S. Heib, and S. Plot. The Onera elsA CFD software: input from research and feedback from industry. *Mechanics & Industry*, 14(3):159–174, 2013.
- [17] T. R. Camp and I. J. Day. A Study of Spike and Modal Stall Phenomena in a Low-Speed Axial Compressor. *Journal of Turbomachinery*, 120(3):pp. 393–401, 1998. ISSN 0889504X. doi: 10.1115/1.2841730. URL <http://Turbomachinery.asmedigitalcollection.asme.org/article.aspx?articleid=1465430>.
- [18] D. Chapman. Computational aerodynamics development and outlook. *AIAA Journal*, 1979.
- [19] N. Chauvet, S. Deck, and L. Jacquin. Zonal Detached Eddy Simulation of a Controlled Propulsive Jet. *AIAA Journal*, pages 2458–2473, 2007.
- [20] G. T. Chen, E. M. Greitzer, C. S. Tan, and F. E. Marble. Similarity analysis of compressor tip clearance flow structure. In *ASME 1990 International Gas Turbine and Aeroengine Congress and Exposition*, pages V001T01A049–V001T01A049. American Society of Mechanical Engineers, 1990.
- [21] M. Choi, S. H. Oh, H. Y. Ko, and J. H. Baek. Effects of the Inlet Boundary Layer Thickness on Rotating Stall in an Axial Compressor. In *Volume 6: Turbomachinery, Parts A, B, and C*, pages 497–507, Berlin, Germany, Jan. 2008. ASMEDC. ISBN 978-0-7918-4316-1. doi: 10.1115/GT2008-50886. URL <https://asmedigitalcollection.asme.org/GT/proceedings/GT2008/43161/497/334418>.
-

- [22] G. Comte-Bellot and S. Corrsin. Simple Eulerian time correlation of full-and narrow-band velocity signals in grid-generated, 'isotropic' turbulence. *Journal of Fluid Mechanics*, 48(2): 273–337, 1971. Publisher: Cambridge University Press.
- [23] N. Courtiade. *Experimental analysis of the unsteady flow and instabilities in a high-speed multistage compressor*. PhD, Ecole Centrale de Lyon, Nov. 2012.
- [24] N. Courtiade and X. Ottavy. Experimental Study of Surge Precursors in a High-Speed Multistage Compressor. *Journal of Turbomachinery*, 135(6):061018 (9 pp.), Sept. 2013. ISSN 0889-504X. doi: 10.1115/1.4023462. URL <http://dx.doi.org/10.1115/1.4023462>.
- [25] F. Crevel. *Simulation numérique de l'écoulement en régime de pompage dans un compresseur axial multi-étage*. phdthesis, Ecole Centrale de Lyon, Ecully, France, Sept. 2013.
- [26] F. Crevel, N. Gourdain, and X. Ottavy. Numerical Simulation of Aerodynamic Instabilities in a Multistage High-Speed High-Pressure Compressor on Its Test Rig—Part II: Deep Surge. *Journal of Turbomachinery*, 136(10):101004–101004, July 2014. ISSN 0889-504X. doi: 10.1115/1.4027968. URL <http://dx.doi.org/10.1115/1.4027968>.
- [27] L. Crocco. Eine neue Stromfunktion für die Erforschung der Bewegung der Gase mit Rotation. *ZAMM-Journal of Applied Mathematics and Mechanics/Zeitschrift für Angewandte Mathematik und Mechanik*, 17(1):1–7, 1937. Publisher: Wiley Online Library.
- [28] A. J. Crook. *Numerical investigation of endwall/casing treatment flow phenomena*. Thesis, Massachusetts Institute of Technology, 1989. URL <https://dspace.mit.edu/handle/1721.1/41316>. Accepted: 2008-04-23T14:44:58Z.
- [29] A. J. Crook, E. M. Greitzer, C. S. Tan, and J. J. Adamczyk. Numerical Simulation of Compressor Endwall and Casing Treatment Flow Phenomena. *Journal of Turbomachinery*, 115(3):501–512, July 1993. ISSN 0889-504X, 1528-8900. doi: 10.1115/1.2929280. URL <https://asmedigitalcollection.asme.org/turbomachinery/article/115/3/501/420192/Numerical-Simulation-of-Compressor-Endwall-and>.
- [30] R. M. Cummings, W. H. Mason, S. A. Morton, and D. R. McDaniel. *Applied computational aerodynamics: A modern engineering approach*, volume 53. Cambridge University Press, 2015.
- [31] N. A. Cumpsty. *Compressor aerodynamics*. Longman Scientific & Technical, 1989.
- [32] U. Dallmann. Topological structures of three-dimensional vortex flow separation. In *16th Fluid and Plasmadynamics Conference*. American Institute of Aeronautics and Astronautics. doi: 10.2514/6.1983-1735. URL <https://arc.aiaa.org/doi/abs/10.2514/6.1983-1735>. _eprint: <https://arc.aiaa.org/doi/pdf/10.2514/6.1983-1735>.
- [33] I. J. Day. Stall Inception in Axial Flow Compressors. *Journal of Turbomachinery*, 115(1): pp. 1–9, Jan. 1993. doi: 10.1115/1.2929209.

-
- [34] I. J. Day. Stall, Surge and 75 Years of Research. In *Proceedings of ASME Turbo Expo 2015*, Montreal, Canada, June 2015. doi: 10.1115/GT2015-44109. URL <http://dx.doi.org/10.1115/GT2015-44109>.
- [35] S. Deck. Recent improvements in the zonal detached eddy simulation (ZDES) formulation. *Theoretical and Computational Fluid Dynamics*, 26(6):523–550, 2012.
- [36] S. Deck and R. Laraufie. Numerical investigation of the flow dynamics past a three-element aerofoil. *Journal of Fluid Mechanics*, 732:401–444, 2013.
- [37] S. Deck and N. Renard. Towards an enhanced protection of attached boundary layers in hybrid RANS/LES methods. *Journal of Computational Physics*, 400:108970, Jan. 2020. ISSN 0021-9991. doi: 10.1016/j.jcp.2019.108970. URL <http://www.sciencedirect.com/science/article/pii/S0021999119306758>.
- [38] S. Deck, P.-E. Weiss, M. Pamies, and E. Garnier. Zonal detached eddy simulation of a spatially developing flat plate turbulent boundary layer. *Computers & Fluids*, 48(1):1–15, 2011.
- [39] I. Delbende and M. Rossi. The dynamics of a viscous vortex dipole. *Physics of Fluids*, 21(7):073605, 2009. Publisher: American Institute of Physics.
- [40] J. Denton. Loss Mechanisms in Turbomachines. Technical report, The American Society of Mechanical Engineers, New York, 1993.
- [41] J. D. Denton. Some limitations of turbomachinery CFD. Proceedings of ASME Turbo Expo 2010 GT2010-22540, Whittle Laboratory, Glasgow, June 2010.
- [42] B. Deveaux. *Analyse et contrôle de l'écoulement de jeu d'une aube fixe isolée*. PhD thesis, Hesam Université, Ecole Nationale Supérieure d'Arts et Métiers, Mar. 2020.
- [43] B. Deveaux, C. Fournis, V. Brion, J. Marty, and A. Dazin. Experimental analysis and modeling of the losses in the tip leakage flow of an isolated, non-rotating blade setup. *Experiments in Fluids*, 61(5):1–23, 2020. Publisher: Springer.
- [44] S. Dixon and C. Hall. *Fluid Mechanics and Thermodynamics of Turbomachinery*. Butterworth-Heinemann, 7th edition, Oct. 2013. ISBN 978-93-5107-177-8.
- [45] Y. Dong, Z. Xinqian, and L. Qiushi. An 11-stage axial compressor performance simulation considering the change of tip clearance in different operating conditions. *Proceedings of the Institution of Mechanical Engineers, Part A: Journal of Power and Energy*, 228(6):614–625, Sept. 2014. ISSN 0957-6509, 2041-2967. doi: 10.1177/0957650914535389. URL <http://journals.sagepub.com/doi/10.1177/0957650914535389>.
- [46] A. Doukelis, K. Mathioudakis, and K. Papailiou. The effect of tip clearance gap size and wall rotation on the performance of a high-speed annular compressors cascade. *The American Society of Mechanical Engineers*, (98-GT-98):1–8, 1998.
-

- [47] M. Drela. XFOIL: An Analysis and Design System for Low Reynolds Number Airfoils, 1989.
- [48] R. P. Dring, H. D. Joslyn, and L. W. Hardin. An Investigation of Axial Compressor Rotor Aerodynamics. *Journal of Engineering for Power*, 104(1):84–96, Jan. 1982. ISSN 0022-0825. doi: 10.1115/1.3227270. URL <https://asmedigitalcollection.asme.org/gasturbinespower/article/104/1/84/405228/An-Investigation-of-Axial-Compressor-Rotor>.
- [49] H. W. Emmons, C. Pearson, and H. Grant. Compressor Surge and Stall Propagation. In *Trans. ASME* 77, pages pp. 455–469, 1955.
- [50] M. Furukawa, M. Inoue, K. Saiki, and K. Yamada. The role of tip leakage vortex breakdown in compressor rotor aerodynamics. 1999.
- [51] F. Gao, W. Ma, G. Zambonini, J. Boudet, X. Ottavy, L. Lu, and L. Shao. Large-eddy simulation of 3-D corner separation in a linear compressor cascade. *Physics of Fluids*, 27(8):085105, Aug. 2015. ISSN 1070-6631, 1089-7666. doi: 10.1063/1.4928246. URL <http://aip.scitation.org/doi/10.1063/1.4928246>.
- [52] C. W. Gear. Algorithm 407: DIFSUB for solution of ordinary differential equations [D2]. *Communications of the ACM*, 14(3):185–190, 1971. Publisher: ACM New York, NY, USA.
- [53] C. W. Gear. Numerical initial value problems in ordinary differential equations. *nivp*, 1971.
- [54] W. K. George, P. D. Beuther, and R. E. Arndt. Pressure spectra in turbulent free shear flows. *J. Fluid Mech*, 148:155–191, 1984.
- [55] B. Gothert. Plane and three-dimensional flow at high subsonic speeds. 1946.
- [56] N. Gourdain, F. Wlassow, and X. Ottavy. Effect of Tip Clearance Dimensions and Control of Unsteady Flows in a Multi-Stage High-Pressure Compressor. *Journal of Turbomachinery*, 134(5), Sept. 2012. ISSN 0889-504X. doi: 10.1115/1.4003815. URL <https://asmedigitalcollection.asme.org/turbomachinery/article/134/5/051005/456812/Effect-of-Tip-Clearance-Dimensions-and-Control-of>. Publisher: American Society of Mechanical Engineers Digital Collection.
- [57] L. Graftieux, M. Michard, and N. Grosjean. Combining PIV, POD and vortex identification algorithms for the study of unsteady turbulent swirling flows. *Measurement Science and technology*, 12(9):1422, 2001. Publisher: IOP Publishing.
- [58] E. M. Greitzer. Surge and rotating stall in axial flow compressors, Part I: Theoretical compression system model. *transactions for the ASME*, pages 190–198, Apr. 1976. 00913.
- [59] E. M. Greitzer, C. S. Tan, and M. B. Graf. *Internal flow: concepts and applications*, volume 3. Cambridge University Press, 2007.

-
- [60] J. Grilliat. *Contribution à l'étude aéroacoustique des écoulements de jeu*. PhD Thesis, Ecole Centrale de Lyon, Dec. 2009.
- [61] C. Hah. Effects of double-leakage tip clearance flow on the performance of a compressor stage with a large rotor tip gap. *Journal of Turbomachinery*, 139(6), 2017. Publisher: American Society of Mechanical Engineers Digital Collection.
- [62] M. Hewkin-Smith, G. Pullan, S. D. Grimshaw, E. M. Greitzer, and Z. S. Spakovszky. The Role of Tip Leakage Flow in Spike-Type Rotating Stall Inception. In *Volume 2D: Turbomachinery*, page V02DT46A009, Charlotte, North Carolina, USA, June 2017. American Society of Mechanical Engineers. ISBN 978-0-7918-5081-7. doi: 10.1115/GT2017-63655. URL <https://asmedigitalcollection.asme.org/GT/proceedings/GT2017/50817/Charlotte,%20North%20Carolina,%20USA/242105>.
- [63] P. G. Hill, U. W. Schaub, and Y. Senoo. Turbulent Wakes in Pressure Gradients. *Journal of Applied Mechanics*, 30(4):518–524, Dec. 1963. ISSN 0021-8936. doi: 10.1115/1.3636612. URL <https://asmedigitalcollection.asme.org/appliedmechanics/article/30/4/518/386986/Turbulent-Wakes-in-Pressure-Gradients>. Publisher: American Society of Mechanical Engineers Digital Collection.
- [64] D. A. Hoying, C. S. Tan, H. D. Vo, and E. M. Greitzer. Role of blade passage flow structures in axial compressor rotating stall inception. In *ASME 1998 International Gas Turbine and Aeroengine Congress and Exhibition*, pages V001T01A138–V001T01A138. American Society of Mechanical Engineers, 1998.
- [65] M. Inoue and M. Kuroumaru. Structure of Tip Clearance Flow in an Isolated Axial Compressor Rotor. *ASME Journal of Turbomachinery*, 111(3):250–256, 1989.
- [66] M. Inoue, M. Kuroumaru, and M. Fukuhara. Behavior of Tip Leakage Flow Behind an Axial Compressor Rotor. *Journal of Engineering for Gas Turbines and Power*, 108(1):7–14, Jan. 1986. ISSN 0742-4795, 1528-8919. doi: 10.1115/1.3239889. URL <https://asmedigitalcollection.asme.org/gasturbinespower/article/108/1/7/406572/Behavior-of-Tip-Leakage-Flow-Behind-an-Axial>.
- [67] R. M. James. On the remarkable accuracy of the vortex lattice method. *Computer Methods in Applied Mechanics and Engineering*, 1(1):59–79, 1972.
- [68] N. Jarrin, S. Benhamadouche, D. Laurence, and R. Prosser. A synthetic-eddy-method for generating inflow conditions for large-eddy simulations. *International Journal of Heat and Fluid Flow*, 27(4):585–593, 2006.
- [69] V. John. *Large Eddy Simulation of turbulent incompressible flows: analytical and numerical results for a class of LES models*. Springer Science & Business Media. 2003.
- [70] S. Kang and C. Hirsch. Tip leakage flow in linear compressor cascade. *Journal of Turbomachinery*, 116:657–664, 1994.
-

- [71] S. Kang and C. H. Hirsch. Experimental study on the three-dimensional flow within a compressor cascade with tip clearance: Part II—the tip leakage vortex. 1993.
- [72] J. Katz and A. Plotkin. *Low-Speed Aerodynamics*. 2001.
- [73] S. A. Khalid. *The Effects of Tip Clearance on Axial Compressor Pressure Rise*. PhD Thesis, Massachusetts Institute of Technology, Boston, 1995.
- [74] S. A. Khalid, A. S. Khalsa, I. A. Waitz, C. S. Tan, E. M. Greitzer, N. A. Cumpsty, J. J. Adamczyk, and F. E. Marble. Endwall blockage in axial compressors. In *Turbo Expo: Power for Land, Sea, and Air*, volume 78620, page V001T01A047. American Society of Mechanical Engineers, 1998.
- [75] S. A. Khalid, A. S. Khalsa, I. A. Waitz, C. S. Tan, E. M. Greitzer, N. A. Cumpsty, J. J. Adamczyk, and F. E. Marble. Endwall Blockage in Axial Compressors. *Journal of Turbomachinery*, 121:499–509, 1999.
- [76] A. S. Khalsa. *Endwall Blockage in Axial Compressors*. PhD Thesis, Massachusetts Institute of Technology, Boston, 1996.
- [77] C. C. Koch and L. H. Smith. Loss Sources and Magnitudes in Axial-Flow Compressors. *Journal of Engineering for Power*, 98(3):411–424, July 1976. ISSN 0022-0825. doi: 10.1115/1.3446202. URL <https://asmedigitalcollection.asme.org/gasturbinespower/article/98/3/411/402736/Loss-Sources-and-Magnitudes-in-AxialFlow>.
- [78] W. M. Kutta. Auftriebskräfte in strömenden Flüssigkeiten. *Illustrierte Aeronautische Mitteilungen*, 6(133):133–135, 1902.
- [79] B. Lakshminarayana. Methods of predicting the tip clearance effects in axial flow turbomachinery. 1970.
- [80] B. Lakshminarayana and J. Horlock. Tip-clearance flow and losses for an isolated compressor blade. Technical report, Aeronautical Research Council Reports and Memoranda, London, 1963.
- [81] B. Lakshminarayana and J. t. Horlock. *Leakage and secondary flows in compressor cascades*. HM Stationery Office, 1965.
- [82] H. Lamb. *Hydrodynamics*. University Press, 1932.
- [83] V. M. Lei, Z. S. Spakovszky, and E. M. Greitzer. A Criterion for Axial Compressor Hub-Corner Stall. In *Volume 6: Turbomachinery, Parts A and B*, pages 475–486, Barcelona, Spain, Jan. 2006. ASMEDC. ISBN 978-0-7918-4241-6 978-0-7918-3774-0. doi: 10.1115/GT2006-91332. URL <https://asmedigitalcollection.asme.org/GT/proceedings/GT2006/4241X/475/316859>.

- [84] S. Lieblein. Loss and Stall Analysis of Compressor Cascades. *Journal of Basic Engineering*, 81(3):387–397, Sept. 1959. ISSN 0021-9223. doi: 10.1115/1.4008481. URL <https://asmedigitalcollection.asme.org/fluidsengineering/article/81/3/387/367840/Loss-and-Stall-Analysis-of-Compressor-Cascades>. Publisher: American Society of Mechanical Engineers Digital Collection.
- [85] S. Lieblein, F. C. Schwenk, and R. L. Broderick. Diffusion factor for estimating losses and limiting blade loadings in axial-flow-compressor blade elements. Technical report, DTIC Document, 1953. URL <http://oai.dtic.mil/oai/oai?verb=getRecord&metadataPrefix=html&identifier=AD0011178>. 00210.
- [86] D. Lilly. The representation of small scale turbulence in numerical simulation experiments. pages 195–210, 1967.
- [87] R. Mailach, I. Lehmann, and K. Vogeler. Periodical Unsteady Flow Within a Rotor Blade Row of an Axial Compressor—Part II: Wake-Tip Clearance Vortex Interaction. *Journal of Turbomachinery*, 130(4):041005, Oct. 2008. ISSN 0889-504X, 1528-8900. doi: 10.1115/1.2812330. URL <https://asmedigitalcollection.asme.org/turbomachinery/article/doi/10.1115/1.2812330/433673/Periodical-Unsteady-Flow-Within-a-Rotor-Blade-Row>.
- [88] J. Marty and B. Aupoix. Interaction of shrouded stator flow and main flow and its influence on performances of a three-stage high pressure compressor <sup/>. *Proceedings of the Institution of Mechanical Engineers, Part A: Journal of Power and Energy*, 226(4): 489–500, June 2012. ISSN 0957-6509, 2041-2967. doi: 10.1177/0957650911414322. URL <http://journals.sagepub.com/doi/10.1177/0957650911414322>.
- [89] J. Marty and C. Uribe. Impact of Underlying RANS Turbulence Models in Zonal Detached Eddy Simulation: Application to a Compressor Rotor. *International Journal of Turbomachinery, Propulsion and Power*, 5(3):22, Aug. 2020. ISSN 2504-186X. doi: 10.3390/ijtp5030022. URL <https://www.mdpi.com/2504-186X/5/3/22>.
- [90] R. S. Mazzawy. Surge-Induced Structural Loads in Gas Turbines. *Journal of Engineering for Power*, 102(1):162–168, Jan. 1980. ISSN 0022-0825. doi: 10.1115/1.3230217. URL <https://asmedigitalcollection.asme.org/gasturbinespower/article/102/1/162/405102/SurgeInduced-Structural-Loads-in-Gas-Turbines>.
- [91] G. L. Mellor and G. M. Wood. An axial compressor end-wall boundary layer theory. *Journal of Basic Engineering*, 93(2):300–314, 1971.
- [92] L. M. Milne-Thomson. *Theoretical Hydrodynamics*. Courier Corporation, Jan. 1996. ISBN 978-0-486-68970-8. Google-Books-ID: PMyRvLX714MC.
- [93] J.-F. Monier, J. Boudet, J. Caro, and L. Shao. Turbulent Energy Budget in a Tip Leakage Flow: A Comparison Between RANS and LES. In *Volume 2B: Turboma-*

- chinery, page V02BT41A020, Charlotte, North Carolina, USA, June 2017. American Society of Mechanical Engineers. ISBN 978-0-7918-5079-4. doi: 10.1115/GT2017-63611. URL <https://asmedigitalcollection.asme.org/GT/proceedings/GT2017/50794/Charlotte,%20North%20Carolina,%20USA/241507>.
- [94] J.-F. Monier, N. Poujol, M. Laurent, F. Gao, J. Boudet, S. Aubert, and L. Shao. LES Investigation of Boussinesq Constitutive Relation Validity in a Corner Separation Flow. In *Volume 2C: Turbomachinery*, page V02CT42A023, Oslo, Norway, June 2018. American Society of Mechanical Engineers. ISBN 978-0-7918-5101-2. doi: 10.1115/GT2018-75792. URL <https://asmedigitalcollection.asme.org/GT/proceedings/GT2018/51012/Oslo,%20Norway/272387>.
- [95] C. Montsarrat, B. Deveaux, J. Boudet, J. Marty, and E. Lippinois. Vortex lattice method for the calculation of the tip leakage flow: Evaluation on a single blade. In *Turbo Expo: Power for Land, Sea, and Air*, volume 84065, page V02AT32A034. American Society of Mechanical Engineers, 2020.
- [96] F. K. Moore. Lift hysteresis at stall as an unsteady boundary-layer phenomenon. 1956.
- [97] J. Moore and J. S. Tilton. Tip Leakage Flow in a Linear Turbine Cascade. *Journal of Turbomachinery*, 110(1):18–26, Jan. 1988. ISSN 0889-504X, 1528-8900. doi: 10.1115/1.3262162. URL <https://asmedigitalcollection.asme.org/turbomachinery/article/110/1/18/418212/Tip-Leakage-Flow-in-a-Linear-Turbine-Cascade>.
- [98] I. N. Moyle. An Experimental and Analytical Study of Tip Clearance Effects in Axial Flow Compressors. Technical report, Naval Postgraduate School, Monterey, California, 1991.
- [99] B. G. Newman. Flow in a Viscous Trailing Vortex. *The Aeronautical Quarterly*, 10(2): 149–162, May 1959. ISSN 0001-9259. doi: 10.1017/S0001925900001554. URL <https://www.cambridge.org/core/journals/aeronautical-quarterly/article/flow-in-a-viscous-trailing-vortex/C0A892BBF58BD8D678BC6877BF57F224>. Publisher: Cambridge University Press.
- [100] J. N. Newman. *Marine hydrodynamics*. The MIT press, 2018.
- [101] I. K. Nikolos, D. I. Douvikas, and K. D. Papailiou. Theoretical Modelling of Relative Wall Motion Effects in Tip Leakage Flow. In *Volume 1: Turbomachinery*, page V001T01A017, Houston, Texas, USA, June 1995. American Society of Mechanical Engineers. ISBN 978-0-7918-7878-1. doi: 10.1115/95-GT-088. URL <https://asmedigitalcollection.asme.org/GT/proceedings/GT1995/78781/Houston,%20Texas,%20USA/246427>.
- [102] P. R. Owen. The decay of a turbulent trailing vortex. *The Aeronautical Quarterly*, 21(1): 69–78, 1970. Publisher: Cambridge University Press.
- [103] M. Pamiès, P.-E. Weiss, E. Garnier, S. Deck, and P. Sagaut. Generation of synthetic turbulent inflow data for large eddy simulation of spatially evolving wall-bounded flows. *Physics of Fluids*, 21(4):045103, 2009.
-

- [104] V. Perrot, A. Touyeras, and G. Lucien. Detailed cfd analysis of a grooved casing treatment on an axial subsonic compressor. In *Proceedings of the 7th European Turbomachinery Conference*, 2007.
- [105] U. Piomelli and J. Van Beeck. Lecture Series - Large Eddy Simulation Theory and Applications. Von Karman Institute, May 2018.
- [106] U. Piomelli, Y. Yu, and R. J. Adrian. Subgrid-scale energy transfer and near-wall turbulence structure. 8(215), 1996.
- [107] S. Pope. *Turbulent Flows*. 2000.
- [108] S. B. Pope. Ten questions concerning the large-eddy simulation of turbulent flows. *New journal of Physics*, 6(1):35, 2004.
- [109] L. Prandtl. Tragflügeltheorie. Technical report, Göttingen Universität, Göttingen, Feb. 1919.
- [110] G. Pullan, A. M. Young, I. J. Day, E. M. Greitzer, and Z. S. Spakovszky. Origins and Structure of Spike-Type Rotating Stall. *Journal of Turbomachinery*, 137(5):051007 (11 pp.), May 2015. ISSN 0889-504X. doi: 10.1115/1.4028494. URL <http://dx.doi.org/10.1115/1.4028494>.
- [111] D. A. Rains. *Tip clearance Flows in Axial Compressors and Pumps*. PhD Thesis, California Institute of Technology, Pasadena, California, 1954.
- [112] L. Reid and D. C. Urasek. Experimental evaluation of the effects of a blunt leading edge on the performance of a transonic rotor. 1973.
- [113] W. Riéra. *Evaluation of the ZDES method on an axial compressor: analysis of the effects of upstream wake and throttle on the tip-leakage flow*. PhD Thesis, Université de Lyon, Lyon, Nov. 2014.
- [114] W. Riéra, J. Marty, L. Castillon, and S. Deck. Zonal detached-eddy simulation applied to the tip-clearance flow in an axial compressor. *AIAA Journal*, pages 2377–2391, 2016.
- [115] N. Rochuon. *Analyse de l'écoulement tridimensionnel et instationnaire dans un compresseur centrifuge à fort taux de pression*. These de doctorat, Ecully, Ecole centrale de Lyon, Jan. 2007. URL <https://www.theses.fr/2007ECDL0005>.
- [116] A. Sadikin, N. A. M. Yunus, S. A. Abd Hamid, S. M. Salleh, M. N. A. Rahman, S. Mahzan, and S. S. Ayop. A comparative study of turbulence models on aerodynamics characteristics of a NACA0012 airfoil. *International Journal of Integrated Engineering*, 10(1), 2018.
- [117] P. Sagaut and I. Mary. Large Eddy Simulation of flow around an airfoil near stall. *AIAA Journal*, pages 1139–1145, 2002.

- [118] P. Sagaut, S. Deck, and M. Terracol. *Multiscale and Multiresolution Approaches in Turbulence*. Imperial College Press, 2006.
- [119] H. Schlichting. *Boundary-Layer Theory*. Mc Graw Hill. 1979.
- [120] H. Schoenenborn and T. Breuer. Aeroelasticity at Reversed Flow Conditions — Part II: Application to Compressor Surge. *Journal of Turbomachinery*, 134(6): 061031, Nov. 2012. ISSN 0889-504X, 1528-8900. doi: 10.1115/1.4006309. URL <https://asmedigitalcollection.asme.org/turbomachinery/article/doi/10.1115/1.4006309/477426/Aeroelasticity-at-Reversed-Flow-Conditions-Part-II>.
- [121] H. D. Schulz, H. E. Gallus, and B. Lakshminarayana. Three-Dimensional Separated Flow Field in the Endwall Region of an Annular Compressor Cascade in the Presence of Rotor-Stator Interaction: Part 1—Quasi-Steady Flow Field and Comparison With Steady-State Data. *Journal of Turbomachinery*, 112(4):669–678, Oct. 1990. ISSN 0889-504X. doi: 10.1115/1.2927707. URL <https://asmedigitalcollection.asme.org/turbomachinery/article/112/4/669/433524/Three-Dimensional-Separated-Flow-Field-in-the>. Publisher: American Society of Mechanical Engineers Digital Collection.
- [122] D. Schönweitz, M. Voges, G. Goinis, G. Enders, and E. Johann. Experimental and numerical examinations of a transonic compressor-stage with casing treatment. In *ASME Turbo Expo 2013: Turbine Technical Conference and Exposition*. American Society of Mechanical Engineers Digital Collection, 2013.
- [123] M. Shur, P. Spalart, and M. Travin. Detached-eddy simulation of an airfoil at high angle of attack. *Proceedings of the Fourth International Symposium on Engineering Turbulence Modelling and Measurements*, pages 669–678, 1999.
- [124] B. T. Sirakov and C.-S. Tan. Effect of unsteady stator wake—rotor double-leakage tip clearance flow interaction on time-average compressor performance. *J. Turbomach.*, 125(3):465–474, 2003.
- [125] J. S. Smagorinsky. General circulation model of the atmosphere. *Mon. Weather Rev.*, 91: 99–164, 1963.
- [126] H. J. Smith, L. The radial-equilibrium equation of turbomachinery. In *Transactions of the American Society of Mechanical Engineers*, 1966.
- [127] L. H. Smith. Casing boundary layers in multistage axial-flow compressors. *Flow Research on Blading*, pages 275–304, 1970.
- [128] P. Spalart. Strategies for turbulence modelling and simulations. *International Journal of Heat and Fluid Flow*, 2000.

-
- [129] P. Spalart and S. Allmaras. A one-equation turbulence model for aerodynamic flows. In *30th Aerospace Sciences Meeting and Exhibit*, Reno,NV,U.S.A., Jan. 1992. American Institute of Aeronautics and Astronautics. doi: 10.2514/6.1992-439. URL <http://arc.aiaa.org/doi/10.2514/6.1992-439>.
- [130] P. Spalart and S. Allmaras. A one-equation turbulence model for aerodynamics flows. *La recherche Aérospatiale*, pages 5–21, 1994.
- [131] P. R. Spalart. Comments on the feasibility of LES for wings, and on a hybrid RANS/LES approach. 1997.
- [132] P. R. Spalart, S. Deck, M. L. Shur, K. D. Squires, M. K. Strelets, and A. Travin. A new version of detached-eddy simulation, resistant to ambiguous grid densities. *Theoretical and computational fluid dynamics*, 20(3):181, 2006. Publisher: Springer.
- [133] H. B. Squire. *The growth of a vortex in turbulent flow*, volume 16. ARC, 1954.
- [134] J. Storer and N. Cumpsty. An Approximate analysis and prediction method for tip clearance loss in axial compressors. *The American Society of Mechanical Engineers*, (93-GT-140):1–10, 1993.
- [135] J. A. Storer and N. A. Cumpsty. Tip leakage flow in axial compressors. *Journal of Turbomachinery*, 113(2):252–259, 1990.
- [136] C. Tan, I. Day, S. Morris, and A. Wadia. Spike-Type Compressor Stall Inception, Detection, and Control. *Annual Review of Fluid Mechanics*, 42(1):275–300, Jan. 2010. ISSN 0066-4189, 1545-4479. doi: 10.1146/annurev-fluid-121108-145603. URL <http://www.annualreviews.org/doi/10.1146/annurev-fluid-121108-145603>.
- [137] G. I. Taylor. Statistical theory of turbulence III-distribution of dissipation of energy in a pipe over its cross-section. *Proceedings of the Royal Society of London. Series A-Mathematical and Physical Sciences*, 151(873):455–464, 1935. Publisher: The Royal Society London.
- [138] E. O. Tuck. Some accurate solutions of the lifting surface integral equation. *The ANZIAM Journal*, 35(2):127–144, 1993.
- [139] C. Uribe. *Développement d’une approche ZDES à deux équations de transport et application turbomachines*. PhD Thesis, Université de la Sorbonne, Paris, Sept. 2018.
- [140] J. Van Geffen and G. F. van Heijst. Viscous evolution of 2D dipolar vortices. *Fluid dynamics research*, 22(4):191–213, 1998. Publisher: Elsevier.
- [141] M. H. Vavra. *Aerothermodynamics and Flow in turbomachines*. 1960.
- [142] H. D. Vo, C. S. Tan, and E. M. Greitzer. Criteria for spike initiated rotating stall. *Journal of turbomachinery*, 130(1):011023, 2008.
-

- [143] Y. Wang and W. J. Devenport. Wake of a Compressor Cascade with Tip Gap, Part 2: Effects of Endwall Motion. *AIAA Journal*, 42(11):2332–2340, Nov. 2004.
- [144] P. Welch. The use of fast Fourier transform for the estimation of power spectra: a method based on time averaging over short, modified periodograms. *IEEE Transactions on audio and electroacoustics*, 15(2):70–73, 1967. Publisher: IEEE.
- [145] D. C. Wilcox. *Turbulence modeling for CFD*, volume 2. DCW industries La Canada, CA, 1998.
- [146] D. C. Wisler. Loss Reduction in Axial-Flow Compressors Through Low-Speed Model Testing. *Journal of Engineering for Gas Turbines and Power*, 107(2): 354–363, Apr. 1985. ISSN 0742-4795, 1528-8919. doi: 10.1115/1.3239730. URL <https://asmedigitalcollection.asme.org/gasturbinespower/article/107/2/354/407811/Loss-Reduction-in-AxialFlow-Compressors-Through>.
- [147] F. Wlassow. Analyse instationnaire aérothermique d’un étage de turbine avec transport de points chauds. page 205, 2012.
- [148] K. Yamada, M. Furukawa, Y. Tamura, S. Saito, A. Matsuoka, and K. Nakayama. Large-Scale DES Analysis of Stall Inception Process in a Multi-Stage Axial Flow Compressor. In *Volume 2D: Turbomachinery*, page V02DT44A021, Seoul, South Korea, June 2016. American Society of Mechanical Engineers. ISBN 978-0-7918-4972-9. doi: 10.1115/GT2016-57104. URL <https://asmedigitalcollection.asme.org/GT/proceedings/GT2016/49729/Seoul,%20South%20Korea/239576>.
- [149] M. Yaras and S. A. Sjolander. Development of the tip-leakage flow downstream of a planar cascade of turbine blades: vorticity field. *Journal of Turbomachinery*, 112(4):609–617, 1990.
- [150] M. Yaras, Y. Zhu, and S. A. Sjolander. Flow Field in the Tip Gap of a Planar Cascade of Turbine Blades. *Journal of Turbomachinery*, 111(3):276–283, July 1989. ISSN 0889-504X, 1528-8900. doi: 10.1115/1.3262266. URL <https://asmedigitalcollection.asme.org/turbomachinery/article/111/3/276/419883/Flow-Field-in-the-Tip-Gap-of-a-Planar-Cascade-of>.
- [151] M. I. Yaras, S. A. Sjolander, and R. J. Kind. Effects of Simulated Rotation on Tip Leakage in a Planar Cascade of Turbine Blades: Part II—Downstream Flow Field and Blade Loading. *Journal of Turbomachinery*, 114(3):660–667, July 1992. ISSN 0889-504X, 1528-8900. doi: 10.1115/1.2929190. URL <https://asmedigitalcollection.asme.org/turbomachinery/article/114/3/660/419988/Effects-of-Simulated-Rotation-on-Tip-Leakage-in-a>.
- [152] R. E. York and H. S. Woodard. Supersonic compressor cascades—an analysis of the entrance region flow field containing detached shock waves. 1976.

- [153] D. You, M. Wang, P. Moin, and R. Mittal. Large-eddy simulation analysis of mechanisms for viscous losses in a turbomachinery tip-clearance flow. *Journal of Fluid Mechanics*, 586: 177–204, Apr. 2007.
- [154] D. You, M. Wang, P. Moin, and R. Mittal. Vortex dynamics and low-pressure fluctuations in the tip-clearance flow. 2007.

AUTORISATION DE SOUTENANCE

Vu les dispositions de l'arrêté du 25 mai 2016,

Vu la demande du directeur de thèse

Monsieur J. BOUDET

et les rapports de

M. M. MANNA

Professeur - Dipartimento di Ingegneria Industriale - Università degli Studi di Napoli Federico II
Via Claudio 21 - 80125 Naples - Italie

et de

M. N. BINDER

Professeur - Département d'Aérodynamique, Energétique et Propulsion - ISAE - SUPAERO
BP 54032 - 31055 Toulouse cedex 4

Monsieur MONTSARRAT Christophe

est autorisé à soutenir une thèse pour l'obtention du grade de **DOCTEUR**

Ecole doctorale Mécanique, Energétique, Génie Civil et Acoustique

Fait à Ecully, le 7 avril 2021

P/Le directeur de l'E.C.L.
Le directeur des Etudes


Grégory VIAL

ABSTRACT

Tip-leakage flow (TLF) represents a major limitation in compressor performance, complexifying the blade designs at the tips. Affecting both the losses and the performance, the tip-leakage vortex (TLV) forming at the tip of rotor blades is a dominant vortical structure that all designers aim to reduce. The TLV is mostly influenced by three parameters whose increase is detrimental to the performance of the compressor: the blade loading, the boundary layer at casing, and the tip gap size τ . The present thesis investigates the influence of the tip gap size on TLF. More specifically, the present work focuses on the evolution of three mean characteristics of the TLV with τ , whose variations can be directly related to the performance of the compressor rotor: the position where the TLV detaches from the blade, its trajectory, and its circulation Γ .

In order to investigate the influence of the tip gap size, two different methods are used in the present work. The first method relies on a Zonal Detached Eddy Simulation (ZDES), a hybrid RANS/LES approach, enabling to resolve the largest turbulent eddies where it is required. Such a method, generally more costly, is also generally more appropriate for secondary flows such as TLF than simulations based on RANS turbulence models. In particular, this enables a refined analysis on the turbulent fluctuations within the TLV. The second method is a low-order method, whose development is here carried out on tip-leakage flow configurations, gauging its capabilities when accounting for the tip gap size. The Vortex Lattice Method (VLM) relies on the use of vortex singularities to replicate the presence of an aerodynamic body, which induces a perturbation on the velocity field. This approach is computationally cheap and is dedicated to preliminary design, when a large quantity of geometries have to be evaluated.

A sensitivity study on the tip gap size is conducted on the third rotor of an experimental high-speed compressor with the use of ZDES. Three tip gap sizes are tested. The time-averaged analysis confirms results from the literature on the position of the detachment point. It also indicates that the mean trajectory of the TLV could be predicted by a model, based on the knowledge of the midspan loading. Finally, it puts forward the increase of circulation with the tip gap size, with a larger TLV core and higher levels of axial vorticity. The unsteady analysis focuses on the interaction between the neighbouring TLV and the TLF developing within the gap: the intensity of the double leakage phenomenon is largely affected by the tip gap size. The vortex fragmentation only observed with the largest gap could be related to the more intense double leakage and a possible vortex wandering, with low-frequency oscillations.

The use of the VLM on a simplified experimental TLF configuration, consisting of a single blade interacting with a casing endwall, shows that it is accurate for predicting the TLV circulation for large tip gaps but it requires improvements to account for the viscous effects on the diffusion of the TLV detaching from the blade and its interaction with the casing endwall. A diffusion model is developed as a correction to the original VLM in order to account for these effects. By considering the turbulent mixing of pairs of contra-rotating analytical vortices, the experimental increase of the circulation is well captured by the corrected VLM over a large range of tip gaps. Further developments are needed regarding the prediction of the blade loading, in order to predict the position of the detachment point. Also, in the continuity of this work, further developments are needed to use the VLM module on compressor rotors, in the long-term objective of building a fast and accurate predesign tool.

Keywords: Axial compressor, Tip-leakage flow (TLF), Tip-leakage vortex (TLV), Vorticity, Circulation, Zonal-Detached Eddy Simulation (ZDES), Vortex Lattice Method (VLM), Modelling